

INCLUSION REMOVAL AND GRAIN REFINEMENT OF MAGNESIUM ALLOY
CASTINGS

By

Abdallah Elsayed
MASc., Ryerson University, 2010
B.Eng., Ryerson University, 2008

A dissertation
presented to Ryerson University
in partial fulfillment of
the requirements for the degree of

Doctor of Philosophy

in the Program of
Mechanical and Industrial Engineering

Toronto, Ontario, Canada, 2015

© Abdallah Elsayed 2015

AUTHOR'S DECLARATION FOR SUBMISSION OF ELECTRONIC DISSERTATION

I hereby declare that I am the sole author of this dissertation. This is a true copy of the dissertation, including any required final revisions, as accepted by my examiners.

I authorize Ryerson University to lend this dissertation to other institutions or individuals for the purpose of scholarly research.

I further authorize Ryerson University to reproduce this dissertation by photocopying or by other means, in total or in part, at the request of other institutions or individuals for the purpose of scholarly research.

I understand that my dissertation may be made electronically available to the public.

ABSTRACT

Magnesium alloys show promise to be materials for lightweighting of automotive and aerospace vehicles improving fuel efficiencies and vehicle performance. A majority of magnesium alloy components are produced using casting where susceptibility to forming inclusions and coarse grain sizes could result. Development of effective inclusion removal techniques and better understanding of grain refinement of magnesium alloys could help in improving their mechanical properties to advance them to more structurally demanding applications. This research aimed to develop an environmentally friendly alternative to the grain refinement and inclusion removal capabilities of carbon based hexachloroethane as it releases dioxins, chlorine gas and corrodes foundry equipment. A secondary aim was to pioneer in-situ neutron diffraction to examine the solidification of magnesium alloys.

The research involved preparing tensile samples of AZ91E magnesium alloy using permanent mould casting. Inclusion removal was conducted by using filtration and argon gas bubbling. Castings grain refined using hexachloroethane (0.25, 0.50 and 0.75 wt.%) were compared against ex-situ aluminum-silicon carbide and in-situ aluminum-carbon based grain refiners combined with filtration and argon gas bubbling. Further, in-situ neutron diffraction was utilized for phase analysis and fraction solid determination of magnesium-zinc and magnesium-aluminum alloys.

There was a significant improvement in yield strength, ultimate tensile strength and elongation with filtration plus argon bubbling, carbon inoculation or both filtration plus argon bubbling and carbon inoculation. The results indicated that the mechanism of the observed ~20% reduction in grain sizes with carbon inoculation (hexachloroethane, ex-situ aluminum-silicon carbide and in-situ aluminum-carbon) was explained through duplex nucleation of Mn-Al and Al-Mg-C-O (likely Al_2MgC_2) phases. Finally, in-situ neutron diffraction was used to follow the formation of $\text{Mg}_{17}\text{Al}_{12}$ eutectic phase in a magnesium-9 wt.% aluminum alloy. For the magnesium-zinc alloys, in-situ neutron diffraction enabled characterization of the effects of zirconium to the fraction solid growth of $(10\bar{1}0)$, (0002) and $(10\bar{1}1)$ α -Mg planes.

The societal and environmental impact of this research is significant. There is a clear demonstration of alternatives to the universally used hexachloroethane grain refiner promoting harmful emissions. Improved mechanical properties resulting from new grain refinement and

inclusion filtration are a major advancement in promoting weight reduction, improved castability and decreased environmental impact for automotive and aerospace industries.

ACKNOWLEDGEMENTS

First and foremost, I would like to thank my supervisor, Prof. C. (Ravi) Ravindran for his continued guidance, support and instruction. His kindness and thoughtfulness aided me in both my academic and personal endeavours.

I also have great appreciation for Prof. B.S. Murty and the Micro-Nano Research Group at IIT-Madras (Chennai, India) namely Mr. S.L. Pramod, Mr. K. Akkiraju and Mr. A. Rao for material support and great hospitality during my research visit. Appreciation also goes to Dr. D. Sediako and all the technical staff at the Canadian Neutron Beam Centre for scheduling and setup for the neutron experiments.

I would also like to thank the technical support staff at Ryerson University; in particular, Mr. A. Machin, Mr. J. Amankrah, Mr. R. Churaman and Mr. Q. Li for their help with experimental setup, sample preparation and scanning electron microscopy analysis.

The staff and faculty at the University of Toronto namely, Prof. A. McLean, Prof. M. Barati, Dr. A. Danaei, Dr. P. Wu and Mr. G. Kretschmann deserve recognition for their help in the wettability experiments, characterisation and dissertation editing.

Further, I would like to thank Dr. S. L. Sin, Dr. F. D'Elia, Dr. A. Lombardi and the other members of the Centre for Near-net-shape Processing of Materials (Mr. S. Saha, Mr. E. Vandersluis and Mr. S. Ahmad) for experimental help and technical discussion.

The financial support from the Natural Science and Engineering Research Council of Canada and the Department of Mechanical and Industrial Engineering was necessary for completion of this dissertation and is well appreciated.

Finally, I would like to thank my family and friends for their continuous love and support. I could not have done it without them.

TABLE OF CONTENTS

	Page
AUTHOR’S DECLARATION FOR SUBMISSION OF ELECTRONIC DISSERTATION	ii
ABSTRACT.....	iii
ACKNOWLEDGEMENTS.....	v
TABLE OF CONTENTS.....	vi
LIST OF TABLES	xiii
LIST OF FIGURES	xvi
NOMENCLATURE	xxii
CHAPTER 1 INTRODUCTION	1
CHAPTER 2 LITERATURE REVIEW	3
Part I: Inclusions in Mg Alloys.....	5
2.1 Characterisation of Inclusions in Mg Alloys.....	5
2.2 Origin of Inclusions in Mg Alloys.....	7
2.2.1 Reactions with Air	7
2.2.2 Reactions with Fluxes.....	8
2.2.3 Reactions with Protective Gases.....	8
2.2.4 Reactions During Melt Treatment and Alloying	9
2.2.5 Reactions During Casting.....	9
2.3 Control of Inclusions in Mg Alloys.....	9
2.3.1 Addition of Flux	10
2.3.2 Fluxless Refining.....	10
2.3.2.1 Protective Atmospheres.....	11
2.3.2.2 Filtration of Inclusions	12
2.3.2.3 Inert Gas Bubbling (Sparging)	15
2.3.2.4 Degassing	16
2.4 Effect of Inclusions on the Properties of Mg Alloys	16
2.4.1 Tensile and Fatigue Properties	16
2.4.2 Corrosion Resistance	19
Part II: Grain Refinement of Mg Alloys.....	20

2.5	Benefits of Grain Refinement.....	20
2.6	Grain Growth Restriction	21
2.7	Nucleation of Metals and Alloys	23
2.7.1	Homogeneous Nucleation.....	23
2.7.2	Heterogeneous Nucleation.....	25
2.8	Selection of Effective Nucleants for Grain Refinement.....	27
2.9	Predictive Methods for Grain Refiner Effectiveness.....	28
2.9.1	Lattice Disregistry	28
2.9.2	Planar Disregistry	28
2.9.3	Edge-to-edge Model	30
2.9.4	Interdependence Theory	32
2.10	Grain Refinement of Mg Alloys Free of Al	34
2.11	Grain Refinement of Mg Alloys Containing Al	35
2.11.1	Melt Superheating.....	39
2.11.2	Native Grain Refinement	42
2.11.3	Elfinel (FeCl ₃) Addition and Other Fe Additions	43
2.11.4	Carbon Based Grain Refiners	44
2.11.4.1	Hexachloroethane (C ₂ Cl ₆), Hexachlorobenzene (C ₆ Cl ₆), Calcium Carbide (CaC ₂) and Calcium Cyanamide (CaCN ₂)	45
2.11.4.2	Carbonaceous Gases and Carbonates.....	49
2.11.4.3	Carbon, Aluminum-Carbon (Al-C) or Magnesium-Aluminum-Carbon (Mg-Al-C) Refiners	49
2.11.4.4	Silicon-Carbide (SiC) Grain Refiner.....	56
2.12	Wettability of Al Alloys on SiC	63
2.13	Spark Plasma Sintering.....	65
2.14	Solidification Analysis Using In-situ Neutron Diffraction.....	66
2.15	Chapter Summary and Present Study	67
CHAPTER 3 EXPERIMENTAL PROCEDURE.....		68
3.1	Materials	68
3.1.1	AZ91E Magnesium Alloy for Casting Experiments	68
3.1.2	Hexachloroethane (C ₂ Cl ₆)	68

3.1.3	Silicon Carbide, Aluminum and Graphite Powders	68
3.1.4	Titanium and Calcium Sponges.....	69
3.1.5	Silicon Carbide Wettability Substrates.....	69
3.1.6	Graphite Moulds	69
3.1.7	Tensile Mould.....	71
3.1.7.1	Mould Coating.....	71
3.1.7.2	Installation of Thermocouples.....	72
3.1.7.3	Mould Heating.....	72
3.1.8	Filters	73
3.1.9	Cover and Bubbling Gases	73
3.2	Melting and Casting Procedures.....	73
3.2.1	In-situ Neutron Diffraction Experiments.....	73
3.2.1.1	Casting of Neutron Diffraction Samples.....	74
3.2.1.2	Solidification Analysis of Mg-Zn and Mg-Al Alloys Using In-situ Neutron Diffraction	74
3.2.1.3	FactSage™ Modeling.....	77
3.2.2	Inclusion Removal Experiments.....	77
3.2.2.1	Argon Bubbling Experiments.....	78
3.2.3	Modeling Experiments	79
3.2.3.1	Model Setup	80
3.2.4	Grain Refinement Experiments Using C ₂ Cl ₆	81
3.2.5	Wettability Experiments.....	81
3.2.5.1	Preparation of Samples.....	82
3.2.5.2	Sample Setup and Melting	82
3.2.5.3	Contact Angle Measurements	83
3.2.6	Al-SiC Grain Refiner Preparation	83
3.2.6.1	Preparation of Al-Si-Mg Alloy	84
3.2.6.2	Casting of Al-SiC Grain Refiner.....	84
3.2.7	Grain Refinement Experiments Using Al-SiC Refiners.....	85
3.2.8	Spark Plasma Sintered Al-C Grain Refiner Preparation	86
3.2.8.1	Ball Milling of Al-C Refiners	86

3.2.8.2	Spark Plasma Sintering of Al-C Refiners	86
3.2.9	Grain Refinement Experiments Using Al-C Refiners	87
3.3	Microstructure Analysis	87
3.3.1	Optical Microscopy of Mg and Al Alloys	87
3.3.1.1	Etching	88
3.3.1.2	Grain Size Measurement	88
3.3.2	Scanning Electron Microscopy.....	88
3.4	X-ray Diffraction Analysis	88
3.4.1	Powders Extracted from Solid Samples	88
3.5	Differential Scanning Calorimetry	89
3.5.1	Preparation of Differential Scanning Calorimetry Samples	89
3.6	Composition Analysis.....	89
CHAPTER 4 SOLIDIFICATION AND GRAIN REFINEMENT OF MAGNESIUM ZINC ALLOYS.....		90
4.1	Solidification Behaviour of Mg-3 wt.% Zn Alloys Using In-situ Neutron Diffraction ...	90
4.1.1	Microstructure of Mg-3 wt.% Zn Alloy	90
4.1.2	In-situ Neutron Diffraction Plots of Mg-3 wt.% Zn Alloy.....	92
4.2	Solidification Behaviour of Mg-Zn and Mg-Zn-Zr Alloys Using In-situ Neutron Diffraction.....	95
4.2.1	Microstructure of Mg-Zn and Mg-Zn-Zr Alloys.....	95
4.2.2	X-ray and Neutron Diffraction of Mg-Zn and Mg-Zn-Zr Alloys.....	97
4.2.3	In-situ Neutron Diffraction of Mg-Zn and Mg-Zn-Zr Alloys	99
4.2.4	Fraction Solid Determination Using In-situ Neutron Diffraction	101
4.3	Chapter Summary	105
CHAPTER 5 INCLUSION REMOVAL AND CARBON GRAIN REFINEMENT OF MAGNESIUM ALUMINUM ALLOYS.....		107
5.1	Melt Filtration and Ar Bubbling.....	107
5.1.1	Effect of Melt Filtration.....	107
5.1.1.1	Mechanical Properties of Filtered Castings	107
5.1.1.2	Fractography of Filtered Castings.....	108
5.1.1.3	Effect of Melt Filtration on AZ91E Microstructure.....	111

5.1.2	Effect of Ar Bubbling and Filtration	112
5.1.2.1	Mechanical Properties of Ar Bubbled and Filtration Castings	112
5.1.2.2	Fracture Surfaces of Ar Bubbling and Filtration Castings	113
5.1.2.3	Effect of Filtration and Ar Bubbling on AZ91E Microstructure	114
5.1.2.4	Porosity Measurements of Unfiltered, Filtered and Ar Bubbled Castings.....	115
5.2	Modeling of Melt Filtration During Casting	116
5.2.1	Thermal Analysis of Melt Filtration During Casting	116
5.2.2	Velocity Predictions of Flow During Melt Filtration	118
5.3	In-situ Grain Refinement Using C_2Cl_6	120
5.3.1	Effect of C_2Cl_6 Addition on Grain Size of AZ91E.....	120
5.3.2	Effect of C_2Cl_6 Addition on Microstructure of AZ91E.....	122
5.3.3	Fractography of C_2Cl_6 -Treated AZ91E	126
5.3.4	Porosity of C_2Cl_6 -Treated AZ91E	129
5.3.5	Effect of C_2Cl_6 Addition on Mechanical Properties of AZ91E.....	129
5.4	Wettability of Al-Si-Mg Alloys on SiC.....	132
5.4.1	Compositions of Prepared Wettability Alloys.....	132
5.4.2	Contact Angle Measurements.....	133
5.4.2.1	Pure Al.....	133
5.4.2.2	Al-Si Alloys.....	134
5.4.2.3	Al-Si-Mg Alloys.....	135
5.4.3	Microstructure of Wettability Samples.....	136
5.4.3.1	Pure Al.....	136
5.4.3.2	Al-Si Alloys.....	138
5.4.3.3	Al-Si-Mg Alloys.....	140
5.4.3.4	Mechanism of Wettability with Si and Mg Addition.....	142
5.5	Wettability of Al-2 wt.% Si-1.25 wt.% Mg Alloy on SiC.....	142
5.5.1	Contact Angle Measurements of Al-2 wt.% Si-1.25 wt.% Mg Alloy	143
5.5.2	Microstructure of Al-2 wt.% Si-1.25 wt.% Mg Alloy	144
5.6	Ex-situ Grain Refinement Using Al-SiC Refiners	145
5.6.1	Differential Scanning Calorimetry of Al-SiC Refiners	145
5.6.2	X-ray Diffraction of Al-SiC Grain Refiners.....	147

5.6.3	Microstructure of Al-SiC Refiners	149
5.6.4	Effects of Al-SiC Refiner Addition on Grain Size of AZ91E.....	151
5.6.5	Effects of Al-SiC Refiner Addition on Microstructure of AZ91E	153
5.6.6	Fractography of Al-SiC Refiner Treated AZ91E	156
5.6.7	Porosity of Al-SiC Treated AZ91E	158
5.6.8	Effects of Al-SiC Refiner Addition on Mechanical Properties of AZ91E.....	158
5.7	In-situ Grain Refinement Using SPS Al-C Refiners	160
5.7.1	X-ray Diffraction of SPS Al-C Refiners.....	160
5.7.2	Microstructure of SPS Al-C Refiners	161
5.7.3	Effects of SPS Al-C Refiner Addition on Grain Size of AZ91E.....	162
5.7.4	Effects of SPS Al-C Refiner Addition on Microstructure of AZ91E.....	164
5.7.5	Fractography of SPS Al-C Refiner Treated AZ91E.....	166
5.7.6	Porosity of SPS Al-C Refiner Treated AZ91E.....	169
5.7.7	Effects of SPS Al-C Refiner Addition on Mechanical Properties of AZ91E.....	169
5.8	Solidification Behaviour of Mg-6 wt.% Al and Mg-9 wt.% Al Alloys Using In-situ Neutron Diffraction.....	171
5.8.1	Microstructure of Mg-6 wt.% Al and Mg-9 wt.% Al Alloys	171
5.8.2	In-situ Neutron Diffraction Plots of Mg-6 wt.% Al and Mg-9 wt.% Al Alloys.....	175
5.8.3	Fraction Solid Curves of Mg-6 wt.% Al and Mg-9 wt.% Al Alloys	178
5.9	Chapter Summary	181
CHAPTER 6 CONCLUSIONS		182
6.1	Solidification of Mg-Zn and Mg-Zn-Zr Alloys Using In-situ Neutron Diffraction	182
6.2	Inclusion Removal by Melt Filtration and Ar Bubbling.....	182
6.3	Modeling of Melt Filtration During Casting	182
6.4	Grain Refinement Using C ₂ Cl ₆	183
6.5	Preparation of Al-SiC Refiners.....	183
6.6	Grain Refinement Using Al-SiC.....	183
6.7	Grain Refinement Using SPS Al-C	183
6.8	Solidification of Mg-Al Alloys Using In-situ Neutron Diffraction.....	184
6.9	Academic, Industrial and Societal Impact of the Dissertation	184
CHAPTER 7 FUTURE WORK		185

7.1	Grain Refiner Preparation and Addition Parameters	185
7.2	In-situ Neutron Diffraction	185
	APPENDICES	186
A.1	Phase Diagrams	186
A.2	Additional Grain Refinement Techniques	188
A.2.1	Aluminum-Boron (Al-B) Grain Refiner	188
A.2.2	Titanium Based Additions	188
A.2.2.1	Aluminum-Titanium (Al-Ti) Grain Refiners	189
A.2.2.2	Aluminum-Titanium-Boron (Al-Ti-B) Grain Refiners	189
A.2.2.3	Aluminum-Titanium-Carbon (Al-Ti-C) Grain Refiners	190
A.2.3	Grain Refinement by ZnO, Al ₂ Y and AlN Additions	191
A.2.4	Grain Refinement by ZrB ₂ Additions	192
A.2.5	Grain Refinement by Sr Additions	193
A.2.6	Grain Refinement by Ca Additions	194
A.2.7	Grain Coarsening Additions	196
A.3	X-ray Diffraction Plot of SiC Substrate Used for Wettability Experiments	197
A.4	Differential Scanning Calorimetry Plot	197
	REFERENCES	199

LIST OF TABLES

	Page
Table 2-1: Key Advantages for Improved Properties, Design, and Manufacturing with Mg [1]... 3	3
Table 2-2: Mg Casting Alloys: Properties and Automotive Applications [7,12]	4
Table 2-3: Comparison of the Typical Mechanical Properties of Die Cast A380 Al and AZ91D Mg Automotive Alloys at 20°C [1,13]	5
Table 2-4: Inclusions in Mg Alloys [21-23]	6
Table 2-5: Standard Gibbs Free Energy ($\Delta G^{\circ}_{\text{reaction}}$) as a Function of Temperature of Selected Reactions [27,28]	8
Table 2-6: Effect of Filtration and Ar Bubbling on the UTS and the Elongation of AZ91 [85] ..	18
Table 2-7: Effect of Inclusion Content on the Corrosion Rate of Mg-10 wt.% Gd-3 wt.% Y-0.5 wt.% Zr Alloy [54].....	20
Table 2-8: Summary of m, k and m(k-1) for Different Elements in Mg [18,92,107,118].....	22
Table 2-9: Planar Disregistries of Potential Nucleants with Mg	29
Table 2-10: Edge-to-edge Model Applied to TiB ₂ , TiC, SiC, TiN [144], Al ₄ C ₃ , Al ₂ CO, Al ₈ (Mn,Fe) ₅ [152], γ -AlMn, ϵ -AlMn, τ -AlMn, β -Mn [10], ZnO [154], Al ₂ Y [155] and AlN [156].....	31
Table 2-11: Summary of Zr Grain Refinement Mechanism	34
Table 2-12: Influence of Alloying Additions on Zr Grain Refinement in Mg	35
Table 2-13: Summary of Grain Refinement Techniques for Mg-Al Alloys.....	37
Table 2-14: Summary of Results of Superheating Experiments [197]	39
Table 2-15: Fe Inoculation in High-purity Mg-3 and 9 wt.% Al Alloys [212]	43
Table 2-16: Tensile Properties of AM60B Before and After C ₂ Cl ₆ Addition	46
Table 2-17: Grain Size and Tensile Properties of AZ91 and Mg-3 wt.% Al Alloy Before and After Charcoal Addition [232,233].....	50
Table 2-18: Grain Refining Results of Direct Carbon Based Additions	51
Table 2-19: Grain Refining Results of Direct Al ₄ C ₃ Additions.....	52
Table 2-20: Grain Refining Results of Al-C Additions	54
Table 2-21: Grain Refining Results of Mg-Al-C and Misc. C Additions.....	56
Table 2-22: Grain Refining Results of SiC based Additions	58

Table 2-23: Grain Refining Results of Al-SiC based Additions.....	59
Table 2-24: Grain Refining Results of Mg-SiC based Additions.....	61
Table 2-25: Summary of Grain Refinement by C Inoculation in Mg-Al Alloys.....	62
Table 2-26: Influence of Si Wettability of Al on SiC Substrates	63
Table 3-1: Composition of AZ91E Alloy (wt.%).....	68
Table 3-2: Composition and Average Particle Sizes of SiC, Al and Graphite Powders	69
Table 3-3: Dimensions of Graphite Moulds	70
Table 3-4: Filter Dimensions and Placement.....	73
Table 3-5: Holding Temperatures for In-situ Neutron Diffraction Experiments.....	76
Table 3-6: Experimental Procedure for Inclusion Removal Experiments	78
Table 3-7: Summary of Modeling Conditions	81
Table 3-8: Experimental Procedure for C ₂ Cl ₆ Grain Refinement Experiments	81
Table 3-9: Summary of Prepared Alloys for Wettability Experiments	82
Table 3-10: Summary of Prepared Al-SiC Grain Refiners.....	85
Table 3-11: Experimental Procedure for Al-SiC Refiner Experiments	85
Table 3-12: SPS Experimental Procedure for Al-C Refiner Preparation	86
Table 3-13: Grinding and Polishing Procedure for Mg and Al Alloys.....	87
Table 3-14: Parameters for DSC Analysis of Al-SiC Alloys	89
Table 4-1: Observed 2θ and d-spacing Values of Mg Peaks During In-situ Neutron Diffraction Experiments	94
Table 5-1: Summary of Inclusion Count and Inclusion Size of Fracture Surfaces Produced Using Different Filter Types and Locations	109
Table 5-2: Summary of Inclusion Count and Inclusion Size of Ar Bubbled and Ar Bubbling with Filtration.....	114
Table 5-3: Summary of Porosity Results for Filtered and Ar Bubbled Castings	116
Table 5-4: Summary of Porosity Results for C ₂ Cl ₆ Refined AZ91E.....	129
Table 5-5: Composition of Prepared Wettability Alloys	132
Table 5-6: Summary of DSC Results for Al-5.9 and 11.6 wt.% SiC Alloys.....	146
Table 5-7: Summary of Porosity Results for C ₂ Cl ₆ and Al-SiC Refiner Addition on AZ91E ...	158
Table 5-8: Summary of Porosity Results for C ₂ Cl ₆ and Al-C Refiner Addition on AZ91E	169
Table 5-9: Summary of Diffraction Plot Features of Mg-6 wt.% Al and Mg-9 wt.% Al Alloys	178

Table A-1: Grain Size and Mechanical Properties with the Addition of Al-4 wt.% B to AZ91 and Pure Mg.....	188
Table A-2: Grain Refining Results of Ti-Al based Additions	189
Table A-3: Grain Refining Results of Al-Ti-B based Additions	190
Table A-4: Grain Refining Results of Al-Ti-C based Additions	191
Table A-5: Grain Refining Results of ZnO, Al ₂ Y and AlN Additions.....	192
Table A-6: Grain Refining Results of Sr Addition	194
Table A-7: Grain Refining Results of Ca Addition	195
Table A-8: Grain Size Versus Be Content for Various Mg Alloys [321].....	196

LIST OF FIGURES

	Page
Figure 1-1: Outline of Dissertation Results	2
Figure 2-1: Optical Micrographs of a) an Oxide Cluster in AZ91 Alloy and b) a “Snaky” Oxide in AM50 Alloy [24]	7
Figure 2-2: Effect of Filtration on the Size and Amount of Inclusions in Mg-Gd-Y-Zr Magnesium Alloy [81].....	14
Figure 2-3: Effect of Metal Cleanliness on the Mechanical Properties of Die Cast AM50 [97]..	17
Figure 2-4: Homogeneous Nucleation a) Only Liquid Melt b) Solid in Liquid Melt [122].....	24
Figure 2-5: Heterogeneous Nucleation on a Mould Wall [122]	25
Figure 2-6: Mechanical Property Data Using C ₂ Cl ₆ and Ar Rotary Degasser [217].....	46
Figure 2-7: Gibbs Free Energy of Al ₄ C ₃ Formation as a Function of Al wt.% in a Mg-Al Alloy Melt [233]	47
Figure 2-8: Al-1C Grain Refiner Microstructure [236]	53
Figure 2-9: Schematic of SPS Machine [301]	65
Figure 2-10: Summary of Present Work.....	67
Figure 3-1: Graphite Mould Used for a) Al-SiC Grain Refiner Preparation and b) Wettability Sample Preparation (Dimensions in mm).....	70
Figure 3-2: Tensile Mould	71
Figure 3-3: Thermocouple Placement in Tensile Mould (Dimensions in mm)	72
Figure 3-4: a) Graphite Crucible Used for In-situ Neutron Diffraction Experiments, b) Furnace Lid with Crucible Holder Assembly and c) Magnified Image of Crucible Holder	75
Figure 3-5: Diffractometer Setup for In-situ Neutron Diffraction Experiments.....	76
Figure 3-6: Experimental Setup for Wettability Experiments	83
Figure 3-7: Contact Angle (θ) Measurement During Wettability Experiments.....	83
Figure 3-8: a) Al-Si-Mg Alloy Chips and b) After Ball Milling with SiC Powder	84
Figure 4-1: Grain Structures of Mg-3 wt.% Zn Alloy a) Before and b) After In-situ Neutron Diffraction Experiment	90

Figure 4-2: SEM Micrographs of Mg-3 wt.% Zn Alloy a) Before In-situ Neutron Diffraction Experiments with EDX in c) and b) After In-situ Neutron Diffraction Experiments with EDX in d).....	91
Figure 4-3: Neutron Diffraction Pattern of Mg-3 wt.% Zn Alloy at Different Temperatures (°C, Selected Isotherms Omitted for Clarity).....	93
Figure 4-4: Grain Structures of a) Mg-Zn and b) Mg-Zn-Zr Alloys	96
Figure 4-5: SEM Images of a) Mg-Zn and b) Mg-Zn-Zr Alloys.....	97
Figure 4-6: a) XRD at Room Temperature and b) In-situ Neutron Diffraction Results at 200°C of Mg-Zn and Mg-Zn-Zr Alloys.....	98
Figure 4-7: In-situ Neutron Diffraction Plot of Mg-Zn Alloy ($10\bar{1}0$), (0002) and ($10\bar{1}1$) planes (°C, Selected Isotherms Omitted for Clarity)	100
Figure 4-8: In-situ Neutron Diffraction Plot of Mg-Zn-Zr Alloy ($10\bar{1}0$), (0002) and ($10\bar{1}1$) planes (°C, Selected Isotherms Omitted for Clarity)	100
Figure 4-9: a) Deviation in Diffraction Background with Temperature for Mg-5 wt.% Zn-0.7 wt.% Zr Alloy, ($10\bar{1}0$) Plane and b) Fraction Solid of α -Mg Versus Temperature for Mg-5 wt.% Zn-0.7 wt.% Zr Alloy, ($10\bar{1}0$) Plane.....	102
Figure 4-10: Fraction Solid of α -Mg for Mg-Zn and Mg-Zn-Zr Alloys.....	104
Figure 4-11: Graphical Representation of Growth of Mg-Zn and Mg-Zn-Zr Alloys.....	105
Figure 5-1: Effect of Filter Type and Location on Mechanical Properties of AZ91E with Error Bars Representing One Standard Deviation	108
Figure 5-2: Optical Macrographs of Fracture Surfaces of Castings Produced Using Different Filter Types and Locations.....	109
Figure 5-3: a) AZ91E Coarse Filter Atop Pouring Cup Casting Fracture Surface Showing Shrinkage Porosity in Between Dendrites and b) Crack Propagation through MgO-Mg Interface in AZ91E Coarse Filter Atop Pouring Cup Casting	110
Figure 5-4: Unfiltered AZ91E Casting Showing Micron Sized MgO Particles with Corresponding EDX Analyses.....	111
Figure 5-5: Effect of Filter, Ar Bubbling and Filter + Ar Bubbling on the Mechanical Properties of AZ91E with Error Bars Representing One Standard Deviation.....	113

Figure 5-6: Optical Macrographs of Fracture Surfaces of Ar Bubbled and Ar Bubbling with Filtration.....	114
Figure 5-7: a) AZ91E Fine Filter Within Well + Ar Bubbling Casting with b) Corresponding Fracture Surface	115
Figure 5-8: Oxide Lumps and Oxide Films Observed Near Filter Wall in Fine Filter with Ar Bubbling Casting (Arrow Indicates Direction Towards Filter Wall)	115
Figure 5-9: Cooling Curves of Experimental and Simulated Castings a) Effect of HTC on the Simulated Temperature Profiles (Unfiltered, 1 mm Node Size) b) EXP and SIM Curves (Filtered, 0.5 mm Node Size).....	117
Figure 5-10: Velocity Profiles of a1) Unfiltered: 10% Filled (1.26 sec.), a2) 15% Filled (1.89 sec.), a3) 20% Filled (2.52 sec.) and a4) 25% Filled (3.15 sec.) and b1) Filtered Castings: 10% Filled (1.26 sec.), b2) 15% Filled (1.89 sec.), b3) 20% Filled (2.52 sec.) and b4) 25% Filled (3.15 sec.)	119
Figure 5-11: Grain Structures of AZ91E with C ₂ Cl ₆ Addition and Filter + Ar Bubbling	121
Figure 5-12: Effect of C ₂ Cl ₆ Addition on Grain Size of AZ91E with Error Bars Representing One Standard Deviation	121
Figure 5-13: SEM Image of AZ91E Alloy Showing a) General Microstructure, b) Mn-Al Based Particle Indicated by the Arrow and c) Another Mn-Al Particle	122
Figure 5-14: SEM Image of AZ91E + 0.25 wt.% C ₂ Cl ₆ Alloy Showing a) General Microstructure, b) Mn-Al Based Intermetallic Indicated by Arrow and c) EDX Element Maps of Mn-Al Intermetallic in b)	124
Figure 5-15: SEM Image of AZ91E + Filter + Ar Bubbling Showing a) General Microstructure, b) Mn-Al Based Intermetallic Indicated by Arrow and c) EDX Element Maps of Mn-Al Intermetallic in b)	125
Figure 5-16: Optical Macrographs of Fracture Surfaces of AZ91E, AZ91E + C ₂ Cl ₆ and AZ91E + Filter + Ar Bubbling	127
Figure 5-17: Fracture Surfaces of a) AZ91E, b) AZ91E + 0.75 wt.% C ₂ Cl ₆ and c) AZ91E + Filter + Ar Bubbling	128
Figure 5-18: Effect of C ₂ Cl ₆ Addition on Mechanical Properties of AZ91E with Error Bars Representing One Standard Deviation.....	130
Figure 5-19: Images of a) Pure Al and b) Al-10 wt.% Si-1.25 wt.% Mg Both at 800°C	133

Figure 5-20: Variation in Contact Angle for Al and Al + x wt.% Si Alloys with Time at a) 800°C and b) 900°C with Error Bars Representing One Standard Deviation	134
Figure 5-21: Variation in Contact Angle for Al, Al + x wt.% Si and Al + x wt.% Si + y wt.% Mg Alloys with Time at a) 800°C and b) 900°C with Error Bars Representing One Standard Deviation.....	136
Figure 5-22: SEM Microstructure of Pure Al Sample Heated to 800°C with Corresponding EDX Spot Analyses for Points A and B	137
Figure 5-23: SEM Microstructure of Pure Al Sample Heated to 900°C Showing Interface Microstructure with Corresponding EDX Spot Analyses for Points A, B and C	137
Figure 5-24: SEM Microstructure of Al-10 wt.% Si Sample Heated to 800°C Showing Interface Microstructure with Corresponding EDX Spot Analyses for Points A, B and C.....	139
Figure 5-25: SEM Microstructure of Al-10 wt.% Si Sample Heated to 900°C Showing Interface Microstructure with Corresponding EDX Spot Analyses for Points A and B	139
Figure 5-26: SEM Microstructure of Al-10 wt.% Si-1.25 wt.% Mg Sample Heated to 800°C Showing Interface Microstructure with Corresponding EDX Spot Analyses for Points A, B and C.....	140
Figure 5-27: SEM Microstructure of Al-10 wt.% Si-1.25 wt.% Mg Sample Heated to 900°C Showing Interface Microstructure with Corresponding EDX Spot Analyses for Points A and B	141
Figure 5-28: Schematic Diagram Showing Changes in Contact Angle With Temperature, Si and Mg Additions	142
Figure 5-29: Variation in Contact Angle for Al and Al + 2 wt.% Si + 1.25 wt.% Mg Alloys with Time at a) 800°C and b) 900°C with Error Bars Representing One Standard Deviation...	143
Figure 5-30: SEM Microstructure of Al-2 wt.% Si-1.25 wt.% Mg Sample Heated to 800°C Showing Interface Microstructure with Corresponding EDX Spot Analyses for Points A and B	144
Figure 5-31: SEM Microstructure of Al-2 wt.% Si-1.25 wt.% Mg Sample Heated to 900°C Showing Interface Microstructure with Corresponding EDX Spot Analyses for Points A and B	145
Figure 5-32: XRD Plot of Al-SiC Refiners	148
Figure 5-33: XRD Plot of Al-SiC Refiners After Al Matrix Dissolution.....	149
Figure 5-34: SEM Microstructure of Al-SiC Refiners at a) 700°C, b) 800°C for 1 Hour, c) 800°C for 2 Hour, d) 900°C for 1 Hour and e) 900°C for 2 Hour	150

Figure 5-35: SEM Microstructure of Al-SiC Alloys Produced at 800°C for 2 Hour With EDX Spectrums from Points A and B.....	151
Figure 5-36: Grain Structures of AZ91E with C ₂ Cl ₆ Addition, Filter + Ar Bubbling and Al-SiC Addition	152
Figure 5-37: Effect of Al-SiC Addition on Grain Size of AZ91E with Error Bars Representing One Standard Deviation.....	153
Figure 5-38: SEM Image of AZ91E + Filter + Ar Bubbling + 0.50 wt.% Al-SiC Showing a) General Microstructure, b) Mn-Al-Fe Based Intermetallic Alongside Al-Mg-C-O Phase and c) EDX Element Maps of Phases in b)	154
Figure 5-39: SEM Image of AZ91E + Filter + Ar Bubbling + 0.50 wt.% Al-SiC Showing Agglomerated Particles.....	155
Figure 5-40: Optical Macrographs of Fracture Surfaces of a) AZ91E, b) AZ91E + 0.75 wt.% C ₂ Cl ₆ , c) AZ91E + Filter + Ar Bubbling and d) AZ91E + Filter + Ar Bubbling + 0.50 wt.% Al-SiC.....	157
Figure 5-41: Fracture Surface of AZ91E + Filter + Ar Bubbling + 0.50 wt.% Al-SiC.....	157
Figure 5-42: Effect of C ₂ Cl ₆ Addition, Filtration + Ar Bubbling and Al-SiC Refiner Addition on Mechanical Properties of AZ91E with Error Bars Representing One Standard Deviation...	159
Figure 5-43: Influence of Milling Time and SPS on XRD of Al-C Refiner Powder	160
Figure 5-44: Influence of Milling Time and SPS on XRD of Al-C Refiner Powder of a) Graphite Basal Peak and b) Al (110) Peak	161
Figure 5-45: SEM Microstructure of Al-C Grain Refiner Showing Al Matrix and Fine C Rich Layers with Corresponding EDX Spot Analyses for Points A, B and C.....	162
Figure 5-46: Grain Structures of AZ91E with C ₂ Cl ₆ Addition, Filter + Ar Bubbling, Al-SiC Addition and Al-C Addition	163
Figure 5-47: Effect of Al-C Addition on Grain Size of AZ91E with Error Bars Representing One Standard Deviation.....	164
Figure 5-48: SEM Image of AZ91E + 0.50 wt.% Al-C Showing a) General Microstructure, b) Mn-Al-Fe Based Intermetallic Alongside Al-Mg-C-O Phase and c) EDX Element Maps of Phases in b)	165
Figure 5-49: SEM Image of AZ91E + Filter + Ar Bubbling + 0.50 wt.% Al-C Showing EDX Spectrums of A and B.....	166

Figure 5-50: Optical Macrographs of Fracture Surfaces of a) AZ91E, b) AZ91E + 0.75 wt.% C ₂ Cl ₆ , c) AZ91E + Filter + Ar Bubbling, d) AZ91E + Filter + Ar Bubbling + 0.50 wt.% Al-SiC, e) AZ91E + Filter + Ar Bubbling + 0.25 wt.% Al-C, f) AZ91E + Filter + Ar Bubbling + 0.50 wt.% Al-C and g) AZ91E + 0.50 wt.% Al-C.....	167
Figure 5-51: Fracture Surfaces of a) AZ91E + Filter + Ar Bubbling + 0.50 wt.% Al-C and b) AZ91E + 0.50 wt.% Al-C.....	168
Figure 5-52: Effect of C ₂ Cl ₆ Addition, Filter + Ar Bubbling, Al-SiC Refiner Addition and Al-C Refiner Addition on Mechanical Properties of AZ91E with Error Bars Representing One Standard Deviation.....	170
Figure 5-53: SEM Micrograph of Mg-6 wt.% Al Showing a) Primary Mg Matrix with Eutectic Mg ₁₇ Al ₁₂ and b) Magnified Micrograph Showing Eutectic Mg ₁₇ Al ₁₂ with Corresponding EDX Spot Analyses of Points b1, b2 and b3	172
Figure 5-54: SEM Micrograph of Mg-9 wt.% Al Showing a) Primary Mg Matrix with Eutectic Mg ₁₇ Al ₁₂ and b) Magnified Micrograph Showing Eutectic Mg and Alternating Al, Mg Rich Lamella with Corresponding EDX Spot Analyses of Points b1, b2 and b3	173
Figure 5-55: Neutron Diffraction Plot of Mg-6 wt.% Al, Mg (10 $\bar{1}$ 1) Plane	176
Figure 5-56: Neutron Diffraction Plot of Mg-9 wt.% Al, Mg (10 $\bar{1}$ 1) Plane and Mg ₁₇ Al ₁₂ (330, 411) Planes (Selected Isotherms Omitted for Clarity).....	177
Figure 5-57: Fraction Solid Curves of Mg (10 $\bar{1}$ 1) from In-situ Analysis of Mg-6 wt.% Al and Mg-9 wt.% Al Alloys' Solidification.....	180
Figure A-1: Tentative Representation of the Al-C-Mg Phase Equilibria below 1000 K [280]..	186
Figure A-2: Mg-Zn Phase Diagram [1]	186
Figure A-3: Mg-Al Phase Diagram [1].....	187
Figure A-4: Al-Si Phase Diagram [13]	187
Figure A-5: XRD Spectrum of As-received SiC Substrate Showing α Polytype.....	197
Figure A-6: Differential Scanning Calorimetry Plot of Al-5.9 wt.% SiC Alloy Heated to 700°C for 15 Minutes.....	198

NOMENCLATURE

Symbol	Description	Units
Greek		
γ_{ml}	Interfacial tension of the mould-liquid interface	J/m ²
γ_{sl}	Interfacial tension of the solid-liquid interface	J/m ²
γ_{sm}	Interfacial tension of the solid-mould interface	J/m ²
δ	Lattice disregistry	%
$\delta_{(hkl)_s}^{(hkl)_n}$	Planar disregistry	%
θ	Contact angle	Degrees
θ_d	Angle between two low index directions in (hkl)	Degrees
θ_{diff}	Diffraction angle	Degrees
λ	Wavelength	nm
μ	Coefficient of viscosity	kg/ms
ν	Fluid kinematic viscosity	m ² /s
ρ	Fluid density	kg/m ³
σ_o	Stress to initiate dislocation motion	MPa
σ_y	Yield strength	MPa
English		
A_{sl}	Surface area of the solid-liquid interface	m ²
a	Lattice parameter	nm
a_o	Lattice parameter a for nucleated phase	nm
Δa	Difference in lattice parameter a between nucleant and nucleated phase	nm
C_i	Initial concentration of solute in the melt	wt.%
C_o	Alloy composition	wt.%
$C_1(x)$	Liquid concentration at point x	wt.%
C_1^*	Composition of the liquid at the solid-liquid interface	wt.%
c	Lattice parameter	nm
c_p	Specific heat	J/K
D	Diffusion coefficient of solute in alloy	m ² /s

d	Average grain diameter	μm
d_{gs}	Grain diameter predicted using interdependence theory	m
d_{inter}	Interatomic spacing	nm
d_s	Width of substrate	μm
$d_{[\text{uvw}]}$	Lattice spacing along direction [uvw]	nm
d^*	Critical diameter of nucleus	μm
f_d	Atomic misfit along planes	%
f_r	Atomic misfit along rows	%
G_1	Free energy of liquid	J
G_2	Free energy of solid in liquid	J
G_v^l	Free energy of the liquid per unit volume	J/m^3
G_v^s	Free energy of the solid per unit volume	J/m^3
ΔG_r	Change in free energy ($G_2 - G_1$) assuming spherical nucleus	J
$\Delta G_{\text{reaction}}^\circ$	Gibbs free energy for reaction	kJ/mol
ΔG_v	$G_v^s - G_v^l$	J/m^3
ΔG^*	Maximum free energy	J
k	Equilibrium partition coefficient	wt.%/wt.%
k_{th}	Thermal conductivity coefficient	W/mK
k_y	Unpinning constant (measure dislocation pile-up at barriers)	$\text{MPa}\mu\text{m}^{1/2}$
L_v	Latent heat of fusion per unit volume	J/m^3
m	Liquidus slope on a phase diagram	$\text{K}/\text{wt.}\%$
n	Order of diffraction	
p	Fluid pressure	Pa
Q	Growth restriction factor	K
r	Radius of nucleus	m
r^*	Critical radius of nucleus	μm
s and n	Representation of the substrate and the nucleated crystal, respectively	
T	Temperature	K
T_m	Melting point of the liquid	$^\circ\text{C}$
ΔT	Undercooling	$^\circ\text{C}$ or K
$\Delta T_{n-\text{min}}$	Undercooling required for nucleation on the most potent particle	K
t	Time	s

u	Velocity component in x	m/s
V_l	Volume of liquid	m^3
V_s	Volume of solid	m^3
v	Velocity component in y	m/s
v_g	Growth rate of solid-liquid interface	m/s
w	Velocity component in z	m/s
x_{sd}	Distance from the point of critical constitutional supercooling to the location of the most potent nucleant particle	m
$z\Delta T_{n-min}$	Incremental amount of undercooling required to activate each subsequent nucleation event	K
(hkl)	Low index plane	
[uvw]	One of the three low index directions in (hkl)	

Elements		Abbreviations	
Ag	Silver	BSE	Back-scattered electron
Al	Aluminum	CFF	Ceramic foam filters
Ar	Argon	DSC	Differential scanning calorimetry
B	Boron	EDX	Energy dispersive X-ray spectroscopy
Be	Beryllium	EPMA	Electron probe micro-analysis
Bi	Bismuth	EXP	Experimental
C	Carbon	FK	Fluorinated ketones
Ca	Calcium	HCP	Hexagonal close-packed
Cd	Cadmium	HFC	Hydrofluorocarbons
Ce	Cerium	HTC	Heat transfer coefficient
Cl	Chlorine	RE	Rare earth
Cr	Chromium	SEM	Scanning electron microscopy
Cu	Copper	SIM	Simulated
Fe	Iron	SPS	Spark plasma sinter/sintering
Gd	Gadolinium	TEM	Transmission electron microscopy
H	Hydrogen	UTS	Ultimate tensile strength
He	Helium	XRD	X-ray diffraction
K	Potassium	YS	Yield strength
La	Lanthanum		

Mg	Magnesium
Mn	Manganese
N	Nitrogen
Na	Sodium
Ni	Nickel
O	Oxygen
Pr	Praseodymium
Si	Silicon
Sn	Tin
Sr	Strontium
Th	Thorium
Ti	Titanium
W	Tungsten
Y	Yttrium
Zn	Zinc
Zr	Zirconium

CHAPTER 1

INTRODUCTION

Lightweighting of automotive and aerospace vehicles is a crucial strategy to improve fuel efficiencies, reduce exhaust emissions, improve performance and reduce impact on the environment. The low density (1.74 g/cm^3 [1]) and high strength to weight ratio of magnesium (Mg) and its alloys give impetus for its use as a structural material. An economical technique for producing Mg components is casting such as permanent mould or sand casting. These casting processes are effective for producing large structural automotive components such as wheel rims and engine blocks.

Two major drawbacks to Mg alloys are their relatively low mechanical properties and their reactivity that make them highly susceptible to forming inclusions that could be entrapped in the casting during melting and pouring. With improved mechanical properties, Mg alloys have potential to be used in more structurally demanding applications at room and elevated temperatures. This could expand their application from small components such as seat frames and steering wheels to more structurally demanding applications such as engine blocks, wheel rims and transmission cases. The drawbacks of Mg alloys can be countered by grain refinement which imparts improvements in strength without hindering ductility [2,3] and inclusion removal techniques such as filtration and inert gas bubbling.

For grain refinement of Mg alloys free of aluminum, zirconium is nearly the perfect grain refiner [4] while for Mg alloys containing aluminum, carbon inoculation is considered as the most effective refinement method [5].

A better understanding of the solidification mechanisms of Mg and its alloys will help promote it as a structural material. In-situ neutron diffraction offers unique opportunities to gain a better understanding to Mg alloy solidification because neutrons are electrically neutral, can analyze both heavy and light elements and are easy to diffract because they obey Bragg's law [6].

Objectives

The objectives of this dissertation are to develop an environmentally friendly alternative to the grain refinement and inclusion removal capabilities of the benchmark carbon refiner,

hexachloroethane (C_2Cl_6). Inclusion removal will be accomplished by filtration and inert gas bubbling while carbon alternatives to C_2Cl_6 will be produced by casting and powder metallurgy routes. The mechanism of carbon grain refinement and the influence of their addition to the mechanical properties will be investigated. The potential to use in-situ neutron diffraction to examine the solidification behaviours of Mg alloys will also be examined.

Outline of Dissertation

To better organize the dissertation, the literature review was split into two sections. The first section discusses inclusions in Mg alloys and the second section outlines grain refinement of Mg alloys. An outline of the dissertation is provided in Figure 1-1.

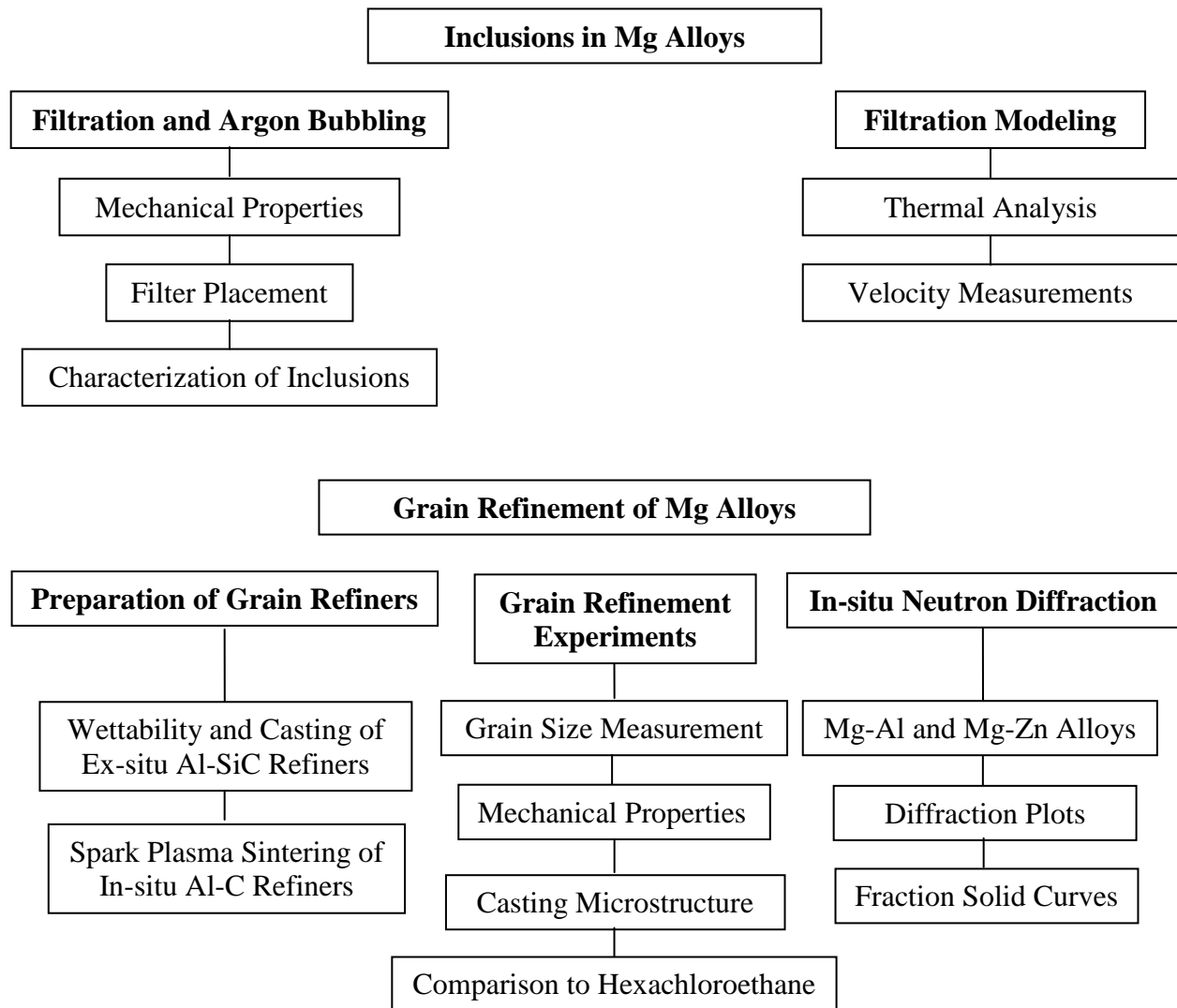


Figure 1-1: Outline of Dissertation Results

CHAPTER 2
LITERATURE REVIEW

Magnesium was first used commercially for pyrotechnics and due to its high chemical reactivity, organic chemistry and pharmaceuticals. Magnesium has also been used as a sacrificial anode in corrosion applications and for alloying aluminum (Al) and desulphurization and nodularization in ferrous alloys in metallurgical applications [7]. Further, Mg alloys are 100% recyclable, offer good heat dissipation and good shielding against electromagnetic and radio frequencies unlike plastics [8]. The potential advantages for Mg as a structural material are presented in Table 2-1.

Table 2-1: Key Advantages for Improved Properties, Design, and Manufacturing with Mg [1]

Property	Advantage
Specific Strength	Mg has specific strength similar to cast iron and similar or greater than many traditional automotive Al alloys
Specific Stiffness	Mg has high specific stiffness relative to many polymeric materials and composites
Fluidity	Relatively high fluidity allows for thin walled castings
Hot Formability	Mg can be formed into many complex shapes using elevated temperature forming processes
Machining	Machining tools last longer with Mg than Al. The only issue is that more care must be taken handling Mg machining chips
Damping	Mg alloys have excellent damping capacity
Low Temperature Properties	Mg does not exhibit a brittle to ductile transition so it can be used at low temperatures

The attractive structural properties of Mg have rendered it applicable to aerospace [9] applications such as: missile skins and frames, aircraft air frames, engines, transmission cases and electronic housings while consumer applications include: power tools, cameras, luggage, cell phones and portable computers [7]. In the same regard, the automotive industries adapt Mg-Al-Zn and Mg-Al-Mn alloys [10] for lightweighting, improved fuel economy and environmental performance [11] with various automotive applications shown in Table 2-2.

Table 2-2: Mg Casting Alloys: Properties and Automotive Applications [7,12]

Alloy family	Mg-Al-Zn	Mg-Al-Mn	Mg-Al-Si	Mg-Al-RE¹	Mg-Al-Sr/Ca
Typical alloys	AZ91D	AM60B, AM50A	AM20	AS41, AS21	AE42, AE44 AJ52, AJ62, AXJ530, MRI 153M, MRI 230D
Properties	Excellent castability and good strength	Excellent ductility and energy-absorbing properties	High ductility and impact strength	Good strength and good creep resistance up to about 150°C	
Applications	Steering column brackets, cylinder block, transmission case	Automobile seat frames, steering wheel, instrument panel, brackets	Automotive safety parts, seat frames	High temperature applications (e.g., engine cradle, powertrain components)	

¹RE denotes rare earth elements

Currently, the automotive industry is striving to further improve fuel efficiencies (and the consequent reduction in harmful exhaust emissions) to combat climate change. Automobile weight reduction is one of the primary means to achieve this goal. Magnesium alloys continue to be considered as candidate materials to replace Al alloys and further reduce the vehicle weight, since Mg alloys are 35% lighter than Al (1.74 g/cm³ for Mg [1] as compared to 2.74 g/cm³ for Al [13]). Despite the potential weight savings, the average use of Mg in North American automotive vehicles represents only 0.3% of the total vehicle weight as compared to 8.3% for Al [14]. Or in other words ~5 kg of Mg and 120-140 kg of Al in a passenger car [15].

Magnesium alloys have been used for automotive applications for approximately 80 years, and the applications have expanded to include instrument panels, seat frames, engine valve covers, transmission housings, intake manifolds, steering column components [11] steering wheels and inner door frames [16]. A common manufacturing technique for the production of Mg components is by casting. In particular, 90% of all Mg alloys are produced by die casting [8]. Comparison of the mechanical properties of die cast AZ91D Mg alloy and A380 Al alloy (Table 2-3) shows that the Mg alloy is at a disadvantage relative to the Al alloy, as it exhibits lower yield strength (YS) and ultimate tensile strength (UTS). Magnesium alloys also have poor formability and limited ductility because of their hexagonal closed packed (HCP) crystal

structures [2,3]. The strength and ductility of Mg alloys need to be improved, thus rendering them as viable automotive weight saving materials. The automotive applications for Mg alloys must also expand to large structural components such as wheel rims, engine blocks and suspensions. These large components can only be produced by permanent mould or sand casting processes where a fine cast grain structure cannot be readily achieved due to relatively low cooling rates [17] unlike high pressure die casting where fine grains result from high cooling rates [18]. For these processes, removing inclusions and grain refinement are essential to achieving these goals aiding in the pursuit of Mg alloys with improved mechanical properties for use in structurally demanding applications at room and elevated temperatures.

Table 2-3: Comparison of the Typical Mechanical Properties of Die Cast A380 Al and AZ91D Mg Automotive Alloys at 20°C [1,13]

Metal	Alloy	Density (g/cm³)	YS (MPa)	UTS (MPa)	Elongation (%)
Al	A380	2.71	165	330	3.0
Mg	AZ91D	1.81	150	230	3.0

There are two parts in CHAPTER 2. Part I describes the types and source of inclusions in Mg alloys and is a portion of a recently published literature survey by the candidate and colleagues (Lun Sin *et al.* [19]). Methods to remove inclusions in Mg alloys are also presented ending with their influence on mechanical properties and corrosion resistance. Part II discusses grain refinement in Mg alloys. The text begins with a review of nucleation and grain growth restriction. The focus then shifts to models for selection of effective grain refiners and the performance of grain refiners in experimental trials.

Part I: Inclusions in Mg Alloys

2.1 Characterisation of Inclusions in Mg Alloys

Inclusions present in molten Mg can be categorized into two major groups [20]:

1. Nonmetallic inclusions: These include oxides and nitrides; Na-, Mg- and K-based chlorides; Al- and Ca-based carbides, Mg-based sulphides (MgS), fluorides (MgF₂), and sulphates (MgSO₄). Oxides are the most predominant non-metallic inclusions, followed by nitrides.

2. Intermetallic inclusions: These include Fe-rich intermetallic phases, which precipitate during iron removal. Almost all intermetallic inclusions contain Fe.

Both inclusion types are potentially harmful to the properties of Mg alloys, in particular UTS, elongation and corrosion resistance. Further description of the influence of inclusions on the properties of Mg alloys is discussed in Section (2.4). The characteristics of the various inclusions found in Mg alloys are summarized in Table 2-4, and the typical inclusions observed are shown in Figure 2-1.

Table 2-4: Inclusions in Mg Alloys [21-23]

Type	Morphology	Dimensions (μm)	Density (g/cm ³)
Oxides			
MgO	Particles Films	10-300 0.5-1 (thickness) 50-400 (length)	3.58
MgO·Al ₂ O ₃ (spinel)	Particles		3.58
Nitrides			
Mg ₃ N ₂	Particles Films	10-300 0.5-1 (thickness) 50-400 (length)	2.71
Carbides			
Al ₄ C ₃	Particles	0.1-10	2.36
CaC ₂	Particles	2-20	2.22
Chlorides and salts			
MgCl ₂			2.32
NaCl	Particles	10-50	2.17
CaCl ₂			2.15
KCl			1.98
Other non-metallic inclusions			
Fluorides (MgF ₂)			3.15
Sulphides (MgS)	Particles		2.68
Sulphates (MgSO ₄)			2.66
Borides (FeB)			7.15
Iron-rich intermetallic compounds			
Al ₈ (Mn,Fe) ₅ , α-AlMnFe, (Mn,Fe) ₅ Si ₃ , Al ₈ (Mn,Fe) ₄ RE, α-Fe, Fe ₂ (Si,B), Fe ₃ (Al,Si), (Fe,Mn) ₃ Si	Particles, needles	<20	4-7

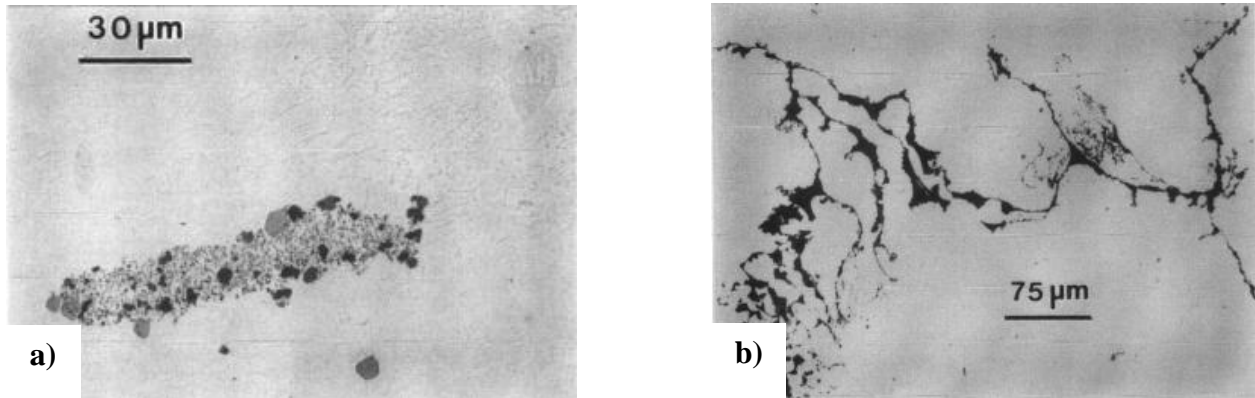


Figure 2-1: Optical Micrographs of a) an Oxide Cluster in AZ91 Alloy and b) a “Snaky” Oxide in AM50 Alloy [24]

2.2 Origin of Inclusions in Mg Alloys

2.2.1 Reactions with Air

During melting, molten Mg reacts with oxygen to form magnesium oxide (MgO) when the melt is exposed to the atmosphere [20,25]. Molten Mg reacts with the moisture in air to form MgO and hydrogen, which can result in a fire or explosion. Therefore, all tools to be used must be preheated before immersion in the melt. The casting process, stirring, charging, ladling, poor venting, removal of dross and sludge and excessive movement of the mould before solidification is complete [26] almost always leads to some melt turbulence, which entraps inclusions. It also exposes a fresh melt surface to the atmosphere, further increasing the number of inclusions in the melt. Oxide defects exhibit various morphologies, from particles to films with films measuring up to 50 μm in length with a thickness of 0.5 μm . The oxide particles are commonly seen as clusters less than 50 μm in diameter. Both oxide films and clusters have high surface to volume ratios and cannot be removed by melt settling [25].

Magnesium nitrides (Mg_3N_2), may appear together with oxide clusters. As can be seen in Table 2-5, the standard Gibbs free energy associated to the oxidation of Mg is more negative than the Gibbs free energy associated with the formation of magnesium nitride, meaning that Mg preferentially reacts with oxygen over nitrogen. Magnesium nitride will not form unless the partial pressure of oxygen becomes extremely low [25] and there is no indication that nitride inclusions appear independently of oxide inclusions.

Table 2-5: Standard Gibbs Free Energy ($\Delta G^\circ_{\text{reaction}}$) as a Function of Temperature of Selected Reactions [27,28]

Reaction	$\Delta G^\circ_{\text{reaction}} \text{ (kJ/mol)} = a + b.T.\log T + c.T$			Temperature range K ($^\circ\text{C}$)	$\Delta G^\circ_{\text{reaction}} \text{ (kJ/mol)}$
	a	b	c		
$\text{Mg}_{(l)} + 1/2 \text{O}_{2(g)} = \text{MgO}_{(s)}$	-608	-1.00	0.1128	923-1380 (650-1107)	-3240 to -4785
$\text{Mg}_{(l)} + 1/3 \text{N}_{2(g)} = 1/3 \text{Mg}_3\text{N}_{2(s)}$	-162	0	0.0757	923-1061 (650-788)	-92 to -81

2.2.2 Reactions with Fluxes

Fluxes are used to protect Mg melts from oxidation and for refining (removal of inclusions). Flux inclusions (e.g., MgCl_2 , CaCl_2) occur if unabsorbed protective flux remains on the metal surface, the flux is not viscous enough, there is brittle or powdery flux due to long handling, pouring is too fast or if there is incomplete removal of the flux adhering to the lip of the pot before pouring [29]. Magnesium chloride in the flux can react with oxygen and water in the air to form MgO , which can become entrapped in the casting [30]. Similarly, the use of boride-containing fluxes could lead to the formation of FeB inclusions [31]. Considerations related to flux entrapment and melt loss [32] led to a shift to the use of protective atmospheres [33].

2.2.3 Reactions with Protective Gases

Protective atmospheres [34-43] are used to prevent oxidation or burning of molten Mg and consequently to reduce the formation of inclusions in the melt. Some cover gases, including sulphur dioxide (SO_2), sulphur hexafluoride (SF_6), hydrofluorocarbons (HFC) and fluorinated ketones (FK), modify the natural oxide film such that Mg vaporization is suppressed and reactive gases are excluded. For example, SO_2 reacts with Mg to form MgSO_4 , MgO or MgS [37]. With SF_6 , HFC and FK, the reaction products are MgO and MgF_2 [34-36,38-43]. All these compounds can enter the melt and lead to the formation of inclusions. Although protective gases may lead to the formation of inclusions, their absence would be more detrimental to the properties of Mg alloys.

2.2.4 Reactions During Melt Treatment and Alloying

Inclusions can be introduced during the process of Fe removal using Mn. With the addition of Mn, intermetallic particles containing Fe, Mn and Al form [20]. Inclusions can also result from degassing and grain refinement by the addition of C_2Cl_6 , calcium cyanamide ($CaCN_2$) or by the addition of alloying elements (e.g., Al_4C_3 in Mg alloyed with Al) [20].

2.2.5 Reactions During Casting

During casting, poor running system design is generally associated with high surface turbulence and greater entrainment of oxide films typically double oxide film defects (bifilms) comprised of folded MgO films [44,45]. The high reactivity of Mg results in rapid formation of MgO films during pouring that quickly thickens to produce a tube of oxide that surrounds the falling metal stream. This tube of oxide is not in danger of becoming entrapped within the liquid metal if the oxide film is unbroken. A similar phenomenon occurs in Al alloys and is due to the same mechanism of rapid thickening of oxide films [46]. The oxide film forming at the surface of the Al melt is relatively thin and elastic as compared to the thick and cracked oxide film forming at the surface of the Mg melt. As a result, Mg alloys may be more prone to bifilm formation than Al alloys.

Inclusions can also be generated during die casting from oxidation in the shot sleeve, entrapment of air during casting, and absorption of lubricants spread on the die surface [20,47,48]. In sand casting, turbulent flow may cause sand grains to detach from the mould wall and be entrained within the Mg melt, with which they react. The inclusions formed are called “reacted sand inclusions” [20,48,49].

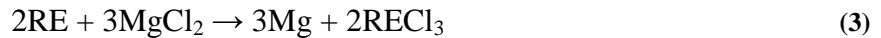
2.3 Control of Inclusions in Mg Alloys

Inclusions can be minimized by the application of best practices in the foundry. These include strict attention to charge selection, melting conditions, careful skimming of slag or dross, development and improvement of gating system design to minimize turbulence and process control (e.g., temperature control to minimize the precipitation of intermetallic particles and good settling practice). The inclusion content in the melt can be further decreased by refining techniques (cleaning or separation of nonmetallic inclusions from the melt) or alloying additions. These are described in the following sections.

2.3.1 Addition of Flux

In flux-based refining, the melt is heated to approximately 705°C, a flux is added and the melt is stirred thoroughly. The flux absorbs the oxides present in the melt to produce a sludge. After stirring, the sludge is allowed to settle to the bottom of the crucible, thereby enabling the refined melt to be separated from the sludge. Typical fluxes used in Mg refining are composed of magnesium chloride (MgCl₂), other chlorides (e.g., potassium chloride KCl, sodium chloride NaCl) and calcium fluoride (CaF₂) [1]. Recently developed fluxes can also contain up to 30 wt.% TiO₂. The added TiO₂ facilitates Fe removal in melts by forming Ti-Fe compounds that settle at the bottom of the crucible [50].

The actual composition of the flux, however, will depend to a large extent on the type of Mg alloy to be refined. The major alloying elements (Al, Zn, Mn) are stable in the melt [32,48] as their free energies for chloride formation are higher than that of Mg. However, strontium chloride (SrCl₂), calcium chloride (CaCl₂) and chlorides containing RE elements (YCl₃, CeCl₃, GdCl₃) are more stable than MgCl₂ [51,52]. This indicates that MgCl₂ in the flux should react with Sr, Ca and RE elements, resulting in the loss of these elements. The reactions are shown below:



In order to solve this problem, two approaches were considered. In the first one, fluxes were specially formulated to minimize the loss of rare earth elements [53-58] but even with properly designed fluxes, the possibility of flux inclusions becoming entrapped within the melt are still possible especially during the turbulent stages during casting such as ladle handling, skimming and pouring. The second approach consisted in using fluxless refining [59].

2.3.2 Fluxless Refining

Fluxless refining includes all refining processes where salt is not used. Inclusions are removed from the bulk melt and transferred either to the melt surface, settle to the bottom or stick to the crucible walls prior to casting [60]. Fluxless refining processes are based on sedimentation (settling), flotation, interception or electromagnetic forces to separate inclusions from the melt.

2.3.2.1 *Protective Atmospheres*

Protective atmospheres [34-43] are used to prevent oxidation or burning of molten Mg and consequently to reduce the formation of inclusions in the melt. There are two types of protective gas atmospheres [61]: non-reactive gases and oxide film modifiers.

Non-reactive gases, such as CO₂, N₂ and Ar, prevent burning. However, use of such gases alone is impractical outside of the laboratory as they do not suppress Mg vaporization which can result in melt loss. In addition, as Mg vaporizes, it condenses into pyrophoric size particles on the cooler surfaces of the furnace [30].

The other method of melt protection involves the use of a gas which modifies the magnesium oxide film forming naturally on the surface of the melt, thereby suppressing vaporization. Since the 1970s, the Mg industry has largely used SF₆ to protect Mg melts [30,34,35,42,61-66]. Sulphur hexafluoride is an effective cover gas due to its ability to react with Mg to form a dense film containing magnesium oxide (MgO) and magnesium fluoride (MgF₂) on the molten Mg surface. This film prevents further oxidation and evaporation of Mg [34,35,66]. Sulphur hexafluoride is also attractive as a cover gas since it is odourless, colourless, non-toxic and non-flammable. It has been found that a combination of SF₆ and CO₂ is better than SF₆ alone for pure Mg and most Mg alloys. The optimum SF₆ concentration is 0.1 to 0.2 vol.% as an excess concentration of SF₆ will cause severe crucible corrosion [30]. However, SF₆ is becoming increasingly expensive and is also an extremely powerful greenhouse gas, with a 100-year global warming potential estimated at 23,900 times that of CO₂. In addition, SF₆ is chemically stable in the atmosphere and remains present for over 3,200 years [67].

Environmental concerns have thus prompted the Mg industry to seek alternatives to SF₆. Sulphur dioxide (approximately 1.5 in air) was demonstrated to adequately protect molten Mg. However, SO₂ is a toxic gas causing corrosion of foundry equipment [65]. Experiments also proved that pure CO₂ effectively protects molten Mg, as long as the CO₂ atmosphere is not contaminated with substantial quantities of air [65].

Other potential alternatives include HFCs [36,39,41,43,68,69], FKs [40], BF₃ [70] and solid CO₂ [71,72]. Hydrofluorocarbons, which include HFC-134a (1,1,1,2-tetrafluoroethane C₂H₂F₄) [39,41], HFC-152a (1,1-difluoroethane C₂H₄F₂) [43] and HFC-125 (pentafluoroethane C₂HF₅) [69], have global warming potentials 8.5 to 170 times lower than SF₆. The protection mechanism is similar to that of SF₆ with the formation of MgF₂ and

MgO [36,68]. Boron trifluoride is not a greenhouse gas and is well known for its excellent protective behaviour. However, BF_3 is highly toxic and expensive. Boron trifluoride must also be stored as a concentrated, highly compressed gas and, as a result, special storage conditions are required to minimize explosion hazard. The MagShield system was developed to enable safe distribution of BF_3 . Specifically, the gas was produced in-situ by the controlled decomposition of KBF_4 [70]. Fluorinated ketones [40] have global warming impact similar to that of CO_2 . They thermally decompose on the molten Mg surface, producing MgF_2 and CO_2 and has provided protection at significantly lower concentrations than SF_6 . The use of solid CO_2 pellets to protect magnesium was accomplished by injecting CO_2 into the furnace chamber by a specially designed nozzle. The CO_2 pellets precipitate at the molten metal surface and reduced the tendency of Mg to evaporate. Sublimated CO_2 snow also causes the CO_2 gas to expand and displace all oxygen from the bath surface area [71,72]. For all cover gases, care should be taken to ensure that the gases are free of moisture and a continuous supply of fresh cover gases is optimal. The use of cover gases is the best preventative measure to minimize inclusion formation during casting operations. Many alternatives and combinations have been examined and for this research, the protective atmosphere utilized was CO_2 or CO_2 with SF_6 as it provides a good compromise between performance, safe usage, availability and cost effectiveness. Even with effective protective atmospheres, inclusions in Mg alloys could form and become detrimental to the casting properties. Additional techniques that could be used with protective atmospheres are filtration, inert gas bubbling and degassing.

2.3.2.2 *Filtration of Inclusions*

One simple method to reduce the presence of inclusions in castings is to reduce metal turbulence during melt handling [48,73]. High melt turbulence increases the probability of entraining gases or oxide films during mould filling, introducing more inclusions into the casting. Incorporating filters into the casting process helps reduce melt turbulence by regulating metal flow. Filters must be inert, rigid, thermally stable and thermally shockproof [74]. Ideally, the filter should be placed in the gating system of the mould (closest location to casting) as determined by examining the filling of a Mg plate casting using a mould with a pyrex glass cover at a pouring temperature of 680°C . With all other conditions being constant, the melt velocity

with no filter was 0.18 m/s and with a filter in the runner, 0.13 and 0.14 m/s with a filter at the gate [75]. There are three stages of melt filtration [75]:

1. **Initial surge:** Metal enters the filter pores and brings the filter temperature up to the melt temperature.
2. **Normal flow:** The metal flow through the filter is constant.
3. **Filter blockage:** The filter becomes blocked and metal flow stops.

Ceramic foam filters (CFF) consist of several open cells arranged in foam-like structures. Ceramic foam filters are typically used to lower inclusion levels in liquid Al alloys and steels. In contrast, the performance of CFFs for Mg alloy melts has not been studied extensively.

Bakke *et al.* [76] studied the effect of CFFs on the level of inclusions in AZ91 alloy. The CFFs used in their study consisted of 68.2% Al_2O_3 , 14.6% SiO_2 , 15.2% ZrO_2 , 1.3% TiO_2 and 0.7% others (K_2O , CaO , HfO_2 , Fe_2O_3 and MgO). Their results indicated that the filtration efficiency of the CFFs was very good. Griffiths and Lai [45] observed that CFFs in combination with a well designed gating system could reduce double oxide film defects (folded MgO films).

However, it was reported that CFFs have limited and controversial efficiency:

1. CFFs can react with Mg melt and contaminate the melt [77,78]. Wu *et al.* [78] studied the potential reactions between various CFF materials (MgO , Al_2O_3 , ZrO_2 and SiC) and AZ91 melt during filtration. The authors observed that molten Mg reacted with SiC filters to form Mg_2Si phases. Under the solidification conditions studied, Mg_2Si phases exhibited a Chinese script morphology, which could reduce the mechanical properties of the alloy. The formation of Mg_2Si was confirmed by thermodynamic calculations, which also revealed that Mg melt would react with Al_2O_3 and ZrO_2 but not MgO . In conclusion, only MgO CFFs were suitable for filtration purification of Mg melts.
2. The CFFs' adsorption ability for inclusions can be very poor. For example, thermodynamic calculations showed that Al_2O_3 filters cannot adsorb flux inclusions in the melt. This makes it difficult to eliminate inclusions with diameters below 20 μm and liquid flux inclusions. In contrast, MgO proved to have good adsorption ability [78].
3. There is no way to determine the point at which a filter becomes ineffective and needs replacement [77].

Stainless steel meshes are typically used for the filtration of Mg melts due to their relatively low cost, high availability and non-reactivity with Mg melts. Le *et al.* [79] used stainless steel filters of decreased pore size in AZ91 + 2 wt.% Ca alloy. They found that the finest mesh caused a reduction in the number and maximum size of the inclusions. Also, they determined that low pouring temperatures ($\sim 700^{\circ}\text{C}$) reduced the oxidation potential of the melt and the inclusion levels [79]. Tardif *et al.* [80] also examined the use of knitted steel mesh filters to remove melt inclusions in permanent moulds. Two and four ply filter configurations were examined and were found to entrap mainly MgO and some Al-Mn-Fe intermetallic particles.

Wang *et al.* [81] also showed that using stainless steel filters was an effective method to purify Mg-Gd-Y-Zr magnesium melts. The results indicated that the average size and volume fraction of the inclusions were significantly reduced (56% for the average size and 76% for the volume fraction), as shown in Figure 2-2.

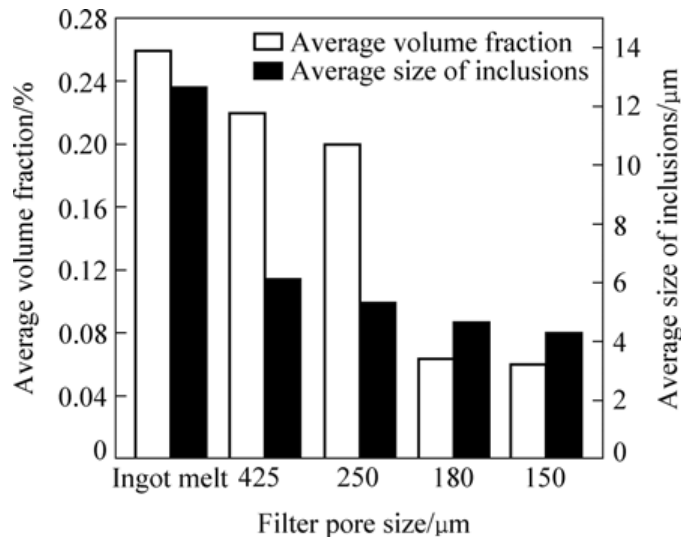


Figure 2-2: Effect of Filtration on the Size and Amount of Inclusions in Mg-Gd-Y-Zr Magnesium Alloy [81]

Wang *et al.* [82] studied the effect of stainless steel mesh filters with various pore sizes on the melt cleanliness of AZ31 magnesium alloy. They observed that the use of filters proved to be an effective way to reduce the amount of inclusions in the alloy. The average size of the inclusions decreased from 16.5 to 2.0 μm .

Contradictory results were obtained by Emadi *et al.* [83]. In their study, the use of steel mesh filters did not lead to a reduction in the amount of inclusions in AZ91D permanent mould casting, with consequent absence of improvement in mechanical properties.

The applicability of CFFs seems to be limited due to lack of research and compatibility issues with Mg. The use of steel mesh filters appears to be more reliable, established and easier to implement on a casting scale. However, there has been limited research as to what locations filters should be placed within the mould and how pore sizes influence filter performance. The many variations between researchers regarding filter type, alloy examined and filter placement makes comparisons difficult. Therefore, for this research a steel mesh filter will be utilized and filter parameters of filter location and pore size will be examined.

2.3.2.3 *Inert Gas Bubbling (Sparging)*

The refining method of gas sparging utilizes an inert gas to float melt inclusions to the surface of the melt where they could be skimmed away. Typical gases used are Ar or CO₂. The efficiency of gas bubbling to remove inclusions depends on bubbling time, gas flowrate, bubble size and melt temperature [84]. Typical usage of Ar gas sparging was a flowrate of 1.8 L/min at a melt temperature of 740°C for a bubbling time of 30 minutes for 6 kg of melt [84]. With increasing bubbling time and/or flowrate the rate of inclusion removal and hence, mechanical properties improved. Excess gas bubbling resulted in additional porosity in the melt that reduced strength and elongation. Argon bubbling was effective in removing inclusions less than 80 µm but was unable to remove inclusions larger than 800 µm in size [32]. The limited availability of quantitative results on the efficiency of gas bubbling has sparked the need to determine the optimal processing variables (e.g., Ar flowrate, residence time, bubble diameter, melt temperature) to enable efficient melt refining.

A combination of Ar gas sparging at 11.8 L/min and a stainless steel filter with openings of 1.14 mm (smaller openings were more prone to plugging and choking of metal) on 1360 kg of recycled AZ91D Mg alloy, has been shown to reduce the number of non-metallic inclusions/cm² from 124 to 65 for the unfiltered and the filtered and bubbled melts respectively [32]. A similar result was observed with the simultaneous use of a 20 pores per inch Al₂O₃ based ceramic foam filter and Ar bubbling by Wu *et al.* [85]. Argon was bubbled into the molten Mg using a rotary impeller and the optimum bubbling conditions were determined to be 0.033 L/min flowrate for

30 minutes at a melt temperature of 740°C. Argon bubbling appears to be an effective technique to remove fine inclusions in Mg alloys. However, few researchers examined the influence of simultaneous Ar bubbling and filtration treatments and those that did utilized ceramic filters and not steel filters. Therefore, it would be advantageous to examine the influence of Ar bubbling with filtration with steel mesh filters.

2.3.2.4 *Degassing*

Melt degassing utilizes typically reactive Cl_2 gas or C_2Cl_6 to reduce dissolved hydrogen gas content within melts. The addition of C_2Cl_6 has the added advantage of grain refining melts [86-90], but causes environmental problems due to the emission of Cl_2 gas [87,88,91], chlorinated hydrocarbons [86,87,90,92,93] and dioxins [94,95]. Both methods benefit from the formation of MgCl_2 (common flux component), which can remove inclusions as discussed previously but may become an inclusion itself if it becomes entrapped within the melt during pouring. Typical usage of Cl_2 gas bubbling involves heating the melt to 735-750°C and bubbling for 5-15 minutes [26]. The use of degassers is effective and has added benefits of grain refinement, however, it is not environmentally friendly. This research aims to utilize environmentally friendly methods to clean Mg melts while effectively grain refining using carbon (C) based grain refiners.

2.4 Effect of Inclusions on the Properties of Mg Alloys

There is limited data in the literature on the effects of non-metallic inclusions on die cast Mg [96]. In this section, the available data are reviewed.

2.4.1 Tensile and Fatigue Properties

It is known that inclusions lead to premature failure of the material by reducing the effective cross section of metal under load and by the concentration of stresses at the inclusion. The direct impact of inclusions on the mechanical properties is, however, difficult to quantify, since casting defects such as cold shuts, hot tears and porosity will normally be present alongside inclusions and dominate over inclusions in determining the properties of a cast part [97].

This is illustrated in the work of Chen *et al.* [98] and Yim *et al.* [84] where Chen *et al.* [98] studied the effect of ultrasonic treatment on the microstructural and mechanical properties of AZ91 and AM60 alloys. It was found that the application of ultrasound to the melt led to smaller,

more numerous and more evenly distributed oxide films in the melt and was expected to result in improved mechanical properties. However, gas pores and air pockets were also entrapped in the alloys during solidification, leading to a reduction of the UTS and the elongation.

Similarly, gas bubbling led to the removal of inclusions in AZ91D melt [84]. This was however accompanied by the formation of pores in the casting. Consequently, the tensile elongation of the alloy was found to decrease.

For castings free of defects (hot tears, porosity, folds, etc.), the inclusion content and distribution of inclusions are assumed to be a critical factor in determining mechanical properties [97]. A significant improvement in the UTS and elongations [32,50,53-56,75,80,81,96,99,100] and the impact strength [96,100] with the reduction of inclusion content in the melt was indeed observed by several researchers.

The stress-strain curves (Figure 2-3) for AM50 alloy containing different levels of inclusions suggest that clean melts fracture at significantly higher strain than contaminated melts [97]. An inclusion level of 500 ppm was found to be the highest acceptable inclusion content.

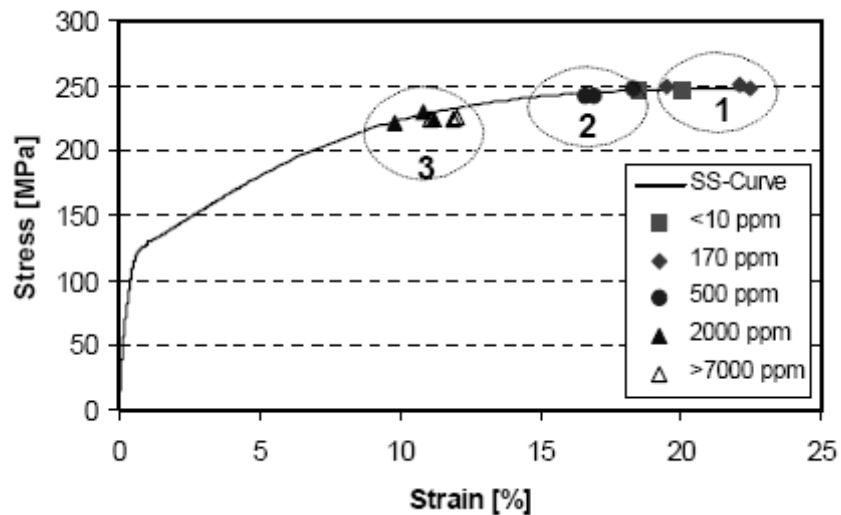


Figure 2-3: Effect of Metal Cleanliness on the Mechanical Properties of Die Cast AM50 [97]

Mirak *et al.* [44] showed that improving the running system design can lead to increased ultimate bend strength from 180 to 400 MPa, as a result of the reduction of the in-gate velocity from 1 to 0.25 m/s. The Weibull modulus also increased with a reduction of the in-gate velocity, indicating decreased scatter of mechanical properties and improved reliability of the castings. This was attributed to a reduction of surface turbulence and double oxide films in the castings.

Wang *et al.* [82] observed that the tensile properties of AZ31 alloy improved with the use of stainless steel mesh filters. The UTS and elongation of the alloy increased from 194 MPa and 13.8% to 212 MPa and 20.3% respectively.

Similarly, Tardif *et al.* [80] showed that melt filtration of AZ91 alloy produced consistently sound castings with improved tensile properties. Nazari *et al.* [75] and Griffiths *et al.* [45] also showed that filtered castings exhibited higher Weibull moduli than unfiltered castings, indicating that the mechanical properties of the alloy were more consistent and reproducible.

Wu *et al.* [78,85] investigated the effect of filtration and Ar bubbling on the UTS and elongation of AZ91. There was significant improvement in the UTS (10%) and the elongation (54%) with Ar bubbling and filtration (Table 2-6).

Table 2-6: Effect of Filtration and Ar Bubbling on the UTS and the Elongation of AZ91 [85]

Refining treatment	UTS (MPa)	Elongation (%)
No treatment	175.3	2.74
Filtration (CFF, 20 pores per inch, 20 mm thick)	189.1	4.02
Ar bubbling (flowrate: 2 L/min, bubbling time: 30 minutes)	180.6	3.53
Ar bubbling + Filtration	192.1	4.22

Haerle *et al.* [100] obtained similar results. There was a further improvement of the mechanical properties when gas bubbling was combined with melt filtration, in agreement with Housh and Petrovich [32].

In regards to C_2Cl_6 addition, Emadi *et al.* [83] showed that without any pretreatment, the as-cast YS, UTS and elongation of AZ91D alloy were 78 MPa, 176 MPa and 4.4% respectively. With the addition of 0.3 wt.% C_2Cl_6 , the grain size decreased from 88 to 56 μm and the castings showed much fewer and smaller inclusions on the fracture surface. The YS, UTS and elongation increased to 92 MPa, 200 MPa and 5.1% respectively. In the case of AZ31 alloy, the YS, UTS and elongation were 52 MPa, 161 MPa and 14.5% respectively. When 0.2 wt.% CaO was added to AZ31, these properties increased to 74.9 MPa, 175.9 MPa and 18.0% respectively [101]. In both cases, the improvement in mechanical properties was attributed to both grain refinement and inclusion removal.

The addition of a C_2Cl_6 -KCl mixture was also found to improve melt cleanliness of recycled AZ91E castings [102]. Upon remelting twice, the casting elongation reduced from 3.18% to 2.15% as compared to the virgin casting. The melt was cleaned of oxides with the addition of 1.0 wt.% C_2Cl_6 -KCl mixture resulting in an improvement in mechanical properties and elongation. The casting remelted twice had a UTS and elongation of 171 MPa and 2.15% respectively and increased to 195 MPa and 4.03% respectively with the addition of the C_2Cl_6 -KCl mixture.

Researchers performed several studies on a Mg-10 wt.% Gd-3 wt.% Y type alloy [53,54,56,81,99] investigating the separate and combined effect of filters and various fluxes on mechanical properties. The use of fluxes resulted in the removal of inclusions in the melt, which in turn led to a significant increase of the UTS and elongation. Wang *et al.* [54] also studied the effect of MgO CFFs on the properties of Mg-10 wt.% Gd-3 wt.% Y. As compared to the untreated samples, the mechanical properties were higher but remained inferior to those obtained by using a flux, as the filter only removed large inclusions. In another study on Mg-Gd-Y-Zr alloy, the YS, UTS and elongation improved from 156 MPa, 200 MPa and 3.4% to 167 MPa, 232 MPa and 7.0% respectively with the use of filters [81]. A similar study was performed on AZ91 alloy [50]. Again, it was found that the use of flux improved the mechanical properties of the alloy. The mechanical properties were further enhanced by combining the use of flux with ceramic foam filtration.

It should be noted that small oxide inclusions play a minor role in influencing tensile properties of castings. In a study by Wang *et al.* [103], the results indicate that oxide contents up to 1000 ppm levels have apparently no effect on tensile properties when most oxides are less than 15 μm and oxide films are less than 50 μm in size.

It is also accepted that fatigue life decreases significantly with inclusion size. In AZ91E alloys, Horstemeyer *et al.* [104] have shown that if the inclusion size is reduced from several millimetres to several hundred microns, the fatigue life in the high cycle fatigue regime can be increased by two orders of magnitude.

2.4.2 Corrosion Resistance

Inclusions have a deleterious effect on the corrosion resistance of Mg alloys [54-56,81,96]. As an example, Wang *et al.* [54] studied the effect of inclusions on the corrosion rate of

Mg-10 wt.% Gd-3 wt.% Y-0.5 wt.% Zr alloy. They observed that the corrosion rate increased with an increase of the average volume fraction of inclusions, as shown in Table 2-7. This was attributed to the difference in electronegativity between the inclusions and Mg matrix. The inclusions act as cathodes and form galvanic coupling with the matrix, leading to pitting corrosion. With an increase of inclusion content, the cathodic area increases, thereby adversely affecting the corrosion resistance of the alloy [105].

Table 2-7: Effect of Inclusion Content on the Corrosion Rate of Mg-10 wt.% Gd-3 wt.% Y-0.5 wt.% Zr Alloy [54]

Average volume fraction of inclusions (%)	Corrosion rate (mg/cm²d)
4.07	2.0
2.84	1.8
0.87	1.3

The potential benefits to mechanical properties (namely UTS and elongation) and corrosion resistance with inclusion removal are very large and cannot be ignored if the performance gap between Mg and Al is to be minimized. Additional measures in improving Mg alloy performance would include the development of effective and environmentally friendly grain refiners.

Part II: Grain Refinement of Mg Alloys

2.5 Benefits of Grain Refinement

Grain refinement improves mechanical properties [106], enables uniform distribution of solute and secondary phases [87], decreases solution heat treatment times [89], increases pressure tightness [15] and increases feeding while reducing segregation, porosity and hot tearing [15,89,107,108]. On a processing level, grain refinement provides consistent mechanical properties after heat treatment, improved machinability [15] and formability [109] by weakening texture [110]. Unlike solid solution strengthening, precipitation hardening and work hardening, grain refinement imparts improvements in strength without hindering ductility [2,3]. Therefore, grain refinement is very beneficial to control the grain size of the alloy ensuring consistent performance of cast products [111], particularly in casting processes where the cooling rate is low [107].

With fine grains, dislocation motion is easily impeded by the large grain boundary area as compared to a coarse grained material. For many materials including Mg, the YS is a function of grain size [112,113] according to the Hall-Petch equation:

$$\sigma_y = \sigma_o + k_y d^{-1/2} \quad (4)$$

Where:

σ_y : YS

σ_o : Stress to initiate dislocation motion

k_y : Unpinning constant (measure dislocation pile-up at barriers)

d : Average grain diameter

Thus, a material with a fine grain structure is expected to have higher YS than a coarse grained material. Grain refinement is especially beneficial for HCP metals such as Mg because of their few slip systems [107]. Unfortunately, there is no universal, reliable grain refiner for Mg alloys [92,107,114,115] effective over long holding times without adversely influencing castability or corrosion resistance so more research is required to gain a better understanding of grain refinement [18]. Part II of CHAPTER 2 outlines how grain refinement can be achieved by alloying to cause grain growth restriction or by adding nucleants.

2.6 Grain Growth Restriction

One method to control the grain size and enable grain refinement is to add solute elements into the melt that control the growth of the nucleated grains [92]. The added solute tends to diffuse and concentrate at the solid-liquid interface building a constitutionally undercooled zone that promotes solidification at a lower temperature as compared to low solute areas of the melt. This solute diffusion slows the solidification front and causes grain refinement. For high cooling rates, constitutional undercooling could be utilized to obtain a homogeneous and fine microstructure [116]. Grain growth restriction of an element can be quantified using the growth restriction factor (Q) [117]:

$$Q = mC_i (k - 1) \quad (5)$$

Where:

m: Liquidus slope on a phase diagram

k: Equilibrium partition coefficient

C_i : Initial concentration of the solute in the melt

Values of Q are additive for all the solutes in the melt [92] but assumes linear relationships and no interactions between alloying elements [111]. The higher the value of Q, the higher will be the constitutional undercooling and, consequently, the smaller will be the grain size [117]. A comparison of the m, k and $m(k-1)$ values of various elements in Mg melts are summarized in Table 2-8.

Table 2-8: Summary of m, k and $m(k-1)$ for Different Elements in Mg [18,92,107,118]

Solute	Type of System	m (K/wt.%)	k	$m(k-1)$ (K/wt.%)
Ti [118]	peritectic	~500	~120	~ 5.95×10^4
Fe	eutectic	-55.56	0.054	52.56
Zr	peritectic	6.90	6.55	38.29
Ca	eutectic	-12.67	0.06	11.94
Si	eutectic	-9.25	~0.00	9.25
Ni	eutectic	-6.13	~0.00	6.13
Zn	eutectic	-6.04	0.12	5.31
Cu	eutectic	-5.37	0.02	5.28
Ge	eutectic	-4.41	~0.00	4.41
Al	eutectic	-6.87	0.37	4.32
Sc [92,107]	peritectic	4.02	1.99	3.96
Sr	eutectic	-3.53	0.006	3.51
Sc [18]	peritectic	4.02	1.65	2.61
Ce	eutectic	-2.86	0.04	2.74
Yb	eutectic	-3.07	0.17	2.53
Y	eutectic	-3.40	0.50	1.70
Sn	eutectic	-2.41	0.39	1.47
Pb	eutectic	-2.75	0.62	1.03
Sb [18]	eutectic	-0.53	~0.00	0.53
Mn [18]	peritectic	1.49	1.10	0.15

While the $m(k-1)$ value is highest for Ti, the results in Table 2-8 do not consider solubility and hence, restrict the amount of possible solute restriction that is possible. As a major alloying element in Mg alloys, Al addition imparts a significant amount of grain refinement by grain growth restriction as observed by increasing Al concentrations from 0.5 to 4 wt.% resulting in

grain size reductions from ~1400 to ~400 μm (71% reduction) for Mg-0.5 wt.% Al and Mg-4.0 wt.% Al alloys respectively [119]. The grain size of the centre of a cast pure Mg sample was ~1000 μm and continually decreased with Al addition up to 5 wt.% where the grain size was ~175 μm (83% reduction) then remained constant with further Al addition [92,107].

The refining effect of Si is significant but recovery is poor as dissolution of Si to levels beyond 0.5 wt.% were difficult despite constant stirring and long holding times [92,107].

Additions of La to AZ91 refined the grain size by solute restriction, $\text{Mg}_{17}\text{Al}_{12}$ particle size and introduced $\text{Al}_{11}\text{La}_3$ that strengthened the alloy [120].

Grain growth restriction also enables nucleation as the generated constitutionally undercooled diffusion layer ahead of the solid/liquid interface allows nucleating crystals a chance to grow [92,107,121].

2.7 Nucleation of Metals and Alloys

The transformations of a liquid metal with a non-crystallographic structure to a solid with crystallographic structure are the first signs of solidification. The two types of nucleation processes possible are (1) homogeneous nucleation and (2) heterogeneous nucleation [122].

2.7.1 Homogeneous Nucleation

In homogeneous nucleation, the liquid metal solidifies by the clustering of small groups of atoms called nuclei. In many instances, the transformation of a pure liquid metal to a solid does not occur at a single temperature. The melt must be undercooled for the liquid to solid transformation to occur and this undercooling is the driving force for nucleation [122]. The nucleation of a solid is best understood using a diagram similar to Figure 2-4.

Nucleation processes play a key role in the solidification of castings. The beginning of solidification requires a free energy change. The free energies (G_1 and G_2) of the system before and after nucleation are in Figure 2-4a and b respectively and can be described as [122]:

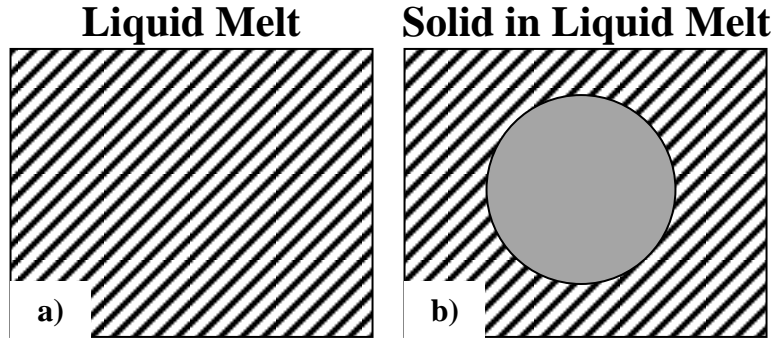


Figure 2-4: Homogeneous Nucleation a) Only Liquid Melt b) Solid in Liquid Melt [122]

$$G_1 = (V_s + V_l)G_v^l \quad (6)$$

$$G_2 = V_s G_v^s + V_l G_v^l + A_{sl} \gamma_{sl} \quad (7)$$

Where:

V_s : Volume of solid

V_l : Volume of liquid

G_v^s : Free energy of the solid per unit volume

G_v^l : Free energy of the liquid per unit volume

A_{sl} : Surface area of the solid-liquid interface

γ_{sl} : Interfacial tension of the solid-liquid interface

Assuming the densities of the liquid and solid are equal (at nucleation), γ_{sl} is isotropic and r represents the radius of a spherical nucleus the change in free energy ($\Delta G_r = G_2 - G_1$) is [122]:

$$\Delta G_r = -\frac{4}{3} \pi r^3 \Delta G_v + 4\pi r^2 \gamma_{sl} \quad (8)$$

Where ΔG_v is $G_v^s - G_v^l$. Examination of Equation 8 shows that with increasing radius, the volume free energy change ($\frac{4}{3} \pi r^3 \Delta G_v$) tends to favour nucleation while the interfacial energy ($4\pi r^2 \gamma_{sl}$) tends to resist nucleation.

For a given undercooling ΔT , there is a critical radius r^* associated with a maximum free energy ΔG^* . If $r < r^*$, the system lowers its energy by dissolving the embryo. If $r > r^*$, the free energy decreases if the solid grows [122].

By differentiating Equation 8 with respect to r and setting $\Delta G_r = 0$, the critical radius (r^*) can be calculated as [122]:

$$r^* = \frac{2\gamma_{sl}}{\Delta G_v} \quad (9)$$

With a given undercooling (ΔT), ΔG_v is given by [122]:

$$\Delta G_v = \frac{L_v \Delta T}{T_m} \quad (10)$$

Where:

L_v : Latent heat of fusion per unit volume

T_m : Melting point of the liquid

Substitution of (ΔG_v) into Equation 9 shows that r^* , and subsequently ΔG^* , can be decreased by increasing the undercooling or by lowering the interfacial surface energy.

$$r^* = \left(\frac{2\gamma_{sl} T_m}{L_v} \right) \frac{1}{\Delta T} \quad (11)$$

For Mg, r^* is $\sim 1.3 \mu\text{m}$ [16].

2.7.2 Heterogeneous Nucleation

In practice, homogeneous nucleation rarely takes place because of the relatively large activation barrier required for nucleus formation and heterogeneous nucleation dominates. In heterogeneous nucleation undulations on the mould walls promote crystallization by lowering the activation barrier ΔG^* (reduction of the interfacial energy component of Equation 8). Figure 2-5 depicts how heterogeneous nucleation takes place at a mould wall.

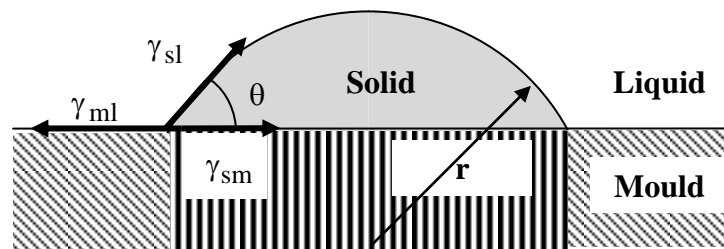


Figure 2-5: Heterogeneous Nucleation on a Mould Wall [122]

With the presence of a mould wall gap, the critical radius (r^*) required for nucleation is much smaller than that for homogeneous nucleation. Equation 12 models heterogeneous nucleation using a surface tension balance between the solid-mould, mould-liquid and solid-liquid interfaces [122].

$$\gamma_{ml} = \gamma_{sm} + \gamma_{sl} \cos \theta \quad (12)$$

Where:

γ_{ml} : Interfacial tension of the mould-liquid interface

γ_{sm} : Interfacial tension of the solid-mould interface

γ_{sl} : Interfacial tension of the solid-liquid interface

θ : Contact angle

Rearranging Equation 12 for $\cos \theta$ yields [122]:

$$\cos \theta = \frac{\gamma_{ml} - \gamma_{sm}}{\gamma_{sl}} \quad (13)$$

A surface with a small interfacial energy with the solid (low γ_{sm}) would require a small contact angle to act as a good nucleating site.

Instead of utilizing the mould wall to act as a heterogeneous nucleating site, effective substrates could be added to the melt. Considering Figure 2-5 once again, the spherical cap could grow laterally and increase r to ensure $r > r^*$ to continue nucleation. However, if we assume a substrate being represented by the vertical lined portion of the mould only, the growth of the nucleating crystal is limited by the width of the substrate (d_s). According to the Free Growth Theory by Greer *et al.* [123], thickening of the nucleating crystal reduces r and there is a barrier to free growth if $d_s < 2r^*$. Further growth is then possible by increasing undercooling (reducing r^*). Therefore, nucleation was thought to be limited by not the nucleation process itself but by the free growth on flat substrates. The issue then arises as to which substrates could be effective nucleants.

2.8 Selection of Effective Nucleants for Grain Refinement

Inoculation involves the introduction of nucleating agents to a melt (ex-situ), either by adding a nucleus, or by generating the nucleus in the melt via a chemical reaction (in-situ). Some of the characteristics of good grain refiners as outlined by Campbell [46] and Murty *et al.* [124] are:

1. Borides, carbides and intermetallic particles which form metallic or weak covalent bonds are more suitable as grain refiners rather than metal oxides which are strongly covalently bonded [125].
2. The nucleating solid and the grain refiner should have a good lattice match [46]. Namely, they should be larger than a critical radius size to initiate freezing at small undercooling [124].
3. The grain refiner should not melt or dissolve [46,124].
4. Sufficient number of nucleating particles should be uniformly distributed [124].

Melting or dissolution of a grain refiner within the melt shortly after addition is undesirable and indicates grain refiner fading. Fading is the loss of grain refiner efficiency after holding of the refiner in the melt for a long period of time. With increasing holding time the added grain refining particles tend to settle or float in the melt due to density differences. The loss of grain refiner efficiency could also be the result of refining particles agglomerating together.

To quickly determine the grain refining efficiency of an added nucleant, cooling curves for the solidifying melt could be analyzed. By comparing the undercooling observed in the refined and un-refined castings, an indirect measure of grain refinement could be obtained. As discussed in Section 2.7.1, the critical radius (r^*) for nucleation could be reduced by increasing undercooling. The relative amount of undercooling could be used as an indicator of grain refiner effectiveness [126]. In addition, grain refiner addition increases nucleation temperature and duration of recalescence [127].

One of the criteria for effective nucleants is a good lattice match with the nucleating solid. Difficulty arises in defining models to quantify lattice matching in materials for grain refiner selection. Some of the methods used are described in Sections 2.9.1-2.9.3.

2.9 Predictive Methods for Grain Refiner Effectiveness

This section outlines some techniques used to predict the suitability of grain refiners based on their crystallographic match with the nucleating phase and a model for grain size prediction.

2.9.1 Lattice Disregistry

The simplest method to quantify lattice matching is by calculating a parameter called lattice disregistry (δ) described in Equation 14 [128].

$$\delta = \frac{|\Delta a|}{a_o} \times 100\% \quad (14)$$

Where:

Δa : Difference in lattice parameter a between nucleating substrate and nucleated phase

a_o : Lattice parameter a for nucleated phase

Issues with Equation 14 are that it limits the analysis to only planes of similar atomic arrangement in materials with the same crystal structures. A two dimensional method that incorporates the angular difference between directions within the planes is planar disregistry.

2.9.2 Planar Disregistry

Calculation of planar disregistry ($\delta_{(hkl)_n}^{(hkl)_s}$) can be accomplished using Equation 15 [128].

$$\delta_{(hkl)_n}^{(hkl)_s} = \frac{1}{3} \sum_{i=1}^3 \frac{|d_{[uvw]_s} \cos \theta_d - d_{[uvw]_n}|}{d_{[uvw]_n}} \times 100\% \quad (15)$$

Where:

s and n : Representations of the substrate and the nucleated crystal, respectively

(hkl) : Low index plane

$[uvw]$: One of the three low index directions in (hkl)

θ_d : Angle between two low index directions in (hkl)

$d_{[uvw]}$: Lattice spacing along direction $[uvw]$

Effective nucleants have planar disregistries less than 12% [128] and would result in a low γ_{sm} that would reduce the contact angle (Equation 13). A summary of planar disregistries of potential nucleants with Mg are listed in Table 2-9.

Table 2-9: Planar Disregistries of Potential Nucleants with Mg

Phase	Structure	Lattice Parameters (nm)	Matching Planes	Planar Disregistry (%)
Mg	Hexagonal	a = 0.320 nm c = 0.520 nm [26,92,129]	-	-
Zr	Hexagonal	a = 0.323 nm c = 0.514 nm [92,129,130]	-	<0.5 [131]
SiC	Hexagonal	a = 0.307 c = 1.508 [132]	(0001)SiC/(10 $\bar{1}$ 0)Mg [133,134]	2.3 [133,134] and 4.23 [132]
Al ₄ C ₃	Hexagonal	a = 0.338 c = 2.499 [132]	(0001)Mg/(0001)Al ₄ C ₃ [17,117,135-137]	4.05 [17,117], 3.35 [135] and 3.79 [136,137]
			(10 $\bar{1}$ 0)Mg/(10 $\bar{1}$ 0)Al ₄ C ₃ [135,136]	3.79 [135] and 3.35 [136]
			-	3.35 [138] and 4.05 [132]
Al ₂ CO	Hexagonal	a = 0.317 c = 0.507	-	1.21 [132]
Al ₂ MgC ₂	Hexagonal	a = 0.337 c = 0.582 [132]	(0001)Mg/(0001)Al ₂ MgC ₂	5.32 [132,139]
AlCMn ₃	Cubic	-	{0001}Mg/{111}AlCMn ₃	15 [140]
AlB ₂	Hexagonal	a = 0.301 c = 0.352 [141]	(0001)Mg/(0001)AlB ₂ [142]	6.09 [141] and 6.25 [142]
Al ₃ BC	Hexagonal	a = 0.349 c = 1.154	(0001)Mg/(0001)Al ₃ BC	8.8 [143]
TiB ₂	Hexagonal	a = 0.303 c = 0.322 [144]	(0002)Mg/(0001)TiB ₂ [144]	5.6 [91,144,145]
			(0001)Mg/(0001)TiB ₂ [142]	5.34 [142]
TiC	Cubic	a = 0.432 [144]	(0001)Mg/(111)TiC [142,146]	4.7 [146] and 4.62 [142]
TiAl ₃	Tetragonal	a = 0.385 c = 0.858 [147]	(0001)Mg/(112)TiAl ₃	11.90 [142]
α -AlB ₁₂	Tetragonal	a = 1.017 c = 1.428 [147]	-	146.6 [91]
AlN	Hexagonal	a = 0.311 c = 0.497 [148,149]	(0001)Mg/(0001)AlN [148,149]	3.05 [148] and 3.04 [149]

Variation in results in Table 2-9 could be due to differences in input crystallographic data. Unfortunately, detailed information about the crystallography of the nucleating particles (lattice parameters, crystallographic form, etc.) is required which can be difficult to obtain. In addition, experimental trials show that lower disregistries do not automatically lead to better refinement and will be discussed further in subsequent sections. An even more thorough theoretical method to identify effective nucleants is the edge-to-edge model.

2.9.3 Edge-to-edge Model

The edge-to-edge model operates on the premise that the interfacial energy between the grain refiner substrate and nucleating phase is minimized when there is sufficient matching along close packed rows and planes [144] and incorporates orientation relationships rather than just comparing lattice parameters [4]. A grain refiner nucleating phase pair should have close packed or nearly close packed rows with atomic misfits (f_r) of <10% while close packed or nearly close packed planes should have misfits (f_d) of <6% [144,150,151]. The matching row and plane pairs must also not be significantly rotated away from each other. Even with a $f_d > 6\%$ a refiner may still be effective but is expected to not be very potent [152].

The edge-to-edge model has also been used to predict the refining potential of TiB_2 , TiC, SiC, TiN [144], Al_4C_3 , Al_2CO , $Al_8(Mn,Fe)_5$ (treated as Al_8Mn_5) [152,153], γ -AlMn, ϵ -AlMn, τ -AlMn, β -Mn [10], ZnO [154], Al_2Y [155] and AlN [156] summarized in Table 2-10.

Qiu *et al.* [144] determined a potency ranking of $TiB_2 > SiC > TiC > TiN$ and Zhang *et al.* [152,153] demonstrated $Al_2CO > Al_4C_3 > Al_8(Mn,Fe)_5$ with Al_2CO having f_d and f_r values of 3.6% and 1.23% respectively [152] similar to TiB_2 [144]. Also, the τ -AlMn was the only phase that could possibly act as a nucleant during superheating [10]. The f_d value for ZnO was only 1.7% and 0.59% for f_r , indicating a high degree of matching with Mg even better than that of Al_2CO [154]. Similarly, Al_2Y was seen as very effective [155] and for AlN, f_d and f_r were 2.67% and 2.6% respectively [156]. However, the edge-to-edge model does not consider chemical stability, particle size or wettability [152] and these factors should be incorporated as the effectiveness of a nucleating substrate is not just determined by crystallographic matching [111].

Table 2-10: Edge-to-edge Model Applied to TiB₂, TiC, SiC, TiN [144], Al₄C₃, Al₂CO, Al₈(Mn,Fe)₅ [152], γ -AlMn, ϵ -AlMn, τ -AlMn, β -Mn [10], ZnO [154], Al₂Y [155] and AlN [156]

Phase	Structure	Lattice Parameters (nm, 25°C)	f _d /f _r (%)	Favourable Orientation Relationship
Mg	Hexagonal	a = 0.320 c = 0.520	-	-
TiB ₂	Hexagonal	a = 0.303 c = 0.322	~1/~1	(0 $\bar{1}$ 10)TiB ₂ /(0002)Mg [0001]TiB ₂ /[2 $\bar{1}$ $\bar{1}$ 0]Mg
TiC	Cubic	a = 0.432	~1/~6 & ~5.5/~6	(11 $\bar{1}$)X/(01 $\bar{1}$ 1)Mg [110]X/[2 $\bar{1}$ $\bar{1}$ 0]Mg
SiC	Cubic	a = 0.435	~1/~5.5 & ~5.5/~5.5	& (111)X/(0002)Mg
TiN	Cubic	a = 0.423	~1.5/~8 & ~8/~8	[110]X/[2 $\bar{1}$ $\bar{1}$ 0]Mg
Al ₄ C ₃	Hexagonal	a = 0.333 c = 2.493	3.4/7.5	(10 $\bar{1}$ 2)Al ₄ C ₃ /(0002)Mg [1 $\bar{2}$ 10]Al ₄ C ₃ /[11 $\bar{2}$ 0]Mg
Al ₂ CO	Hexagonal	a = 0.317 c = 0.508 [147]	3.6/1.23 & 5.5/1.23	(0002)Al ₂ CO/(1 $\bar{1}$ 01)Mg [1 $\bar{2}$ 10]Al ₂ CO/[11 $\bar{2}$ 0]Mg & (10 $\bar{1}$ 0)Al ₂ CO/(0002)Mg [1 $\bar{2}$ 10]Al ₂ CO/[11 $\bar{2}$ 0]Mg
Al ₈ (Mn,Fe) ₅ (Al ₈ Mn ₅)	Rhombohedral	a = 1.263 c = 0.793 [130]	17.8/7.4	{30 $\bar{3}$ 3}Al ₈ (Mn,Fe) ₅ /{0002}Mg <10 $\bar{1}$ 1>Al ₈ (Mn,Fe) ₅ / $\bar{1}$ 010>Mg
γ -AlMn	Cubic	a = 0.303 [147]	-	None
ϵ -AlMn	Hexagonal	a = 0.269 c = 0.435 [147]	-	None
τ -AlMn	Tetragonal	a = 0.392 c = 0.357 [147]	~1/~2.5	{011} τ -AlMn/{0002}Mg <111> τ -AlMn /<2 $\bar{1}$ $\bar{1}$ 0>Mg
β -Mn	Cubic	a = 0.631 [147]	-	None
ZnO	Hexagonal	a = 0.326 c = 0.521 [130]	1.7/0.59	(1 $\bar{1}$ 01)ZnO/(1 $\bar{1}$ 01)Mg [2 $\bar{1}$ $\bar{1}$ 3]ZnO/[2 $\bar{1}$ $\bar{1}$ 3]Mg
Al ₂ Y	Cubic	a = 0.786 [130]	0.1/0.1 & 6.5/0.1	(40 $\bar{4}$)Al ₂ Y/(0 $\bar{1}$ 10)Mg [121]Al ₂ Y/[2 $\bar{1}$ $\bar{1}$ 0]Mg & (440)Al ₂ Y/(0002)Mg [1 $\bar{1}$ 0]Al ₂ Y/[1 $\bar{1}$ 00]Mg
AlN	Hexagonal	a = 0.311 c = 0.497 [148]	2.67/2.6	{101 $\bar{1}$ }AlN/{101 $\bar{1}$ } <11 $\bar{2}$ 0>AlN/<11 $\bar{2}$ 0>Mg

Another challenge is to predict the grain size of a solidified alloy in an analytical fashion [157]. The interdependence theory links heterogeneous nucleation, grain growth, formation of a constitutionally undercooled zone and the subsequent nucleation events for prediction of grain size [4,158].

2.9.4 Interdependence Theory

The interdependence theory evolved from a model relating grain size to the inverse of Q and potency of refining particles [111,159,160]. This relationship was examined to predict the influence of cooling rate, superheat and ultrasonic treatment [131] under the assumption that the nucleation of a grain occurs when the undercooling at that point reaches the undercooling required for nucleation which depends on the potency of the nucleant [158,161]. An increase in the rate of development of the constitutionally undercooled zone decreases the time and amount of growth required for a nucleation event to occur and the grain size will be smaller [161]. With increasing cooling rate more nucleants become active and development of constitutional undercooling increases [131]. Decreasing superheat only increases the proportion of active nucleant particles similar to ultrasonic treatment but neither increase the potency of the nucleating particles [131]. Extension of the inverse growth restriction model was required to deal with the interaction between nucleation caused by thermal undercooling and nucleation due to constitutional undercooling [131] and led to the development of the interdependence theory.

The interdependence theory demonstrated that the grain size is determined by three components [158]:

1. The distance a previously nucleated grain must grow to establish sufficient constitutional supercooling to enable nucleation of the next grain.
2. The distance from a grain interface to the point where the sufficient constitutional undercooling is established.
3. The additional distance from the point where sufficient constitutional undercooling is established to where the most potent nucleant actually nucleates a grain.

The first nucleated grain is assumed to have formed on the mould wall. The interdependence theory showed good prediction of experimentally determined grain sizes for Al-Ti, Mg-Al and Ti based alloys [158] and can be modified to describe Mg-Zr alloys and ultrasonically treated melts [4].

The interdependence model relates grain size, solute content and the potency and number density of the nucleant particles as follows [4,162]:

$$d_{gs} = \frac{Dz\Delta T_{n-min}}{v_g Q} + \frac{4.6D}{v} \left(\frac{C_1^* - C_o}{C_1^* (1-k)} \right) + x_{sd} \quad (16)$$

Where:

d_{gs} : Grain diameter

D: Diffusion coefficient of solute in alloy

ΔT_{n-min} : Undercooling required for nucleation on the most potent particle (ΔT_n comes from Equation 11). More potent particles would have a lower value of

ΔT_{n-min} [4]

$z\Delta T_{n-min}$: Incremental amount of undercooling required to activate each subsequent nucleation event

v_g : Growth rate of solid-liquid interface (increased cooling rate, increases v [4])

Q: Growth restriction factor

4.6: Cut-off factor for the solute profile in front of the solid-liquid interface where

$\frac{C_1(x) - C_o}{C_1^* - C_o} = 1\%$ [162] (essentially when

the liquid concentration at point x ($C_1(x)$) away from the solid liquid interface is 1% above the liquid alloy concentration in the bulk of the melt)

C_1^* : Composition of the liquid at the solid-liquid interface

C_o : Alloy composition

k: Equilibrium partition coefficient

x_{sd} : Distance from the point of critical constitutional supercooling to the location of the most potent nucleant particle

The first part of Equation 16 represents the amount of growth needed to develop enough constitutional supercooling for nucleation and the second term is the length of the diffusion field from the solid-liquid interface in front of the growing grain to where the critical amount of constitutional supercooling is achieved [4,162]. The final term, x_{sd} can be reduced by introducing more nucleating particles [4]. Fluid flow, dendrite fragmentation and coarsening on the final grain structure are considered negligible [158] and may be areas for further improvement of the model.

The interdependence theory shows promise in accurately predicting grain size of many alloy systems prepared by gravity die casting, high pressure die casting and even ultrasonic conditions but can be improved with more data regarding accurate values of D, v and ΔT_{n-min} [4]. For

experimental based analysis of grain refinement, the literature is usually organized according to whether the Mg alloy contains Al or not.

2.10 Grain Refinement of Mg Alloys Free of Al

According to a historical survey by Saunders and Strieter [163] and early efforts by Sauerwald [164], the extraordinary refining effect of Zr was discovered in the late 1930's and observed for Mg alloys free of Al [4,18,26,92,129,131,165-176]. Table 2-11 summarizes the mechanism of Mg refinement using Zr.

Table 2-11: Summary of Zr Grain Refinement Mechanism

Addition Method
<ul style="list-style-type: none"> • Mg-Zr master alloy [167] (commercial Zirmax® is Mg-33.3 wt.% Zr) • Zr particles can be broken up by rolling into finer clusters to improve dissolution [169].
Grain Refinement Results
<ul style="list-style-type: none"> • Pure Mg refined from ~1000 μm to ~100 μm (89% reduction) with 0.32 wt.% Zr [92,107] • Columnar to equiaxed grain transition when 0.2 to 0.3 wt.% Zr was added to Mg-3.8 wt.% Zn-2.2 wt.% Ca alloy [165]. • Interdependence theory predicts Zr refining efficiency of Mg-Gd-Y being only 2-3% of added Zr [175]
Refinement Mechanism
<ul style="list-style-type: none"> • Soluble and appropriately sized insoluble Zr [166-169]
<i>Soluble: Grain Growth Restriction</i>
<ul style="list-style-type: none"> • 70% of grain refinement contribution [166] with $m(k-1)$ for Zr being 38.29 K/wt.% [18,92,107] (Table 2-8) • Addition temperature (680 to 780°C) was negligible on Zr recovery [167] • Stirring for 2 minutes at 730°C dissolves Zr with longer, more intense stirring not increasing dissolution [167,168] • Remelting Mg-Zr melts requires stirring to re-dissolve Zr or further Zr addition to account for losses from reactions with Fe crucibles [172].
<i>Insoluble: Nucleating Site</i>
<ul style="list-style-type: none"> • Effective nucleant [168,170,176] with planar disregistry between Zr and Mg being <0.5% [131] (lowest in Table 2-9) • High resolution transmission electron microscopy (TEM) determined nucleating planes were (0001) and (10$\bar{1}$0) for both Mg and Zr [177] • Active particles 1-5 μm, (~2 μm was the most active) [171]¹, particles >5 [171] or >6 μm [173] being ineffective and <1 μm particles having poor refining efficiencies [171] • Stirring maintains grain size during long holding times [167-169] • Stirring avoids settling of insoluble Zr due to its high density (6.52 g/cm³, 3.7x Mg) [176] with particles <3 μm remaining in the melt and particles >5 μm settling within two hours based on theoretical models and experimental trials [176] at 700 to 780°C

- Small particles settle slowly and are more likely to dissolve [173]
- Zirconium rich cores (<15 μm) usually observed from a peritectic reaction [18] at 653.56°C with 0.45 wt.% Zr [172]
- Zr cores are nearly pure Zr and are typically circular or elliptical found within grains or at grain boundaries [170]

¹Nucleant size of Mg for homogeneous nucleation from Equation 11, r^* is $\sim 1.3 \mu\text{m}$ [16] or d^* is $\sim 2.6 \mu\text{m}$

Improvements in Zr refinement can be made by introducing more appropriately sized Zr particles that are able to act as potent substrates [4] and better understanding of Zr cores [116] to maximize Zr recovery and reduce refining costs. The influence of alloying additions on Zr refinement in Mg is outlined in Table 2-12.

Table 2-12: Influence of Alloying Additions on Zr Grain Refinement in Mg

Al, Mn, Si, Fe, Ni, Co, Sn and Sb Addition
<ul style="list-style-type: none"> • Formation of stable intermetallics [18,26,168,178] • Al: thermally stable Al_2Zr phase [117,168,179] • Fe: Zr circular cores become rosette type mitigated by melting at 730°C or lower [168,174], using Fe free AlTi_2O_5 crucibles or boron nitride coated steel crucibles [174]
Zn Addition
<ul style="list-style-type: none"> • Increasing Zn increases Zr solubility at 680-780°C up to concentrations of $\sim 4 \text{ wt.}\%$ • Zn addition at 730°C best compromise of high Zr solubility without too much oxidation or particle settling [129] • Zn concentrations $>4 \text{ wt.}\%$ forms Zn-Zr intermetallics [129], Zn_2Zr_3 and Zn_2Zr [180]

Zirconium is nearly the perfect grain refiner because of its good lattice matching and high growth restriction [4] and is the most powerful grain refining agent in commercial use [181]. Its behaviour is regarded as an extraordinary phenomenon in materials science but since Mg-Al alloys such as AZ91, AZ31 and AM60 are used for approximately 90% of all structural magnesium products [2], an alternative grain refiner for Mg-Al alloys must be established to match the scientifically and commercially developed Zr refiners [18]. The following section describes some of the benefits and shortfalls of grain refiners for Mg-Al alloys.

2.11 Grain Refinement of Mg Alloys Containing Al

Unlike Al alloys, where well established, reliable grain refiners are commercially available, a similar universally reliable grain refiner system does not exist for the range of Mg

alloys [90,92,107]. Research to develop a commercially viable [4,140], reliable and easy to apply grain refiner [10] for Mg-Al alloys has been ongoing since the 1930's [18,26]. The lack of predictability and understanding in grain refinement may be a reason for the lack of a commercial grain refiner for Mg-Al alloys [18]. There are three approaches to solving the grain refinement problem of Mg-Al alloys, 1) develop a new additive, 2) significantly improve the efficiency of an existing process or 3) use a non-chemical approach [4].

Table 2-13 summarizes literature regarding the numerous potential grain refiners that have been developed for Mg-Al alloys but these techniques are far from achieving the grain refinement obtained in Al alloys [182]. Therefore, further research has to focus on improving the efficiency of Mg refiners. A detailed discussion focusing on developed grain refining additions follows. With the exception of melt superheating and native grain refinement, the grain refinement methods discussed in this dissertation focus on additions made to molten Mg. Techniques such as ultrasonic vibration and other “physical grain refinement techniques” are not discussed because they pose practical processing and economic challenges [4,90] and are beyond the scope of this dissertation.

Table 2-13: Summary of Grain Refinement Techniques for Mg-Al Alloys

Technique	Mechanism	Future Opportunities	References
Solute Additions			
Al, Si, La, Ca, Sr and Sc Addition	Grain growth restriction	Better understanding of the role of solute on nucleation	[2-4,15,18,90,92,106,107,109,118-121,183-194]
Historical Methods			
Melt Superheating	Carbides or Mn-Al-Fe particles	Influence of Fe and Mn needs clarification	[4,10,15,18,26,89,90,92,111,119,121,160,178,195-208]
Native Grain Refinement	Carbides or Mn-Al-Fe particles	Correlation with superheating needs clarification	[4,18,90,111,160,196,201,204,206,209,210]
Elfinal Process (FeCl₃) Addition and Other Fe Additions	Growth restriction or Fe-Mn-Al particles	None, Fe corrodes Mg	[4,15,18,26,90,92,121,178,196,211-213]
Carbon Additions			
Hexachloroethane (C₂Cl₆) Hexachlorobenzene (C₆Cl₆), Calcium Carbide (CaC₂) and Calcium Cyanamide (CaCN₂)	Carbides, duplex particles or globular Al-Mn-Fe particles	Optimization of addition to limit fumes released	[4,15,18,26,87,89,90,92,95,108,115,119,121,178,185,196,201,202,214-223]
Carbonaceous Gases (CO, CO₂, Propane, Methane) and Carbonates (MgCO₃ and MnCO₃)	Carbides or duplex particles	None, not practical	[4,15,18,89,90,92,93,136,196,205,207,208,214,223-229]

Carbon Based Grain Refiners (C, Al-C, Mg-Al-C, SiC, etc.)	Carbides or duplex particles	Optimization of refiner preparation and addition	[2,4,5,9,15,17,18,87-90,92,94,95,106,107,109,110,115,119,121,132,135,137-140,178,182,185,193,194,200,201,205,207,208,216,223,230-254]
Al-B Based Additions			
Al-B Grain Refiners	AlB ₂ or Al ₃ BC particles	Optimization of refiner preparation and addition	[141,143,255,256]
Al-Ti Based Additions			
Al-Ti Based Grain Refiners (Al-Ti, Al-Ti-B, Al-Ti-C, Al-Ti-C-Y)	Ti solute, AlB ₂ , TiB ₂ and TiC particles	Optimization of refiner preparation and addition Removal of TiAl ₃ phases	[2,91,107,118,142,144-146,185,250,257-269]
Other Additions			
ZnO	ZnO	Addition method to avoid formation of Mg oxides	[154,270,271]
Al₂Y	Al ₂ Y	Mechanical property data	[155]
AlN	AlN	Mechanical property data	[107,148,156,185]
Mg₃N₂	AlN	Addition method to avoid formation of Mg oxides	[149]
ZrB₂	ZrB ₂	Effect in high Al content alloys	[16]

2.11.1 Melt Superheating

Melt superheating was first described in a 1931 British patent [195] and involves heating the melt to 150 to 260°C (or 180 to 300°C [18]) above the liquidus temperature [196] and holding the melt at this temperature for an extended period of time depending on crucible size and Al content [92] with higher superheating temperatures shortening refining time [195]. The original patent [195] provided no mechanism but it has been found that Al (beyond 1 wt.% [26]), Fe and Mn (>0.19 wt.% [197]) are essential elements to maximize grain refinement while Zn has a negligible effect [196,197]. Excess Mn [196,197] (>1 wt.%) inhibits superheating [18,26,198]. Binary Mg alloys with Al, Zn, Ag, Sn and Cu can be superheated but alloys with Bi, Th, Cr and Ca either coarsened or were unaffected by superheating [196]. Silicon aids in superheating but its effect disappears at high Fe contents [196]. Superheating is suppressed if the Mg alloy contains even low concentrations of Ca [89], Ce [89], Ti, Zr [26,196-198] and Be [26,89,196-198]. With higher Al content, a more significant superheating response is obtained [26,196]. After holding, the melt must be rapidly cooled to the pouring temperature and poured [18,116,195]. Extended time at the pouring temperature will result in grain coarsening [26,89,92,196]. The superheating effect disappears after remelting [18,198].

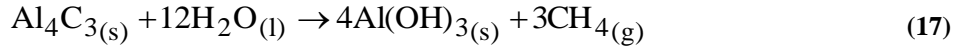
Tiner [197] conducted some of the earliest work on superheating on a Mg-8.6 wt.% Al-2 wt.% Zn-0.3 wt.% Mn alloy with some additional findings summarized in Table 2-14:

Table 2-14: Summary of Results of Superheating Experiments [197]

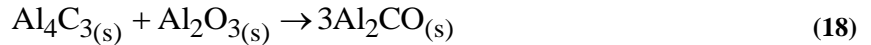
Parameter	Comments
Temperature and Time	<ul style="list-style-type: none"> Above 900°C, grain coarsening occurs
Repeat Treatments	<ul style="list-style-type: none"> No additional benefit to grain size, similar to Nelson's [196] results
Atmosphere	<ul style="list-style-type: none"> Effective in air and vacuum
Alloy Composition	<ul style="list-style-type: none"> Pure Mg, Mg-Mn, Mg-Zn and Mg-Zn-Mn alloys show no refinement Mg-Al and Mg-Al-Zn alloys show refinement

There are discrepancies in the grain refinement mechanism with superheating [116]. Some early theories were formation of MgO or Al₂O₃ with reaction with air at elevated temperatures but additions of these or allowing the melt to burn or pumping O₂ gave no refinement and superheating even worked under a vacuum [196,197]. Bubbling of N, Cl and He gases also produced no refinement. Hydrogen gas bubbling provides refinement but produces casting blowholes [197].

Most researchers have pointed to the nucleation of aluminum carbide (Al_4C_3) particles [26,198] or Al-Mn, Al-Mn-Fe [26,197,199] type compounds, possibly MnAl_4 [178,196]. Early research examining the mechanism of superheating often noted the presence of Al-C-O particles within the centre of grains [200,201]. The nucleants were postulated to be Al_4C_3 as its planar disregistry with Mg is low (Table 2-9). The observation of oxygen in the microstructure was reasoned to be a result of a reaction of Al_4C_3 and water during polishing, according to Equation 17 [200,202].



However, another possibility is that the Al-C-O bearing particles could be Al_2CO that has even lower planar disregistry to Mg than Al_4C_3 (Table 2-9) and formed according to Equation 18 [218]. The source of Al_2O_3 in Equation 18 could be from melt oxidation but this reaction is not possible in Mg melts with Al concentrations lower than 10 at.% [218] and superheating has been observed in Mg alloys with Al concentrations just above 1 wt.% [26]. Therefore, the possibility of the Al-C-O bearing particles being Al_2CO has been ruled out.



Grain refinement by Al_4C_3 requires the presence of C in the melt and is believed to originate from the graphite or steel crucibles used for melting during superheating [26]. Experiments have shown that the superheating effect still prevails despite using magnesia lined Fe crucibles to ensure that Fe and C contamination was minimized [201] putting the C from the crucible mechanism into question.

Manganese based particles come in a variety of shapes and some may be suitable for refinement during superheating [196]. Investigations of Mn particles in rapidly solidified AZ91 showed that cross-shaped Mn bearing particles were observed when cooled to 700°C from superheat temperatures [199]. If Mn is added as either Mn-28 wt.% Al alloy containing ϵ -AlMn or Mn-34 wt.% Al alloy containing both ϵ -AlMn and γ - Al_8Mn_5 grain refinement should occur. However, Mn addition using a Mn-38 wt.% Al alloy containing only γ - Al_8Mn_5 was not effective [272]. Qiu *et al.* [10] used the edge-to-edge model to determine that during superheating ϵ -AlMn forms and that on subsequent cooling partially or fully transforms to τ -AlMn that could act as a nucleant. This transformational aspect matches the features of superheating where both Al and Mn must be present in the alloy, the melt must be heated to

~870°C to form ϵ -AlMn and that rapid cooling and holding at the pouring temperature for limited time avoids the formation of β -Mn and $\text{Al}_8(\text{Mn,Fe})_5/\text{Al}_8\text{Mn}_5$ [10]. These observations are similar to an early temperature solubility nucleation theory where particles that are too large or impure to act as nucleants dissolve at higher temperatures then precipitate as appropriate heterogeneous nuclei [196,203] (in German). The theory was essentially sound in regards to holding at the pouring temperature deteriorates grain refinement as the precipitated nuclei could have coalesced but it failed to explain the existence of the optimal temperature range for the superheating process [92].

The effects of Mn and Fe on superheating of high purity Mg-9 wt.% Al alloys showed that without superheating, increasing concentrations of either Fe or Mn continually increased the grain size. With superheating the grain size decreased [204]. This is unlike Be containing alloys where superheating cannot reverse grain coarsening [196]. The mechanism was explained as follows: for high purity melts, superheating has little influence on the grain size and Mn or Fe additions coarsen the grain size. The grain size can be refined once again with superheating because Mn or Fe compounds are available to refine the Mg grains. In the former case of the high purity alloy, no Fe or Mn compounds are available to refine Mg during superheating. Nelson [196] also noted this effect but Tamura *et al.* [204] noted the grain coarsening effect of Fe and Mn on non superheated Mg-9 wt.% Al. Tiner [197] also showed that Fe addition promotes superheating. Tamura *et al.* [204] noted that in high purity alloys the nucleating particles contained Mg, Al, O and C and the addition of Fe or Mn formed compounds that easily bonded to the nucleating particles and reduced their refining potential. This may be due to the lower matching of Al-Mn-Fe compounds to Mg observed using the edge-to-edge model [152,153].

A summary of the superheating mechanism was given by Cao *et al.* [198]. It is assumed that native Al_4C_3 particles exist within the melt and are contaminated with Fe/Mn. Upon superheating this Fe/Mn dissolve in the melt leaving clean and potent Al_4C_3 particles. Rapid cooling to the pouring temperature and short holding times are required to minimize Fe/Mn from coming out of solution and contaminating the clean and potent Al_4C_3 [198]. Comparison of superheated and non-superheated melts showed similar number of nucleating particles (as nothing is added or removed) but the superheated melts had much more potent nucleating particles supporting the Al_4C_3 cleaning hypothesis [111].

The difficulties associated with superheating such as the considerable time required [89,205,273], the reduction in crucible life [18,89,273], increased fuel/electricity costs [18,89], tendency to exacerbate oxidation [119,224], being impractical [121] and the grain coarsening resulting from holding the melt at lower temperatures stresses the need for a refinement method applicable at lower temperatures [196]. Interestingly, the behaviours of superheating and native grain refinement are similar as their mechanisms may be linked [4,111].

2.11.2 Native Grain Refinement

Native grain refinement is a process exclusive to Mg-Al alloys where high purity alloys result in finer grain structures than commercial purity counterparts [4,18,209]. Examination of native grain refinement in Mg-Al (Al concentrations from 0.5 to 9 wt.%) alloys in Al_2TiO_5 crucibles to avoid Fe and C contamination revealed that across all the Mg-Al compositions examined the high purity alloys had finer grain sizes than the commercial alloys [209]. Motegi *et al.* [201] observed that grain size was independent of Al content in the high purity alloy but alloying elements of Be, Zr, Fe and Mn have all been found to increase the grain size of high purity Mg-9 wt.% Al [206]. In the high purity alloys Al-C-O particles (deduced to be Al_4C_3 [201,206]) were found at grain centres. Commercial alloys had less potent Al-C-Fe or Al-C-Mn based particles [206,209]. Elements such as Be or Zr have a higher affinity to C than Al and would preferentially form their own carbides over Al_4C_3 [206]. The possibility that the Al-C-O particles are Al_2CO has been shown to be thermodynamically impossible in Mg alloys with Al contents less than 10 at.% [218] in Section 2.11.1.

Melt superheating was required to refine the commercial alloy to a level comparable to the high purity alloy but only alloys coarsened by either Fe or Mn could be refined using superheating [196,206] with Fe-Al-C-O or Mn-Al-C-O particles within grains respectively [206]. These particles may be duplex phases of Fe or Mn intermetallics with Al_4C_3 .

Iron or Mn may only poison the Al_4C_3 nucleants in high purity alloys before superheating because of the use of a Mn master alloy that contains ineffective Al_6Mn while a Al-60 wt.% Mn master alloy containing $\epsilon\text{-AlMn}$ could act as a nucleant in high purity Mg-3 wt.% Al, Mg-6 wt.% Al, Mg-9 wt.% Al and commercial AZ31 [210]. The $\epsilon\text{-AlMn}$ was unstable at melting temperatures and would transform to $\gamma_2\text{-Al}_8\text{Mn}_5$ with holding. Manganese addition using Mn flakes or ATLAB™ Mn75 tablets were also not effective [210].

Further research is required to further pinpoint the mechanisms of melt superheating and native grain refinement whether it is cleaning of Al_4C_3 or presence of Fe or Mn intermetallics or a combination of both. Native grain refinement and superheating are both scientifically interesting but impractical as it requires expensive high purity alloys or increased energy costs respectively. The coarsening effect by Fe addition in high purity alloys [206] contradict findings regarding Elfinel ($FeCl_3$) addition.

2.11.3 Elfinel ($FeCl_3$) Addition and Other Fe Additions

The concept of Fe grain refinement emerged from the inventors of superheating [195] who thought that Fe particle pickup from the crucible formed nucleating particles. An Fe inoculation process using $FeCl_3$ (termed Elfinel) was then developed and typically involves submerging 0.4-1.0 wt.% [211] anhydrous $FeCl_3$ at 740-780°C [211] into molten magnesium and was first demonstrated in Mg-4 to 8.5 wt.% Al-0.5 to 3 wt.% Zn alloys [211]. Elfinel addition was later extended to Mg-Zn alloys [26]. Inhibiting elements for Mg-Al alloys are Zr and Be as they remove Fe in the melt while for Mg-Zn alloys, Th, Si and Al [26].

Cao *et al.* [212] examined Fe inoculation on high purity Mg-3 and 9 wt.% Al alloys via three routes: 1) $FeCl_3$, 2) Fe uptake from crucibles at 750°C and 3) Fe-15 wt.% Al-10wt.% Na free flux powder and the results are presented in Table 2-15.

Table 2-15: Fe Inoculation in High-purity Mg-3 and 9 wt.% Al Alloys [212]

Fe Inoculation Route	Grain Size (μm)/% Reduction	Comments
$FeCl_3$	Mg-3 wt.% Al: ~310 to ~112/64	Melts held in Fe free $AlTi_2O_5$ crucibles
	Mg-9 wt.% Al: ~130 to 64/51	
Fe Uptake	Mg-9 wt.% Al: ~144 to 86-89/40-38 after 60 minutes holding	Melts held in mild steel and 316L stainless steel crucibles Fe uptake occurs at temperatures above 730°C [168,174]
Fe-15 wt.% Al-10wt.% Na	Mg-9 wt.% Al: no refinement observed	Unclear as to reasons for no refinement, possible cause is poor wetting or Na content

Cao *et al.* [213] confirmed that Mn was not necessary (conflicting with early investigations [196]) for Fe refinement to occur using FeCl_3 at 750°C held for 10 minutes in Mg-3 and 9 wt.% Al alloys.

Early explanations for the grain refining effect of FeCl_3 from Emley [26] and Nelson [196] were that FeCl_3 addition releases HCl which would in turn corrode crucibles releasing C to form Al_4C_3 to act as a nucleant but Cao *et al.* [212,213] observed refinement in C and Fe free AlTi_2O_5 crucibles [212,213]. New developments pin the mechanism on Fe growth restriction [4] or by Fe-Mn-Al (Fe-Al particles [212,213]) based compounds acting as nucleating sites [4,18,26]. Unfortunately, Fe additions reduce corrosion resistance [18,121,212,224] and the Elfinel process releases Cl or HCl fumes [18]. To minimize corrosion and introduce an effective nucleant, many researchers examined using C inoculation for grain refinement.

2.11.4 Carbon Based Grain Refiners

Carbon inoculation is considered as the most effective refinement method [5] because of its low cost [224], low operating temperatures and little fading [18,26,92,95,106,109,121,138,143, 193,222,231,240] as exemplified in a study using graphite addition to Mg-3wt.% Al where no appreciable fading was observed for holding times up to 120 minutes [274]. Carbon grain refinement is comparable to superheating [18] in effectiveness with coarsening occurring at a slower rate [89,196]. Much of the earliest groundwork for C grain refinement [89,205,208,254] involved introducing solid C containing compounds, organic chlorides, other organic materials (sugars and plant fibres), hydrocarbon gases or carbonates without heating to temperatures far beyond melting [89,208,254]. The challenge is how to effectively introduce sufficient C into the melt [18,89,205,244] because of the poor wettability and low solubility of C in Mg melts [5] without over saturating and reducing the alloy's corrosion resistance [18]. Carbon is introduced into the melt by either in-situ or ex-situ means with Zr, Be, Ti and some RE elements interfering [196,221] likely from the formation poor nucleating carbides [92]. For in-situ C refinement, C is introduced into the melt by some C containing agent such as C_2Cl_6 , C_6H_6 , MgCO_3 , lampblack or CO_2 typically at 760 to 787°C . The added C is held in the Mg-Al alloy for 10 to 30 minutes then poured [221]. For ex-situ C based grain refinement, the grain refining particles are synthesized in a separate alloy and are then added to the Mg-Al alloy melt. In-situ methods of grain refinement are expected to be more potent than ex-situ methods [117] because

the refining particles would be expected to be free of surface contaminants and more easily wetted by the Mg alloy. For grain refinement of Mg-Al alloys using pure C addition, Al is required [89] from a minimum of 0.5 wt.% [221] or 2 wt.% Al [15,18,205,230]. While C inoculation based methods work some of their mechanisms for formation are not clear [4,17,94,117,121,132,139]. There are significant disagreements in 1) amounts needed, 2) appropriate temperature for inoculation and 3) holding time of melt at temperature to ensure uniform dispersion [119]. The nucleant responsible for C grain refinement is not yet clear [232] with many investigators concluding its Al_4C_3 [2,5,9,17,18,26,87,89,92,95,107,121,135,136,138,140,200-202,216,224,230-236,242,244,249,250,253], Al_2MgC_2 [132,139,232,248,251], C segregation [108,218,222] or a duplex nucleation mechanism with Al-Mn-Fe intermetallics [87,88,93,115,205,227,228,235,237,238,241].

2.11.4.1 Hexachloroethane (C_2Cl_6), Hexachlorobenzene (C_6Cl_6), Calcium Carbide (CaC_2) and Calcium Cyanamide ($CaCN_2$)

Some foundries utilize C_2Cl_6 addition as it both degasses and grain refines [87-90,214] but many are reluctant as it causes violent bubbling of the melt that releases Cl_2 gas [87,88,91], chlorinated hydrocarbons [87,90,92,93,214] and dioxins [94,95]. Grain refinement using C_2Cl_6 has been combined with superheating [202] and has been observed in alloys as lean as Mg-0.5 wt.% Al using only 0.01 wt.% addition [119] but since most commercial alloys contain much higher Al concentrations research on the influence of increasing Al concentration is essential. The results of C_2Cl_6 addition on the grain size and tensile properties of AM60B are shown in Table 2-16.

The mechanical properties of AZ91E treated with C_2Cl_6 or degassed with Ar both at 720°C are shown in Figure 2-6. Additions of 0.06, 0.3 and 0.9 wt.% C_2Cl_6 were made with 0.3 wt.% having the highest YS, UTS and elongation. The grain size (measured without heat treatment applied) of the as-cast AZ91E alloy were on average 284 and 42 μm (85% reduction) using 0.3 wt.% C_2Cl_6 . The grain sizes were observed to increase using any heat treatment. The porosity results did not correlate with the mechanical property data indicating that the amount of dissolved hydrogen did not influence the mechanical properties significantly [217].

Table 2-16: Tensile Properties of AM60B Before and After C₂Cl₆ Addition

Alloy (wt.%)	Grain Size (μm)	YS (MPa)	UTS (MPa)	Elongation (%)	Ref.
AM60B	250	-	214	11.4	[215]
AM60B + 1.0 C ₂ Cl ₆	70	-	241	20.1	
AM60B	250	~50	-	-	[216]
AM60B + 1.0 C ₂ Cl ₆	70	~67	-	-	

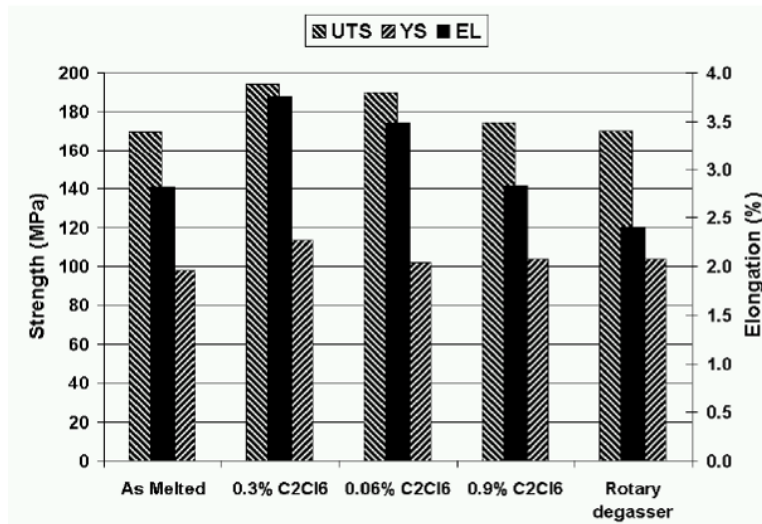


Figure 2-6: Mechanical Property Data Using C₂Cl₆ and Ar Rotary Degasser [217]

When the C₂Cl₆ is added to a molten Mg-Al alloy, the following reactions are expected to occur [219]:



and [136,223],



The Gibbs free energy for Al₄C₃ formation as a function to Al concentration at 700°C is shown in Figure 2-7. The formation of Al₄C₃ is possible at ~3 wt.% Al and becomes more negative (greater susceptibility for Al₄C₃ formation) with increasing Al content.

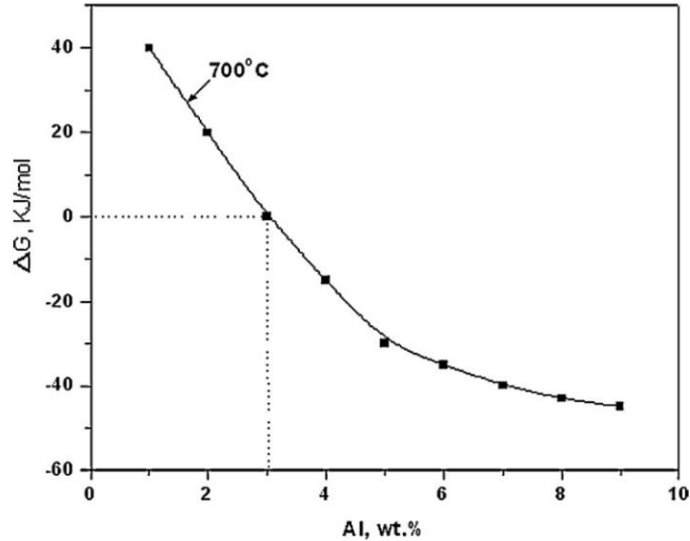


Figure 2-7: Gibbs Free Energy of Al_4C_3 Formation as a Function of Al wt.% in a Mg-Al Alloy Melt [233]

The formation of Al_4C_3 particles is attributed as the source of grain refinement in many C based refinement methods as supported by the need for Al to be present in the alloy, low planar disregistry (Table 2-9) and low interfacial energy between Mg and Al_4C_3 [275], but it has never been observed experimentally [230].

Another mechanism for grain refinement using C_2Cl_6 is that the released C promotes the transition of Al_8Mn_5 from rod-like to more globular particles [87,115]. With C_2Cl_6 addition to AZ91, only globular 3 μm sized Al-Mn-Fe-C particles detected by electron probe micro-analysis (EPMA) and suggested to be $Al_8(Mn,Fe)_5$ by TEM analysis were observed within grains with no Al_4C_3 indicating that $Al_8(Mn,Fe)_5$ was influenced by the added C [87,115]. The globular $Al_8(Mn,Fe)_5$ was also observed with Al_4C_3 addition [115]. The globular Al_8Mn_5 mechanism is further enforced by poor (480 to 450 μm /6% reduction, [87]) to modest (480 to 340 μm /37% reduction, [115]) refining performance of C_2Cl_6 in a high purity and commercial purity Mg-9 wt.% Al alloys respectively with only scarcely observed Al_4C_3 [87,115]. When 0.3 wt.% Mn and C_2Cl_6 were added to the Mg-9 wt.% alloy (340 to 87 μm /74% reduction) grain refinement and $Al_8(Mn,Fe)_5$ particles were observed [115] indicating that Mn was necessary for grain refinement [87,115] (Nelson [196] states that both Mn and Fe are necessary). Also, grain refined AZ91 was remelted, Ar bubbled, filtered and inoculated with C_2Cl_6 and recast with a resulting coarse grain size. The reason was attributed to $Al_8(Mn,Fe)_5$ particle removal with the melt cleaning process shunting grain refinement by C inoculation [87].

In a crystallographic sense, Al_4C_3 should be a better nucleant than $\text{Al}_8(\text{Mn,Fe})_5$ [152,153] but factors such as chemical affinity and particle size are important [87,115]. A duplex nucleation mechanism first suggested by Mahoney *et al.* [205] may be present where C inoculation promotes Al_4C_3 formation and Al and Mn segregate to the carbide surface. Observations of Al-C-O particles within grains and at times alongside Al-Mn particles after adding C_2Cl_6 have been observed [220]. It is thought that globular $\text{Al}_8(\text{Mn,Fe})_5$ form on the surface of the carbide particles which in turn nucleates Mg [87,115]. The reasoning provided is that if both Al_4C_3 and $\text{Al}_8(\text{Mn,Fe})_5$ are effective nucleants for Mg, they could also be nucleants for each other [87,115].

Carbon segregation [108,218,222] where C provided a constitutionally undercooled zone restricting grain growth was proposed as a refining mechanism for C_2Cl_6 . No Al_4C_3 particles were observed in the microstructure of a AZ31 alloy and C was observed alongside Al-Mn particles [222]. Carbon segregation has been disputed by many researchers because C containing etchants or reactions with moisture could be the source of detected elements [87]. Also, the solubility of C in molten Mg is very limited [115,230,240] to where commercial purity Mg has only ~20 ppm and C refinement only occurs in Mg-Al alloys [230,240].

The addition of C_6Cl_6 has been observed to be the faster acting in AZ92A than CaC_2 and CaCN_2 unless CaC_2 was stirred resulting in similar acting times [221]. This refined metal would remain stable if refined at 760°C but when the CaC_2 refined melts were cooled to 676°C they would then coarsen. The C refinement behaviour also altered depending on the Al and Mn concentrations in the alloys. For Mg alloys with Al contents from 8-10 wt.%, no coarsening was observed with Mn addition but if Al concentrations were 2 wt.%, more than 0.2 wt.% Mn would increase the grain size and this coarsening would occur at 0.1 wt.% Mn in alloys with 1 wt.% Al. At 0.5 wt.% Al concentrations, C refinement with Mn was unreliable and difficult to assess.

Kurfman [221] noted that the optimum addition temperature for carbonaceous additions was in the range of ~ 650 to $\sim 900^\circ\text{C}$ and the superior performance of C_6Cl_6 to CaC_2 was attributed to the violent decomposition of C_6Cl_6 as compared to the quiet settling of CaC_2 as evidenced by the improved performance of CaC_2 with stirring.

The addition of C_2Cl_6 is often used as a benchmark to assess the effectiveness of other grain refiners and while itself very effective for Mg-Al alloys [224], is harmful to the environment [116], foundry operators and is suppressed if the Mg alloy contains Be, Zr, Ti or RE [26]. There is also a lack of quantified grain refinement and mechanical property data using

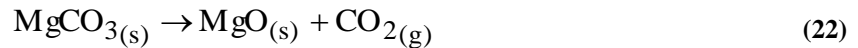
C₂Cl₆. It is then essential to produce a reliable, efficient and convenient grain refiner [228,236] alternative that can produce the same level of refinement in a safe and environmentally friendly manner.

2.11.4.2 Carbonaceous Gases and Carbonates

Gases known to grain refine at 760°C or above are acetylene, methane, natural gas, butylene, carbon tetrachloride, carbon disulphide and alcohol with CO₂ and natural gas being the most promising. Too much bubbling of CO or CO₂ reduced mechanical properties by an unknown mechanism and bubbling Ar, He, H₂, HCl, N, O₂ and dried air gave no significant refinement [196]. The bubbling of CO₂ into Mg is proposed to follow Equation 21 [136] and refinement has been attributed to Al₄C₃ formation [276].



Use of MgCO₃ [136,207,225,226] or MgCO₂-other C source mixtures [227] have been used with success by many researchers. The addition of MgCO₃ releases CO₂ according to Equation 22 [227] and was just as effective as superheating and CO bubbling [207].



The alternative carbonate MnCO₃ [93,228] also showed refinement. The refinement mechanism using carbonates is usually attributed to Al₄C₃ nucleating particles [136] or a duplex phase of Al₈Mn₅ on Al₄C₃ particles [93,227,228]. However, the formation of MgO within the melt may reduce mechanical properties. Wax-fluorspar (CaF₂) or CaF₂-C mix to AZ91 [214,229] also showed grain refinement. Nelson [196] determined that CaC₂ and C₂Cl₆ were the most dependable out of a group including SiC, zinc carbonate and sodium bicarbonate.

Bubbling carbonaceous gases is not practical because of the added production time and is not environmentally friendly, therefore many researchers aimed to develop C containing grain refiners.

2.11.4.3 Carbon, Aluminum-Carbon (Al-C) or Magnesium-Aluminum-Carbon (Mg-Al-C) Refiners

The study by Qian and Cao [230] showed that the addition of 0.6 wt.% graphite powder directly to Mg and Mg-3 wt.% Zn did not yield any grain refinement, while the same 0.6 wt.%

addition to Mg-3 wt.% Al showed grain refinement illustrating the necessity of Al.

Lu *et al.* [231] examined graphite addition in Mg-3 wt.% Al and observed Al-C-O based particles. Carbon is immiscible in Mg and is thought to have very poor refining efficiency in terms of growth restriction and was not the direct nucleant of Mg [231]. The nucleant is likely Al_4C_3 as observed by the same authors in another study [17] and the presence of O is from a reaction with water according to Equation 17. Also, the Gibbs free energy for Al_4C_3 formation is negative at 750 and 850°C when the Al content is ~2 and ~4 wt.% respectively [231], indicating Al_4C_3 formation is energetically favourable.

Instead of adding C as graphite Suresh *et al.* [232,233] added 21 μm charcoal particles to AZ91 and Mg-3 wt.% Al alloys at 740°C. Table 2-17 presents the grain sizes and the as-cast mechanical properties of the base and refined alloys. The nucleating particles were 1-3 μm in size and were Al-C-O-Mg based and were postulated to be Al_4C_3 [232,233] or Al_2MgC_2 [232]. The O content may be from reaction with water during sample preparation [232,233] according to Equation 17. Other researchers have postulated the presence of a Al_2MgC_2 nucleant and found it was reactive with water like Al_4C_3 [132,139,248].

The presence of Al-C-O or Al-C-O-Mg particles within the centre of grains is usually observed using scanning electron microscopy (SEM)-energy dispersive X-ray spectroscopy (EDX) or EPMA techniques. Since these techniques are volumetric in nature, nucleants composed of Al-C-O or Al-C-O-Mg are considered to be equal and the presence of Mg is often attributed to the Mg matrix in the spectroscopy analysis and assumed not be originating from the nucleant. However, Table 2-9 illustrates that Al_2MgC_2 has a low planar disregistry and may act as a nucleant. Therefore, Al_2MgC_2 may be misinterpreted as Al_4C_3 in many studies because Al_4C_3 has a larger presence in literature.

Table 2-17: Grain Size and Tensile Properties of AZ91 and Mg-3 wt.% Al Alloy Before and After Charcoal Addition [232,233]

Alloy (wt.%)	YS (MPa)	UTS (MPa)	Elongation (%)
Mg-3Al	55	112	7.1
Mg-3Al + 0.5 Charcoal	71	147	9.1
AZ91	95	180	3.3
AZ91 + 0.2 Charcoal	114	227	3.8

Yano *et al.* [95] and Motegi *et al.* [201] used a Ar carrier gas to add 5 μm C powder and found increasing C addition times or temperatures lead to reduced grain size and was attributed to a higher concentration of nucleating particles and higher temperatures “activating” the C powder. About 2 g of C powder was required to get equivalent grain refinement to 1.3 g of C from C_2Cl_6 (7.0 g total) indicating that C_2Cl_6 is very active [95]. However, other researchers showed that addition of pure graphite showed comparable refinement to C_2Cl_6 addition in AZ91 [216].

Motegi *et al.* [201] found that the average grain size using C_2Cl_6 addition was $\sim 70 \mu\text{m}$. Excessive C addition coarsened grains similar to the results of others [89,205]. Also, C additions at higher temperatures would give finer grain sizes with shorter holding times. For example, addition of C at 750°C for 30 minutes resulted in a grain size of $\sim 75 \mu\text{m}$ while addition at 800°C for 10 minutes produced $\sim 60 \mu\text{m}$ sized grains [200]. A summary of C based grain refiners using direct C addition, Al_4C_3 addition, Al-C refiners or Mg-Al-C refiners is presented in Table 2-18 to Table 2-21 respectively. These developed C grain refiners were meant to be effective, environmentally friendly alternatives to C_2Cl_6 .

Table 2-18: Grain Refining Results of Direct Carbon Based Additions

Addition	Alloy (wt.%)	Grain Size (μm)/% Reduction	Mechanism	Ref.
Graphite	Mg	no refinement	N/A	
Graphite	Mg-3Zn	no refinement	N/A	[230]
Graphite	Mg-3Al	400 to 170/58	Al-C-O (Al_4C_3)	
Graphite	Mg-3Al	380 to 175/54	Al-C-O (Al_4C_3)	[231]
Graphite	Mg-3Al	~ 610 to $\sim 170/72$	Al-C-O (Al_4C_3)	[234]
Charcoal	Mg-3Al	500 to 80/84	Al-C-O-Mg (Al_4C_3 or Al_2MgC_2)	[233]
Graphite	AZ91E	~ 150 to $\sim 70/53$	Al-C-O (Al_4C_3 or Al_2CO)	[95]
Graphite	AZ91E	~ 140 to $\sim 65/54$ (300 to 1800 seconds of inoculation)	Al-C-O (Al_4C_3)	[201]
Graphite	AZ91E	~ 300 to $\sim 75/75$	Al-C-O (Al_4C_3)	[200]
Graphite	AZ91	415 to 50/88 ¹	Al_4C_3	[216]
Charcoal	AZ91	100 to 30/70	Al-C-O-Mg (Al_4C_3 or Al_2MgC_2)	[232]

¹Grain size decrease from 415 to 55 μm (87% reduction) was obtained using C_2Cl_6

Instead of adding C as graphite or charcoal Nimityongskul *et al.* [235] directly added 5 wt.% Al_4C_3 powders to AM60B and pure Mg using an ultrasonic probe. The YS, UTS and elongation of the AM60B were also 71 MPa, 197 MPa and 8.4% and increased to 89 MPa, 218 MPa and 9.4% with 5 wt.% Al_4C_3 addition. For AM60B, a duplex nucleation mechanism was proposed with Al_4C_3 promoting Al_8Mn_5 formation then Mg nucleation. Further confirmation was provided with no grain refinement being observed when Al_4C_3 was added to Mg-6 wt.% Al similar to the results when 0.6 wt.% C_2Cl_6 was added to Mg-9 wt.% Al [115], indicating the necessity for Mn. The study by Nimityongskul *et al.* [235] used a high quantity of Al_4C_3 (5 wt.%). Therefore, improvements may be a result of a combined refinement and composite effect and may not be representative of Al_4C_3 addition alone unlike the mechanical property improvements observed when 0.5 wt.% Al_4C_3 was added to pure Mg and AZ31. The Al_4C_3 outperformed TiAl_3 and Ca additions for both pure Mg and AZ31 alloy [2].

Lu *et al.* [17] added 1 wt.% of 14.9 μm sized Al_4C_3 directly to Mg-3 wt.% Al and open pores composed of Al-C-O postulated to be Al_4C_3 nucleating particles that reacted with water during sample preparation according to Equation 17 were observed similar to Motegi *et al.* [201]. Also, the planar disregistry between the basal planes of Mg and Al_4C_3 is low (Table 2-9).

Table 2-19: Grain Refining Results of Direct Al_4C_3 Additions

Addition	Alloy (wt.%)	Grain Size (μm)/% Reduction	Mechanism	Ref.
Al_4C_3	Mg	383 to 49/87	Al_4C_3	[235]
Al_4C_3	Mg	5000-6000 to 600-800/88-86	Al_4C_3	[2]
Al_4C_3	Mg-3Al	not specified	Al-C-O (Al_4C_3)	[17]
Al_4C_3	AM60B	254 to 60/76	duplex: Al_4C_3 promoting Al_8Mn_5 nucleants	[235]

Development of Al-C and Mg-Al-C based refiners was thought to improve grain refinement by easing C addition to Mg alloys. Yichuan *et al.* [223] developed a Al-1 wt.% C grain refiner by melting Al in a graphite crucible containing C preforms. The developed refiner added at 2 wt.% outperformed C_2Cl_6 and MgCO_3 at an equivalent addition level despite Al-1wt.% C addition providing only 0.02 wt.% C addition while C_2Cl_6 and MgCO_3 each provided 0.21 and 0.28 wt.% C addition respectively. Due to low solubility, poor wettability and high density

differences, reactions between Al and C to form Al_4C_3 are difficult so opportunities exist in optimizing the production of these refiners to improve refiner performance.

To avoid wettability issues, Han *et al.* [236] developed a Al-1 wt.% C grain refiner by ball milling, compacting and sintering (710-730°C for 1-2 hour) C and Al powders. An optical micrograph of the Al-1 wt.% C grain refiner is shown in Figure 2-8. The refiner contained solid Al with layers of Al-C solid solution and Al_4C_3 at the grain boundaries. The formation of the Al_4C_3 is governed by Equation 20.

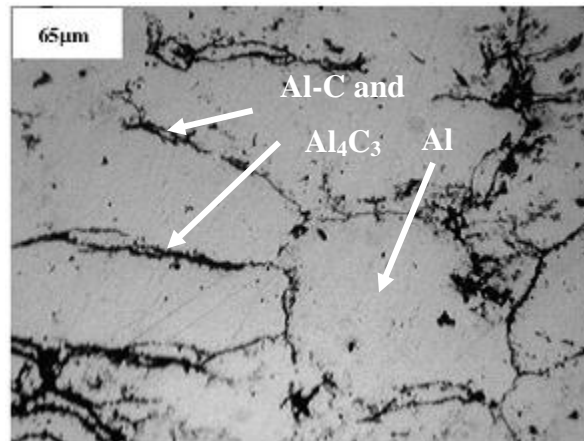


Figure 2-8: Al-1C Grain Refiner Microstructure [236]

In two studies, Han *et al.* [135,236] attributed refinement of AZ31 and AZ91D using different C containing Al-C refiners to Al_4C_3 nucleants while in another, Han *et al.* [237] observed duplex nucleation from Al-Mn particles coated with Al_4C_3 in AZ31 and AZ63 alloys. In AZ31 the Al-Mn particles were $\text{Al}_{0.89}\text{Mn}_{1.11}$ and Al_8Mn_5 for AZ63. Extraction of the particles from the matrix and examining them using X-ray diffraction (XRD) and TEM was done to determine their structure. The Al-Mn phases were not expected to have caused direct nucleation of Mg because both $\text{Al}_{0.89}\text{Mn}_{1.11}$ (examined in Mg-3wt.% Al alloy with 0-0.5wt.% Mn addition where grain size remained $\sim 390 \mu\text{m}$) [277] and Al_8Mn_5 [152,153,278] are not very effective grain refiners. However, the role of Mn must be considered since it is necessary in Mg alloys as a Fe remover to improve corrosion resistance [277]. Also, the concentration of Al and C in the alloy and refiner seems to have a role as well.

Table 2-20: Grain Refining Results of Al-C Additions

Refiner Details (wt.%)	Alloy	Grain Size (μm)/% Reduction	Mechanism	Ref.
Al-5C	AZ31	-	Al-C-Mn (duplex: Al_4C_3 promoting Al-Mn nucleants)	[88]
Al-1C	AZ31	400 to 140/65	Al_4C_3	[236]
Al-C (not specified)	AZ31	850 to 180/79	duplex: $\text{Al}_{0.89}\text{Mn}_{1.11}$ coated with Al_4C_3	[237]
Al-C (not specified)	AZ63B	650 to 170/74	duplex: Al_8Mn_5 coated with Al_4C_3	
Al-1C	AZ63B	~275 to ~80/71	-	[223]
Al-1.5C	AZ63B	270 to 50/81	Al-C-O-Fe-Mn	[94]
Al-25C	AZ91D	360 to 243/33	Mg-O-C-Al (Al_4C_3)	[135]

Du *et al.* [238] added C and/or Mn to Mg-3Al and observed refinement in both cases. With Mn addition, Al-Mn particles corresponding to AlMn and Al_3Mn_2 phases were observed with AlMn phases dominating. With simultaneous Mn and C additions, only Al-C-O-Mn phases were observed. A duplex nucleation mechanism of τ -AlMn coated with Al_4C_3 acting as a nucleant was proposed. The τ -AlMn particle was thought to be responsible for grain refinement by superheating using the edge-to-edge model [10].

The addition of Al_4C_3 and the role of Mn in C grain refinement was also examined by Liu *et al.* [138,239]. The addition of both C and Mn was more effective than C alone with additional Mn providing no additional benefit. Al-C-O-Mn-Fe particles with Al-C-O coatings, acted as nucleants. The Mn did not poison the Al_4C_3 particles [239] similar to others observations [94,238].

Other research combining C and Fe additions resulted in a grain size of 135 μm with Mg-3 wt.% Al-0.2 wt.% Fe and 120 μm for Mg-3 wt.% Al-0.2 wt.% Fe-0.2 wt.% C [240] with Fe (as Al-Fe intermetallics, possibly Al_3Fe_2) as an effective refiner (with agreement of [213]). These findings contradict others [198,209,230] who observed that Al-C-O particles acted as nucleants and that Fe and/or Mn additions poisoned these nucleants to less effective Al-C-O-Fe(Mn) particles.

However, the addition sequence of Fe and C influences grain size significantly. If 0.1 wt.% Fe was added to a Mg-3 wt.% Al alloy prior to 0.2 wt.% C addition the grain size would decrease from a base alloy size of 610 to 525 μm (14% reduction) then 188 μm

(69% reduction) for the alloys refined by Fe only (by Al-Fe intermetallics [241]) or Fe then C respectively [241,242]. If the alloy was refined by C first then Fe the grain size would increase from 183 (70% reduction) to 582 μm (5% reduction) for the alloys refined by C only or C then Fe respectively [241,242]. The C refined alloy had Al-C-O particles while the Fe then C refined alloy had both Al-C-O and Al-C-O-Fe particles. In the C then Fe refined alloy only Al-C-O-Fe particles were observed [242]. Possible formation mechanisms were 1) direct reaction of Al, C and Fe 2) Al-C first, then reaction with Al-Fe compounds or 3) C reacting with Al-Fe compounds [241]. In summary, Fe has a minor refining effect on its own, no effect if it is present in the alloy prior to C inoculation and a negative effect if it is added after C inoculation as the Fe would poison Al_4C_3 nucleants [241,242].

Generally, when Fe or Mn is added before C inoculation, no poisoning occurred [94,138,238,239,241,242] while additions after C inoculation caused poisoning [198,206,209,230]. Combined Fe and Mn additions of 0.2 wt.% each poisoned 0.2 wt.% C inoculation of Mg-3 wt.% Al regardless of addition procedure [234]. With C inoculation only, Al-C-O (Al_4C_3) was observed but were poisoned to form only less potent Al-C-O-Mn-Fe rich phases (namely Al-C-Mn-Fe particles) if Fe and Mn were added [234].

The Al-C-O based particles detected after C inoculation for many studies indicates that Al_2CO may also be responsible for grain refinement do to its similar lattice geometry to Al_4C_3 and Mg (Table 2-10). As discussed in Section 2.11.1 the Al-C-O bearing particles are actually $\text{Al}(\text{OH})_3$ particles that formed as a result of a reaction between Al_4C_3 and water during sample preparation (Equation 17).

Alternative grain refiners include a Mg-50 wt.% Al_4C_3 -6 wt.% Ce alloy containing Mg, Al_4C_3 and Al_4Ce that refined AZ91D by Al_4C_3 nucleants and Ce growth restriction. The Al_4Ce was observed at the grain boundaries and may improve thermal stability of the alloy [137]. A $\text{CaAl}_{0.5}\text{W}_{0.5}$ (C-Al-W) compound [243] refiner showed efficiently in refining Mg-4 wt.% Al but the influence of W is not well known.

Table 2-21: Grain Refining Results of Mg-Al-C and Misc. C Additions

Refiner Details (wt.%)	Mg Alloy (wt.%)	Grain Size (μm)/% Reduction	Mechanism	Ref.
Mg-Al-C Addition				
Mg-40Al-10C	Mg-3Al	300 to 140/53 ¹	Al-C-O-Mn (duplex: Al ₄ C ₃ coated τ -AlMn)	[238]
Mg-50Al₄C₃	AZ91D	360 to 154/57	Mg-Al-C-O (Al ₄ C ₃)	[138]
Misc. C Addition				
Mg-50Al₄C₃-6Ce	AZ91D	360 to 65/82	Al ₄ C ₃ nucleants and Ce growth restriction	[137]
C-Al-W	Mg-4Al	~550 to ~100/80	Al ₂ CO	[243]
Ni-1.6C	Mg-3Al	290 ² to 170 (flakey graphite)/41 or 110 (spherical graphite)/62	Al ₄ C ₃	[5]

¹Same result adding Mn and C together

²Alloy grain size with 1 wt.% Ni

Previous research has demonstrated that effective alternative grain refiners avoiding C₂Cl₆ can be developed. The reason as to why C inoculation has not replaced current C₂Cl₆ addition is because of conflicting experimental observations with regards to holding times and addition amounts and temperatures [119].

The conflicting experimental observations and uncertainty in their grain refinement mechanisms warrants the development of alternative grain refiners that are able to introduce C into Mg melts in a well distributed manner. Techniques that prepare Al-C grain refiners by adding C to liquid Al should be avoided because as Han *et al.* [236] stated, the poor wettability between Al and C and uncontrollable graphite absorption made addition of C to liquid Al unpractical. An alternative may be to use SiC as a C source as there is a multitude of literature regarding its use as reinforcement in Al and Mg based composites.

2.11.4.4 Silicon-Carbide (SiC) Grain Refiner

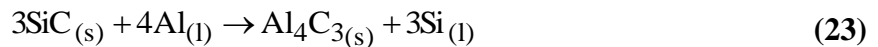
Silicon carbide addition has been identified as a possible effective grain refiner for Mg-Al alloys. Its environmentally friendly nature, low cost and abundance [244] make it an attractive

alternative to other C refiners. Unfortunately, the real nucleating mechanisms have not been clearly identified [140,182,230]. Silicon carbide has been used to produce Mg composites and permanent mould cast AZ91-10 vol.% SiC composites showed grain refinement from 127 to 42 μm (67% reduction) with SiC at grain centres and grain boundaries [245]. Studies have also shown grain refinement (181 to 72 μm , 60% reduction, using 1 wt.% SiC nanoparticles in pure Mg) with no interfacial products between SiC and Mg [246,247].

The lattice disregistry (Equation 14) between Mg and SiC is only 4% along (111)SiC/(0002)Mg planes suggesting SiC could act as a nucleant [279] and TEM studies on Mg-SiC composites showed that SiC nucleates Mg and $\text{Mg}_{17}\text{Al}_{12}$ according to the orientation relationships (0001)SiC/(10 $\bar{1}$ 0)Mg (with low planar disregistry, Table 2-9) and (01 $\bar{1}$ 1)SiC/(110) $\text{Mg}_{17}\text{Al}_{12}$ respectively [133,134]. Another explanation was that Al_4C_3 forms from a reaction between SiC and Al and nucleates Mg [9,140,231].

Easton *et al.* [140] used SiC particle addition to grain refine Mg-Al alloys with Al concentrations of 1, 2, 3, 6 and 9 wt.%. With the addition of SiC there were also clusters of Mg_2Si at the grain boundaries. It is believed that the SiC particles reacted with the Al in the melt to form an Al_4C_3 layer and liberated Si to form Mg_2Si [140]. However, Lee *et al.* [107] suggested that the liberated Si could instead provide grain growth restriction and might explain their results of observing SiC addition outperforming Al_4C_3 addition in Mg-1 wt.% Al alloys. They also note that the performance characteristics could also be due to settling and agglomeration tendencies or particle size differences in the refiners [107].

The reaction between Al and SiC would occur according to Equation 23 [140] and was found to be thermodynamically possible for a Mg-3 wt.% Al-0.1 wt.% Si alloy at 800°C [231].



The presence of Al_4C_3 particles was not seen most likely because of a reaction of the particles upon contact with water [17] according to Equation 17. For the Easton *et al.* [140] study, Mn addition increased the grain size for all alloys except Mg-1 wt.% Al and was attributed to the formation of less potent AlMn_3 that has a planar disregistry of 15% [140] (Table 2-9) correlating to other studies where Mn and Fe poison Al_4C_3 [206,209]. Table 2-22 summarizes literature including Easton *et al.* [140] who used direct SiC additions.

Table 2-22: Grain Refining Results of SiC based Additions

Refiner Details (wt.%)	Alloy (wt.%)	Grain Size (μm)/% Reduction	Mechanism	Ref.
SiC	Mg-1Al	~700 to ~330/53 (0.15 wt.% addition)	Al_4C_3	[140]
		~700 to ~300/57 (0.3 wt.% addition)		
SiC	Mg-9Al	~130 to ~100/23 (0.15 wt.% addition)	Al_4C_3	
		~130 to ~90/31 (0.3 wt.% addition)		
SiC	Mg-3Al	380 to 180/53	Al-C-O (Al_4C_3)	[231]
SiC	AZ31	~1150 to ~400/65 ¹	Al_2MgC_2	[248]

¹A similar result was obtained using Al_4C_3 powder but Al_2MgC_2 was not observed

Liu *et al.* [9] developed an ex-situ grain refiner that already contained Al_4C_3 using 10 μm α -SiC powders which were added to liquid Al at 950°C for 15 minutes in a medium frequency induction furnace then quenched to 700°C followed by pouring. It has been estimated that approximately 60% of 23 μm SiC transforms to 5-6 μm Al_4C_3 platelets (0.1-0.2 μm thick) after 1 hour and 70% after 4 hours in a Al-5 wt.% SiC alloy at 900°C [249]. The refining effects of 0.2 wt.% Al-SiC- Al_4C_3 grain refiner on the grain size of AZ31 was very good (1300 to 225 μm /83% reduction) but remained relatively constant with increasing refiner addition. This may be a result of the latent heat of crystallization with a large number of nuclei. When a relatively small number of heterogeneous nuclei form, the latent heat released would not significantly raise the melt temperature as compared to when a large number of grains begin to form as a result of excess grain refiner addition. This excess nuclei can remelt some of the newly formed nuclei and results in a levelling off of grain refinement as commonly observed with refiners that promote heterogeneous nucleation [9].

The research conducted by Easton *et al.* [140] and Liu *et al.* [9] indicated that SiC is a good grain refiner for Mg melts with low Al content only. The low Al content Mg alloys were easy to refine because the low solute levels produce large grains and the alloy is lacking effective nucleants. For the high Al content Mg alloy, the nucleant density is more important than having sufficient undercooling to initiate nucleation [140]. This is likely the explanation as to why a

Al-44 wt.% SiC refiner was able to reduce the grain size of both pure Mg and Mg-8 wt.% Al alloys [110]. A summary of the grain refining results using Al-SiC refiners are in Table 2-23.

Table 2-23: Grain Refining Results of Al-SiC based Additions

Refiner Details (wt.%)	Alloy (wt.%)	Grain Size (μm)/% Reduction	Mechanism	Ref.
Al-SiC	AZ91E	782 to 281/64	Al_4C_3 nucleants	[250]
Al-5SiC	Mg-3Al	480 to 220/54	Al_4C_3 nucleants with Mg and Si detected from matrix and unreacted SiC respectively	[249]
Al-44SiC	Mg	843 to 203 (5 minutes holding) then 120 (60 minutes holding)/76 then 86	Growth restriction by Si and C	[110]
Al-44SiC	Mg-8Al	226 to 78 (5 minutes holding) then 70 (60 minutes holding)/65 then 69		
Al-44SiC	Mg-3Al	~420 to ~130/69 (0.3 wt.% SiC addition) ~420 to ~120/71 (10 wt.% SiC addition)	Al_2MgC_2 nucleants	[132,139]
Al-SiC- Al_4C_3	AZ31	1300 to 225/83	duplex phase of Al_4C_3 and SiC	[9]
Al-SiC- Al_4C_3	AZ61	300 to 180/40		
Al-SiC- Al_4C_3	AZ91	no reduction	-	
Al-9Mg-10SiC	AZ91	not specified	Al_4C_3 nucleants	[253]

It is estimated that only 1.7% of added SiC become active [140] and experimental trials with modeling determined that the optimum SiC particle size for grain refinement was ~2-4 μm at an addition level of 0.04 wt.% and cooling rate of 5°C/s [182]. This is similar to the ~2 μm being the most effective particle size for Zr refinement [171] and calculated homogenous nucleant size for Mg (Equation 11, r^* is ~1.3 μm [16], d^* is ~2.6 μm). The effects of cooling rate alone were also modeled with cooling rates >6°C/s causing only small changes in grain size [182], emphasizing the need for grain refiners for casting processes with slow cooling rates.

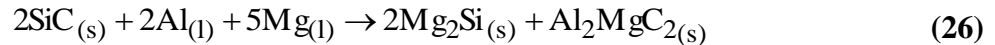
An alternative explanation to SiC grain refinement is that SiC causes Mg_2Si formation according to Equation 24 and not from either reactions between Al and SiC (Equation 23) and Si and Mg (Equation 25) [110]. Justification was provided in the observation of increased $\text{Mg}_{17}\text{Al}_{12}$ with increasing holding time. If Al_4C_3 was being formed with holding, Al depletion would

reduce the amount of Mg₁₇Al₁₂ in the alloy. The release of Si and C is thought to inflict solute enrichment, decreasing growth rate and refining the grain size [110] but since the solubility of C in Mg is thought to be only 20 ppm, it is not expected to cause significant grain refinement through C segregation [230,240].

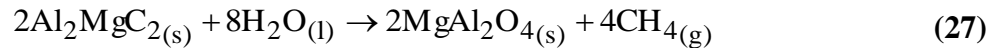


Similar results were observed by Chen *et. al.* [244] (Table 2-24). With increasing SiC addition, there was less Mg₁₇Al₁₂ present and more Mg₂Si and Al-C-O particles were found within grains. The refinement mechanism proposed was that SiC reacts to Al according to Equation 23 to form Al₄C₃ nucleants then Si reacts with Mg according to Equation 25 to form Mg₂Si [244]. However, C₂Cl₆ was added to the melts for degassing so the introduced C could be the source of Al₄C₃ observed and conflicted with the SiC addition.

In Mg-3 wt.% Al alloy melts, SiC additions conducted using a Al-44 wt.% SiC alloy contained Mg₁₇Al₁₂, Mg₂Si and Al₂MgC₂ (confirmed by extracting the particle and using electron diffraction in a TEM) [132,139]. The Al₂MgC₂ probably formed according to Equation 26 [248]:



The SiC was thought to form Al₂MgC₂ rather than Al₄C₃ and nucleate Mg as the planar disregistry between Al₂MgC₂ and Mg is only 5.32% [132,139]. Although the planar disregistry between Mg and Al₄C₃ is lower than that of Al₂MgC₂, the c parameter for Al₂MgC₂ is closer to that of Mg than Al₄C₃ as shown in Table 2-9. Pores alongside SiC and Mg₂Si were observed with elements corresponding to Mg-Al-C-O based phases postulated to be the by-products of the reaction of Al₂MgC₂ with water according to Equation 27 [280]:



To the author's knowledge, the observation of Al₂MgC₂ using TEM [132,139] is the only direct experimental confirmation of the often observed Al-C-O or Al-Mg-C-O nucleants and provides the strongest evidence for the mechanism of grain refinement using SiC.

Formation of AlCMn₃ was also identified as a potential poisoning phase using Al-50 wt.% SiC spark plasma sinter (SPS) refiner in AZ91E where Mg-C phases (possibly

Al₂MgC₂) was thought to be the nucleant [251]. A summary of the grain refinement experiments using Mg-SiC based additions is provided in Table 2-24.

Table 2-24: Grain Refining Results of Mg-SiC based Additions

Refiner Details (wt.%)	Alloy (wt.%)	Grain Size (μm)/% Reduction	Mechanism	Ref.
Mg-SiC	Mg-3Al	414 to 165/60 ¹		[252]
Mg-SiC	AZ31	~150 to 50/67 (high cooling rate) ~300 to 150/50 (low cooling rate)	-	[182]
Mg-SiC	AM60B	317 to 46/85	Al ₄ C ₃ nucleants with Mg ₂ Si forming as well	[244]

¹Obtained using 0.3 wt.% SiC, similar result was obtained using 0.1 wt.% Al₄C₃

Nucleating particles Al₄C₃ and Al₂MgC₂ may both be the sources of grain refinement with C inoculation with each particle dominating depending on the Al content in the Mg alloy. A tentative Al-C-Mg phase equilibria is shown in Figure A-1 (Appendix A.1). In a Mg alloy with Al content below 0.1 wt.%, the Al would react in the solid state with C. When the Al content is 0.1 to 6 wt.%, Al₂MgC₂ forms while above 19 wt.% Al, Al₄C₃ forms [280]. It seems unlikely that the composition would reach 19 wt.% Al in a particular area of a Mg alloys unless it possibly forms by a duplex mechanism alongside a Al-Fe-Mn particle where sufficient Al would be present.

Table 2-25 summarizes C based grain refinement techniques according to their characteristics and observed mechanisms. The carbonaceous compounds are most effective and most practical on the foundry but are damaging to the environment. The direct C, Al-C, Mg-Al-C and SiC additions are also effective but often have issues with wettability resulting in inconsistent results. The development of an easily wetted C based refiner would enable replacement of carbonaceous compounds and enhance the applicability of Mg-Al alloys for structural applications. Additional grain refinement techniques beyond the scope of this dissertation using B, Ti, ZnO, Al₂Y, AlN, ZrB₂, Sr, Ca and grain coarsening additions are discussed in Appendix A.2.

Table 2-25: Summary of Grain Refinement by C Inoculation in Mg-Al Alloys

		Carbon Source			
		Carbonaceous Compounds (C ₂ Cl ₆ , C ₆ Cl ₆ , CaC ₂)	Carbonaceous Gases and Carbonates	Graphite, Al-C or Mg-Al-C Additions	SiC Additions
Characteristics	Effective	+	+	+	+
	Ease of Wetting	+	+	+/-	+/-
	Environmentally Friendly	-	-	+	+
	Practical	+	+/-	+	+
Mechanism	Carbides	✓	✓	✓	✓
	Growth Restriction	✓			✓
	Duplex	✓		✓	✓

The literature regarding the grain refinement of Mg-Al alloys encompasses a wide range of additives and the refining performance of 0.05 wt.% of SiC, CaC₂, Sr, Al₄C₃, TiC, AlN, Sc and 0.5 wt.% C₂Cl₆, with AZ91E and AM50A alloys were compared by Wallace *et al.* [185]. The addition of C₂Cl₆ was the most effective for AZ91E and AM50A alloys but Sr addition was better situated to reduce the grain size of thick, slowly cooled casting sections with long holding times [185]. While the comparison of many grain refiners was useful, the addition temperatures were fixed and the addition levels were low for each addition except C₂Cl₆ possibly influencing the results. Since it is important to seek the most cost effective, eco-friendly grain refining additives for Mg-Al alloys [231], the C based additions seem the most suitable. Much of the previous research paid little attention to the preparation of C refiners. Therefore, for this dissertation C grain refiners were prepared with an emphasis on processing parameters. Since excess addition of any carbides can be harmful (carbides are considered as inclusions in Table 2-4), the aim is to produce a refiner where a minimum amount of refining particles are added without hindering mechanical properties. Since AZ91 is the most commercially and commonly used Mg alloy [255], the focus of this dissertation will be on this alloy. Results also examining the refining potential of Zr in Mg-Zn alloys will also be presented for better understanding of Mg grain refinement.

One major issue related to the production of effective C grain refiners is related to the poor wettability between C sources and Al or Mg. The wetting behaviour of Al alloys on SiC has been extensively studied in the late 1980's and 1990's [281-288] for production of homogeneous metal matrix composites [281,285,289] and application of that same research for the current study can help develop a successful Al-SiC based grain refiner with maximum contact between Al and SiC to encourage carbide formation.

2.12 Wettability of Al Alloys on SiC

Wettability of a system is tested using a sessile drop experiment and characterized by measuring the contact angle (Equation 13) [290]. A sessile drop experiment examines the spreading behaviour of a liquid droplet over a horizontal solid substrate until it reaches equilibrium [290]. One method to reduce the contact angle is to increase temperature [291]. Aluminum and SiC tend to react at temperatures above 650°C [288] to form Al₄C₃ [288,290,292] and its kinetics can be influenced by Si and Mg addition. A summary of the research on Si addition on the wettability of Al alloys on SiC substrates is in Table 2-26.

Table 2-26: Influence of Si Wettability of Al on SiC Substrates

Al Alloy (wt.%)	Temperature/Time (°C/min)	Contact Angle (°)	Ref.
Al	800/60	60	[282]
Al-5Si	800/60	60	
Al-12Si	800/60	60	
Al-18Si	800/60	30	
Al	900/60	100	[281]
Al	800/60	~150	
Al-5.1Si	800/60	140	
Al-12.3Si	800/60	120	

Microstructurally, the only observable change in the Al and Al-Si systems was the formation of Al₄C₃ in the former but not the latter case. Depending on the researcher, the presence of Al₄C₃ did or did not influence the contact angle significantly. Examinations of changes in surface tension also show contradictory results. At 1410°C, the surface tensions of Al and Si are 753 and 775 mN/m respectively [293], meaning an Al-SiC interface will have similar wetting behaviour to a Si-SiC interface. Similarly, the wetting behaviour of Al on SiC and Al on Al₄C₃ are similar [284]. However, surface tension measurements of an Al-0.2 wt.% Si alloy were 727 and

686 mN/m at 800 and 900°C respectively [294], noticeably lower than that of pure Al at the same temperatures (864 and 846 mN/m, [293]) indicating that Si addition can reduce surface tension and perhaps contact angle.

Discrepancies in contact angle results are common and could be attributed to Al purity [290], substrate roughness [290], chemical heterogeneities in the substrate [295], oxygen partial pressure [290], composition and structure type (single crystals have fewer impurities and are easier to prepare smoother surfaces than polycrystals [290]). To further complicate investigations of wettability, oxides are almost always present, influencing contact angle results [296]. It is thought that below 900°C, wetting of Al is dominated by the presence of an Al₂O₃ film, while at higher temperatures the oxide layer is broken up allowing a fresh Al surface to make contact with the SiC substrate further reducing the contact angle [281]. Similarly, an oxidized SiO₂ surface on SiC can also yield higher contact angles with Al than a clean SiC surface if the wetting experiment is carried out below 770°C. Oxidation of the SiC was observed to have no effect above 770°C [282] while others claim 800°C [283]. However, few of these studies examined the wetting behaviour of Al-Si alloys containing Mg and its influence on contact angle and oxide presence.

Magnesium is known to be highly beneficial in improving the wettability of Al alloys on SiC substrates primarily because Mg reacts with any oxygen layers to form a stable reducing oxide (MgO·Al₂O₃ spinel). The reducing oxide removes any Al₂O₃ films allowing fresh molten metal to come in contact with the reinforcement [297]. Increasing additions of either Si alone, Mg alone or Si and Mg to Al reduced surface tension as shown by Goicoechea *et al.* [298] and a similar result was observed with pure Al and Al alloy A356 (Al-7 wt.% Si-0.3 wt.% Mg) [299] where the measured surface tensions were 1007 mN/m and 889 mN/m for pure Al (at 680°C) and A356 Al alloy (at 630°C) respectively [299].

Previous studies examined the influence of Mg, Si or both together on Al, but few have measured changes in contact angle or the influence of low concentrations of Mg (<1.5 wt.%). Therefore, there is a need to determine the combined influence of Mg and Si additions to Al on the contact angle with SiC with the goal of improving wettability for Al-SiC refiner production.

To avoid wettability issues entirely, powder metallurgy via spark plasma sintering can be utilized to develop uniform, Al-C grain refiners with the added advantage of high heating rates minimizing grain coarsening during sintering.

2.13 Spark Plasma Sintering

Spark plasma sintering (SPS) is an advanced sintering technique because its versatility allows a wide variety of materials to be sintered with full density while retaining grain size at much lower homologous temperatures. The sintering duration is also much shorter as compared to conventional sintering processes [300]. Figure 2-9 is a schematic of a SPS machine showing press, current generator and controller. There are four main stages of SPS: 1) vacuum is generated inside the sintering chamber 2) pressure is applied 3) resistance heating via a direct current discharge and 4) cooling of sample [301].

The formation of plasma in SPS has not been identified directly [302] but it is thought that Joule heating which originates from contact resistances between particles is the heating mechanism. During initial sintering, there is a high resistance from the surface oxide layers on metal powders that saturates due to the breakdown of oxide layers [300]. This is especially advantageous for Al based samples because usually Al particles are covered with an aluminum oxide film and cannot be sintered by normal sintering procedures [302].

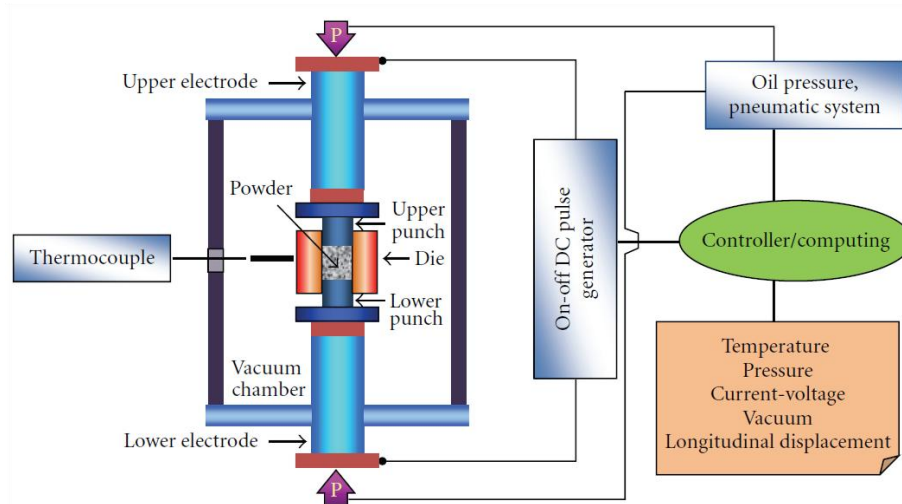


Figure 2-9: Schematic of SPS Machine [301]

An Al-50 wt.% SiC SPS refiner for AZ91E had high density with clean interfaces and uniform microstructure [251]. In this study, a Al-C refiner will be produced using ball milled Al and graphite powders. The aim is to produce a high density, uniform grain refiner and avoid wettability issues commonly observed with C additions.

In addition to grain refinement, the understanding of the solidification mechanisms of Mg alloys is not as developed as that for Al alloys. It is therefore necessary to further understanding of Mg solidification mechanisms for development of new methodologies/compositions for casting of Mg alloys while minimizing solidification defects. Typical thermal analysis techniques cannot distinguish growth of individual phases and metallographic techniques must be carried out after the sample is cooled. A new methodology utilizing in-situ technique to examine the solidification of Mg and its alloys is possible offering new opportunities for characterization of materials because of the unique properties of neutrons.

2.14 Solidification Analysis Using In-situ Neutron Diffraction

Neutron diffraction is a powerful technique for characterizing materials [6] as neutrons are electrically neutral and are only scattered by atomic nuclei giving them high penetration depths unlike X-rays and electrons that are scattered by electron clouds. Also, bulk samples of both heavy and light elements can be examined as neutron diffraction intensity is not influenced by the number of protons, electrons or neutrons in the diffracting atom. Neutrons behave similar to X-rays and electrons in that they obey Bragg's law for diffraction shown in Equation 28.

$$n\lambda = 2d_{\text{inter}} \sin \theta_{\text{diff}} \quad (28)$$

Where:

n: Order of diffraction

λ : Wavelength

d_{inter} : Interatomic spacing

θ_{diff} : Diffraction angle

By examining the change in neutron diffraction intensity during solidification of alloys at the diffraction angles that correspond to specific (hkl) diffracting planes, it is possible to examine the growth of individual crystallographic planes and relate it to fraction solid.

Previous studies have examined the in-situ solidification of Al and its alloys using neutron diffraction [303-309]. Early research examined only the early stages of solidification and showed that TiB₂ addition increased the nucleation rate of Al by an order of magnitude as compared to a pure Al sample [303,304]. More recent research examined the solidification of Al alloys over a wide temperature range in a step-wise fashion by holding the sample at each temperature for an

extended period of time. In-situ neutron diffraction has shown to quantify the growth of primary Si and Al independently in an Al-19 wt.% Si alloy [306,307] not possible by using thermal analysis or metallographic techniques. In-situ neutron diffraction has also been used to detect Al₂Cu formation and growth in a Al-Cu alloy and related to hot tearing mechanisms [308,309].

Neutron diffraction offers a unique opportunity to examine bulk specimens while discriminating between individual planes and phases not possible using X-ray or electrons. The suitability of in-situ neutron diffraction to examine and compare the solidification behaviours of different Mg alloys for advanced solidification analysis has never been conducted and would be a novel contribution to literature.

2.15 Chapter Summary and Present Study

Previous literature has indicated that inclusion removal and C grain refinement can improve the mechanical properties of AZ91E Mg alloy. The benchmark, C₂Cl₆ accomplishes both. The current study aims to replace C₂Cl₆ and utilize environmentally friendly methods such as filtration and Ar gas bubbling to clean Mg melts while effectively grain refining using C based grain refiners. The C grain refiners will be produced via in-situ and ex-situ methods by SPS with Al-C alloys and melting Al-SiC alloys respectively. The feasibility of using in-situ neutron diffraction to examine the solidification of Mg-Zn and Mg-Al alloys with and without grain refinement will also be examined enabling new perspectives in understanding of solidification, growth and phase analysis. A diagram summarizing the present study is shown in Figure 2-10.

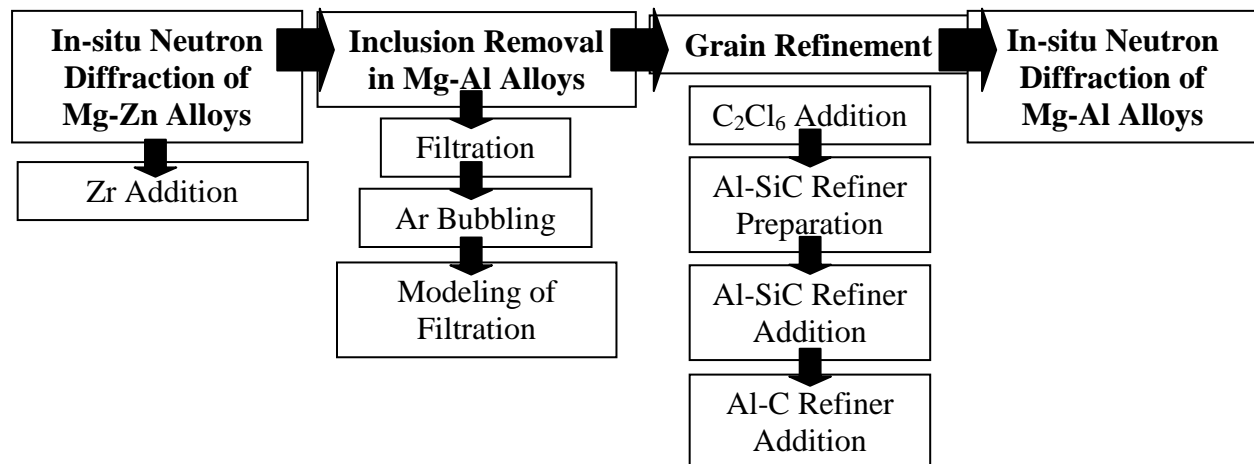


Figure 2-10: Summary of Present Work

CHAPTER 3
EXPERIMENTAL PROCEDURE

3.1 Materials

This section describes the materials used to conduct all the experiments throughout this study.

3.1.1 AZ91E Magnesium Alloy for Casting Experiments

The AZ91E Mg alloy was received as ingots (Haley Industries, Haley, ON) and its chemical composition (batch analysis from the supplier) is presented in Table 3-1.

Table 3-1: Composition of AZ91E Alloy (wt.%)

Mg	Al	Zn	Mn	Ce	Cu	Fe	Ni
Bal.	9.3	0.65	0.24	0.01	0.005	0.002	0.0009

Commercial purity Al (99.7 wt.%), Mg (99.8 wt.%) and Zn (99.9 wt.%) were used as starting materials for the neutron diffraction experiments, wettability experiments and Al-SiC refiner preparation experiments. Any Si addition was made using a Al-53 wt.% Si master alloy.

3.1.2 Hexachloroethane (C₂Cl₆)

The C₂Cl₆ was obtained from Alfa Aesar (Ward Hill, MA, USA) with a 99.7 wt.% purity. The particle size distribution of the C₂Cl₆ was measured using a Malvern Mastersizer 2000 and the 10, 50 and 90% average particle diameters were 37, 92 and 258 μm respectively.

3.1.3 Silicon Carbide, Aluminum and Graphite Powders

The 2 μm α-SiC powder was obtained from Alfa Aesar (Ward Hill, MA, USA) with a 99.8 wt.% purity. The SiC powder was obtained from two different lots. The Al and graphite powders were obtained from Loba Chemie (Mumbai, India) with purities of 99.7 wt.% and 98 wt.% respectively. The compositions and 10, 50 and 90% average particle sizes are presented in Table 3-2. The particle sizes were measured using a Microtrac S3500 Dry Powder Particle Size Analyzer.

Table 3-2: Composition and Average Particle Sizes of SiC, Al and Graphite Powders

Powder	Composition (wt.%)						Particle Size (μm)			
	Si	C	O	Al	Ca	Fe	10%	50%	90%	
SiC	Lot 1	Bal.	29.5	0.7	0.02	<0.002	0.03	0.23	0.74	2.00
	Lot 2	Bal.	29.9	0.9	0.02	<0.01	0.03	0.20	0.80	1.90
	Average	Bal.	29.7	0.8	0.02	<0.006	0.03	0.22	0.77	1.95
Al	Al	Fe	Si	Cu	Mn	Mg				
	Bal.	0.17	0.131	0.001	0.002	0.001	8.6	25.5	59.4	
Graphite	C	Fe	S	Ash						
	Bal.	0.4	0.1	0.5			3.5	32.5	83.4	

3.1.4 Titanium and Calcium Sponges

The Ca (3 mm) and Ti (3-13 mm) sponges were both obtained from Alfa Aesar (Ward Hill, MA, USA) and had compositions of 99 and 99.95 wt.% respectively.

3.1.5 Silicon Carbide Wettability Substrates

The polycrystalline α -SiC substrates were obtained from Saint Gobain Ceramics (Niagara Falls, NY, USA). The alpha polytype of SiC was confirmed using a XRD scan shown in Figure A-5 (Appendix A.3). For the wettability experiments, the square substrates measured 50.8 x 50.8 x 3 mm and were sectioned into four equal sized squares using a diamond blade. The average (three repeats) roughness of the SiC substrates were 0.66 μm measured using a profilometer.

3.1.6 Graphite Moulds

Five different graphite moulds were used throughout this dissertation. The moulds were machined from graphite rods (Speer Canada Inc., Kitchener, ON). Features and dimensions of all the graphite mould used are described in Table 3-3.

Table 3-3: Dimensions of Graphite Moulds

Experiment	Dimensions	Comments
Neutron Diffraction	8.5 and 12.8 mm diameter, 40 mm long with 1 mm wall thickness	Crucible lid with thermocouple port
Al-SiC Refiners	31.8 mm in diameter, 101.8 mm long with 3.2 mm wall thickness	Figure 3-1a Mould caps were 25.4 mm in diameter, 6.4 mm in height
Wettability	68 mm in diameter, 62 mm tall	Figure 3-1b
SPS Al-C Refiners	70 mm diameter with 20 mm wall thickness, 60 mm tall	Hallow cylinder sealed with 30 mm tall graphite rods

For the neutron diffraction experiments, graphite crucibles were used for melting and holding the samples at the specified temperatures. For the wettability experiments, the graphite moulds were machined to produce castings with circular bottoms 50 mm tall and 40 mm in diameter. Graphical representations of the graphite moulds for the Al-SiC grain refiners and wettability experiments are shown in Figure 3-1a and b respectively.

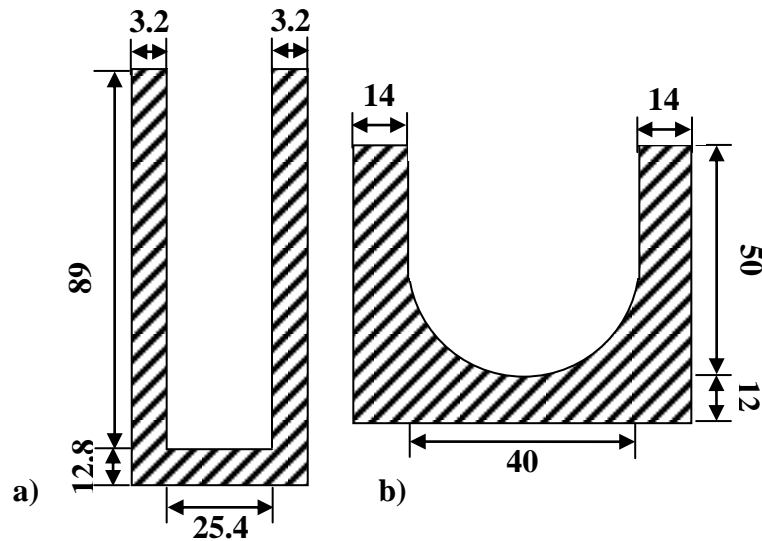


Figure 3-1: Graphite Mould Used for a) Al-SiC Grain Refiner Preparation and b) Wettability Sample Preparation (Dimensions in mm)

The graphite moulds used for preparation of the SPS Al-C grain refiners had a 10 mm deep slot machined at the centre of the cylinder height for K-type thermocouple placement. The required amount of powders for sintering were placed within the graphite mould and sealed using

the graphite rods. A graphite sheet was placed in between the graphite mould ends and the powders to maintain thermal and electrical contact.

3.1.7 Tensile Mould

An ASTM standard (B108-06) permanent mould (Figure 3-2) was utilized to produce the AZ91E Mg castings. The mould ensured similar melt flow and turbulence for each casting trial and minimized cold shuts, hot tears and porosity. The mould produced rounded tensile specimens with a gauge diameter of 12.7 mm and a gauge length of 50.8 mm. Two pours resulting in four tensile specimens were produced to represent each casting condition, for repeatability.

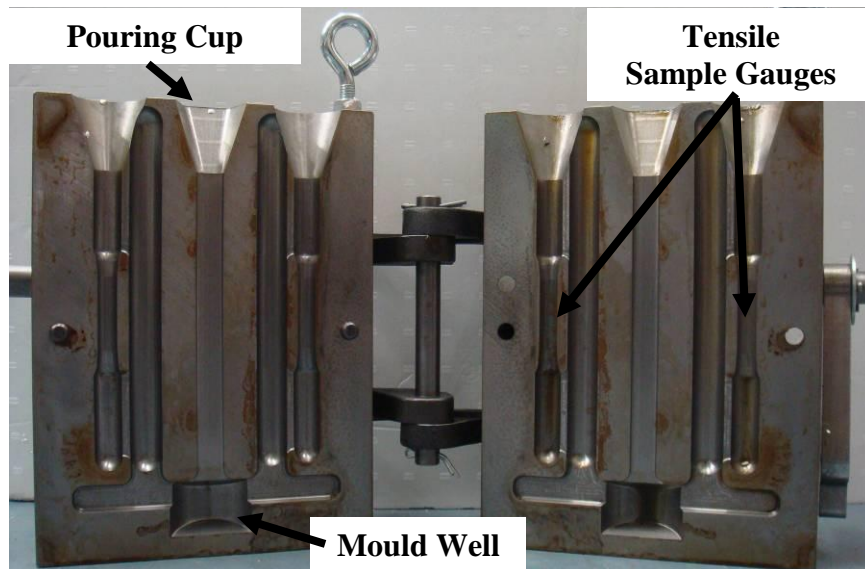


Figure 3-2: Tensile Mould

3.1.7.1 *Mould Coating*

A Foseco Dycote® (36 or 39ESS) mould coating was applied on the permanent mould to reduce wear and ease casting ejection. The mould was cleaned by hand using steel wool, then heated to 300°C, and cooled in air to 200°C before coating. A compressed air gun at a pressure between 30-40 kPa at a distance ~30 cm from the mould surface was used to apply the coating. The coating thickness was ~100 µm thick measured using an optical microscope on a test steel sample.

3.1.7.2 Installation of Thermocouples

Six K-type thermocouples (Omega Engineering Inc., Laval, QC) with 3.175 mm diameter ceramic sleeves were inserted into slots machined into the tensile mould to measure the mould temperature during the casting experiments. The slots extended 34 mm into the mould cavity (10 mm away from gauge wall) at the parting line and the thermocouples were connected to a data acquisition system (Daytronic System 10, DataPAC) for temperature monitoring. Figure 3-3 depicts the locations of the thermocouple probes and the area simulated for the melt velocity modeling experiments in Section 5.2.2.

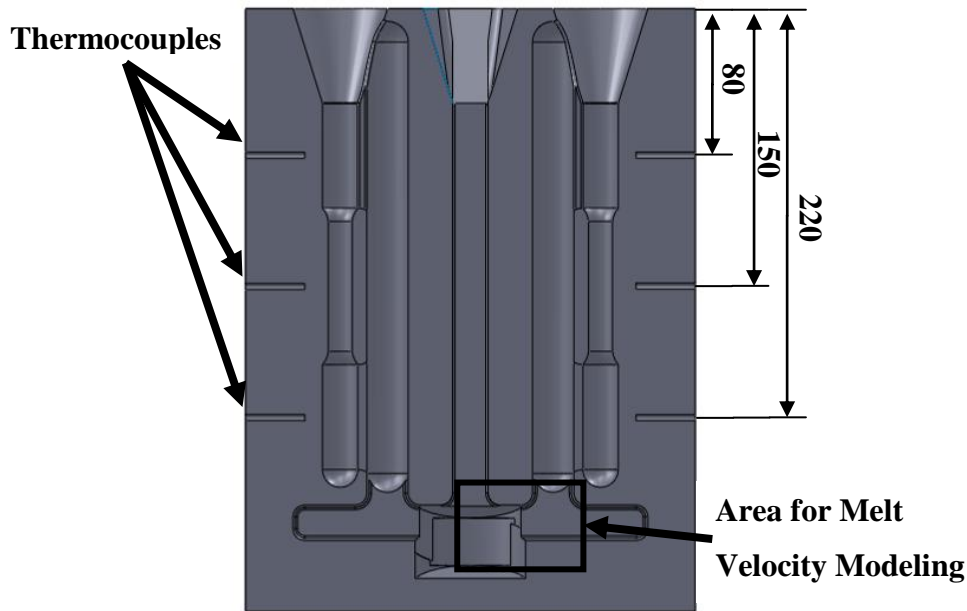


Figure 3-3: Thermocouple Placement in Tensile Mould (Dimensions in mm)

3.1.7.3 Mould Heating

The tensile mould was preheated using a natural gas furnace in two steps. At first, the mould was placed with pouring cup facing down then flipped with pouring cup facing up halfway through the heating cycle. A typical heating cycle lasted 20 minutes and resulted in a mould temperature $\sim 100^{\circ}\text{C}$ above the desired mould temperature. The mould was then allowed to cool in still air and homogenize in temperature before pouring. The mould flipping and homogenization resulted in a temperature difference of $\sim 5\text{-}10^{\circ}\text{C}$ between thermocouples located at each tensile sample gauge. The mould was held closed using three C-clamps during pouring.

3.1.8 Filters

The filters for the inclusion removal experiments were knitted stainless steel wires in a square weave pattern. Both one layer of a coarse and fine weave filter arrangement were examined. The filters were cleaned in a commercial metal cleaner (CLR®) for 2 minutes, washed with water then dried prior to their placement in the tensile mould before preheating. A summary of the filter dimensions and placement is outlined in Table 3-4.

Table 3-4: Filter Dimensions and Placement

Filter Type	Filter Dimensions (mm)	Filter Placement
Coarse	Wire Diameter: 0.64 Square Mesh Size: 1.78	<ul style="list-style-type: none">• Atop Pouring Cup• Pouring Cup• Within Well
Fine	Wire Diameter: 0.38 Square Mesh Size: 0.81	<ul style="list-style-type: none">• Within Well

3.1.9 Cover and Bubbling Gases

For melting of Mg melts, a cover gas mixture of CO₂ or CO₂ + 0.5 vol.% SF₆ was used. The purities of the CO₂ and SF₆ were 99.8 and 99.9 vol.% respectively. The neutron experiments were conducted with a cover gas of Ar. For preparation of the wettability alloys, a low purity Ar (99.9 vol.%) cover gas was used during addition of alloying elements. During the wettability experiments, the cover gas was Ar + 0.5 vol.% H₂. For Mg bubbling experiments, a high purity Ar (99.999 vol.%) was used.

3.2 Melting and Casting Procedures

This section details the procedures used for the in-situ neutron diffraction experiments, inclusion removal experiments, modeling experiments, AZ91E Mg alloy refined by C₂Cl₆, wettability experiments, preparation of Al-SiC grain refiners, AZ91E Mg alloy refined by Al-SiC refiners and AZ91E Mg alloy refined by Al-C refiners.

3.2.1 In-situ Neutron Diffraction Experiments

The in-situ neutron diffraction experiments of the Mg-Zn and Mg-Al alloy castings was done because neutron diffraction is the only technique that had a combination of high penetration with

diffraction not being influenced by the number of protons, electrons or neutrons in the diffracting atom unlike X-rays or electrons.

3.2.1.1 Casting of Neutron Diffraction Samples

The alloys examined for the in-situ neutron diffraction experiments were Mg-3 wt.% Zn, Mg-5 wt.% Zn, Mg-5 wt.% Zn-0.7 wt.% Zr, Mg-6 wt.% Al and Mg-9 wt.% Al. The alloys were prepared using commercial purity Mg, Zn and Al. The required amounts of Mg and Al or Mg and Zn were melted in a furnace at 750°C and stirred for 30 seconds at 200 RPM using a hand drill prior to pouring. The melts were poured into a steel mould preheated to 700°C. The resulting cylindrical castings measured 20 mm in diameter and 100 mm in length.

3.2.1.2 Solidification Analysis of Mg-Zn and Mg-Al Alloys Using In-situ Neutron Diffraction

The castings were machined to prepare cylinders 6.5 mm or 10.8 mm in diameter and 40 mm in length. A 2.05 mm diameter hole was machined 10 mm into the top of each alloy cylinder to accommodate a K-type thermocouple with sleeve for temperature measurement and control during the neutron experiments. The depth of the hole was limited to only 10 mm into the sample to minimize the thermocouple's contribution to the diffraction pattern.

The machined castings were placed into the graphite mould depicted in Figure 3-4a and connected to the furnace lid (Figure 3-4b and Figure 3-4c) with a setscrew. The furnace lid contained a port for a K-type thermocouple and cooling water. During heating and cooling, the alloys were protected with an Ar cover gas at a positive pressure of 7-20 kPa. The furnace cover with mould assembly was lowered into an infrared furnace and a positive pressure within the furnace chamber was maintained to prevent oxidation.

The in-situ neutron diffraction experiments were performed using the C2 powder diffractometer at the Canadian Neutron Beam Centre in Chalk River, Ontario. The NRU reactor operates at power levels of 135 MW with a neutron flux at the reactor core of $\sim 3 \times 10^{14}$ neutrons/cm²·s. The complete furnace assembly showing the furnace, incident beam and detector are shown in Figure 3-5. For the Mg-5 wt.% Zn and Mg-5 wt.% Zn-0.7 wt.% Zr alloys the entire furnace was oscillated a total of 36° and a vibratory motor connected to the crucible holder was used to agitate the sample.

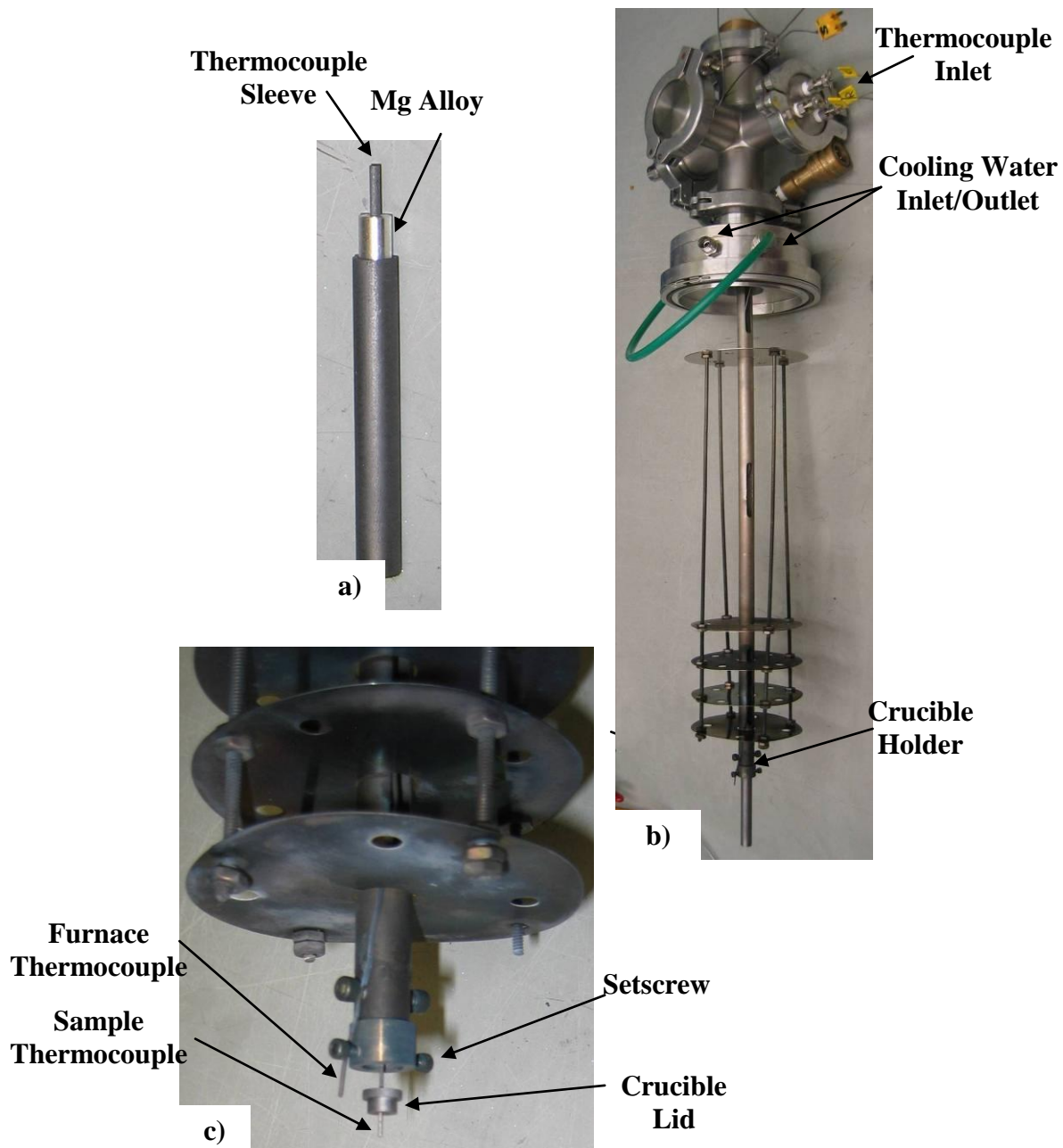


Figure 3-4: a) Graphite Crucible Used for In-situ Neutron Diffraction Experiments, b) Furnace Lid with Crucible Holder Assembly and c) Magnified Image of Crucible Holder

The Mg-Al and Mg-Zn alloys were heated 10-20°C above their liquidus temperatures then cooled in a stepwise fashion to the temperatures presented in Table 3-5. The alloy temperature was controlled using a K-type thermocouple and proportional-integral-derivative circuit. The thermocouples were calibrated in comparison to the melting point of pure Al and were accurate to +/- 0.5°C. The Mg alloys were held at each temperature for one hour (to allow for sufficient

neutron peak statistics) while being irradiated by monochromatic thermal neutrons with wavelength of 2.37 Å using a Si single crystal and a {311} reflection. The high wavelength provided wider peaks simplifying peak area measurements. The examined sample volume encompassed the entire casting length (40 mm) and the neutron diffraction intensity versus diffraction angle (2θ) data was collected for diffraction angles ranging from 37 to 117°. The diffraction angles were chosen to include the primary Mg peaks ($10\bar{1}0$), (0002) and ($10\bar{1}1$).

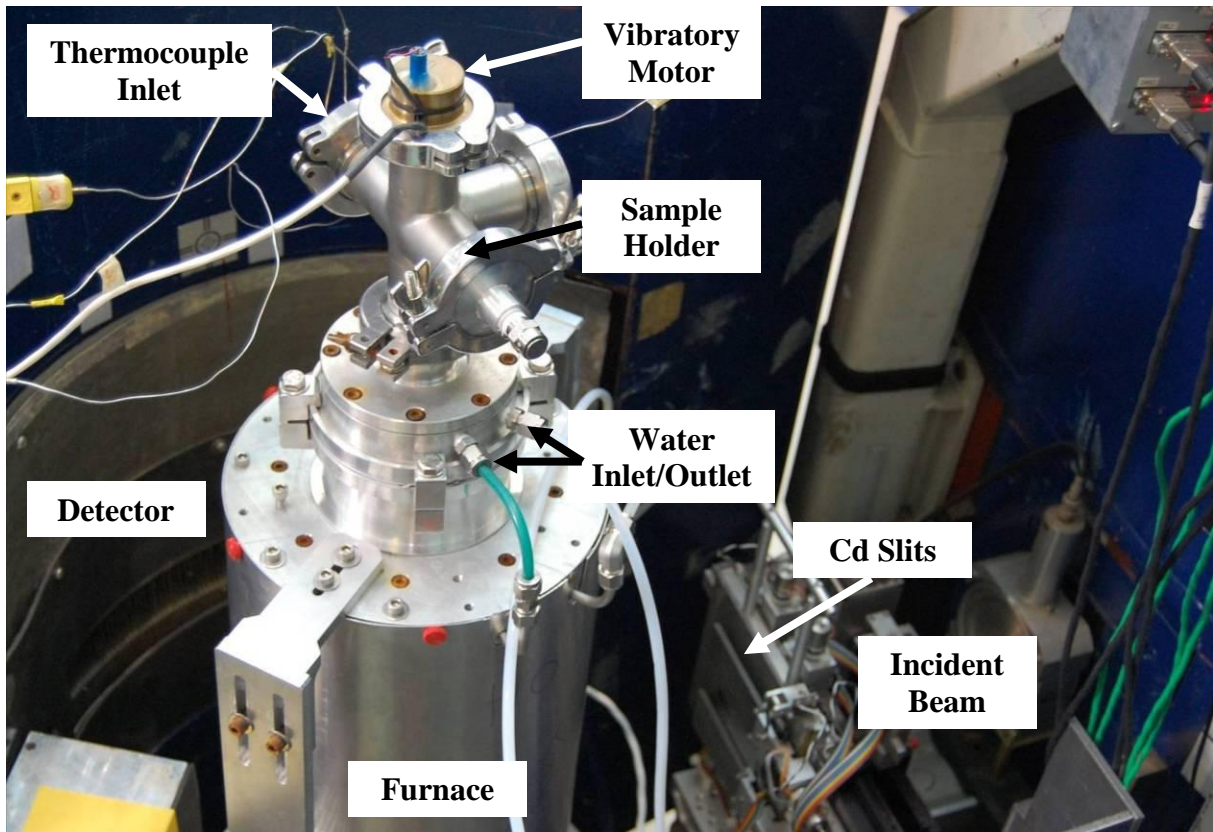


Figure 3-5: Diffractometer Setup for In-situ Neutron Diffraction Experiments

Table 3-5: Holding Temperatures for In-situ Neutron Diffraction Experiments

Alloy	Temperatures (°C)
Mg-6 wt.% Al	640, 630, 620, 610, 600, 590, 580, 570, 560, 550, 540, 530, 520, 500, 480, 460, 440, 435, 430 and 420
Mg-9 wt.% Al	620, 610, 600, 590, 580, 570, 560, 550, 540, 530, 520, 510, 500, 490, 480, 470, 460, 450, 440, 430 and 420
Mg-3 wt.% Zn	650, 635, 620, 600, 580, 560, 540, 520, 500, 480, 460, 440, 420, 400, 385, 370, 355, 345, 340, 335, 330, 325, 320, 310 and 300
Mg-5 wt.% Zn	660, 635, 620, 600, 580, 560, 540, 520, 500, 480, 460, 440, 420,
Mg-5 wt.% Zn-0.7 wt.% Zr	400, 385, 370, 350, 340, 330, 315, 300, 250 and 200

3.2.1.3 *FactSage™ Modeling*

A thermodynamic database software package called FactSage™ was used to simulate the fraction solid curves of the Mg-Zn alloys examined using in-situ neutron diffraction. The temperature range examined was between 660°C and a temperature below solidus (alloy dependant, typically 400-200°C). Both equilibrium (solid-state diffusion is present) and Scheil solidification (no solid-state diffusion) conditions were examined and compared to the in-situ neutron diffraction results. The FactSage™ software was also used to predict the associated phase diagrams and provide preliminary estimations for liquidus and solidus points of the examined alloys. The temperature increments in Table 3-5 were also decided upon using FactSage™ with small increments close to major thermal events such as liquidus, solidus and any phase transformation temperatures and large increments during cooling without any thermal events.

3.2.2 Inclusion Removal Experiments

Approximately 1 kg of virgin AZ91E Mg alloy was preheated atop the furnace for a minimum of 30 minutes before melting. The ingots were melted in a low C steel crucible and placed into a custom designed electric resistance melting furnace (PSH Kilns, 5 kW, Oakville, Ontario) set to a temperature of 750°C. The CO₂ cover gas was maintained at a flowrate of 4.7 L/min to prevent oxidation of the melt.

The melt temperature was checked using a K-type thermocouple. Once the melt temperature reached 740°C, the tensile mould was preheated, removed from the gas furnace and left to cool on a refractory brick. Once the mould sufficiently cooled, the AZ91E alloy was removed from the electric resistance furnace, skimmed of any oxides using a low C steel spoon and poured at 720°C into the tensile mould. The corresponding mould temperature was 475°C at the tensile gauge section. Any remaining melt was poured into a pig and not reused for subsequent experiments.

The melt was protected with the CO₂ cover gas during pouring and for an additional 10 minutes as the casting solidified and cooled. The casting was then removed from the tensile mould and cooled to room temperature without the protection of the cover gas. A summary of the casting procedure is outlined in Table 3-6.

Table 3-6: Experimental Procedure for Inclusion Removal Experiments

Process	Important Parameters
Preparation of Materials	
I	<ul style="list-style-type: none"> • 1 kg of virgin AZ91E ingot
II	<ul style="list-style-type: none"> • AZ91E ingots preheated for 30 minutes atop furnace
Melting of Alloy	
I	<ul style="list-style-type: none"> • AZ91E ingots were placed into melting furnace set at 750°C • 4.7 L/min of CO₂ cover gas
II	<ul style="list-style-type: none"> • Melt temperature was checked using K-type thermocouple (~740°C)
Mould Preheating	
I	<ul style="list-style-type: none"> • Mould was preheated and left to cool on refractory brick
II	<ul style="list-style-type: none"> • Mould was connected to data acquisition system to monitor temperature
Pouring	
I	<ul style="list-style-type: none"> • Melt was removed from furnace and skimmed of any oxides • Melt was poured at 720°C
II	<ul style="list-style-type: none"> • Mould temperature was 475°C at the tensile gauge sections • Remaining melt was poured into a pig
III	<ul style="list-style-type: none"> • Casting was protected for 10 minutes using the cover gas • Casting removed from tensile mould

The inclusion removal experiments were conducted to examine the influence of filter type (Table 3-4) and location on the properties of AZ91E castings. The filters were placed in the mould well prior to mould preheating.

3.2.2.1 Argon Bubbling Experiments

To expand on the inclusion removal experiments (Section 3.2.2), Ar bubbling experiments were conducted independently and simultaneously with the optimum filter casting scenario. The Ar bubbling experiments were carried by bubbling Ar at a flowrate of 1.8 L/min through a low C steel lance with a 0.8 mm opening inserted 10 mm above the bottom of the crucible for five minutes. The bubbling was carried out at 740°C and the melt was then left to sit for five minutes before pouring. The heating of the mould and bubbling experiments were timed accordingly to maintain the mould gauge section temperature and pouring temperature at 475°C and 720°C respectively.

3.2.3 Modeling Experiments

The modeling experiments were conducted to compare castings produced using no filter and a fine filter placed within the well of the mould. The filter was modeled as a square mesh, one layer thick (shown in Table 3-4). The mould temperature was increased to 540°C (gauge section) to increase metal fluidity and ease in mould filling. Measurements of the temperature of the solidifying casting were made by inserting a K-type thermocouple into the centre of the tensile gauge prior to pouring. The casting procedure was identical to that in Table 3-6 except with the increased mould temperature (540°C).

The modeling simulations were conducted using SolidCast (Finite Solutions Inc., Slinger, WI, USA) finite difference modeling software. There was no technical manual provided with SolidCast but for most computational fluid dynamics software packages, the results are obtained by solving the continuity (conservation of mass), Navier-Stokes (conservation of momentum) and energy equations [310]. These equations assume that many fluid properties remain constant but the case for solidification these properties would have to be modified with temperature and time. Assuming an x, y and z coordinate system the component velocity vectors of a fluid can be denoted as u, v and w respectively. With constant fluid density, the unsteady continuity equation can be written as [310]:

$$\frac{\partial u}{\partial x} + \frac{\partial v}{\partial y} + \frac{\partial w}{\partial z} = 0 \quad (29)$$

The unsteady Navier-Stokes or conservation of momentum equation for the x direction can be expressed in terms of time, t as [310]:

$$\frac{\partial u}{\partial t} + u \frac{\partial u}{\partial x} + v \frac{\partial u}{\partial y} + w \frac{\partial u}{\partial z} = -\frac{1}{\rho} \frac{\partial p}{\partial x} + \nu \left(\frac{\partial^2 u}{\partial x^2} + \frac{\partial^2 u}{\partial y^2} + \frac{\partial^2 u}{\partial z^2} \right) \quad (30)$$

Where:

ρ : Fluid density

p: Fluid pressure

ν : Fluid kinematic viscosity

Similar equations for the y and z directions can be generated using appropriate velocity components. Equation 30 outlines that the net momentum is influenced by the net pressure forces on the fluid. The energy equation (Equation 31) can be described as [310]:

$$\frac{\partial T}{\partial t} + u \frac{\partial T}{\partial x} + v \frac{\partial T}{\partial y} + w \frac{\partial T}{\partial z} = \left(\frac{k_{th}}{\rho c_p} \right) \left(\frac{\partial^2 T}{\partial x^2} + \frac{\partial^2 T}{\partial y^2} + \frac{\partial^2 T}{\partial z^2} \right) + \left(\frac{\mu}{\rho c_p} \right) \phi \quad (31)$$

Where:

T: Temperature

c_p : Specific heat

μ : Coefficient of viscosity

k_{th} : Thermal conductivity coefficient

The rightmost term in Equation 31 represents viscous dissipation and accounts for work done because of viscous stresses in a flow. During mould filling the flow is relatively slow and so this term can be considered negligible. Equation 31 assumes incompressible steady flow with constant fluid properties. The continuity and Navier-Stokes equations must be solved simultaneously with the energy equation to obtain the temperature field and determine heat transfer rates for solving solidification problems [310]. In addition, a turbulence model should be applied to account for turbulent flow as the liquid metal passes through a complex geometry during casting.

3.2.3.1 Model Setup

The effective heat transfer coefficient (HTC) used for the ambient air/Mg alloy was 8.5 W/m²K and that for ambient air/mould was 48.8 W/m²K both at 24°C. For the Mg alloy and mould interface, the heat transfer coefficients examined were in the range, 1135 to 3000 W/m²K with node sizes of 2, 1 and 0.5 mm. These parameters were based on previous literature, recommendations from the software developers and software limitations. The modeling software did not allow for a variation in the mould temperature so the temperature of the gauge section was utilized. A pouring time of 12.6 seconds was determined via experimental trials and was used to define the inlet pouring velocity of 0.48 m/s. The pouring temperature was 720°C. Additional boundary conditions were two-axis symmetry and convective heat transfer between the mould and air. The heat transfer between the mould and air (convection and radiation), the influence of a coating, the latent heat released from the Mg and the formation of an air gap between the casting and mould are also key considerations. However, since these parameters are more influential over longer time periods they are thought to not significantly impact the grain

size which is established in the early stages of solidification. A summary of the examined modeling parameters is in Table 3-7.

Table 3-7: Summary of Modeling Conditions

Casting Condition	Node Size (mm)	HTC Between Metal and Mould (W/m ² K)	Casting Fill Time (s)
Unfiltered	2, 1 and 0.5	1135, 1250, 1375 and 1500	12.6
Filtered	0.5	1135	12.6

3.2.4 Grain Refinement Experiments Using C₂Cl₆

For the C₂Cl₆ experiments, the casting procedure was similar to the procedure in Table 3-6 with changes presented in Table 3-8.

Table 3-8: Experimental Procedure for C₂Cl₆ Grain Refinement Experiments

Process	Important Parameters
Preparation of Materials	
III	<ul style="list-style-type: none"> Desired amount of C₂Cl₆ measured and wrapped in Al foil
Melting of Alloy	
I	<ul style="list-style-type: none"> AZ91E ingots were placed into melting furnace set at 750°C 4.7 L/min of CO₂ + 0.5 vol.% SF₆ cover gas
Addition of Grain Refiner	
I	<ul style="list-style-type: none"> Grain refiner was added to melt using steel plunger
II	<ul style="list-style-type: none"> Melt held for 20 minutes
Pouring	
II	<ul style="list-style-type: none"> Melt was poured at 720°C Mould temperature was 540°C at the tensile gauge sections Remaining melt was poured into a pig
III	<ul style="list-style-type: none"> Casting was removed from the mould after 15 minutes

The required amount of C₂Cl₆ was measured using a digital scale (Scientech-SP350). The C₂Cl₆ concentrations examined were 0.25, 0.50 and 0.75 wt.%.

3.2.5 Wettability Experiments

Wettability experiments were conducted in order to optimize the composition for preparation of the Al-SiC grain refiners. The wettability experiments involved casting the alloys of investigation, conducting the wettability experiments and determining the associated contact angles.

3.2.5.1 Preparation of Samples

The wettability samples were prepared by casting Al-Si-Mg alloys using an electric resistance furnace. The Al-Si-Mg alloys were prepared with nominal Si concentrations from 0 wt.% up to 10 wt.% in 2 wt.% increments and Mg nominal concentrations from 0 wt.% to 1.25 wt.% in 0.25 wt.% increments. The alloys were prepared by melting 100 g of Al at 750°C in a graphite crucible shown in Figure 3-1b. The required amounts of Si and Mg were added under low purity Ar gas protection to prevent oxidation. The melt was held at 750°C for 20 minutes to ensure complete dissolution of Si and Mg. The melt was then gently stirred by hand for 30 seconds using a steel rod. The Al-Si-Mg alloy was then degassed by adding 0.2 wt.% fluoroborosilicate and removed from the furnace and allowed to cool in still, ambient air. A summary of the prepared alloys is in Table 3-9. Additional wettability experiments were conducted on samples with compositions of Al-2 wt.% Si-1.25 wt.% Mg.

Table 3-9: Summary of Prepared Alloys for Wettability Experiments

Alloy Composition (wt.%)		
Al	Al-Si	Al-Si-Mg
Pure Al	Al-2Si	Al-10Si-0.25Mg
	Al-4Si	Al-10Si-0.50Mg
	Al-6Si	Al-10Si-0.75Mg
	Al-8Si	Al-10Si-1.00Mg
	Al-10Si	Al-10Si-1.25Mg

3.2.5.2 Sample Setup and Melting

The cast alloys were machined on a lathe into half circle cylinders 10 mm in diameter 4.5 mm thick. The wettability experiments were conducted using the sessile drop technique in a horizontal induction furnace with a Eurotherm 2404 controller. The temperatures examined were 800 and 900°C over a period of 60 minutes. The furnace temperature was measured using a R-type thermocouple placed ~10 mm above the alloy. The cover atmosphere was Ar + 5 vol.% H₂ at a flow rate of 0.05 L/min. Three grams of Ti and Ca sponges were placed on either side of the wettability sample to minimize oxygen levels. The experimental setup for the wettability tests is shown in Figure 3-6.

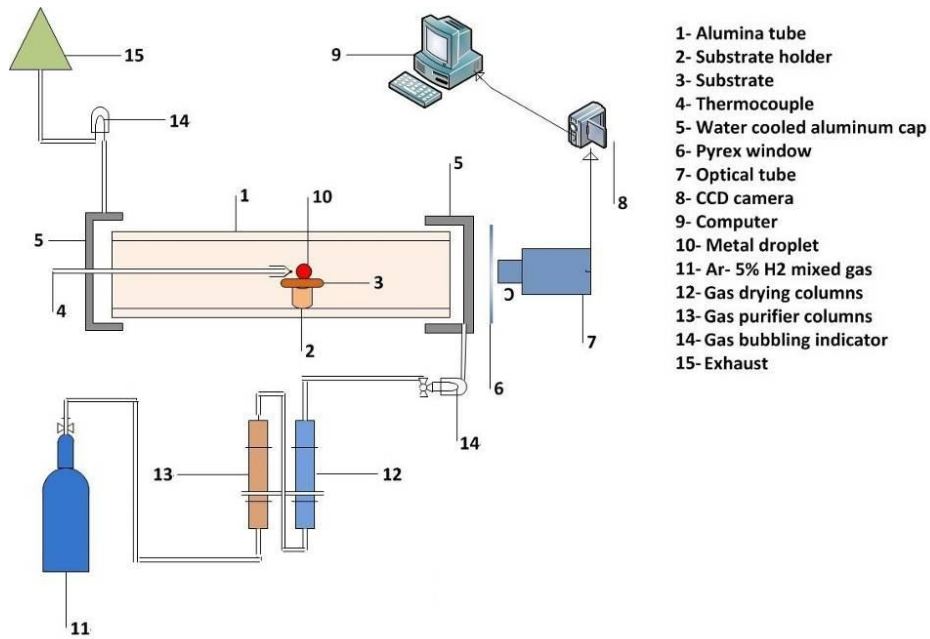


Figure 3-6: Experimental Setup for Wettability Experiments

3.2.5.3 Contact Angle Measurements

Contact angles were determined manually as the angle between the tangent to the drop surface at its line of contact with the substrate at the three phase boundary between the substrate, metal and vapour as shown in Figure 3-7. Measurements of receding contact angle were made after sample melting (time zero) in 20 minute intervals up to a maximum of 60 minutes. Preliminary results indicated that no significant changes in contact angle were observed beyond 60 minutes.

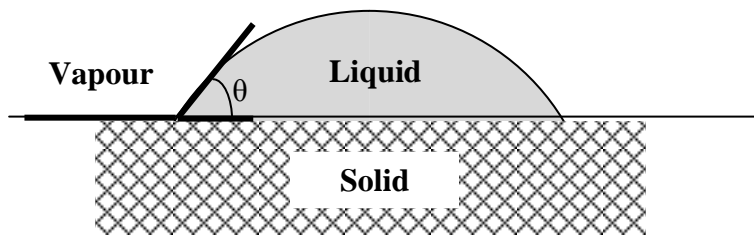


Figure 3-7: Contact Angle (θ) Measurement During Wettability Experiments

3.2.6 Al-SiC Grain Refiner Preparation

The grain refiner composition from the wettability experiments that provided the lowest contact angle with minimal alloy additions was utilized to prepare the Al-SiC grain refiners. The Al-SiC grain refiners were prepared in two casting stages. The first stage was to prepare the

Al-Si-Mg alloy matrix and the second stage was to produce the Al-SiC grain refiner. This two step casting procedure was conducted to evenly distribute the SiC within the grain refiner microstructure.

3.2.6.1 Preparation of Al-Si-Mg Alloy

The Al-Si-Mg alloy was prepared in the same manner as the wettability samples in Section 3.2.5.1 but in batches of approximately 600 g and melted in SiC crucibles. The alloys were poured into the cylindrical graphite moulds (Figure 3-1b) preheated to 450°C.

3.2.6.2 Casting of Al-SiC Grain Refiner

The prepared Al-Si-Mg alloy was machined on a lathe to prepare metal chips. The metal chips were consolidated and placed into a Retsch PM-100 planetary ball mill without grinding balls. One hundred grams of Al-Si-Mg alloy chips were placed into the ball mill with SiC powders corresponding to either 5.9 or 11.6 wt.% (5 or 10 vol.%). The ball mill was operated for five minutes at 350 RPM in one direction.

The ball milling resulted in the Al-Si-Mg chips becoming coated with the SiC powders as shown in Figure 3-8. Approximately 40 g of Al-Si-Mg chip/SiC powder material was then compacted by hand into the graphite crucibles (Figure 3-1a) and sealed with the graphite lids.

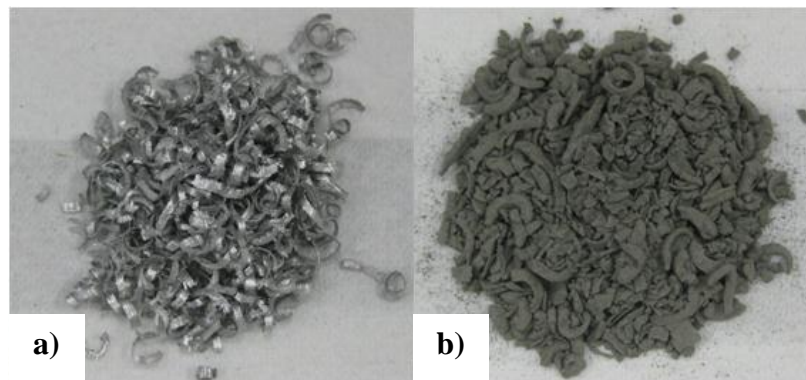


Figure 3-8: a) Al-Si-Mg Alloy Chips and b) After Ball Milling with SiC Powder

The graphite mould containing the compacted Al-Si-Mg chips/SiC powder was then placed into an electric resistance furnace preheated to 710, 810 or 910°C. Once 15 minutes passed, the graphite mould lid was pressed down on the alloy until some molten metal was observed to squeeze out between the spacing between the mould and lid, ensuring that the molten Al-Si-Mg

alloy and SiC powders were fully in contact. The graphite moulds were then held at their respective temperatures for another 60 or 120 minutes except for the samples placed in the furnace at 710°C, as they were removed immediately after being pressed. Finally, the graphite moulds were removed from the furnace and allowed to cool on a steel plate. A summary of the prepared Al-SiC grain refiners is in Table 3-10.

Table 3-10: Summary of Prepared Al-SiC Grain Refiners

Temperature (°C)	Amount of SiC (wt.%)	Holding Time (min)
700	5.9	0
	11.6	0
800	5.9	60
		120
	11.6	60
		120
900	5.9	60
		120
	11.6	60
		120

3.2.7 Grain Refinement Experiments Using Al-SiC Refiners

The experiments involving the Al-SiC grain refiners were conducted with the filtration and Ar bubbling procedures discussed in Section 3.2.2.1. The filters were placed within the mould prior to preheating. The procedures follow those in Table 3-6 with changes shown in Table 3-11.

Table 3-11: Experimental Procedure for Al-SiC Refiner Experiments

Process	Important Parameters
Preparation of Materials	
III	<ul style="list-style-type: none"> Desired amount of Al-SiC grain refiner measured, wrapped in Al foil and preheated atop furnace
Melting of Alloy	
I	<ul style="list-style-type: none"> AZ91E ingots were placed into melting furnace set at 750°C 4.7 L/min of CO₂ + 0.5 vol.% SF₆ cover gas
Ar Bubbling	
I	<ul style="list-style-type: none"> 1.8 L/min of high purity Ar for five minutes at 740°C
II	<ul style="list-style-type: none"> Melt skimmed of surface oxides
Addition of Grain Refiner	
I	<ul style="list-style-type: none"> Grain refiner was added to melt and stirred using blade spinning at 200 RPM for 30 seconds

II	<ul style="list-style-type: none"> • Melt held for 20 minutes
Pouring	
II	<ul style="list-style-type: none"> • Melt was poured at 720°C • Mould temperature was 540°C at the tensile gauge sections • Remaining melt was poured into a pig
III	<ul style="list-style-type: none"> • Casting was removed from the mould after 15 minutes

3.2.8 Spark Plasma Sintered Al-C Grain Refiner Preparation

Another set of grain refiners were prepared using Al and C powders consolidated using SPS. The Al-C SPS refiners (denoted Al-C from this point) were prepared by a two step process of ball milling then SPS.

3.2.8.1 *Ball Milling of Al-C Refiners*

The ball milling (Zoz Simoloyer® horizontal ball mill, Wenden, Germany) was carried out using steel (18 wt.% Cr) balls. Initially, 2 kg of balls with 100 g of Al powder were loaded into the ball mill and run for 30 minutes at 1200 RPM. The Al powder coated the steel balls and excess Al powder was removed from the ball mill. This Al “coating” procedure helped minimize Fe and Cr contamination during Al-C refiner preparation. A mixture of Al-21 wt.% C (Al-25 vol.% C) weighing a total of 200 g was added to the ball mill to represent a ball to powder milling ratio of 10:1. The ball mill was run at 1200 RPM for five hours with 30 minute breaks each hour to allow the powders to cool. Samples for XRD were also taken each hour.

3.2.8.2 *Spark Plasma Sintering of Al-C Refiners*

For each SPS (Dr. Sinter® SPS-5000, Sumitomo Metals, Japan) experiment, 13.5 g of ball milled Al-21 wt.% C powder was placed into the SPS graphite mould described in Section 3.1.6. The Al-21 wt.% C powder and graphite mould assembly were then sintered according to the parameters described in Table 3-12.

Table 3-12: SPS Experimental Procedure for Al-C Refiner Preparation

Parameter	Value and Comments
Atmosphere	Vacuum, <30 Pa
Sintering Temp.	520°C, using a heating rate of 52°C/min
Sintering Time	1, 10 or 60 minutes (not including time to reach sintering temp.)
Pressure	40 MPa, using a rate of 4 MPa/min maintained during cooling until 300°C

3.2.9 Grain Refinement Experiments Using Al-C Refiners

The experiments involving the Al-C grain refiners were conducted using the filtration and Ar bubbling procedures discussed in Section 3.2.2.1. The filters were placed within the mould prior to preheating. The casting procedures are identical to the Al-SiC refiner experiments in Section 3.2.7.

3.3 Microstructure Analysis

3.3.1 Optical Microscopy of Mg and Al Alloys

All polishing for microscopy was conducted by hand and varied depending if the sample to be examined was Mg or Al based. After sectioning a sample using a hacksaw or abrasive wheel, the sample was cold or hot mounted to ease handling. The Mg and Al samples were prepared according to the procedures described in Table 3-13.

Table 3-13: Grinding and Polishing Procedure for Mg and Al Alloys

Alloy	Process	Paper Type	Duration (min)
Grinding			
Mg and Al	I	120 Grit SiC	Until Plane
	II	320 Grit SiC	2.5
	III	600 Grit SiC	2.5
	IV	1200 Grit SiC	2.5
Polishing			
Al	I	LECO LE CLOTH [®] w/ distilled water + 50 vol.% 5 µm alumina suspension	3
Mg	I	LECO LE CLOTH [®] w/ 9 µm diamond suspension	1-1.5
Al	II	LECO LE CLOTH [®] w/ 3 µm diamond suspension	3
Mg	II	LECO LE CLOTH [®] w/ 3 µm diamond extender	1-1.5
Mg and Al	III	BUEHLER CHEMOMET [®] CLOTH w/ 0.05 µm colloidal alumina (Mg) or silica (Al)	0.25-2.5

Grinding steps I-IV, used water as a lubricant and a wheel rotation rate of 150 RPM. After grinding step IV and after each polishing step, the sample was cleaned ultrasonically in distilled water (for Al) or ethanol (for Mg) for one minute. Polishing steps I, II and III for Al were conducted with a wheel rotation rate of 150 RPM while polishing step II for Mg was done with a stationary wheel. Finally the samples were cleaned using ethanol and a blast of compressed air.

3.3.1.1 Etching

Only the Mg samples were etched for grain size measurement. The samples were first heat treated at 412°C for 16 hours with a forced air quench from a household fan. After polishing, the samples were etched in 95 mL distilled water and 5 g citric acid solution for 15-20 seconds similar to the procedure of Lee *et al.* [107] since the alloys contained more than 5 wt.% Al. The etching was stopped with distilled water then ethanol rinses followed by a blast of compressed air. For Mg-Zn alloys the samples were etched in the as-cast condition using a solution of 10 mL ethanol, 10 mL acetic acid, 70 mL distilled water and 4.6 g of picric acid for 15 seconds followed by ethanol and water rinses and dried using compressed air.

3.3.1.2 Grain Size Measurement

The grain size was measured along the cross-section of the tensile gauges 10 mm away from the fracture surfaces over 200 grains. The grain size measurements were conducted using an optical microscope at a magnification of 100X. The grain size measurements represent an average of two or more samples.

3.3.2 Scanning Electron Microscopy

Scanning electron microscopy analysis was performed using a JOEL-SEM using back-scatter electron (BSE) imaging at a working distance of 11 mm and a potential of 20 keV. Only unetched samples were examined using SEM.

3.4 X-ray Diffraction Analysis

The XRD analysis was conducted on a Phillips XRD or PANalytical X'pert Pro XRD using CuK α radiation. For the Phillips XRD, the voltage and current were 40 kV and 40 mA respectively and for the PANalytical X'pert Pro XRD 45 kV and 35 mA respectively. The diffraction angle steps sizes were 0.02° at 2.5 seconds and 0.02° at 20 seconds per step for the Phillips and PANalytical X'pert Pro XRDs respectively.

3.4.1 Powders Extracted from Solid Samples

For Al alloy samples, the alloys were first machined on a lathe to produce 3-4 g of chips. The chips were added to a solution of 20 g of NaOH and 100 mL of distilled water. The chips were

allowed to dissolve for 7 hours then sieved through filter paper. The collected powders were then heated to 100°C for 60 minutes to remove any hydroxides. The powders were crushed using a mortar and pestle and then placed on an amorphous silica slide before examination.

3.5 Differential Scanning Calorimetry

Differential scanning calorimetry (DSC) was conducted on alloys that replicated the Al-SiC grain refiners. To simplify the results, the alloys prepared contained only Al and SiC and no Si or Mg. This was done to ease interpretation of the results. The DSC analysis was conducted on a Netzsch STA 449F3 Jupiter DSC using alumina crucibles with Ar cover gas. The heating and cooling rates were 10°C/min with peak temperatures of 700, 800 and 900°C. The time durations at each peak temperature was 15 minutes for 700°C and 120 minutes for both 800 and 900°C.

3.5.1 Preparation of Differential Scanning Calorimetry Samples

The alloys for DSC examination were prepared by mixing the appropriate amounts of Al and SiC powders in a Fritsch Pulverisette 5 Planetary Ball Mill (Idar-Oberstein, Germany) with WC vials and balls at a ball to powder weight ratio of 10:1 at 300 RPM for 30 minutes in toluene. Approximately 15-20 mg of the mixed powder alloy was used for DSC analysis. A summary of the alloys investigated is shown in Table 3-14.

Table 3-14: Parameters for DSC Analysis of Al-SiC Alloys

Peak Temperature (°C)	Holding Time (min) at Peak Temperature	Alloy Composition (wt.%)
700	15	Al-5.9SiC
		Al-11.6SiC
800	120	Al-5.9SiC
		Al-11.6SiC
900	120	Al-5.9SiC
		Al-11.6SiC

3.6 Composition Analysis

Composition analysis was conducted using a low magnification (50X) EDX map of the samples in 2-3 areas or by using an optical emission spectrometer at the Centre de Métallurgie du Québec (Trois-Rivières, QC) on three different locations.

CHAPTER 4

SOLIDIFICATION AND GRAIN REFINEMENT OF MAGNESIUM ZINC ALLOYS

4.1 Solidification Behaviour of Mg-3 wt.% Zn Alloys Using In-situ Neutron Diffraction

There is no published research examining the solidification of Mg alloys using in-situ neutron diffraction. Thus, the first set of experiments using Mg-3 wt.% Zn was a preliminary study to develop the procedures required for in-situ neutron diffraction experiments of this alloy system. Since one of the foci of this dissertation is to examine grain refinement effects using in-situ neutron diffraction, a Mg-Zn alloy would allow for significant grain refinement with Zr addition (Section 2.10). The microstructure of the Mg-3 wt.% Zn alloy will be presented first then the in-situ neutron diffraction results.

4.1.1 Microstructure of Mg-3 wt.% Zn Alloy

The grain structures of the Mg-3 wt.% Zn alloys cooled in a permanent mould with a high cooling rate and with a slow cooling rate during the in-situ neutron diffraction experiments are shown in Figure 4-1a and b respectively. The average grain sizes of $\sim 840 \mu\text{m}$ and $\sim 1540 \mu\text{m}$ respectively.

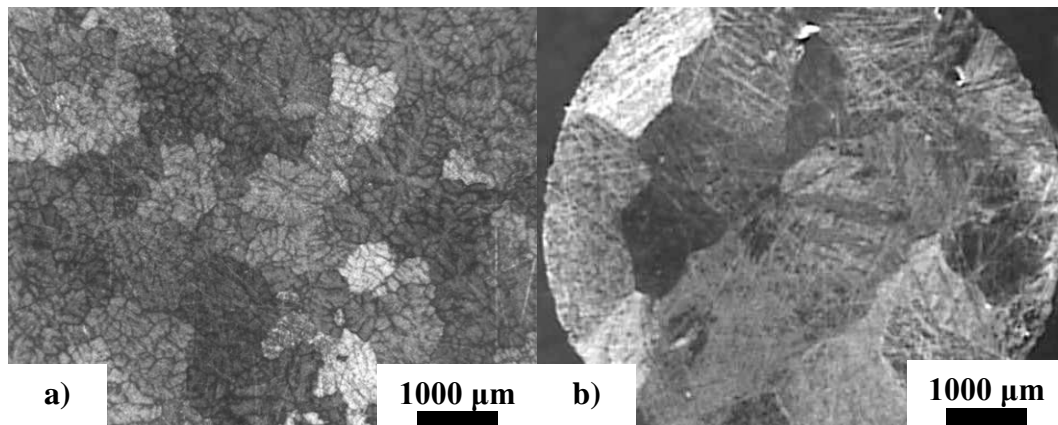


Figure 4-1: Grain Structures of Mg-3 wt.% Zn Alloy a) Before and b) After In-situ Neutron Diffraction Experiment

The large variation in grain size is attributed to the solidification conditions used to prepare each sample. The sample examined before the in-situ neutron experiments was prepared by pouring in a permanent mould providing a high cooling rate. This high cooling rate would be

expected to provide a non-equilibrium solidification behaviour and result in relatively finer grain sizes. For the sample solidified during the in-situ neutron diffraction experiments, the sample was held at each temperature step for one hour and cooled over a total period of almost one day, providing ample time for grains to grow in equilibrium/low-cooling rate type solidification. The intermetallic phases of the alloys were examined by SEM with the samples in the un-etched condition. Scanning electron microscopy images of the Mg-3 wt.% Zn alloy before and after the neutron diffraction experiments are shown in Figure 4-2a and b respectively with corresponding EDX spot analyses in Figure 4-2c and d respectively. The composition analysis using the optical emission spectrometer revealed a composition of 2.8 wt.% Zn with Mn and Fe concentrations of 0.01 wt.% each. These results are similar to low magnification (50X) EDX maps where the average Zn concentration detected was 2.5 wt.% Zn.

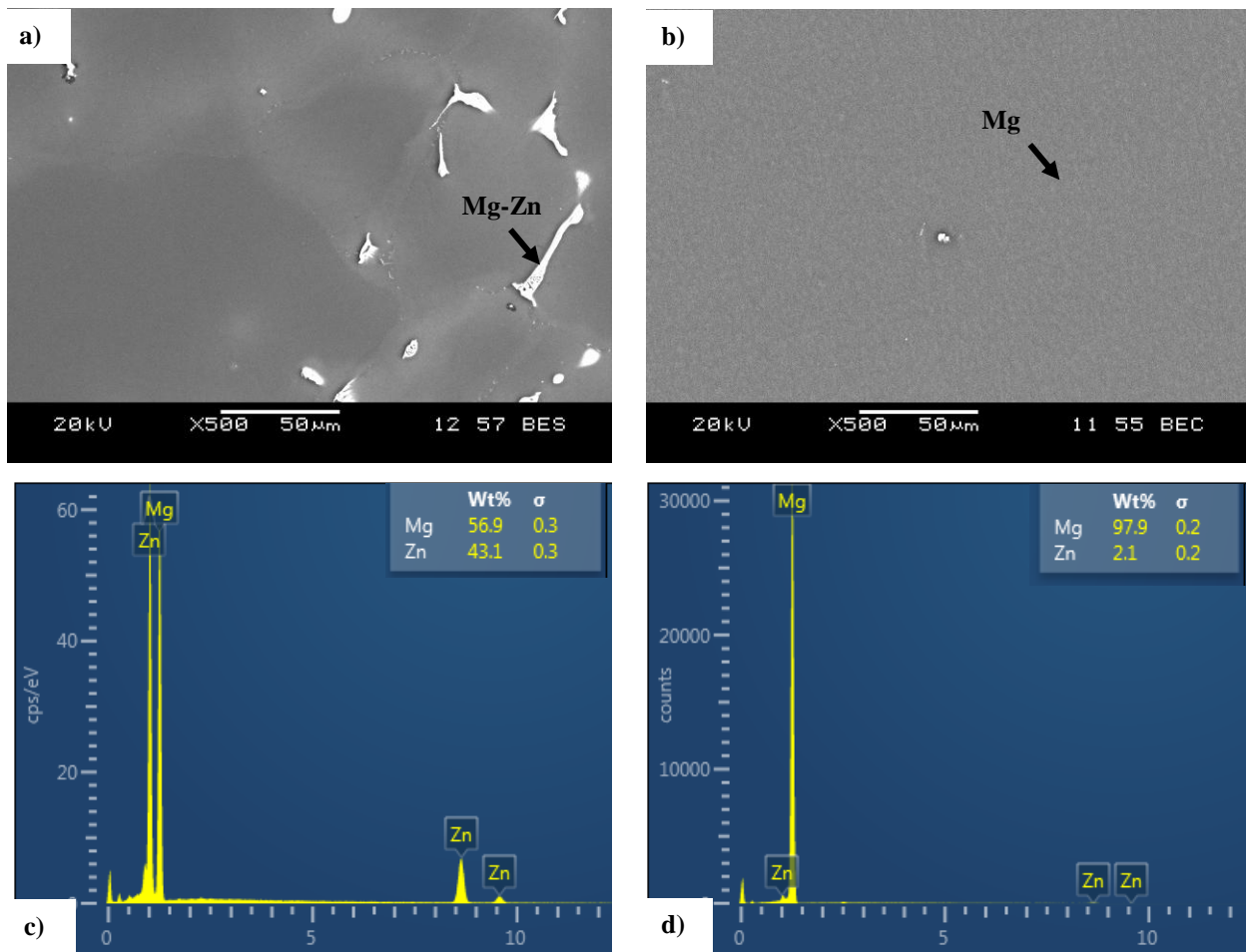


Figure 4-2: SEM Micrographs of Mg-3 wt.% Zn Alloy a) Before In-situ Neutron Diffraction Experiments with EDX in c) and b) After In-situ Neutron Diffraction Experiments with EDX in d)

The Mg-3 wt.% Zn alloy prepared with the high cooling rate prior to the neutron diffraction experiments had a two phase microstructure with a Mg matrix and Mg-Zn intermetallic phase. The Mg matrix contained 1-2 wt.% Zn in solid solution while the remaining Zn segregated to the grain boundaries to form Mg-Zn intermetallics. Spot analysis using EDX was conducted to get an approximate stoichiometry of the intermetallic phase (indicated by arrow) and was typically 56.9 wt.% Mg and 43.1 wt.% Zn or 23.6 wt.% Mg and 76.4 wt.% Zn indicating the phase may be MgZn or MgZn₂ as described by Zhang [180]. Lighter areas of the microstructure also showed that Zn segregation was present. For the Mg-Zn alloy after in-situ neutron diffraction, a single phase microstructure was present with 2.1 wt.% Zn all in solid solution. Any excess Zn would manifest as large Mg-Zn particles but for most areas examined only a Zn enriched Mg matrix was observed. Iron impurities were also observed likely from melting and using commercial quality starting materials. The resulting microstructures in Figure 4-2a and b can be explained by the same justification as the grain size differences in Figure 4-1. Since the alloy was subjected to high cooling rate (non-equilibrium cooling) it is more likely to form intermetallic phases because of the segregation of Zn. For the in-situ neutron diffraction sample, the slow cooling rate allowed for Zn to dissolve and remain within the matrix while the remaining Zn would form large clustered particles. The Zn enriched Mg matrix was the only phase observed during the in-situ neutron diffraction experiments.

4.1.2 In-situ Neutron Diffraction Plots of Mg-3 wt.% Zn Alloy

During the in-situ neutron diffraction experiments, the entire sample volume (6.5 mm diameter, 40 mm long) was contributing to the collected diffraction intensity making the results representative of a bulk analysis. The neutron intensity versus diffraction angle and d-spacing is presented in Figure 4-3. At 650°C (highest temperature from Table 3-5), the sample is completely molten and all the neutrons are undergoing in-elastic diffraction with the liquid metal. This liquid diffraction results in no peaks as the molten alloy has no planes to enable diffraction on preferred planes. Under equilibrium conditions, the Mg-3 wt.% Zn alloy has a liquidus temperature of 640°C from the Mg-Zn phase diagram (Figure A-2, Appendix A.1) [1]. Thus, at 650°C there is relatively even neutron diffraction intensity at all angles as shown in Figure 4-3. At the next temperature step of 620°C, solidification has already started and the small amount of solid is able to diffract neutrons in an elastic manner to produce peaks at specific

diffraction angles (~ 50 and $\sim 57.5^\circ$). As the sample continued to cool, more solid is contributing to elastic diffraction and less liquid is available for in-elastic diffraction. The result is continued growth in the observed peaks and a decrease in the observed background (area around the peaks) with the peak widths remaining relatively constant. Alternatively, the change in liquid background intensity can be used to determine the liquid and solid fraction. However, the liquid fraction was found to be unreliable between samples.

Another observation is the increasing diffraction angle (or decreasing d-spacing) as the temperature decreases. The increase in diffraction angle with decreasing temperature was related to thermal contraction and change in composition of the Mg alloy. The shift to higher diffraction angles was observed by other researchers [306]. Identification of which planes were contributing to the diffraction pattern was conducted by noting the d-spacing of the observed peaks at 600 and 300°C. These two temperatures were chosen to represent the sample near liquidus and solidus temperatures respectively and used as reference points to examine the shift in diffraction peaks during solidification. The results are listed in Table 4-1.

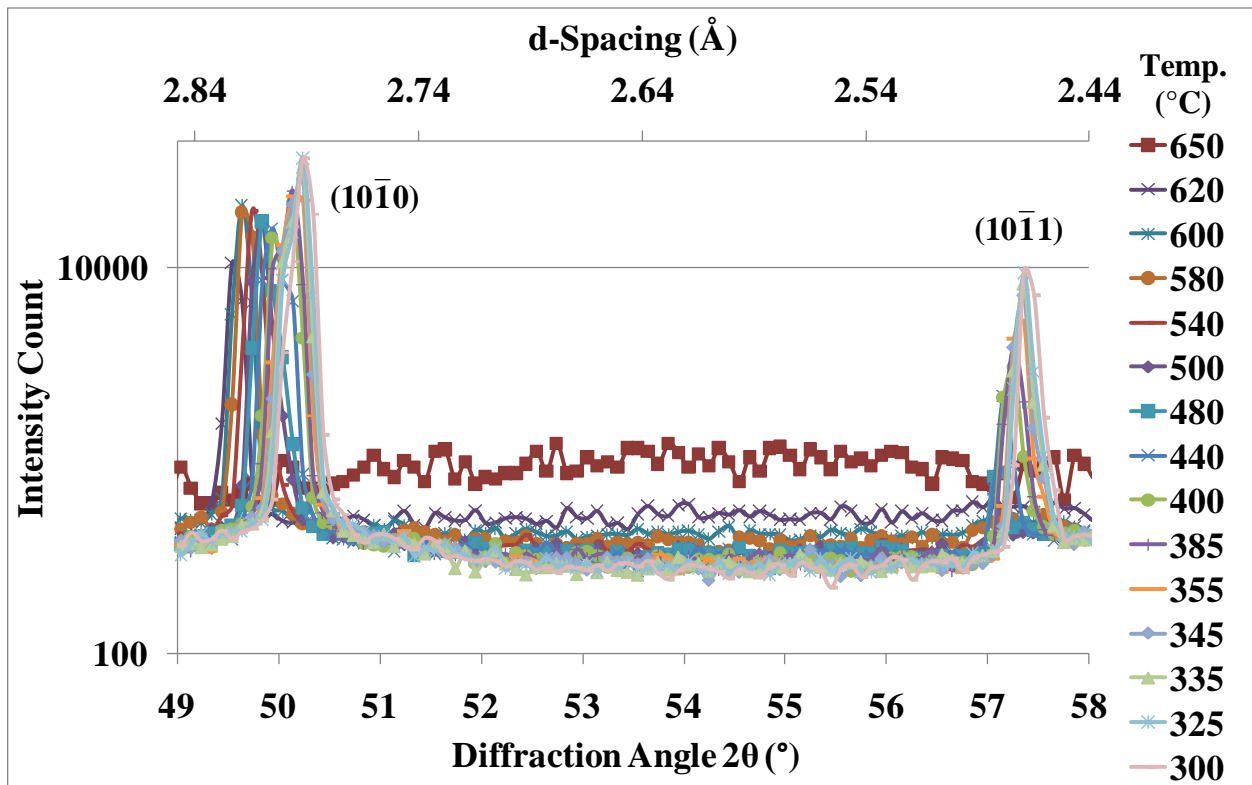


Figure 4-3: Neutron Diffraction Pattern of Mg-3 wt.% Zn Alloy at Different Temperatures (°C, Selected Isotherms Omitted for Clarity)

Table 4-1: Observed 2θ and d-spacing Values of Mg Peaks During In-situ Neutron Diffraction Experiments

	Temperature (°C)	Peak (2θ)	d-spacing (Å)
Peak 1	600	49.63	2.82
	300	50.23	2.79
Peak 2	600	57.15	2.47
	300	57.35	2.46

By using plane spacing to plane index relations, the spacing's observed can be related to specific planes of Mg using Equation 32 [311]. The results from Table 4-1 and Equation 32 with pure Mg lattice parameters of $a=0.320$ and $c=0.520$ nm (Table 2-9) indicated that peak 1 and peak 2 were $(10\bar{1}0)$ and $(10\bar{1}1)$ respectively.

$$\frac{1}{d^2} = \frac{4}{3} \left(\frac{h^2 + hk + k^2}{a^2} \right) + \frac{1}{c^2} \quad (32)$$

The (0002) plane should be located at a d-spacing of 2.60 \AA and diffraction angle of $\sim 54^\circ$ but no peak can be observed in Figure 4-3. Another observation is the neutron diffraction intensity of $(10\bar{1}1)$ is lower than that of $(10\bar{1}0)$ where in typical XRD patterns of Mg, the more packed planes (0002) and $(10\bar{1}1)$ were expected to show higher diffraction intensity than $(10\bar{1}0)$. The missing (0002) plane and irregular intensities were thought to be caused by the coarse microstructure (Figure 4-1b) of the in-situ neutron diffraction sample. The coarse grains appeared to have caused masking of some planes and highlighted others. During the neutron diffraction analysis, the solidifying grains would grow, translate and rotate within the melt as the temperature decreased. At one temperature step, a grain could be highly favourable for diffraction while at the next lower temperature step, that same grain could have shifted to a position unfavourable for diffraction reducing the detected neutron diffraction intensity. In extreme cases, when there are a few coarse grains contributing to the neutron intensity, the detected signal may become dependent on the grain size/orientation, thus detracting from accurate indication of the amount of solid phases present in the melt. With a finer grain size, the neutron diffraction would be less susceptible to this grain movement as there would be more individual grains available for the coherent diffraction.

Assuming spherical grains, an estimate of the number of grains examined by the in-situ neutron diffraction experiments can be made by using the grain size and the volume of the

sample prepared. The prepared samples measured 6.5 mm in diameter and 40 mm in length resulting in a volume of about 1300 mm³. With an average grain size of ~1540 μm, only ~700 grains are examined during the neutron experiments for the Mg-3 wt.% Zn alloy. This low number of grains examined is thought to be the reason for the rise in scatter during data collection for the Mg-3 wt.% Zn alloy. By increasing the sampling volume, adding a potent grain refiner like Zr and introducing sample oscillation during data collection an improvement in counting statistics could be realized. The alloy composition was also adjusted to represent commercial Mg alloy ZK61 with 5-6 wt.% Zn and 0.7 wt.% Zr [1]. The alloys examined were Mg-5 wt.% Zn (denoted Mg-Zn henceforth) and Mg-5 wt.% Zn-0.7 wt.% Zr (Mg-Zn-Zr denoted henceforth).

4.2 Solidification Behaviour of Mg-Zn and Mg-Zn-Zr Alloys Using In-situ Neutron Diffraction

The preliminary research examining the Mg-3 wt.% Zn alloy using in-situ neutron diffraction was unable to produce reliable data for further analysis. With further refinement of the experimental procedure by using larger sampling volumes of 10 mm in diameter (40 mm length), introducing sample oscillation of 36° and using a vibratory motor an improvement in the data collection was realized and grain refinement studies using Zr were conducted. Section 4.2 presents the results regarding the use of in-situ neutron diffraction to examine grain refinement of a Mg-Zn alloy. The microstructural, X-ray and neutron diffraction analyses were carried out after high temperature neutron diffraction experiments. These results will be presented followed by in-situ neutron diffraction results with fraction solid predictions using neutrons and FactSage™ modeling.

4.2.1 Microstructure of Mg-Zn and Mg-Zn-Zr Alloys

The microstructures of the Mg-Zn and Mg-Zn-Zr alloys were first examined to determine their grain size/morphology and observe any present intermetallics. Optical micrographs of the Mg-Zn and Mg-Zn-Zr alloys after the in-situ neutron diffraction experiments are shown in Figure 4-4a and b respectively. The Mg-Zn alloy had a coarse irregular grain structure with a grain size >1000 μm. The addition of Zr offered extreme grain refinement as the Mg-Zn-Zr alloy

had a grain size of $\sim 100 \mu\text{m}$. The grain morphology from irregular to equiaxed shape, similar to the observations of Qian and Das [165].

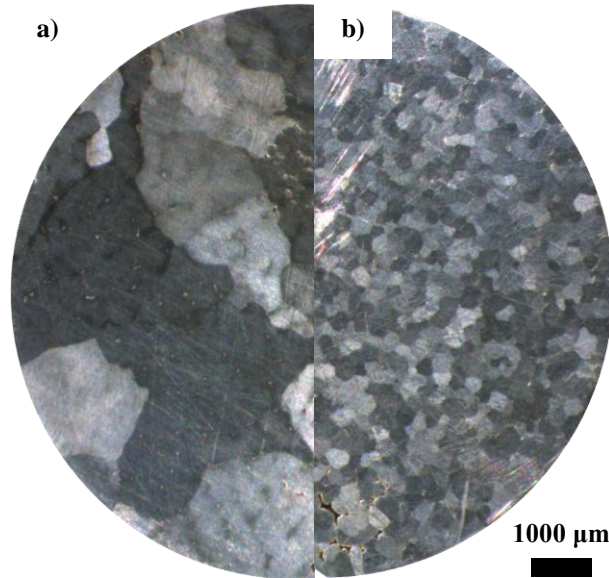


Figure 4-4: Grain Structures of a) Mg-Zn and b) Mg-Zn-Zr Alloys

Scanning electron microscopy combined with EDX spot analysis of the Mg-Zn and Mg-Zn-Zr alloys are shown in Figure 4-5a and b respectively. Other than the α -Mg matrix, the Mg-Zn alloy contained large pockets of a Mg-Zn based intermetallic phase. In addition, the Mg-Zn-Zr alloy contained a Zn-Zr intermetallic phase and Zr rich particles within the centre of grains. Previous research has shown that Zr addition provides heterogeneous nucleation sites and grain growth restriction [166-169]. Both phenomena were observed during this study as excess undissolved Zr reacted with Zn to form Zn-Zr intermetallics as observed by others [129]. The compositions of the Mg-Zn phase corresponded to MgZn while the Zn-Zr phase corresponded to Zn_2Zr , determined using the EDX spot analysis over ten particles. Further XRD analysis was conducted to identify the phases observed in Figure 4-5a and b. The XRD results also served as a comparison to the in-situ neutron diffraction results.

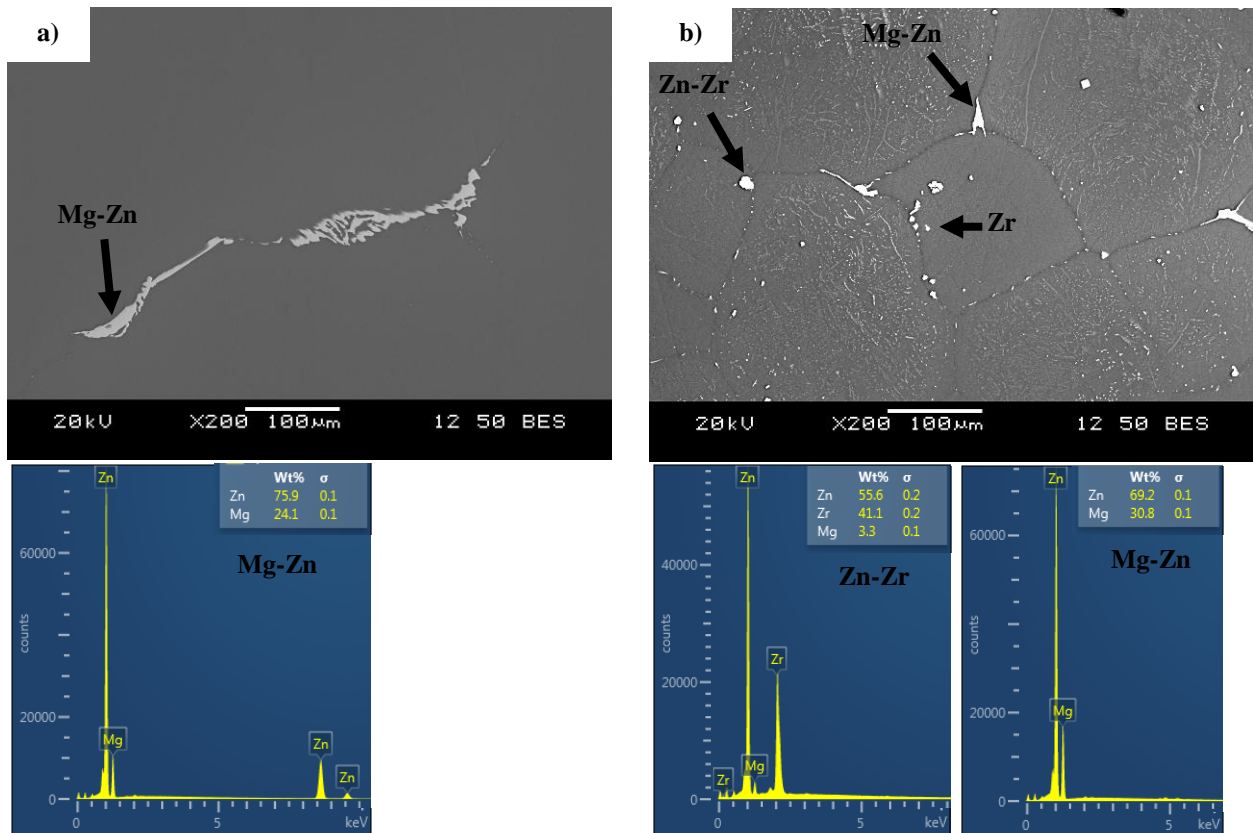


Figure 4-5: SEM Images of a) Mg-Zn and b) Mg-Zn-Zr Alloys

4.2.2 X-ray and Neutron Diffraction of Mg-Zn and Mg-Zn-Zr Alloys

The XRD plots of the alloys are presented in Figure 4-6a. From the XRD analysis, the three shown Mg peaks with increasing diffraction angle represent reflections from the $(10\bar{1}0)$, (0002) and $(10\bar{1}1)$ planes respectively. The Mg-Zn phase observed in Figure 4-5a and b was MgZn or MgZn₂ while the Zn-Zr phase in the Mg-Zn-Zr alloy was Zn₂Zr. These observed phases are similar to the ones identified by Zhang [180] who characterized MgZn₂ and Zn₂Zr and Zn₂Zr₃ intermetallics in Mg alloys with 5-6 wt.% Zn and 0.3-0.9 wt.% Zr using TEM. Comparison of the Mg-Zn and Mg-Zn-Zr alloys in Figure 4-6a shows that the Mg peaks in the Mg-Zn-Zr alloy appears at slightly lower diffraction angles than the Mg-Zn alloy and are attributed to the added Zr in solution for the former as the atomic radius of Zr is larger than that of Mg. The diffraction intensities of the planes differ between the Mg-Zn and Mg-Zn-Zr alloys. For the Mg-Zn alloy, the diffraction intensities of the $(10\bar{1}0)$, (0002) planes are ~75% less than that of the $(10\bar{1}1)$ plane while for the Mg-Zn-Zr alloy, they are ~90 and 65% smaller than the $(10\bar{1}1)$ plane

respectively. The heterogeneous nucleation promoted by Zr addition may be a source for the increased (0002) intensity but even though only 2-3% of added Zr acts as a nucleant as predicted by the interdependence theory in Mg-Gd-Y alloy [175] it still contributes 30% of the refinement with the soluble contribution accounting for 70% [166].

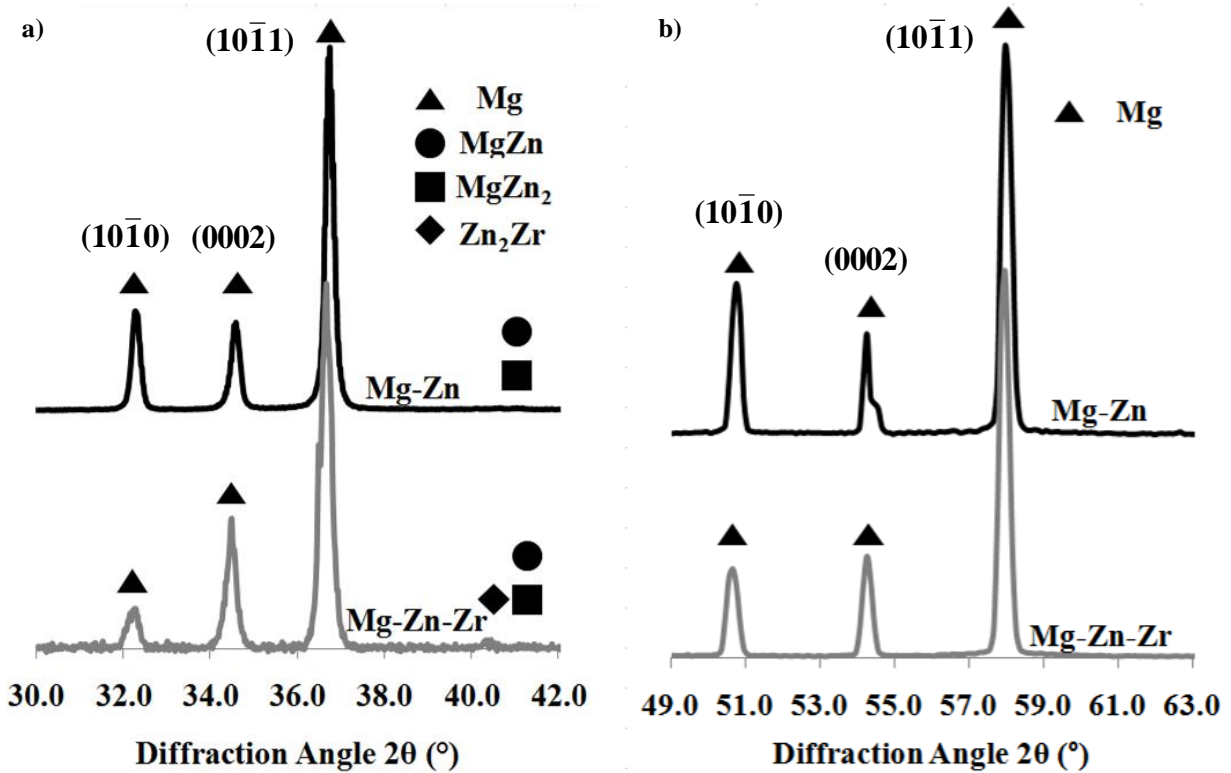


Figure 4-6: a) XRD at Room Temperature and b) In-situ Neutron Diffraction Results at 200°C of Mg-Zn and Mg-Zn-Zr Alloys

As a comparison, the in-situ neutron diffraction plot of the alloys at the lowest temperature examined (200°C) is presented in Figure 4-6b. The neutron diffraction plot in Figure 4-6b represents a snapshot of the casting and should be similar to the XRD plot in Figure 4-6a albeit different diffraction angles because of the 2.37 Å wavelength used for the neutron experiments. The in-situ neutron diffraction plot for the Mg-Zn alloy also contains all three primary Mg peaks. The (0002) peak was not observed in Section 4.1 and was attributed to the large grain size of the sample. The use of larger samples, furnace oscillation and sample agitation during solidification enabled the examination of a coarse grained alloy, which was previously not possible. The modification of the experimental procedure had a profound effect on the reliability and intensity of collected neutron data and can be utilized to examine other coarse grained materials or

samples with subtle diffraction peaks that would otherwise go unnoticed. The neutron diffraction pattern in Figure 4-6b shows that the (0002) peak is smaller than its XRD counterpart in Figure 4-6a for both Mg-Zn and Mg-Zn-Zr alloys and can be explained by the influence of temperature. At elevated temperatures, increased atomic motion gives a reduction in peak intensity for all peaks and more so for peaks at higher diffraction angles [311]. This phenomenon is also known as the Debye-Waller effect. For the Mg-Zn alloy, the $(10\bar{1}0)$, (0002) peak intensities are 61 and 74% smaller than the $(10\bar{1}1)$ peak and 77 and 74% smaller for the Mg-Zn-Zr alloy respectively. Difficulties in detecting intermetallics in Figure 4-6b could also be attributed to the increased temperature and their low weight fraction within the sample. The growth of the $(10\bar{1}0)$, (0002) and $(10\bar{1}1)$ α -Mg peaks were then examined at each temperature step to observe the influence of grain refinement on fraction solid growth.

4.2.3 In-situ Neutron Diffraction of Mg-Zn and Mg-Zn-Zr Alloys

The in-situ neutron diffraction plots of the $(10\bar{1}0)$, (0002) and $(10\bar{1}1)$ planes of the Mg-Zn and Mg-Zn-Zr alloys are shown in Figure 4-7 and Figure 4-8 respectively. At 660°C, both the Mg-Zn and Mg-Zn-Zr alloys were completely molten and all the neutrons were undergoing in-elastic diffraction with the liquid metal evenly across all angles as there were no solid planes for diffraction. Under equilibrium conditions, the Mg-5 wt.% Zn alloy has liquidus and solidus temperatures of ~635 and 420°C respectively as can be observed from the Mg-Zn phase diagram in Figure A-2 [1]. The Mg-5 wt.% Zn-0.7 wt.% Zr alloy is expected to have a similar solidus point but with a higher liquidus because of the peritectic reaction [18] at 653.56°C with 0.45 wt.% Zr [172]. For all the peaks and alloys in Figure 4-7 and Figure 4-8 at 635°C, the solid α -Mg begins to form resulting in the formation of peaks. As solidification progresses, the peak intensity continually increased as more solid was contributing to elastic diffraction while the areas around the peak representing the background continually decreased as less liquid was available for in-elastic diffraction. The peak centre also shifted to higher diffraction angles with decreasing temperature due to the thermal contraction of α -Mg and change in composition similar to observations in previous investigations utilizing in-situ neutron diffraction [306]. By tracking the growth of the α -Mg diffraction peak at every temperature step, a fraction solid plot for each plane versus temperature was produced.

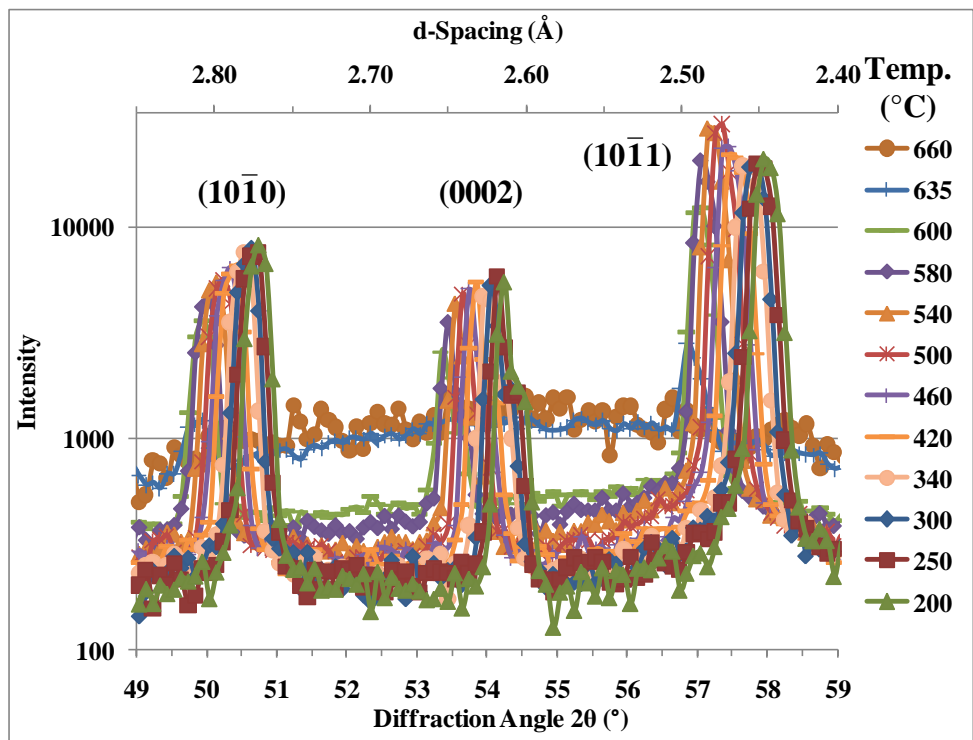


Figure 4-7: In-situ Neutron Diffraction Plot of Mg-Zn Alloy ($10\bar{1}0$), (0002) and ($10\bar{1}1$) planes ($^{\circ}\text{C}$, Selected Isotherms Omitted for Clarity)

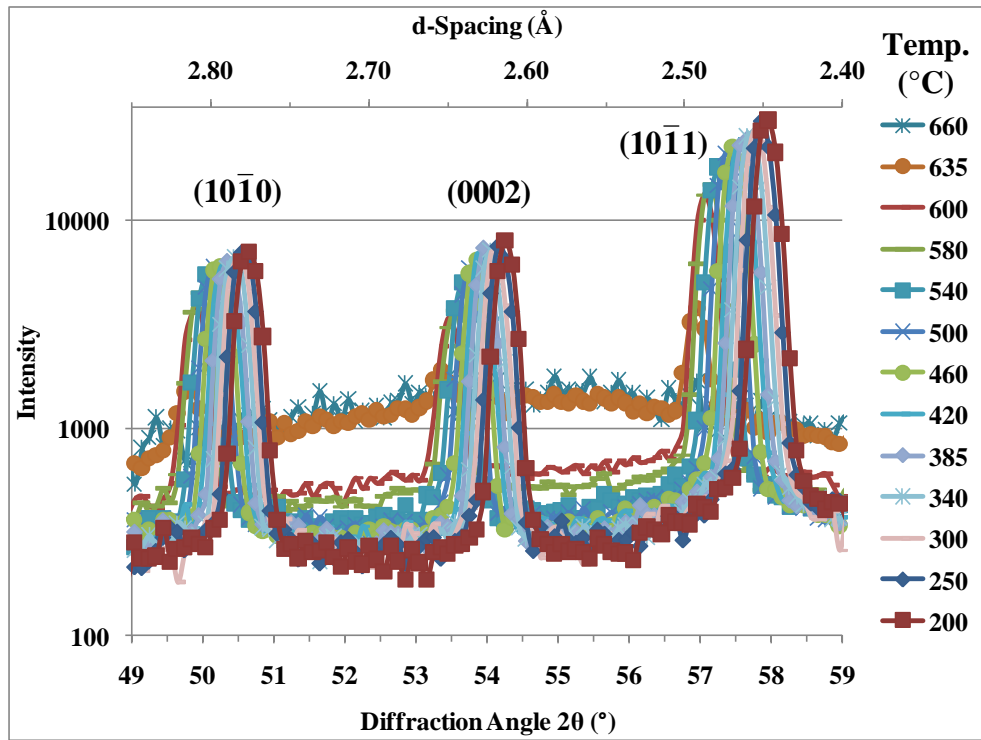


Figure 4-8: In-situ Neutron Diffraction Plot of Mg-Zn-Zr Alloy ($10\bar{1}0$), (0002) and ($10\bar{1}1$) planes ($^{\circ}\text{C}$, Selected Isotherms Omitted for Clarity)

4.2.4 Fraction Solid Determination Using In-situ Neutron Diffraction

The areas under the diffraction peaks were estimated by multiple rectangles spanning across the peak widths and used to determine the fraction solid. By subtracting the background at each temperature step a ratio between the diffraction area at each particular temperature was normalized using limits between the alloy being fully liquid (liquidus) and fully solid (solidus) with every intermediate temperature between these two extremes representing the Mg alloy undergoing solidification. At first, the solidus point was determined by examining the sum of the neutron counts in the areas around the peaks as it changed with temperature. The background consists of both the contribution from the liquid and the experimental set-up (furnace walls, crucible and sample holder). When the alloy was fully solid, no liquid was available for in-elastic diffraction and the background neutron count shown in Figure 4-7 and Figure 4-8 dropped significantly. An iterative approach first assuming the lowest temperature (200°C) representing the alloy being fully solid was used and updated until a clear increase in the deviation from the background neutron count from the selected solidus was observed. Figure 4-9a represents the deviation in background neutron count at each temperature from the count at the estimated solidus point for the α -Mg ($10\bar{1}0$) plane from the Mg-Zn-Zr alloy. It can be observed that at 400°C and below, the deviation in background neutron count fluctuates above and below zero but at temperatures above 400°C, the deviation continually increases. The estimated solidus point was then determined to lie at the average of 385-400°C. Similar curves were prepared for other planes of the Mg-Zn-Zr alloy and Mg-Zn alloys. For each plane an estimated solidus point was determined and used to build the fraction solid curve.

Using the determined solidus of the average of 385-400°C, the fraction solid of the remaining temperatures were determined by examining the ratio of their diffraction peak areas to that of the average of 385-400°C. Any temperatures above the liquidus point would contain no peak and represent zero fraction of solid. The fraction solid versus temperature of the α -Mg ($10\bar{1}0$) plane for the Mg-Zn-Zr alloy is shown in Figure 4-9b. As observed in Figure 4-9b, the fraction solid rapidly increases below the liquidus point of 635°C and continually increases with decreasing temperature. The fraction solid reaches 100% at the solidus between 385-400°C and continues to increase beyond 100% with decreasing temperature to 200°C. This phenomenon does not make physical sense as the fraction solid cannot go beyond 100% but can be explained because of the

influence of temperature on neutron diffraction results (Debye-Waller effect). At elevated temperatures, increased atomic motion gives a reduction in peak intensity [311], therefore the diffraction peaks appear to be continually growing while this is just the influence of elevated temperatures on the diffraction data. Once solidification is complete, the sample is still at an elevated temperature and thermal agitation of the sample is present. This thermal agitation shifts the peaks to lower angles and spreads the intensity profile to lower intensities and was present throughout the in-situ neutron diffraction solidification experiment. As the temperature decreased, the thermal agitation of the sample decreased resulting in increased diffraction intensity [311]. To account for this thermal agitation and correct the diffraction data obtained at all temperatures during solidification, an iterative approach was utilized. Firstly, the change in fraction solid at temperatures below the solidus temperature was fitted to a second order polynomial function. Then, the polynomial function was used to extrapolate a weighted Debye-Waller effect on the fraction solid for temperatures between solidus and liquidus. This iterative approach was repeated until no changes in fraction solid were observed.

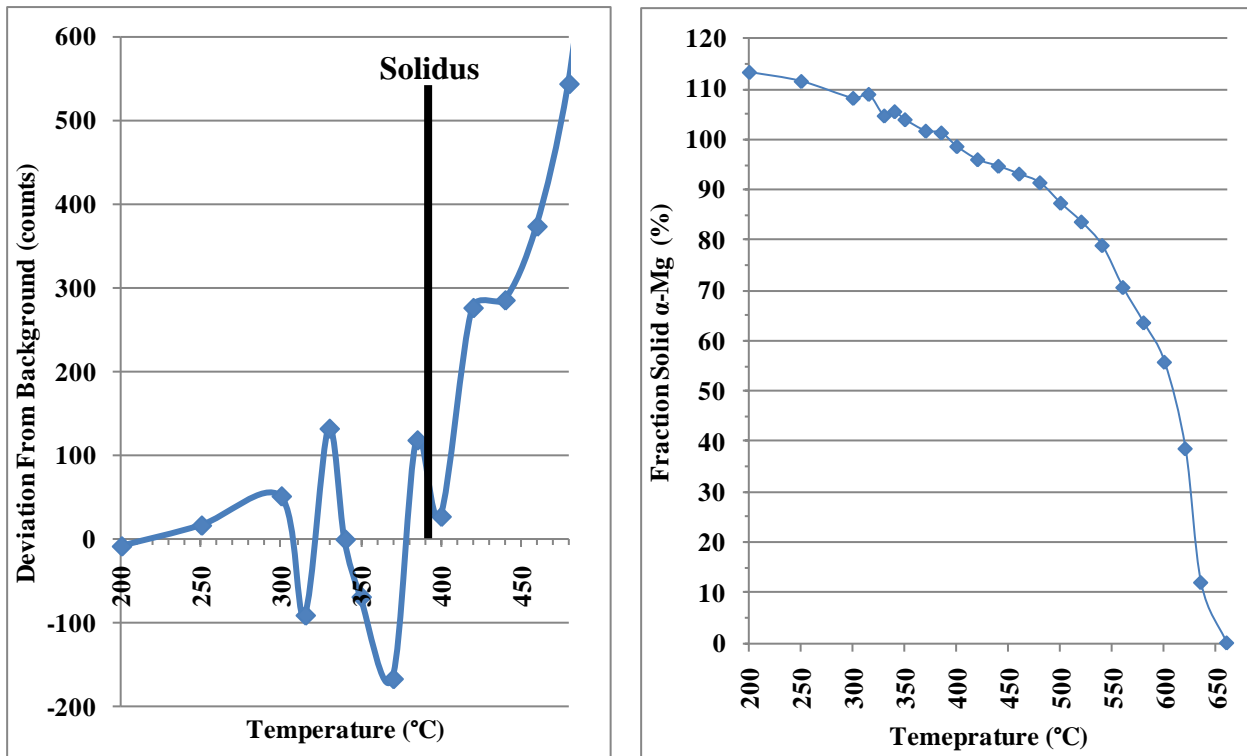


Figure 4-9: a) Deviation in Diffraction Background with Temperature for Mg-5 wt.% Zn-0.7 wt.% Zr Alloy, $(10\bar{1}0)$ Plane and b) Fraction Solid of α -Mg Versus Temperature for Mg-5 wt.% Zn-0.7 wt.% Zr Alloy, $(10\bar{1}0)$ Plane

$(10\bar{1}0)$ Plane

The adjusted fraction solid curves for the $(10\bar{1}0)$, (0002) and $(10\bar{1}1)$ planes from both Mg-Zn and Mg-Zn-Zr alloys are shown in Figure 4-10. The FactSage™ models assuming equilibrium and Scheil solidification are also presented in Figure 4-10 for comparison.

The use of in-situ neutron diffraction enabled observation of the growth of individual α -Mg planes in the Mg-Zn and Mg-Zn-Zr alloys. It is expected that the more close packed planes would tend to grow the slowest [181] and for the Mg-5 wt.% Zn alloy in Figure 4-10, the more packed (0002) and $(10\bar{1}1)$ α -Mg planes grow at a slower rate than the $(10\bar{1}0)$ plane. In addition, at 635°C, the $(10\bar{1}0)$, (0002) and $(10\bar{1}1)$ α -Mg planes had fraction solids of 17, 5 and 3% respectively. This asymmetrical growth in planes is a portion to the reasons as to why the grain structure of the Mg-Zn alloy in Figure 4-4a appears irregular as each plane was growing at a different rate. The FactSage™ simulations representing both equilibrium and Scheil solidification tend to follow the most rapidly growing $(10\bar{1}0)$ plane in Figure 4-10. The samples appear to follow equilibrium solidification as indicated by the close match in solidus temperatures. It can also be observed that the $(10\bar{1}1)$ plane has the largest fluctuations in its fraction solid curve and goes beyond 100% at 480 and 500°C. During solidification, grains would grow, translate and rotate within the melt as the temperature decreases resulting in a variation in neutron diffraction intensity. In the coarse grained Mg-Zn alloy, the detected signal may become dependent on the grain size/orientation, therefore misrepresenting the actual amount of solid phases present in the melt. With a finer grain size, the neutron diffraction intensity would be less susceptible to this grain movement as there would be more individual grains available for the coherent diffraction producing fewer fluctuations in the fraction solid during the in-situ neutron diffraction experiments.

It appears that there still may be some “coarse grain size” effect for the $(10\bar{1}1)$ plane as it had the highest intensity and was most susceptible to fluctuations in diffraction intensity. Another factor is the competition between neighbouring grains as they grow and consume each other and was a source of data fluctuations in the study by Iqbal *et al.* [303,304]. The Mg-Zn and Mg-Zn-Zr alloys examined were 10 mm in diameter and 40 mm in length. The sampling volume encompassed the entire sample equalling to 6000 grains for the Mg-Zn alloy and 6×10^6 grains for the Mg-Zn-Zr alloy, a difference of three orders of magnitude assuming spherical grains. In Section 4.1, examination of a coarse grained sample led to missing peaks and was corrected in

this study by examining larger samples and oscillating the sample during analysis. For the current study, the high number of grains within the Mg-Zn-Zr alloy as compared to the Mg-Zn alloy provided good counting statistics and offer a good representation of the solidifying sample. For the Mg-Zn-Zr alloy in Figure 4-10, the growth of the $(10\bar{1}0)$, (0002) and $(10\bar{1}1)$ planes more closely followed similar paths and grew at similar rates especially at the start of solidification where at 635°C , the $(10\bar{1}0)$, (0002) and $(10\bar{1}1)$ planes had fraction solids of 15, 12 and 14% respectively. This uniform growth of the $(10\bar{1}0)$, (0002) and $(10\bar{1}1)$ planes resulted in the equiaxed grain structure as shown in Figure 4-4b. The addition of Zr promotes nucleation on the $(10\bar{1}0)$ and (0002) planes [177] and this ensured that all the planes were growing at the same rate at temperatures near liquidus.

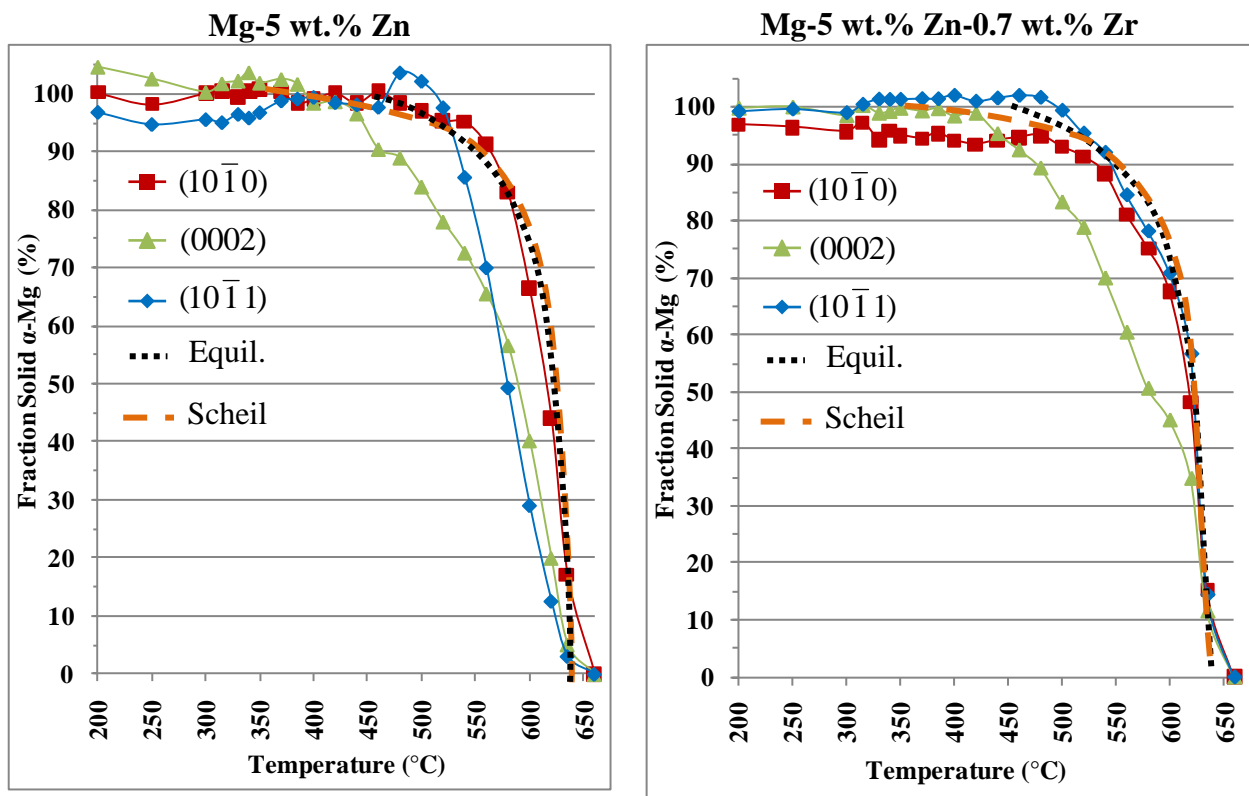


Figure 4-10: Fraction Solid of α -Mg for Mg-Zn and Mg-Zn-Zr Alloys

A graphical representation of the growth of the Mg-Zn and Mg-Zn-Zr alloys is shown in Figure 4-11. For the Mg-Zn alloy, the lack of Zr nucleants resulted in uneven growth of planes

(indicated by arrows of unequal lengths) and an irregular grain structure. For the Mg-Zn-Zr alloy, the presence of Zr nucleants and Zr segregation allowed for a more uniform growth in each plane (equal sized arrows) to form more equiaxed shaped grains.

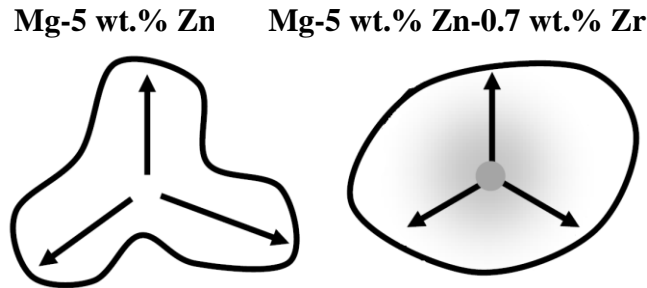


Figure 4-11: Graphical Representation of Growth of Mg-Zn and Mg-Zn-Zr Alloys

It can also be observed that the $(10\bar{1}1)$ plane grows the fastest and closely matches equilibrium solidification from the FactSage™ model. For both the Mg-Zn and Mg-Zn-Zr alloys the FactSage™ models would tend to follow the fastest growing plane but was unable to determine which plane this represented and its relation to other planes growing during solidification. The advantage of using in-situ neutron diffraction is that the fraction solid growth is separately identified for each plane and phase undergoing solidification. This offers greater insight to changes in Mg-Zn solidification with the addition of Zr not possible using traditional thermal analysis or modeling approaches. The error associated with the calculated fraction solid curves in Figure 4-11 was determined by examining the variation in background intensity at each temperature step and was typically 1-2% using a t-student test with a 95% confidence level.

4.3 Chapter Summary

In-situ neutron diffraction was successfully applied to Mg-Zn alloys and characterised nucleation and fraction solid growth of $(10\bar{1}0)$, (0002) and $(10\bar{1}1)$ planes with and without Zr addition. The fraction solid curves were consistent with FactSage™ simulations. With Zr addition, the fraction solid growth of Mg-Zn alloys was more uniform and resulted in equiaxed grains.

The use of Zr for grain refinement of Mg alloys without Al provides a basis for understanding the requirements for effective grain refinement of Mg-Al alloys. Thus far, there is

no equivalent Zr-like refiner for Mg-Al alloys, and an effective alternative needs to be developed and combined with inclusion removal techniques to enhance mechanical properties of Mg-Al alloys. The first portion of CHAPTER 5 examines melt filtration and filtration combined with Ar bubbling. The grain refining potential of C_2Cl_6 is then examined and compared to the refining potential of developed ex-situ Al-SiC and in-situ Al-C refiners. CHAPTER 5 closes with the utilization of in-situ neutron diffraction to examine solidification of Mg-Al alloys.

CHAPTER 5
INCLUSION REMOVAL AND CARBON GRAIN REFINEMENT OF MAGNESIUM
ALUMINUM ALLOYS

5.1 Melt Filtration and Ar Bubbling

There are few studies that examined the combined effects of filter location, filter pore size and Ar gas bubbling on mechanical properties, microstructure, porosity and fractography of AZ91E Mg permanent mould castings. The current research examines these parameters to develop a methodology to remove inclusions without using C_2Cl_6 .

5.1.1 Effect of Melt Filtration

Firstly, the mechanical property results of the filtration treatments will be presented followed by fractography and microstructure results.

5.1.1.1 Mechanical Properties of Filtered Castings

The YS, UTS and elongation of all the filtration conditions are shown in (Figure 5-1) with error bars representing one standard deviation. The unfiltered casting had a YS, UTS and elongation of 93.3 MPa, 153.3 MPa and 2.2% respectively. The reduction in UTS and elongation (134.5 MPa and 1.7%) with the use of a filter atop the pouring cup is related to difficulty in filling the mould and inclusions on the fracture surface that will be discussed in more detail in subsequent sections. A filter within the pouring cup and both fine and coarse filters within the well provided a uniform, more laminar flow where inclusions in the melt could be effectively filtered by the filter walls resulting in improved UTS and elongation.

The highest mechanical properties were obtained with the use of a fine filter within the well. The resulting casting had a UTS of 167 MPa and elongation of 3.1% representing an increase of 9% and 35% respectively as compared to the non filtered sample. The results in Figure 5-1 show that the YS remained relatively constant regardless of filter configuration and size while there were significant changes in UTS and to a lesser degree in elongation with the various filter configurations. Optical micrographs of the fracture surfaces were prepared to examine the number and type of inclusions in the filtered AZ91E castings.

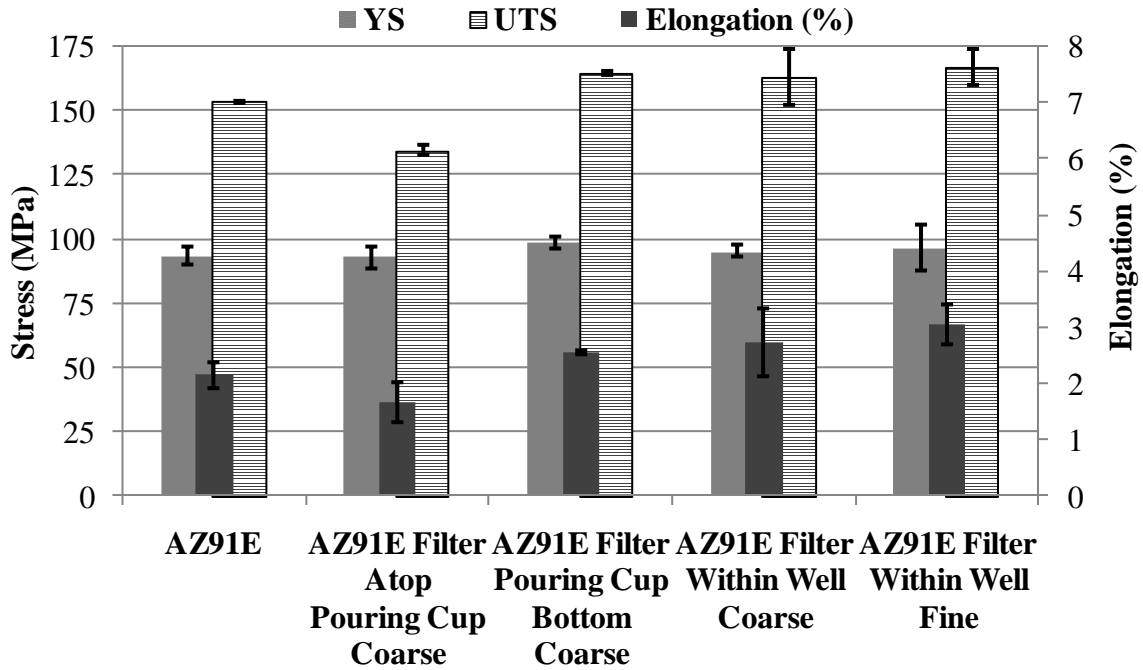


Figure 5-1: Effect of Filter Type and Location on Mechanical Properties of AZ91E with Error Bars Representing One Standard Deviation

5.1.1.2 Fractography of Filtered Castings

Optical macrographs of the fracture surfaces of all the filter castings are shown in Figure 5-2. The fracture surfaces contained dark coloured inclusions similar to the ones observed by Tardif *et al.* [80]. The study by Tardif *et al.* [80] used similar mould (450°C) and pouring (750°C) temperatures and a permanent mould resembling the one used during this study (Figure 3-2), except it contained a machined shoulder in the well of the mould for filter placement. For all cases, the inclusions in Figure 5-2 were scattered along the fracture surface and did not appear to have any preferential location. A summary of the maximum number and maximum size of inclusions observed for each casting condition is in Table 5-1.

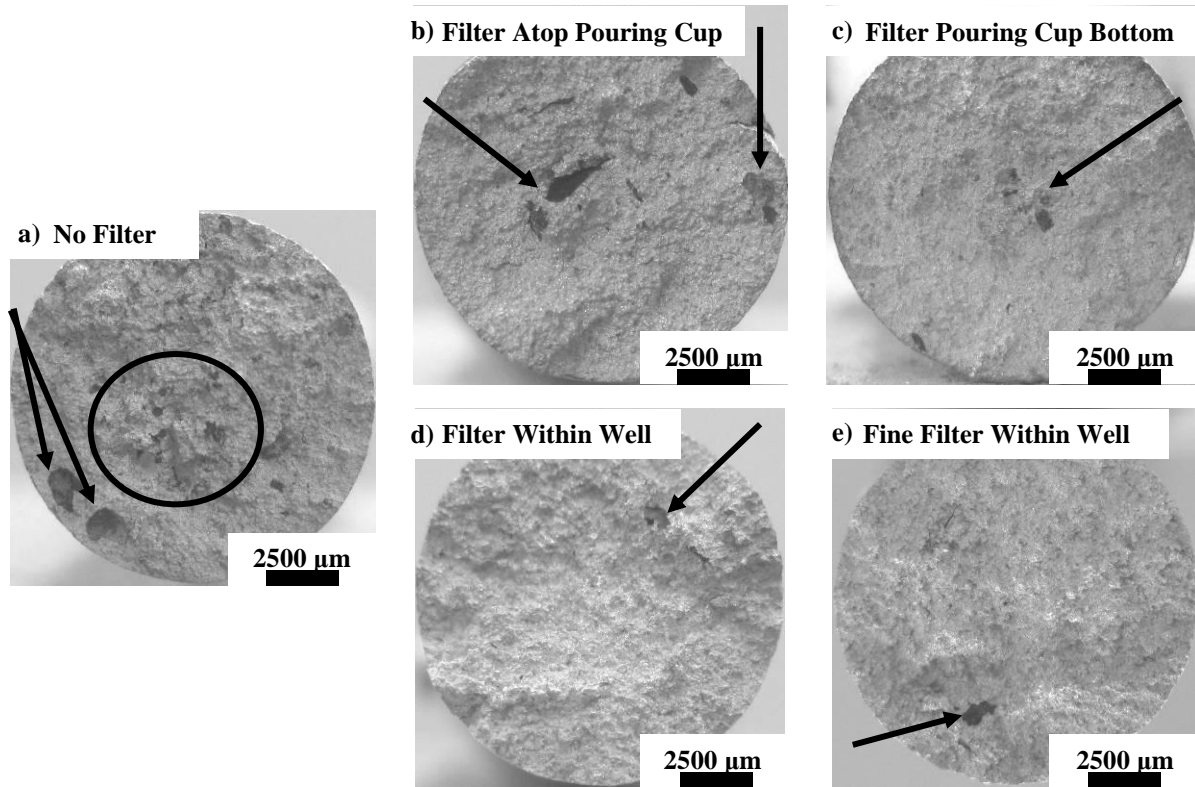


Figure 5-2: Optical Macrographs of Fracture Surfaces of Castings Produced Using Different Filter Types and Locations

Table 5-1: Summary of Inclusion Count and Inclusion Size of Fracture Surfaces Produced Using Different Filter Types and Locations

Casting Condition	Maximum Inclusion Count Across All Samples	Maximum Inclusion Size Across All Samples (μm)
No Filter	41	3800
Filter Atop Pouring Cup Coarse	19	900
Filter Pouring Cup Bottom Coarse	12	500
Filter Within Well Coarse	13	1000
Filter Within Well Fine	9	1100

Without any filter, the fracture surface (Figure 5-2a) of the base AZ91E alloy contained up to 41 inclusions with sizes up to 3800 μm . These inclusions are thought to be from the inherent reactivity of Mg during melting and its filling within the tensile mould. The untreated casting represents a base to compare the influences of filtration and Ar bubbling. The use of a filter atop the pouring cup (Figure 5-2b) also had a high number of inclusions relating to its low UTS and

elongation of 134.5 MPa and 1.7% respectively. The use of the coarse filter within the pouring cup (Figure 5-2c), coarse filter within the well (Figure 5-2d) and fine filter within the well (Figure 5-2e) were all able to significantly reduce the number of inclusions observed on the fracture surfaces. While the fine filter within the well castings still contained inclusions up to 1100 μm in size, the maximum number of inclusions observed was the lowest at nine and out of the filter configurations investigated, thought to have provided the highest cleaning performance resulting in high improvement of mechanical properties as compared to the unfiltered castings (YS: 96.5 MPa, UTS: 167 MPa and elongation: 3.1%). The results corresponded well with the mechanical properties presented earlier and the study by Le *et al.* [79] that showed improvements in UTS and elongation were related to a reduction in the number and size of inclusions observed on the sample fracture surface.

Fractography and SEM analysis of the filtered castings were carried out to examine the morphology and composition of the inclusions in Figure 5-2 with results shown in Figure 5-3. Since failure of the castings occurred at the weakest portion of the gauge section, the fracture surface gave key information on the causes of failure.

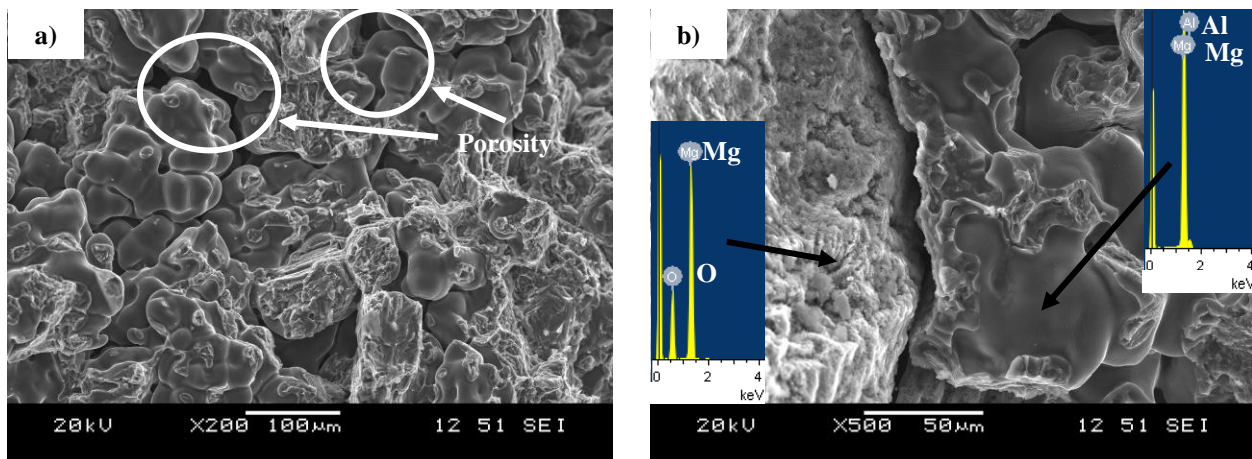


Figure 5-3: a) AZ91E Coarse Filter Atop Pouring Cup Casting Fracture Surface Showing Shrinkage Porosity in Between Dendrites and b) Crack Propagation through MgO-Mg Interface in AZ91E Coarse Filter Atop Pouring Cup Casting

For the filter atop the pouring cup castings, fractography examination revealed that the fracture tip was primarily dendritic (Figure 5-3a) showing areas of interdendritic shrinkage porosity. Often, the fracture could be seen to travel at the interface of a dark inclusion (identified as MgO) and the matrix shown in Figure 5-3b. This SEM image indicates a poor bonding

interface between the matrix and the inclusions that hindered the mechanical properties of the sample and resulted in premature fracture. A casting with a high number of inclusions would contain many sites where premature fracture could occur, compromising mechanical properties of the sample as observed in the unfiltered and filter atop the pouring cup configurations. Castings containing few, small inclusions (coarse filter pouring cup bottom, coarse filter within well and fine filter within well) would be more resistant to fracture and would have increased mechanical properties.

5.1.1.3 Effect of Melt Filtration on AZ91E Microstructure

Figure 5-4 is an SEM micrograph of the unfiltered casting showing finely dispersed Mg-Al-O based particles within the sample matrix, identified to be magnesium oxide (MgO) particles. It was expected that the O peaks would be larger but it was observed that the inclusion particles were fine and the EDX analysis could potentially overestimate the contribution from the matrix. The Al peak is from Al solute in the matrix. These fine inclusions are believed to be the same composition as the large inclusions observed on the fracture surface of the unfiltered casting in Figure 5-2a.

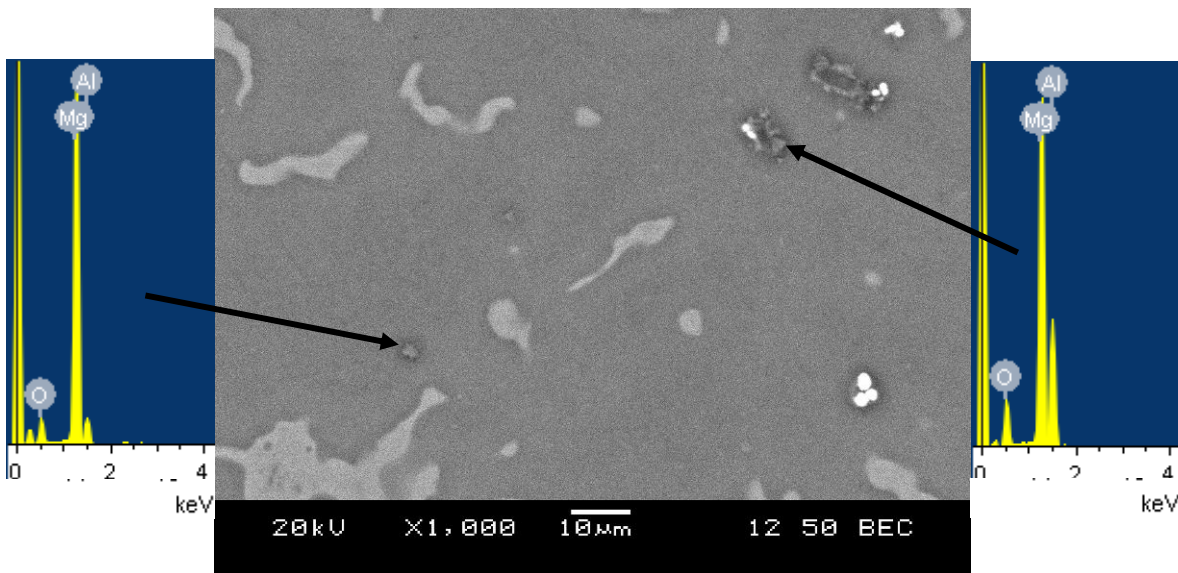


Figure 5-4: Unfiltered AZ91E Casting Showing Micron Sized MgO Particles with Corresponding EDX Analyses

The use of steel mesh filters was effective in reducing the amount of inclusions on the fracture surfaces with the fine filter in the well of the mould being most effective. Further improvements in mechanical properties (especially elongation) could be obtained using Ar bubbling.

5.1.2 Effect of Ar Bubbling and Filtration

Similar to the filtration results, the mechanical property results using Ar bubbling will be presented first followed by fractography and microstructure results.

5.1.2.1 *Mechanical Properties of Ar Bubbled and Filtration Castings*

Figure 5-5 shows the effects of Ar bubbling and Ar bubbling with a fine filter on the mechanical properties alongside the unfiltered casting and the fine filter within well casting results from Figure 5-1. With the use of Ar bubbling only, a small improvement in UTS as compared to the fine filter in well sample was obtained. When Ar bubbling was combined with a fine filter in the well, both improvements in UTS and elongation were observed as compared to the sample treated with a fine filter in well alone resulting in a YS, UTS and elongation of 93.5 MPa, 198.0 MPa and 4.9% respectively. The mechanical property results in Figure 5-1 and Figure 5-5 are very similar to the results presented in Table 2-6. With the use of a CFF, Ar bubbling or CFF+Ar bubbling there was an improvement in UTS and elongation. The highest UTS and elongation were obtained with combined use of CFF+Ar bubbling similar to this study except with the use of steel filters. After applying the Ar bubbling treatment, a black skin layer was observed on the melt surface (result of inclusions being wetted and lifted to the melt surface by the bubbling treatment) and after removal by skimming resulted in a shiny molten surface. Similar to the filter castings in Figure 5-1, the YS remained relatively constant for all casting conditions.

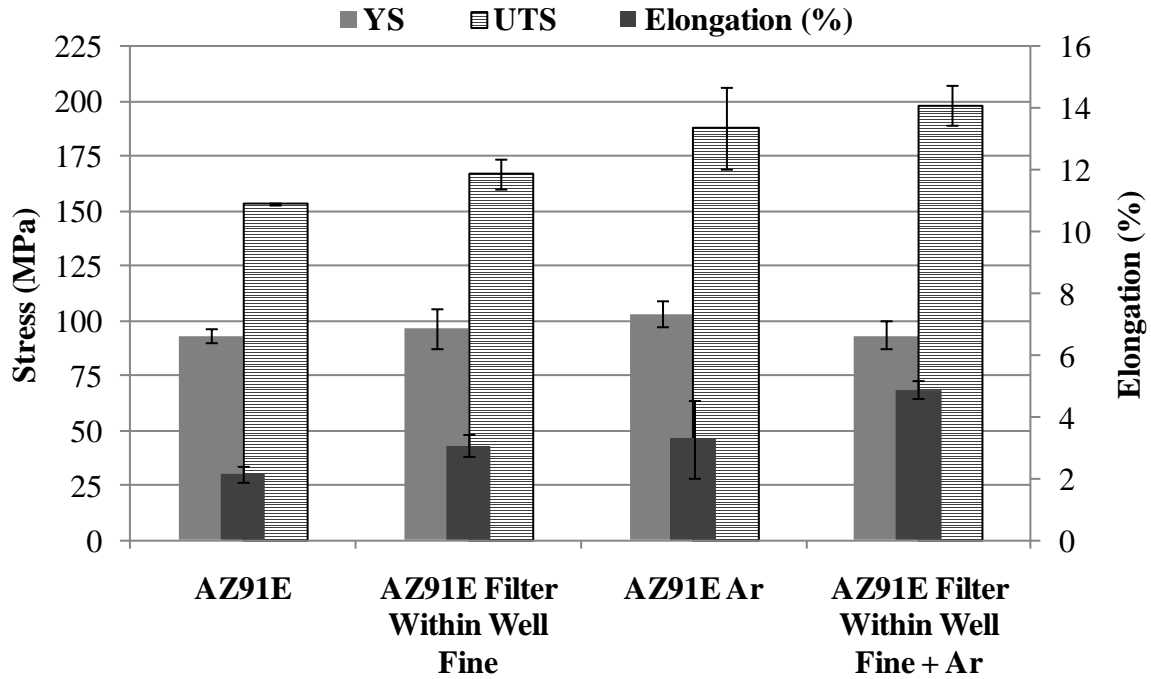


Figure 5-5: Effect of Filter, Ar Bubbling and Filter + Ar Bubbling on the Mechanical Properties of AZ91E with Error Bars Representing One Standard Deviation

5.1.2.2 Fracture Surfaces of Ar Bubbling and Filtration Castings

Examination of the casting fracture surfaces shown in Figure 5-6 showed that Ar bubbling alone was able to significantly reduce the number of inclusions observed on the fracture surface (Figure 5-6a). A summary of the maximum number and size of inclusions observed on the cross section for each casting condition are in Table 5-2. The use of Ar bubbling or Ar bubbling with a fine filter (Figure 5-6b) provided a reduction in the maximum number of inclusions across all samples (four and six inclusions respectively) as compared to the fine filtered sample (nine inclusions). The maximum inclusion size remained constant (1100-1200 μm) and was expected as the maximum inclusion size is limited by the filter openings. These results are in excellent agreement with those of Housh and Petrovich [32]. They demonstrated that filters tend to remove large inclusions ($>80 \mu\text{m}$) while gas sparging removes small inclusions ($<8 \mu\text{m}$). The Ar bubbling resulted in a scatter in observed fracture surfaces, giving rise to a large standard deviation for both tensile strength and elongation in Figure 5-5. The melts treated with Ar bubbling and a filter as shown in Figure 5-6b often contained no inclusions on the fracture surface resulting in the highest mechanical properties of all the samples examined.

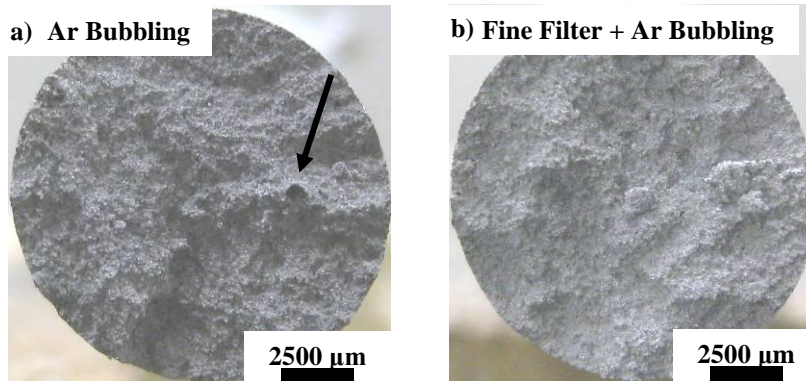


Figure 5-6: Optical Macrographs of Fracture Surfaces of Ar Bubbled and Ar Bubbling with Filtration

Table 5-2: Summary of Inclusion Count and Inclusion Size of Ar Bubbled and Ar Bubbling with Filtration

Casting Condition	Maximum Inclusion Count Across All Samples	Maximum Inclusion Size Across All Samples (μm)
No Filter	41	3800
Filter Within Well Fine	9	1100
Ar Bubbling	4	1200
Filter Within Well Fine + Ar Bubbling	6	1200

5.1.2.3 Effect of Filtration and Ar Bubbling on AZ91E Microstructure

The fine filter with Ar bubbling was examined using SEM analysis to see if fine inclusions were present within the gauge section of the samples. Similar to the unfiltered casting in Figure 5-4, the fine filter with Ar bubbling showed very fine (<15 μm) sized oxides still present within the microstructure as shown in Figure 5-7a. The fracture surface of the castings treated with fine filter with Ar bubbling shown in Figure 5-7b did not contain any observable stress concentrations unlike the filter samples in Figure 5-3. Therefore, the fine filter with Ar bubbling treatment is an effective method to remove inclusions and improve the mechanical properties of AZ91E but its effectiveness needs to be compared with that due to C₂Cl₆ addition and will be presented in Section 5.3.

Microstructural examination of a filter section enabled identification of the inclusions trapped within the filter walls. As shown in Figure 5-8, many oxide lumps and long, tangled oxide films, possibly bifilms as described by Griffiths and Lai [45] were observed, trapped near the filter wall. The results further show that filters were effective in entrapping oxides.

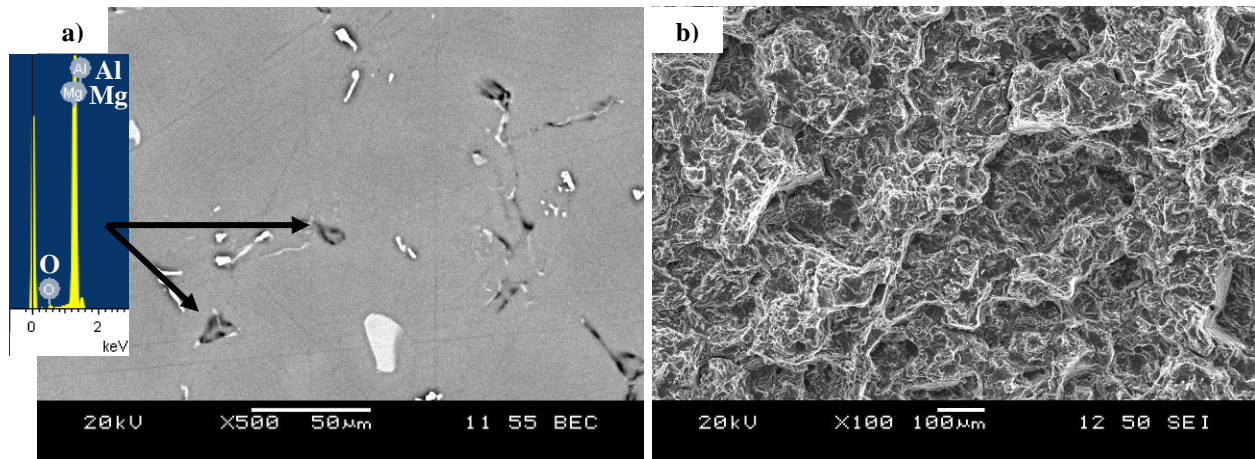


Figure 5-7: a) AZ91E Fine Filter Within Well + Ar Bubbling Casting with b) Corresponding Fracture Surface

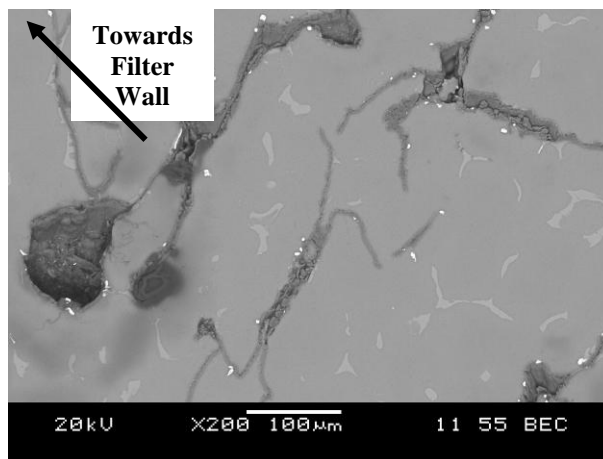


Figure 5-8: Oxide Lumps and Oxide Films Observed Near Filter Wall in Fine Filter with Ar Bubbling Casting (Arrow Indicates Direction Towards Filter Wall)

5.1.2.4 Porosity Measurements of Unfiltered, Filtered and Ar Bubbled Castings

The average porosity results with error ranges representing one standard deviation are presented in Table 5-3. For all samples, porosity was measured using Archimedes principle. For all casting conditions the average porosity was under 2.5% with the highest average porosity being 2.3% for the filter atop pouring cup sample. The low porosity values indicated that the mechanical property results obtained were influenced by inclusion content only and not to feeding or shrinkage causing excessive porosity.

For some of the filtration experiments, the filters would choke the molten metal flow and make mould filling difficult. Therefore, with a view to gaining a better understanding of the effect of filters on the filling behaviour during casting, modeling experiments were conducted to

observe the changes in fluid flow and temperature with the use of a fine filter within the well of the mould.

Table 5-3: Summary of Porosity Results for Filtered and Ar Bubbled Castings

Casting Condition	Average Porosity (%)
AZ91E	1.3 +/- 0.1
AZ91E Filter atop Pouring Cup Coarse	2.3 +/- 0.3
AZ91E Filter Pouring Cup Bottom Coarse	1.5 +/- 0.2
AZ91E Filter within Well Coarse	1.6 +/- 0.6
AZ91E Filter within Well Fine	2.0 +/- 0.2
AZ91E + Ar Bubbling	0.8 +/- 0.3
AZ91E Fine Filter within Well + Ar Bubbling	1.2 +/- 0.2

5.2 Modeling of Melt Filtration During Casting

At first, experimental thermal data of filtered and unfiltered castings were used to determine appropriate thermal constants for the model simulations. Once the proper thermal conditions were determined, comparisons of unfiltered and filtered castings were made. Further, velocity simulations to examine the influence of filtration on metal velocity are presented.

5.2.1 Thermal Analysis of Melt Filtration During Casting

The K-type thermocouples inserted into the gauge section of the mould were used to record the solidification behaviour of the castings. The SolidCast modeling software was used to replicate the solidification conditions of both the unfiltered and filtered castings so that the velocity profile of the molten metal as it passed through the filter could be examined. The unfiltered casting was utilized as a baseline to determine the optimum HTC between the molten metal and mould for the modeling experiments. The optimum HTC was then applied to the filtered casting. The selected HTC values correspond to previous research and the values recommended by the software developers.

The research by Kuo *et al.* [312] examined changes in HTC at the metal mould interface of permanent mould cast AZ91D Mg alloy with varying solid fraction. For the completely molten condition, the HTC was found to vary from 1681 to 2931 W/m²K. Similar research by Weng *et al.* [313] revealed that the HTC ranged from 2000 to 3000 W/m²K. The software developers recommended a HTC of 1135 W/m²K [314] based on previous experience in permanent mould casting. Therefore, the examined HTC values were within the range of 1135 to

3000 W/m²K. A HTC value of 2000 W/m²K resulted in very high solidification rates, and was not investigated further and the HTC examination range was then shortened from 1135 to 1500 W/m²K. The examined node sizes were 2, 1 and 0.5 mm for the unfiltered casting. Limitations of the software restricted the minimum node size to 0.5 mm. The filter dimensions were then expanded from 0.38 mm (wire diameter) to 0.5 mm and a mesh size of 1 mm instead of 0.81 mm. For the filtered castings, larger node sizes of 2 and 1 mm were not examined as they would not accurately replicate the filter dimensions. A summary of the modeling conditions investigated including node size, HTC and fill times are shown in Table 3-7. Cooling curves of the most significant modeled conditions are shown in Figure 5-9.

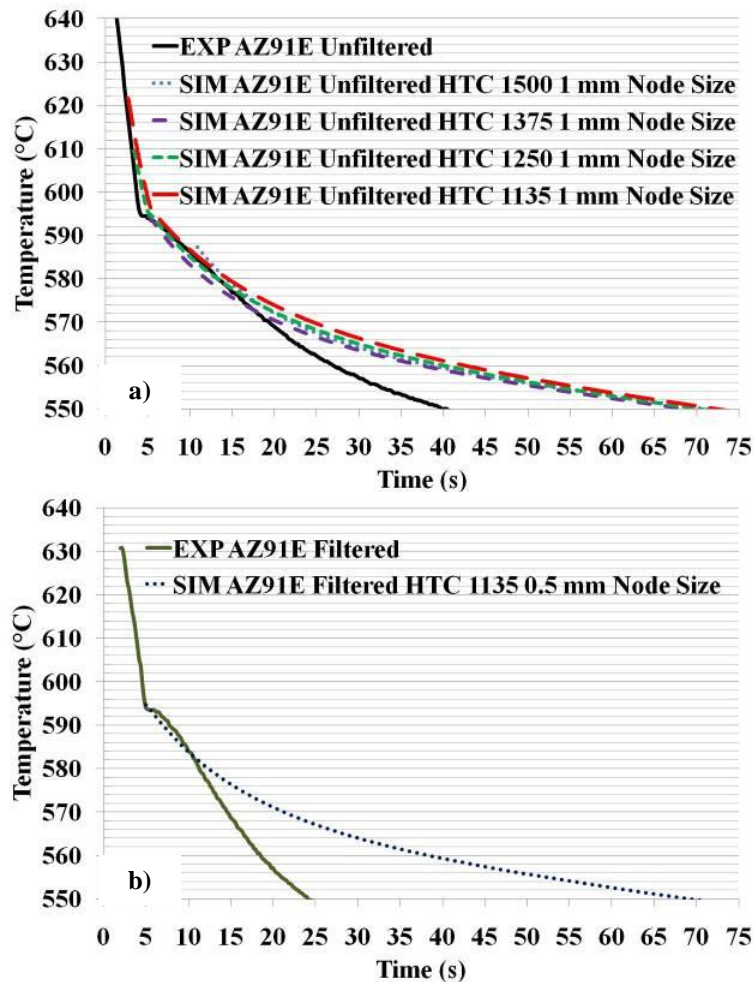


Figure 5-9: Cooling Curves of Experimental and Simulated Castings a) Effect of HTC on the Simulated Temperature Profiles (Unfiltered, 1 mm Node Size) b) EXP and SIM Curves (Filtered, 0.5 mm Node Size)

In Figure 5-9a, the unfiltered experimental (EXP) and simulated (SIM) cooling curves are shown. Comparing changing HTC with a constant 1 mm node size showed that a HTC of $1135 \text{ W/m}^2\text{K}$ was the best fit with the EXP conditions. In all cases, the temperature profiles begin to divert from the EXP curve at approximately the 20 second mark. The cause for this deviation is not immediately clear and could be attributed to the formation of an air gap between the mould and casting, changes in HTC with time, contact between the thermocouple and metal or the influence of the lubricating coating all of which are not fully represented in the SIM curves. A HTC of $1135 \text{ W/m}^2\text{K}$ was applied to the filtered casting as shown in Figure 5-9b. The node size for the SIM filtered castings was fixed to 0.5 mm to accurately replicate the filter dimensions. The presence of a filter resulted in a steeper cooling curve as a result of increased heat transfer at the metal/filter interface. The SIM cooling curve adequately captures the temperature profile from 595 to 580°C but is unable to capture temperatures above nucleation (595°C) and beyond the 15 seconds mark.

For all the SIM cooling curves, the temperature profiles tended to overshoot the EXP cooling curve at times beyond 20 seconds. For the unfiltered castings, the overshoot in temperature is approximately 10°C and is relatively small considering the temperature range examined. However, the difference between the EXP and SIM cooling curves for the filtered casting reaches a maximum of approximately 25°C which can be an issue if accurate temperature measurements are required at lower temperatures. Since this study is more concerned with grain refinement which is heavily influenced by temperature gradients near nucleation which is $\sim 595^\circ\text{C}$ for AZ91E (Figure A-3, Appendix A.1) the deviation of the SIM and EXP curves after nucleation would be of lesser concern. In addition to examining the temperature profiles of the solidifying castings, the modeling software was utilized to examine the velocity profile of the molten metal during filling.

5.2.2 Velocity Predictions of Flow During Melt Filtration

Snapshots of velocity profiles of the unfiltered and filtered castings during casting at the well of the mould (boxed area in Figure 3-3) are shown in Figure 5-10a and b respectively. In the unfiltered casting (Figure 5-10a1-a4), there was significant splashing of molten metal that could have lead to the entrapment of oxide films that would reduce mechanical properties. With the use of a filter, (Figure 5-10b1-b4) the molten metal stream was continuous and was entering the

running system at a lower velocity magnitude of ~ 0.5 m/s as compared to ~ 1 m/s in the unfiltered casting. The filter enabled a more regulated mould filling, reducing the possibility of oxide formation and entrapment, increasing the mechanical properties obtained.

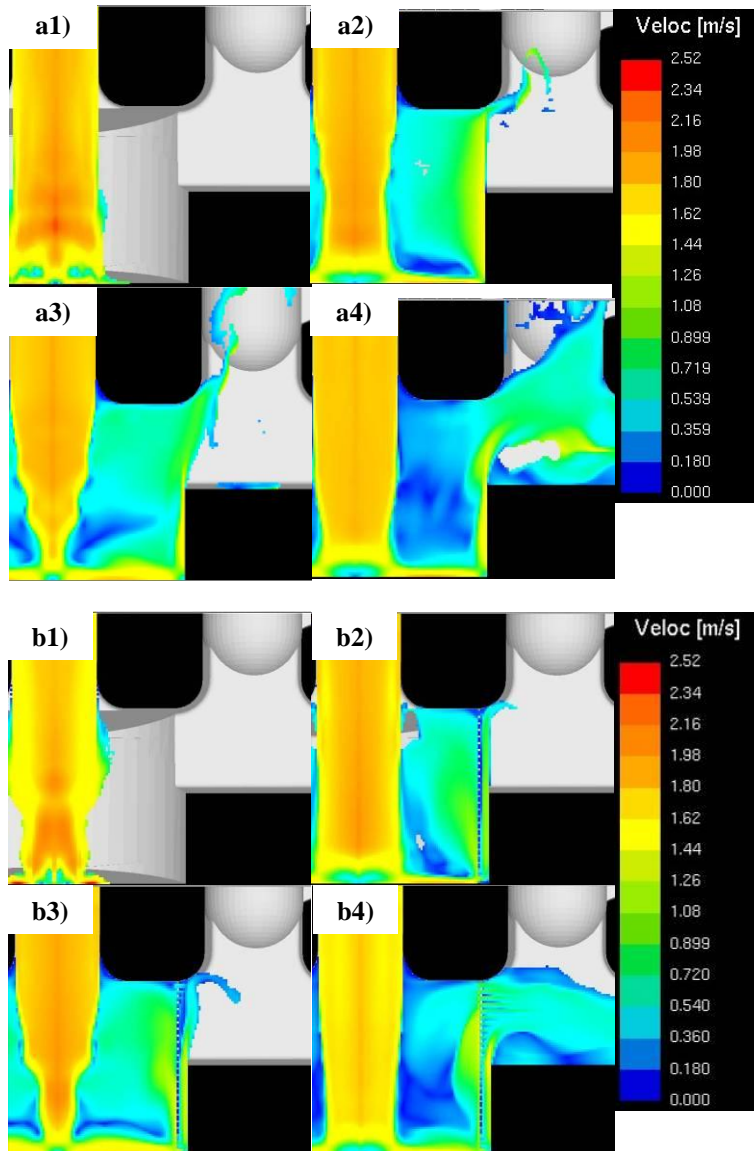


Figure 5-10: Velocity Profiles of a1) Unfiltered: 10% Filled (1.26 sec.), a2) 15% Filled (1.89 sec.), a3) 20% Filled (2.52 sec.) and a4) 25% Filled (3.15 sec.) and b1) Filtered Castings: 10% Filled (1.26 sec.), b2) 15% Filled (1.89 sec.), b3) 20% Filled (2.52 sec.) and b4) 25% Filled (3.15 sec.)

The use of filters during casting then not only entrapped oxides and prevented them from entering the casting cavity, they also enable a more uniform mould filling preventing splashing and possible oxide formation.

Melt filtration has been examined experimentally and modeled using commercial software as well as combined with Ar bubbling to produce AZ91E castings with minimal inclusions and high UTS and elongations. To further improve the mechanical properties of Mg alloys, grain refinement using C based additives should be combined with the inclusion removal techniques to produce superior Mg castings. As a baseline, the refining and inclusion removal performance of C_2Cl_6 was examined.

5.3 In-situ Grain Refinement Using C_2Cl_6

As discussed in Section 2.3.2.4, the addition of C_2Cl_6 is used to reduce hydrogen gas content and has the added advantage of grain refinement [86-90]. Reaction of C_2Cl_6 with Mg forms $MgCl_2$ flux that entraps inclusions. The addition of C_2Cl_6 is often used as a benchmark to assess the effectiveness of other grain refiners and while itself is very effective for Mg-Al alloys [224]. The influence of C_2Cl_6 addition on AZ91E Mg alloy was examined to determine its mechanism and performance as a grain refiner and inclusion remover. Subsequent sections will compare the developed Al-SiC (Section 5.6) and Al-C (Section 5.7) grain refiners against C_2Cl_6 . The previous section determined that the use of a fine filter within the well combined with Ar bubbling was the most effective for increasing mechanical properties and will be referred to as “filter + Ar bubbling” hereafter.

5.3.1 Effect of C_2Cl_6 Addition on Grain Size of AZ91E

Increasing concentrations (0.25, 0.50 and 0.75 wt.%) of C_2Cl_6 was added to AZ91E and its refining effect was observed. Optical micrographs of the grain structures of the C_2Cl_6 treated AZ91E Mg alloy are shown in Figure 5-11. The grain structure of a AZ91E + filter + Ar bubbling casting free of C_2Cl_6 addition is also shown in Figure 5-11e for comparison. For all the casting conditions the Mg grains were equiaxed in shape.

There was a decrease in grain size with the addition of C_2Cl_6 or with Ar bubbling. The grain sizes of the C_2Cl_6 treated castings and filter + Ar bubbling casting with error bars representing one standard deviation are shown in Figure 5-12. The AZ91E alloy had an average grain size of 95 μm . With the addition of 0.25 wt.% C_2Cl_6 , the average grain size reduced by 20% to 75 μm . The addition of 0.50 or 0.75 wt.% C_2Cl_6 resulted in similar grain size reductions to the 0.25 wt.% C_2Cl_6 alloy of 73 and 78 μm respectively. Considering the error bars, increasing C_2Cl_6

concentration did not have a significant effect on average grain size. The use of filter + Ar bubbling reduced the grain size of AZ91E to an average of 73 μm providing similar results to the addition of C_2Cl_6 . The mechanisms of grain refinement were explained by examination of the as-cast microstructures.

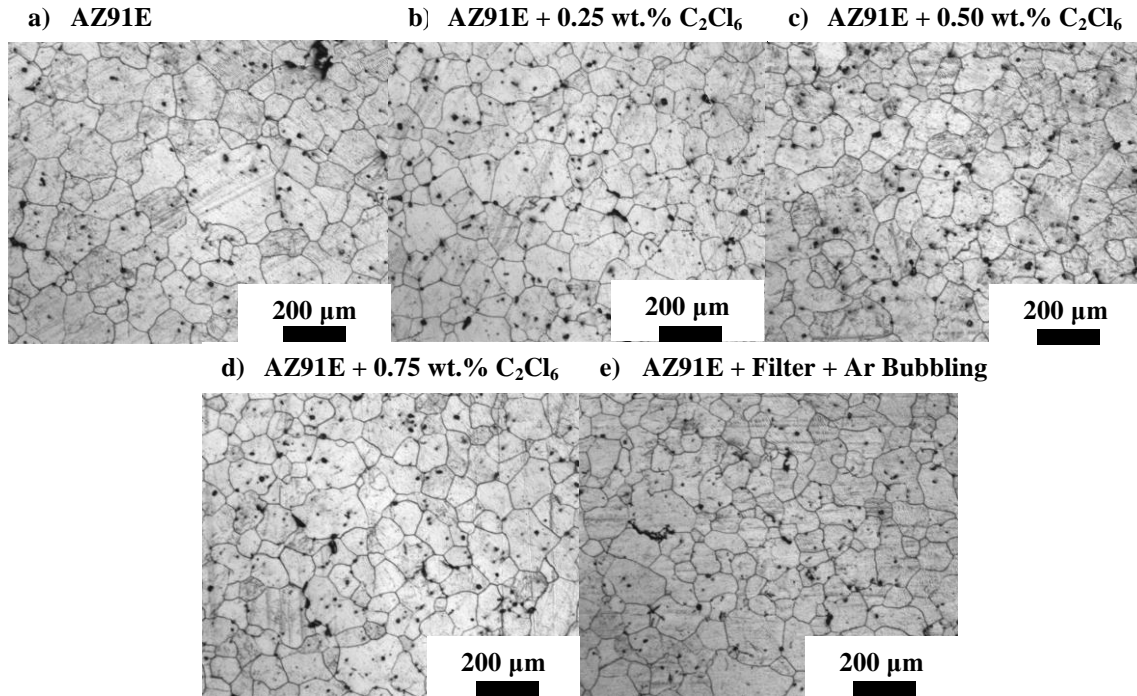


Figure 5-11: Grain Structures of AZ91E with C_2Cl_6 Addition and Filter + Ar Bubbling

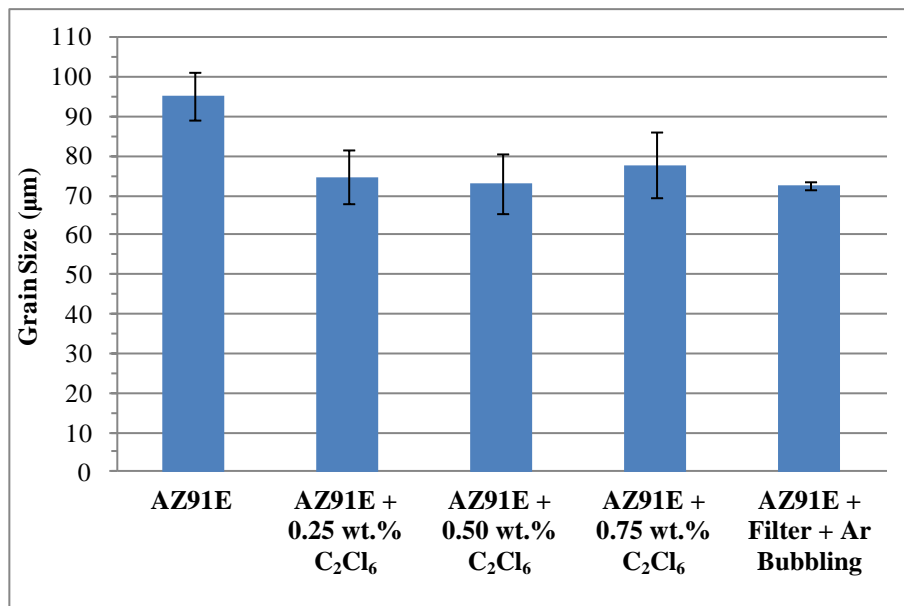


Figure 5-12: Effect of C_2Cl_6 Addition on Grain Size of AZ91E with Error Bars Representing One Standard Deviation

5.3.2 Effect of C_2Cl_6 Addition on Microstructure of AZ91E

Scanning electron microscopy was utilized to determine the mechanism for grain refinement using C_2Cl_6 . The microstructure of AZ91E without any C_2Cl_6 addition is shown in Figure 5-13.

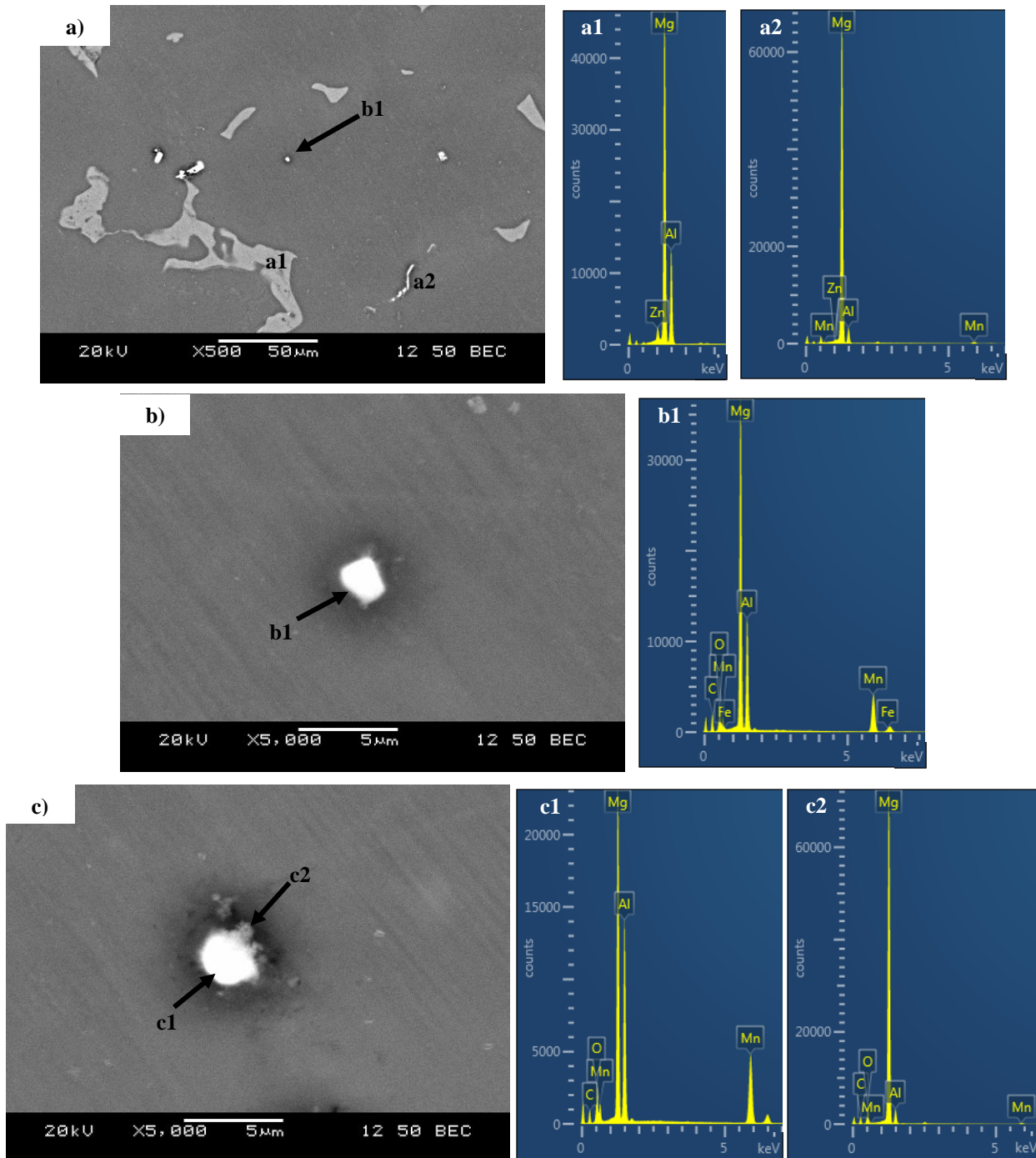


Figure 5-13: SEM Image of AZ91E Alloy Showing a) General Microstructure, b) Mn-Al Based Particle Indicated by the Arrow and c) Another Mn-Al Particle

The microstructure in Figure 5-13a contained the Mg matrix, a Mg-Al (from EDX spectrum a1) based intermetallic likely the eutectic $Mg_{17}Al_{12}$ and a Mn-Al (from EDX spectrum a2) intermetallic, possibly Al_8Mn_5 with a string like shape. There were also blocky Mn-Al particles observed within the centre of grains and along grain boundaries. One such blocky Mn-Al particle observed within the centre of grain indicated by the arrow in Figure 5-13a (b1) was examined further (Figure 5-13b). An EDX spectrum (b1) shows that the particle produces signals that are Mg-Al-Mn-Fe-C-O based. This observed spectrum could be the simultaneous effects of the bright area, areas around the particle and matrix behind the particle making identification difficult. A similar particle is shown in Figure 5-13c with a Mn-Al rich (EDX spectrum c1) core surrounded by a Mg-Al-C-O rich area (EDX spectrum c2). For the base alloy in Figure 5-13, the blocky Mn-Al particles are likely Al_8Mn_5 and these blocky particles ($\sim 2-3 \mu m$ is size) acted as nucleants (from Equation 11, r^* is $\sim 1.3 \mu m$ [16] or d^* is $\sim 2.6 \mu m$) when no other more suitable phases were present.

With the addition of either 0.25 or 0.75 wt.% C_2Cl_6 , only blocky ($\sim 2-3 \mu m$) Mn-Al particles were observed as shown in Figure 5-14a (indicated by arrow) and Figure 5-14b (highlighted particle in Figure 5-14a) from a AZ91E + 0.25 wt.% C_2Cl_6 alloy. These Mn-Al particles were often observed within the centre of grains and had concentrations of C and O on their surfaces as shown in Figure 5-14c, to a much larger extent than the base alloy in Figure 5-13b and c. Many Al-Mg-C-O or Al-C-O particles alongside Al-Mn particles after adding C_2Cl_6 were observed similar to others observations [220]. The mechanism for C_2Cl_6 grain refinement was described in Section 2.11.4.1. Namely, the addition of C_2Cl_6 is expected to result in decomposition to C and Cl_2 according to Equation 19 and C is postulated to form Al_4C_3 according to Equation 20 and act as a nucleant. Another mechanism is that the added C promotes the transition of Al_8Mn_5 from rod-like to more globular particles [87,115]. A similar mechanism is a duplex nucleation phenomena where C inoculation promotes Al_4C_3 formation and Al and Mn segregate to the carbide surface [205] or put another way, globular $Al_8(Mn,Fe)_5$ form on the surface of the carbide particles which in turn nucleates Mg [87,115]. The observations from Figure 5-14 indicate that the addition of C_2Cl_6 promoted duplex nucleation where a Al-Mg-C-O or Al-C-O phase nucleated blocky Al_8Mn_5 and Mg. The Al-Mg-C-O or Al-C-O phase associated with C inoculation is often described to be Al_4C_3 [2,5,9,17,18,26,87,89,92,95,107,121,135,136,138,140,200-202,216,224,230-236,242,244,249,250,253] but recent research point towards

Al_2MgC_2 [132,139,232,248,251]. The observations from Figure 5-14c show indications of the remnants of these phases by the presence of C and O around the blocky Al_8Mn_5 as they are highly hydrophobic as described by Equation 17 and observations in literature [132,139,248]. With the addition of C_2Cl_6 , the phases are able to activate duplex nucleation (they were appropriately sized according to Equation 11, r^* is $\sim 1.3 \mu\text{m}$ [16] or d^* is $\sim 2.6 \mu\text{m}$) and promote grain refinement. The vigorous bubbling with C_2Cl_6 addition [221] would also aid in distribution of C. In the base alloy, grain refinement is limited because of the lack of bubbling and having only appropriately sized blocky Al_8Mn_5 offering potential nucleating sites.

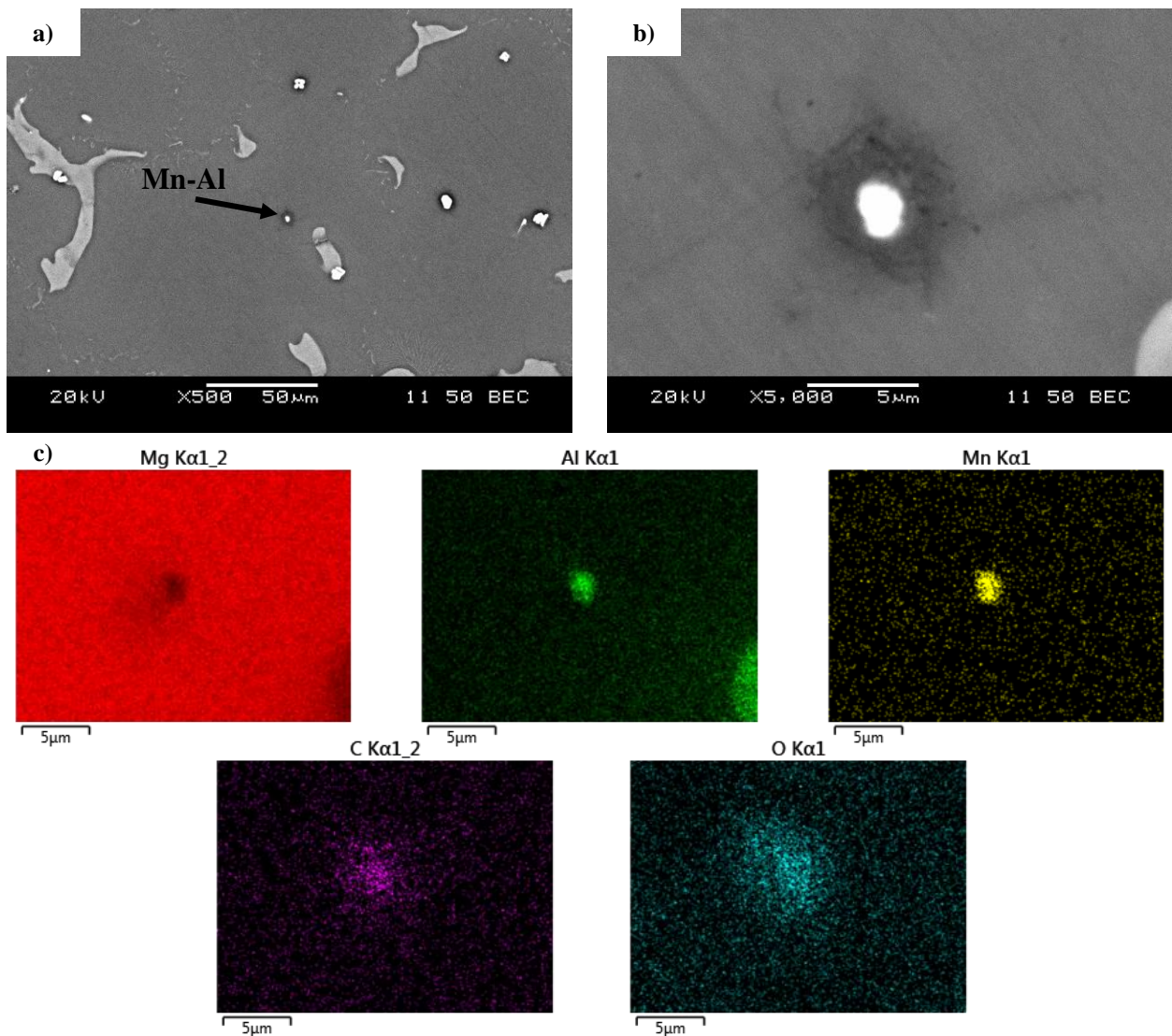


Figure 5-14: SEM Image of AZ91E + 0.25 wt.% C_2Cl_6 Alloy Showing a) General Microstructure, b) Mn-Al Based Intermetallic Indicated by Arrow and c) EDX Element Maps of Mn-Al Intermetallic in b)

The AZ91E + filter + Ar bubbling casting showed a microstructure similar to that of the base AZ91E alloy with both stringy and blocky Mn-Al particles (Figure 5-13a). Only blocky Mn-Al based particles were observed within the centre of grains like the one indicated by the arrow in Figure 5-15a and shown at a higher magnification in Figure 5-15b.

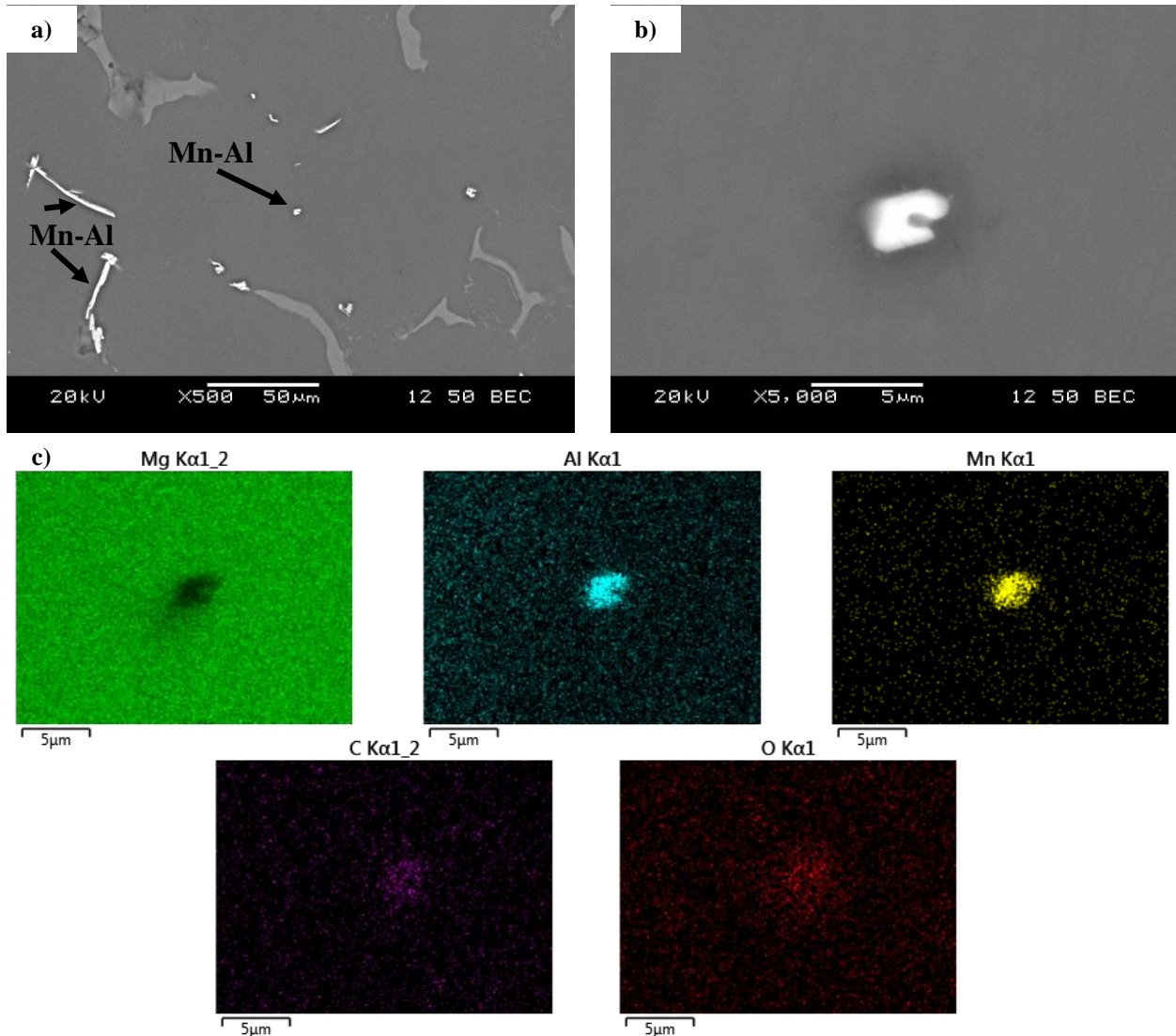


Figure 5-15: SEM Image of AZ91E + Filter + Ar Bubbling Showing a) General Microstructure, b) Mn-Al Based Intermetallic Indicated by Arrow and c) EDX Element Maps of Mn-Al Intermetallic in b)

The element map of the particle shows concentrations of mainly Mn, Al and some C and O. The C and O concentrations are limited to the particle itself and do not extend out to its periphery like the particle in Figure 5-14b and c. Similar to the base AZ91E alloy, the appropriately sized

(d^* is $\sim 2.6 \mu\text{m}$) Mn-Al particles were the most suitable nucleating sites available. It is interesting to note that the AZ91E + filter + Ar bubbling casting had an average grain size similar to that of the AZ91E + 0.25 wt.% C_2Cl_6 alloy (Figure 5-12). Bubbling Ar is thought to give no significant grain refinement [196] or possibly increase grain size because of its potential to remove $\text{Al}_8(\text{Mn,Fe})_5$ particles [87]. The ability of Ar bubbling to remove fine particles is highly dependent on processing parameters and in this study, the filter + Ar bubbling parameters were unable to remove oxide particles smaller than $15 \mu\text{m}$ (Figure 5-7). The grain refinement with Ar bubbling is then considered to result from the mixing action of the bubbling process promoting a more uniform distribution of Mn-Al particles within the melt so that they could readily act as nucleants. The Ar bubbling could also aid in cleaning of the Mn-Al particle surfaces promoting grain refinement.

As mentioned in Section 2.3.2.4, C_2Cl_6 provides melt cleaning by formation of MgCl_2 (common flux component), which can remove inclusions but may become an inclusion itself. The influence of C_2Cl_6 on inclusion removal was examined by examining the fracture surfaces of the produced castings and compared against the filter + Ar bubbling approaches.

5.3.3 Fractography of C_2Cl_6 -Treated AZ91E

Optical macrographs of the fracture surfaces of the C_2Cl_6 and filter + Ar bubbling treated castings are shown in Figure 5-16. The inclusion types looked similar to the inclusions observed in Figure 5-2 and Figure 5-6. Similarly, the untreated AZ91E alloy (a) and AZ91E + 0.25 wt.% C_2Cl_6 (b) castings had large inclusions on their fracture surfaces. It was only with the addition of 0.50 or 0.75 wt.% C_2Cl_6 did the castings have very few inclusions or were completely inclusion free (c and d respectively). The use of a filter + Ar bubbling (e) was just as effective as higher (0.50 and 0.75 wt.%) additions of C_2Cl_6 in removing inclusions. The tensile samples preferentially fractured near stress risers such as inclusions and their influence on the mechanical property results will be discussed further in Section 5.3.5.

Inclusions on the fracture surfaces were also examined using SEM to determine their composition and morphology. Differences in the inclusions observed in the C_2Cl_6 and filter + Ar bubbling treated castings were also noted. Figure 5-17 shows SEM images of the tensile fracture surfaces of AZ91E, AZ91E + 0.75 wt.% C_2Cl_6 and AZ91E + filter + Ar bubbling castings. In Figure 5-17a, the AZ91E alloy showed the presence of a Mg-O-Al-S (a1) phase. This phase

could likely be the traces of a Mg-O based oxide with Mg-S (from the SF₆ cover gas) that could have acted as a stress riser and reduced mechanical properties. An EDX spectrum analysis was also taken near the oxide to ensure the detected O peak was not due to oxidation of the sample surface during preparation or handling. The spectrum (a2) shows the presence of Mg, Al and Zn elements and no traces of O indicating that the detected O peaks originate from the inclusion.

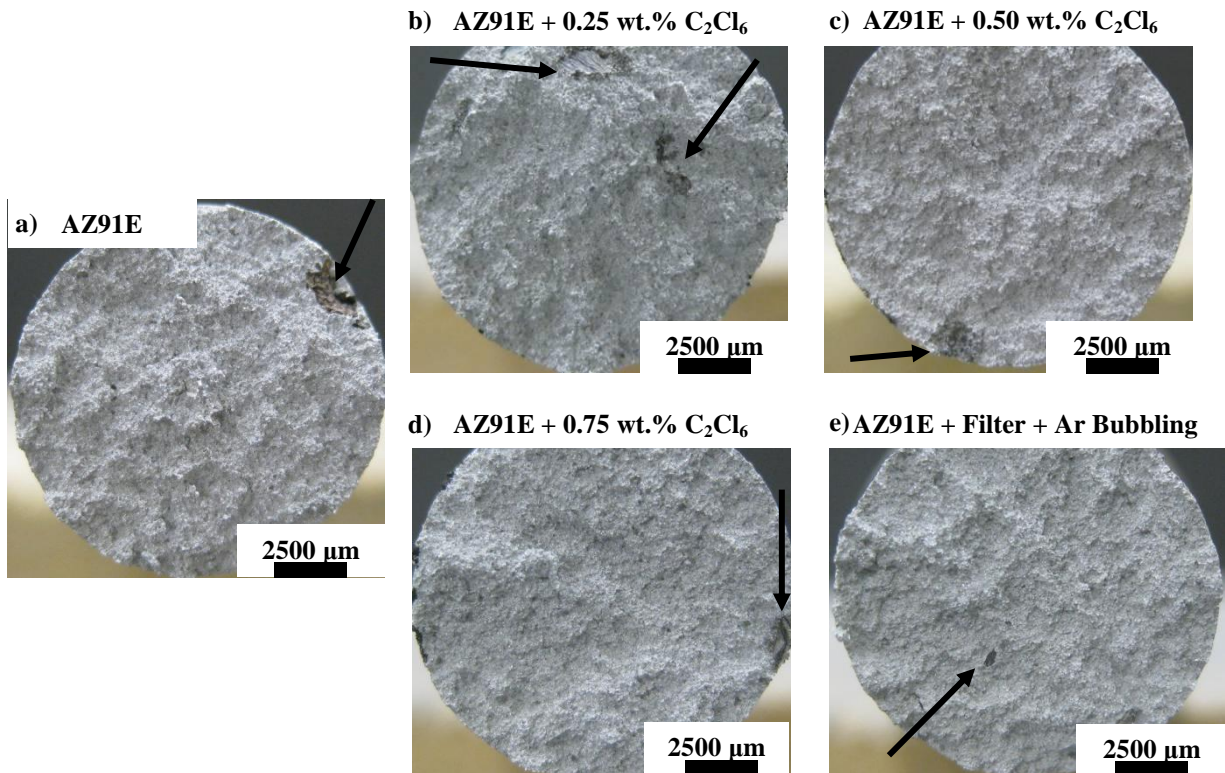


Figure 5-16: Optical Macrographs of Fracture Surfaces of AZ91E, AZ91E + C₂Cl₆ and AZ91E + Filter + Ar Bubbling

Figure 5-17b is an SEM image of AZ91E + 0.75 wt.% C₂Cl₆ which tended to be nearly inclusion free. The fracture surface contains some dimple like features indicating a more ductile type fracture behaviour. In addition, an EDX spectrum of the fracture surface indicates a presence of Mg, Al and Zn without any significant concentrations of O. Figure 5-17c showed the presence of an inclusion film observed on the fracture surface of a AZ91E + filter + Ar bubbling casting. An EDX spectrum (c1) of the film revealed the presence of Mg, Al, Zn and O. The presence of Mg and O is thought to be from the oxide film itself while Al and Zn are thought to be contributions from the matrix underneath the oxide film. A gap (~10 μm) could be observed

between the inclusion film and Mg alloy similar to what was observed in Figure 5-3c. This gap suggests lack of bond between the inclusion and the alloy matrix promoting fracture reducing mechanical properties. In addition to the presence of inclusions, high porosity could deteriorate mechanical properties and was examined.

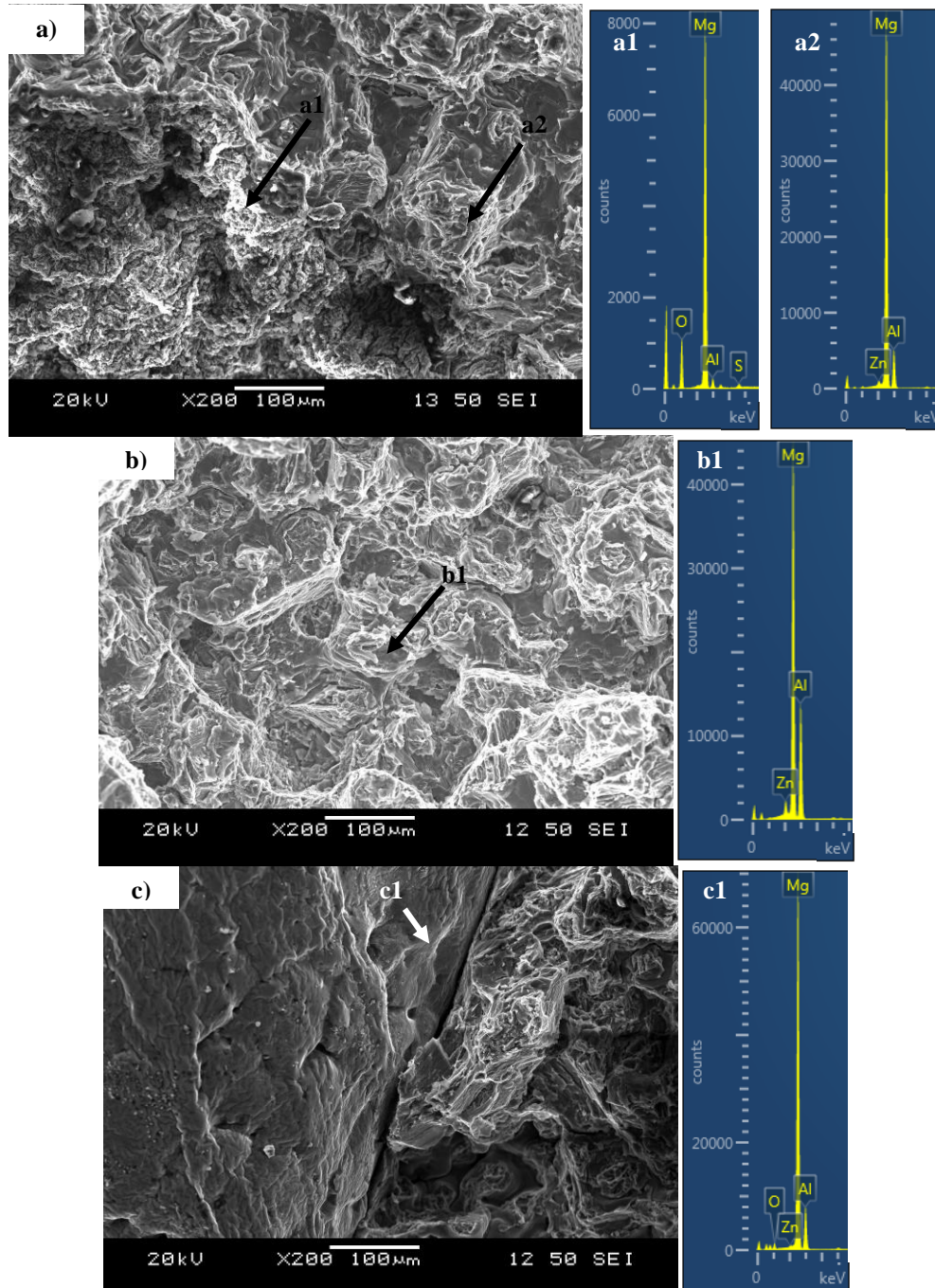


Figure 5-17: Fracture Surfaces of a) AZ91E, b) AZ91E + 0.75 wt.% C₂Cl₆ and c) AZ91E + Filter + Ar
Bubbling

5.3.4 Porosity of C₂Cl₆-Treated AZ91E

Table 5-4 contains the average porosity results with error ranges representing one standard deviation. Porosity was measured using Archimedes principle. For all the conditions examined, the porosity tended to be very low (close to 1%). The obtained porosity values are equal to or lower than that of the filtration results in Table 5-3. The increased mould temperature between the inclusion removal (475°C) and C₂Cl₆ (540°C) experiments offered reduced cooling rates and porosity. The use of a filter + Ar bubbling also resulted in a porosity of 0.9%, equal to that of 0.75 wt.% C₂Cl₆ addition indicating that a filter + Ar bubbling was not detrimental to casting filling. The increased mould temperatures and utilization of a filter increased castability of the alloy aiding to isolate the influences of inclusions and grain refinement. With such high integrity castings (low porosity), the mechanical properties obtained were influenced by inclusion content and grain size only and not to feeding or shrinkage.

Table 5-4: Summary of Porosity Results for C₂Cl₆ Refined AZ91E

Casting Condition	Average Porosity (%)
AZ91E	0.7 +/- 0.2
AZ91E + 0.25 wt.% C₂Cl₆	0.8 +/- 0.4
AZ91E + 0.50 wt.% C₂Cl₆	1.3 +/- 0.1
AZ91E + 0.75 wt.% C₂Cl₆	0.9 +/- 0.1
AZ91E + Filter + Ar Bubbling	0.9 +/- 0.3

5.3.5 Effect of C₂Cl₆ Addition on Mechanical Properties of AZ91E

Previous grain refinement studies focused on the grain size reductions with specific additions to result in higher mechanical properties, such as YS based on the Hall-Petch relation (Equation 4). Instead of focusing only on grain size reductions, this research aimed to present mechanical properties, namely the YS, UTS and elongation as C₂Cl₆ is also used to improve melt cleanliness. It would be inappropriate to investigate only grain size reductions because inclusions contribute to mechanical properties and the developments from this dissertation aim to cover all the beneficial aspects (grain refinement and melt cleaning) of C₂Cl₆ while minimizing negative impact on environment (harmful fumes). Figure 5-18 is a graph of the average mechanical properties (YS, UTS and elongation) of AZ91E + C₂Cl₆ and AZ91E + filter + Ar bubbling castings with error bars representing one standard deviation.

The AZ91E castings had average YS, UTS and elongation of 84.9 MPa, 164.7 MPa and 3.3% respectively. The highest average YS was 100.3 MPa, using 0.25 wt.% C_2Cl_6 . Additions of 0.50 and 0.75 wt.% C_2Cl_6 provided similar YS of 97.9 and 95.9 MPa respectively. However, AZ91E + 0.75 wt.% C_2Cl_6 provided an elongation of 5.2% which was higher than the AZ91E + 0.25 wt.% C_2Cl_6 alloy at 3.9%. Addition of 0.25 wt.% C_2Cl_6 was best suited for maximum YS while 0.75 wt.% C_2Cl_6 provided the highest elongation. All the C_2Cl_6 treated castings had similar average UTS of ~190 MPa.

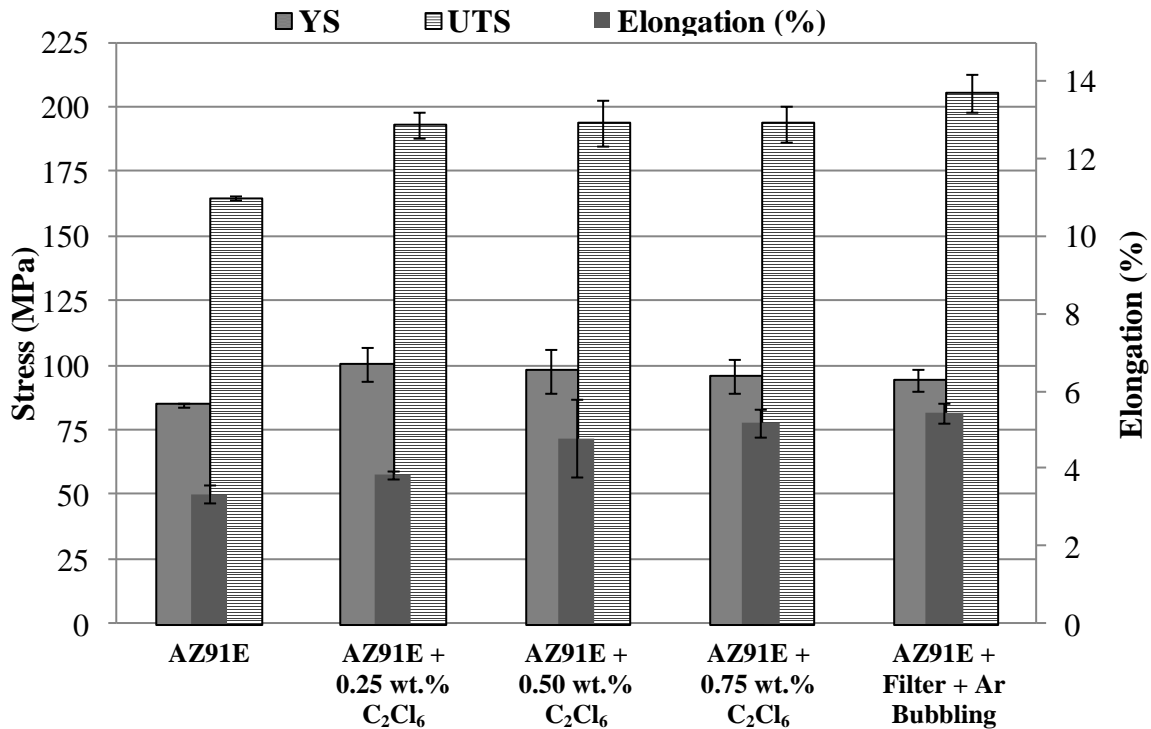


Figure 5-18: Effect of C_2Cl_6 Addition on Mechanical Properties of AZ91E with Error Bars Representing One Standard Deviation

The mechanical properties obtained are a result of a combination of factors including grain size, intermetallic morphology, porosity and inclusion contents. The porosity was near 1% for all the casting conditions and is thought to play a minor and consistent role in influencing mechanical properties. While YS is dependent on grain size [112,113] (Equation 4), UTS and elongation were highly influenced by inclusion contents. The AZ91E + 0.25 wt.% C_2Cl_6 alloy had a fine grain size (Figure 5-12) but often contained inclusions. It was only when 0.75 wt.% C_2Cl_6 was added was there a large reduction in inclusions observed (Figure 5-16d).

The transformation of stringy Mn-Al particles could have also aided in improvement of elongations. AZ91E + 0.75 wt.% C_2Cl_6 would be well suited for applications requiring lower YS but higher UTS and elongation such as extrusion or sheet forming to provide a wide working envelope for deformation. AZ91E + 0.25 wt.% C_2Cl_6 offered the highest average YS but had a lower elongation than AZ91E + 0.75 wt.% C_2Cl_6 (3.9% as compared to 5.2%) and would be better suited for applications where no additional forming was required. The mechanical properties of the AZ91E + filter + Ar bubbling casting are also shown in Figure 5-18. The AZ91E + filter + Ar bubbling casting had average YS, UTS and elongation of 94.1 MPa, 205.3 MPa and 5.4% respectively. The UTS and elongation was higher than that of the C_2Cl_6 treated castings but with lower YS even though it had similar grain sizes. It is thought that the presence of stringy Mn-Al particles in the AZ91E + filter + Ar bubbling castings reduced the YS mitigating the effects of grain refinement. The obtained results are similar to a previous study comparing 0.06, 0.3 and 0.9 wt.% C_2Cl_6 additions to AZ91E as shown in Figure 2-6 [217]. For that study, the highest YS, UTS and elongation were observed using 0.3 wt.% C_2Cl_6 while additions of 0.9 wt.% were similar to the base alloy. The results in Figure 2-6 also show that the Ar rotary degasser was ineffective in increasing UTS and elongation but slightly increased YS. It was unclear as to why the 0.9 wt.% C_2Cl_6 additions did not improve UTS and elongation resulting in properties similar to the base alloy. The grain size, microstructure and fractography results indicate that although increasing C_2Cl_6 concentrations offered enhanced melt cleaning reducing inclusion contents, lower concentrations were better suited for grain refinement but offer little in terms of inclusion removal. A similar over grain refining effect using C inoculation has been observed by others [89,201,205], indicating an optimum addition level for a particular set of casting parameters (composition, pouring temperature, addition temperature). The amount of inclusions observed on the fracture surfaces correlate with the UTS and elongation results in Figure 5-18. With fewer inclusions observed on the fracture surface, the castings tended to have higher UTS and elongation. The 0.75 wt.% C_2Cl_6 and filter + Ar bubbling treated castings had the fewest inclusions on their fracture surfaces and also had the highest UTS and elongation's of nearly 200 MPa and 5% respectively.

Instead of using C_2Cl_6 and deciding between high YS and some inclusions and lower YS with no inclusions, it would be advantageous to utilize a filter plus Ar bubbling to offer inclusion removal while a separate C refiner could be used to provide grain refinement and high YS. The

addition of C₂Cl₆ was used as a baseline for comparison against the prepared Al-SiC and Al-C grain refiners. As stated in Table 2-25, the addition of carbonaceous compounds are advantageous as they are very effective and are easily wetted by the Mg alloy therefore an Al-SiC or Al-C alternative should also be easily wetted while not have any environmentally unfriendly by-products. Sections 5.4, 5.5 and 5.6 present results from wettability experiments to determine compositions with low contact angles between Al and SiC. The subsequent prepared Al-SiC grain refiner was examined when added to an AZ91E Mg alloy.

5.4 Wettability of Al-Si-Mg Alloys on SiC

The wettability experiments were conducted to determine what Al-Si-Mg composition was best suited to wet SiC particles. The composition that provided good wetting with SiC was then used to prepare the Al-SiC grain refiners. The degree of wettability was quantified by using contact angle measurements described in Section 3.2.5.3.

5.4.1 Compositions of Prepared Wettability Alloys

The composition of the prepared wettability alloys was conducted using an optical emission spectrometer and are summarized in Table 5-5. Except for some Si losses, the obtained compositions were close to the target compositions for the Al-Si and Al-Si-Mg alloys.

Table 5-5: Composition of Prepared Wettability Alloys

Target Composition (wt.%)	Average Composition Obtained (wt.%)
Al-Si Alloys	
Al-2Si	Al-2.02Si
Al-4Si	Al-5.63Si
Al-6Si	Al-5.96Si
Al-8Si	Al-7.06Si
Al-10Si	Al-8.78Si
Al-Si-Mg Alloys	
Al-10Si-0.25Mg	Al-10.41Si-0.29Mg
Al-10Si-0.50Mg	Al-9.76Si-0.55Mg
Al-10Si-0.75Mg	Al-9.85Si-0.68Mg
Al-10Si-1.00Mg	Al-9.36Si-1.10Mg
Al-10Si-1.25Mg	Al-8.71Si-1.22Mg

5.4.2 Contact Angle Measurements

Contact angle measurements were made on pure Al, Al-Si alloys and Al-Si-Mg alloys and their results will be presented in that order. Images of the liquid droplets during a contact angle measurement are shown in Figure 5-19.

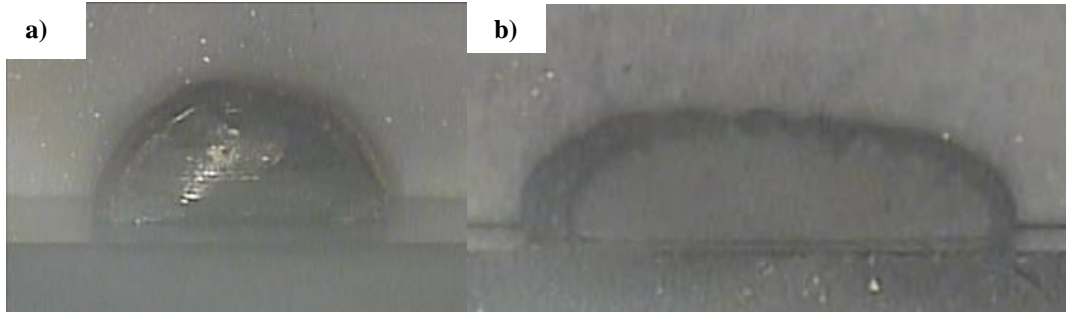


Figure 5-19: Images of a) Pure Al and b) Al-10 wt.% Si-1.25 wt.% Mg Both at 800°C

5.4.2.1 *Pure Al*

Figure 5-20a and b show the average contact angle measurements for pure Al and Al-Si alloys over 60 minutes at 800 and 900°C respectively. The contact angles remained relatively constant during the entire wettability experiment. For pure Al at 800°C (Figure 5-20a) the average contact angle was found to be approximately 100° (error bars represent one standard deviation and generally follow typical contact angle errors of +/- 3° [290]). The results for pure Al coincide well with the results of Laurent *et al.* [284]. For their study, the contact angle between pure Al and SiC at melting was 160° but quickly decreased to 110° within 10 minutes upon further heating to 800°C. Following this initial rapid decrease, the contact angle decreased very slowly until the sample was heated to 900°C after 60 minutes [284]. The absence of the quick drop in contact angle from melting to 800°C in the current study was attributed to the continuous heating of the samples from room temperature to 800°C without a pause. In addition, the sudden drop in contact angle observed by Laurent *et al.* [284] was credited to dissolution of the oxide layer surrounding Al. Therefore, “true” contact between SiC and Al was not achieved until the sample reached 800°C where the respective contact angle was 110°. With the addition of Si to Al, there was a decrease in observed contact angle.

5.4.2.2 Al-Si Alloys

With the addition of Si, the average contact angle decreased to the range of 75-85°. This indicated that the addition of Si resulted in a small decrease in contact angle that promoted a transition from a non-wetting ($>90^\circ$) to wetting ($<90^\circ$) regime [315]. The differences in contact angle between additions of 2, 4, 6, 8 and 10 wt.% Si were difficult to confirm because of the overlapping standard deviations. However, lower average contact angles with increasing Si (down to 75-80° using 10 wt.% Si) concentrations were observed.

In Figure 5-20b, the average contact angle of pure Al at 900°C was approximately 80°. Similar to the results at 800°C, increasing concentrations of Si slightly decreased the contact angle. With Si additions of 8 and 10 wt.%, the average contact angles fell between 70-75°. Considering the contact angle measurements carried out at 800 and 900°C, the addition of Si appeared to decrease contact angle, however the differences in contact angle were more pronounced at 800 than at 900°C. Also, higher temperatures tend to reduce the contact angle as observed by others [291]. The smallest contact angles were observed with Al-10 wt.% Si alloy. Previous studies [286,287] have demonstrated that Mg addition to Al had the highest tendency of reducing contact angle out of Mg, Si and Cu additions and so Mg addition was investigated for further reductions in contact angle (and improved wettability [315]). The wettability of Al alloys with simultaneous additions of Si and low Mg (<1.5 wt.%) has not been investigated in detail, and will be explored in the next section.

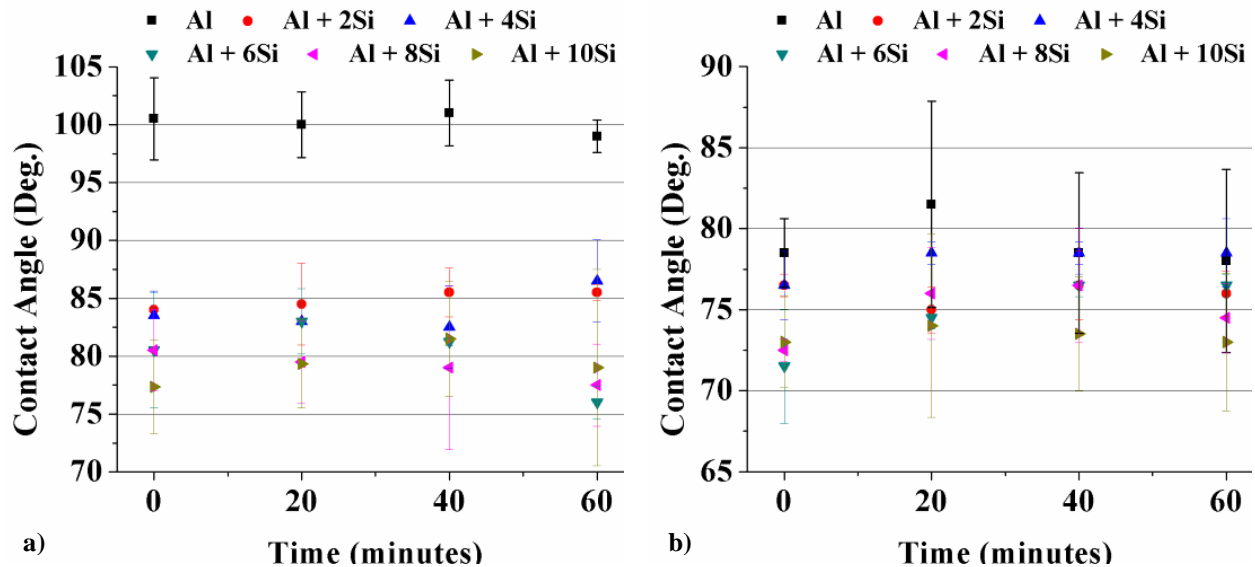


Figure 5-20: Variation in Contact Angle for Al and Al + x wt.% Si Alloys with Time at a) 800°C and b) 900°C with Error Bars Representing One Standard Deviation

5.4.2.3 *Al-Si-Mg Alloys*

Additions of 0 to 1.25 wt.% Mg, in 0.25 wt.% increments were made to Al-10 wt.% Si (lowest contact angle, denoted Al-Si henceforth) and were examined in the same manner as the Al alloys previously. Figure 5-21a and b show the resulting average contact angle measurements for pure Al and Al-Si-Mg alloys over 60 minutes at 800 and 900°C respectively. Pure Al and Al-Si from Figure 5-20a and b are included for comparison. At 800°C (Figure 5-21a), all additions of Mg showed an initial decrease in contact angle from 75-80° for Al-Si to 70-75° at time zero and a further reduction in contact angle to 65-70° in the first 20 minutes. The contact angle remained constant for the remaining 40 minutes. The addition of Mg introduced a changing contact angle over time that was not observed with the addition of Si only, indicating that within the first 20 minutes, a time dependant interfacial reaction was occurring. Similar to the addition of Si, the variation in average contact angle between incremental Mg addition levels (e.g. 0 to 0.25 wt.%) was small, but overall trends indicated that higher addition levels tend to decrease the contact angle (65° using 1.25 wt.% Mg after 60 minutes). At 900°C (Figure 5-21b), a similar changing contact angle over time was observed from zero to 20 minutes followed by a constant contact angle up to 60 minutes. The average contact angle for Al-Si was 70-75° throughout the entire 60 minutes, but for alloys containing Mg, the contact angle changed from 75-80° at time zero and settled at 67-75° from 20 minutes onwards. Surprisingly, the contact angles at 900°C were slightly higher than those measured from the samples tested at 800°C despite a lower surface tension at despite 900°C [293]. The temperature increase from 800 to 900°C appeared to have no additional benefit to Al-Si-Mg alloys. The reason for this poor improvement in wettability with Mg at 900°C is related to an interfacial reaction that was observed when the microstructure of the wettability samples was examined.

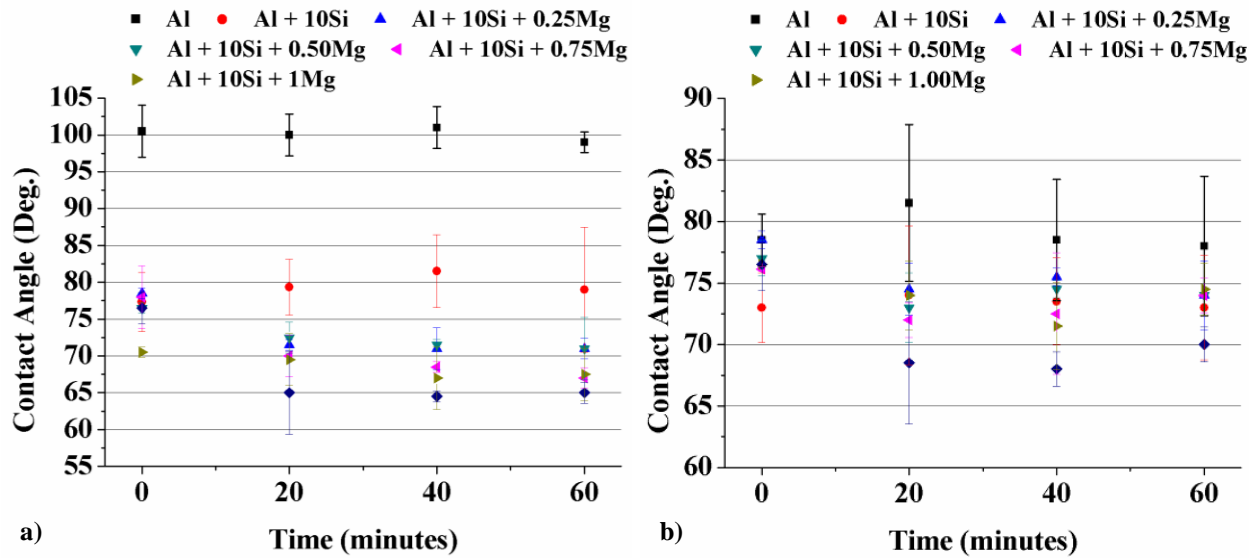


Figure 5-21: Variation in Contact Angle for Al, Al + x wt.% Si and Al + x wt.% Si + y wt.% Mg Alloys with Time at a) 800°C and b) 900°C with Error Bars Representing One Standard Deviation

5.4.3 Microstructure of Wettability Samples

The microstructures of the wettability samples were examined to determine if any interfacial reaction products were being formed during the wettability experiments. An understanding of any interfacial reaction would aid in understanding the changes in wettability with time and composition. It will also provide insight as to the expected reaction products during preparation of the Al-SiC grain refiners.

5.4.3.1 *Pure Al*

Figure 5-22 is an SEM micrograph of the pure Al sample examined at 800°C with corresponding EDX spot analysis. Examination of the interface structure shows fine particulates ~1 μm in size denoted by points A and B. The EDX plots show distinct peaks of Al, C and O for point A indicating that Al₄C₃ may have formed during the wettability experiment. The reaction to form Al₄C₃ occurs above 650°C [288] but is very sluggish below 900°C [290], explaining the presence of Al₄C₃ as clustered particles in localized areas rather than a continuous layer along the interface region. The detection of O, is possibly a by-product from the reaction of Al₄C₃ with water during metallographic sample preparation.

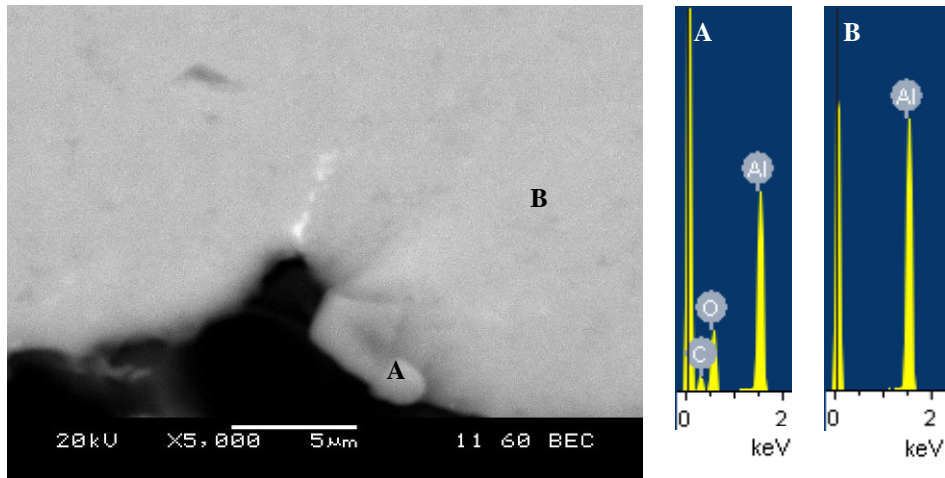


Figure 5-22: SEM Microstructure of Pure Al Sample Heated to 800°C with Corresponding EDX Spot Analyses for Points A and B

Location B was also examined to ensure the detection of O and C was not a result of sample contamination or oxidation during handling and experimentation. The strong Al peak from location B without the presence of other elements reinforces that the elements detected at location A do represent the formation of Al_4C_3 and not a result of sample contamination.

When pure Al was examined at 900°C (Figure 5-23), significantly larger clusters of Al_4C_3 particles (~5 μm, point A) were observed as compared to the pure Al sample at 800°C (Figure 5-22).

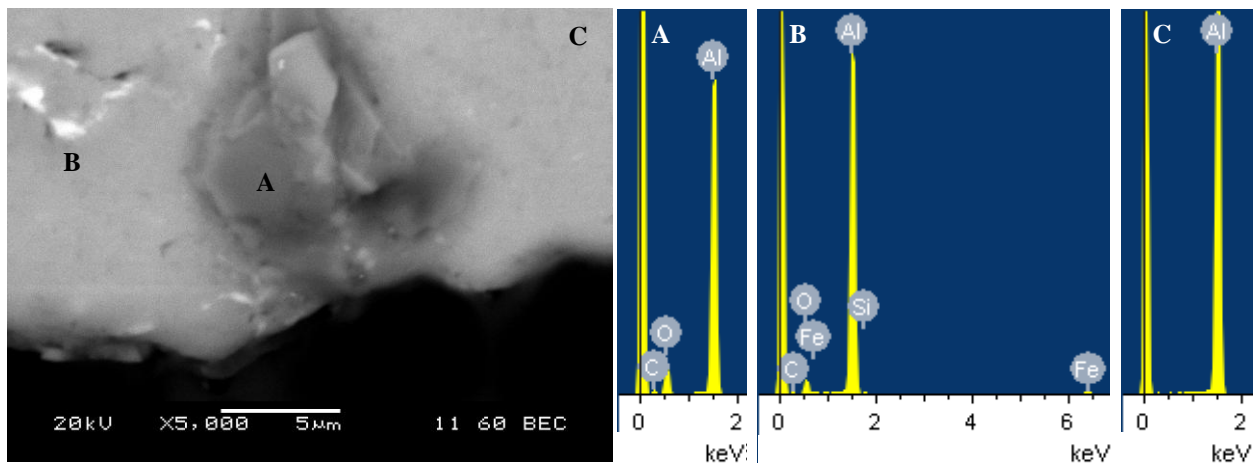


Figure 5-23: SEM Microstructure of Pure Al Sample Heated to 900°C Showing Interface Microstructure with Corresponding EDX Spot Analyses for Points A, B and C

The increased presence of Al_4C_3 in the sample treated at 900°C compared to the sample at 800°C is considered to result from the increased reaction rates at elevated temperatures. The presence of Al_4C_3 at the Al-SiC interface is consistent with the research of Laurent *et al.* [282]. Points B and C correspond to an Al-Fe based intermetallic and alloy matrix respectively. The Al-Fe intermetallic is an impurity in the alloy and the matrix shows no presence of O or C, corresponding to a low probability of sample contamination.

Initially, there was a concern for possible presence of an oxide layer on both Al (Al_2O_3) and SiC (SiO_2). On the Al side, no significant traces of Al_2O_3 were observed as they may have been minimized by the reducing atmosphere ($\text{Ar} + 5 \text{ vol.}\% \text{ H}_2$) and the Ca and Ti sponges. Furthermore, the presence of a SiO_2 layer on SiC is only of concern below $750\text{-}800^\circ\text{C}$ [282,283] and is not thought to have influenced the results during this study. It was expected that the reduction in average contact angle from 100 to 80° when the temperature increased from 800 to 900°C was a result of the removal of any Al_2O_3 layers on Al at 900°C as described by Ferro and Derby [281]. Since, no significant traces of Al_2O_3 were observed, the reduction in average contact angle was likely caused by a reduction in surface tension with increasing temperature.

5.4.3.2 Al-Si Alloys

The addition of Si is used to suppress the formation of Al_4C_3 [316,317]. It is estimated that at 800°C , $7.5 \text{ wt.}\%$ of Si in Al is required to suppress Al_4C_3 formation while just under $10 \text{ wt.}\%$ Si is required at 900°C [288]. Therefore, it is expected that no Al_4C_3 should be present in either Al- $10 \text{ wt.}\%$ Si samples prepared at 800 or 900°C . Figure 5-24 is an SEM micrograph of Al- $10 \text{ wt.}\%$ Si with corresponding EDX spot analysis at points A, B and C. Point A indicates a clean matrix while points B and C indicate a segregation of Si to the Al-Si/SiC interface and a few fine ($\sim 2\text{-}3 \mu\text{m}$) isolated Al_2O_3 particles respectively. No Al_4C_3 particles were observed as expected. A nearly identical interface microstructure was observed with Al- $10 \text{ wt.}\%$ Si at 900°C as shown in Figure 5-25. Again, no significant traces of Al_2O_3 were observed except for a few isolated particles as in the sample prepared at 800°C .

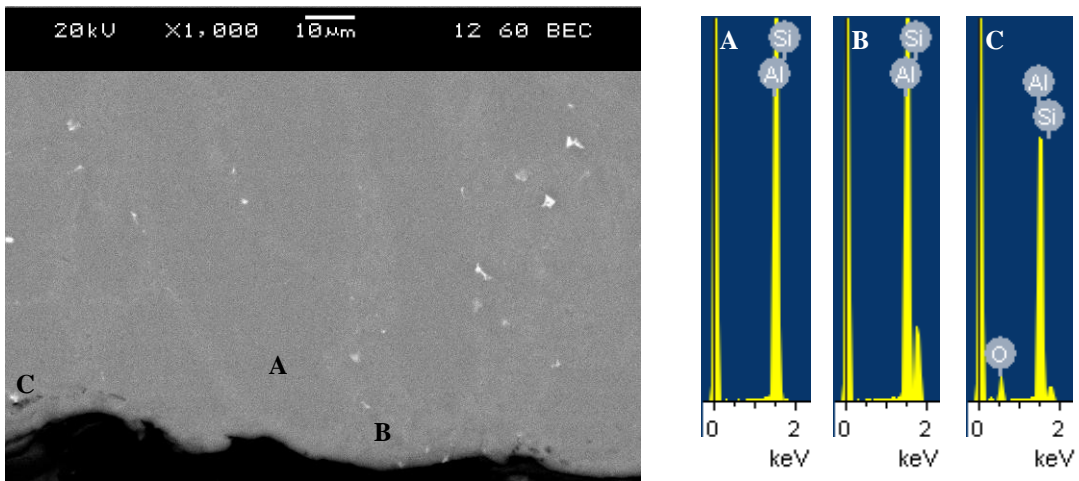


Figure 5-24: SEM Microstructure of Al-10 wt.% Si Sample Heated to 800°C Showing Interface Microstructure with Corresponding EDX Spot Analyses for Points A, B and C

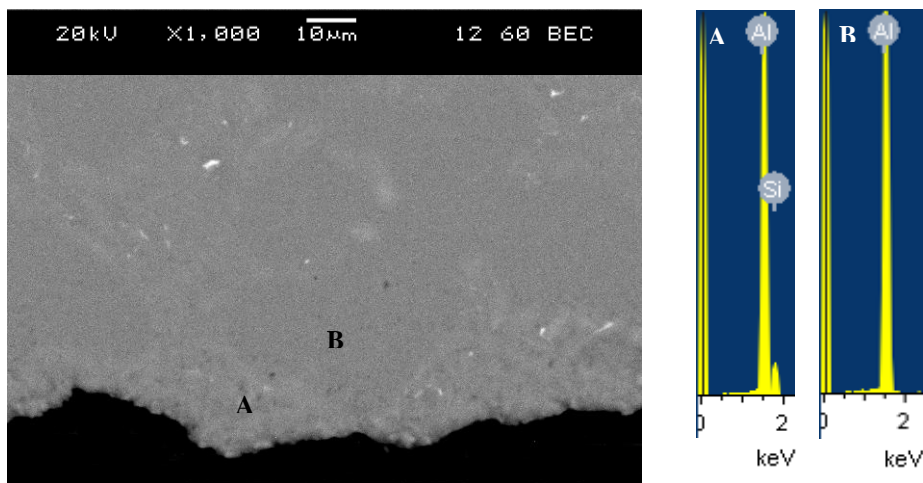


Figure 5-25: SEM Microstructure of Al-10 wt.% Si Sample Heated to 900°C Showing Interface Microstructure with Corresponding EDX Spot Analyses for Points A and B

The Si within the Al-Si alloy samples appear to collect at the SiC interface perhaps because of segregation within the sample. The addition of Si had a small effect on the contact angle as shown in Figure 5-20a and b, coinciding with the results of Ferro and Derby [281]. The average contact angle of Al-10 wt.% Si was 75-80° and 70-75° at 800 and 900°C respectively and remained constant with time. Any changes in contact angle with Si addition were expected to be small because of the similar surface tensions of Al and Si.

5.4.3.3 Al-Si-Mg Alloys

A SEM image of Al-10 wt.% Si-1.25 wt.% Mg treated at 800°C is shown in Figure 5-26. The EDX point analysis for location A appears to be from a mixture of Si particulates and an Mg-Al based oxide most likely the MgO·Al₂O₃ spinel (<10 μm wide). The addition of Mg to the Al alloy was thought to have reduced the surface tension and reduced any oxide films that could be present at the Al-SiC interface increasing wetting [297]. It is also interesting to note that the interface between the Al-Si-Mg alloy and the SiC substrate appears very irregular with many peaks and valleys. This was likely the result of the oxide layer being continuously broken during spreading, allowing for fresh Al-Si-Mg alloy surfaces to come in contact with the SiC substrate and continually reduce the contact angle until equilibrium was reached after 20 minutes. The EDX analysis of location B shows an Al-Fe based intermetallic and location C is likely that of Mg₂Si. The influence of these particles on the average contact angle is not clear and would require further study to characterize. The Al-10 wt.% Si-1.25 wt.% Mg alloy resulted in the lowest average contact angle observed (65°) after 20 minutes at 800°C. The beneficial effect of Mg was also observed by Oh *et al.* [286,287], but this study elucidates their findings using a sessile drop test in combination with Si addition. The current study also demonstrates the presence of a MgO·Al₂O₃ spinel at the Al-10 wt.% Si-1.25 wt.% Mg alloy-SiC interface.

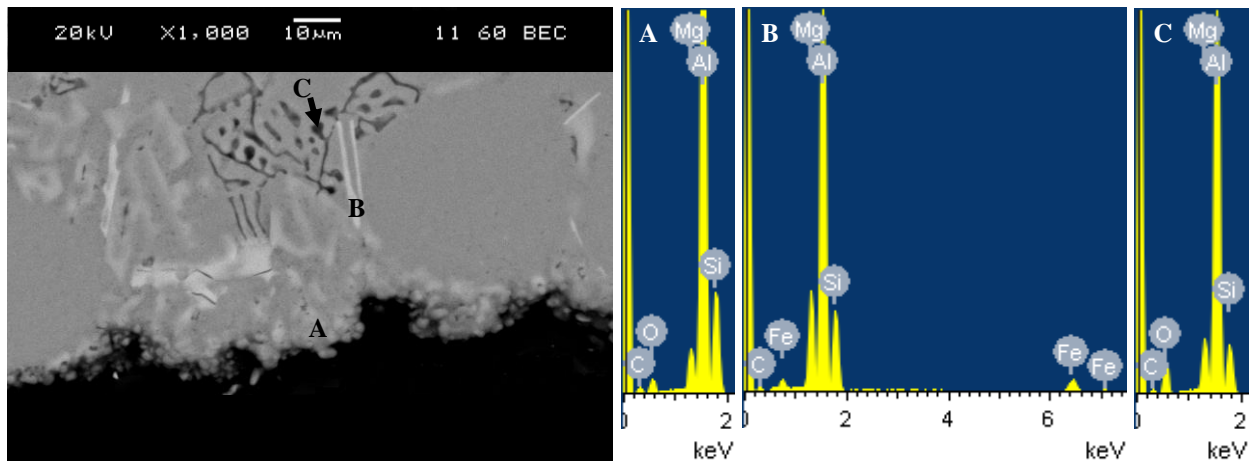


Figure 5-26: SEM Microstructure of Al-10 wt.% Si-1.25 wt.% Mg Sample Heated to 800°C Showing Interface Microstructure with Corresponding EDX Spot Analyses for Points A, B and C

Figure 5-27 is a SEM image of Al-10 wt.% Si-1.25 wt.% Mg treated at 900°C. For this case, the MgO·Al₂O₃ spinel layer observed is much thicker (>10 μm wide) and results in a flat

interface compared to the oxide layer observed at 800°C. The EDX spot analysis of location B demonstrates the very strong Mg, Al and O peaks. Location A shows the Al matrix with Si particles segregating to the interface, similar to the Al-Si alloy as shown in Figure 5-24 and Figure 5-25. The Al-Fe based intermetallic and Mg₂Si were also observed but are not shown in Figure 5-27. It is well established that oxidation on either the alloy or substrate can lead to high contact angles [290]. In the case of Al-10 wt.% Si-1.25 wt.% Mg at 900°C, the MgO·Al₂O₃ spinel appears to have quickly thickened because of enhanced oxidation rates at 900°C. This nearly negated the benefits of Mg to remove any oxides present in the Al alloy or the SiC interface. For instance, the Al-10 wt.% Si-1.25 wt.% Mg at 900°C had a constant contact angle in the range of 67-70° after 20 minutes that was just below the 70-75° contact angle found for Al-10 wt.% Si at 800°C. The equilibrium partial pressure of oxygen for metal–oxide systems at the melting point of Al and Mg are 3×10^{-52} and 1×10^{-57} atm respectively [290]. Using a cover gas with a few ppm of O₂, H₂O and CO₂ corresponds to a partial pressure of 10^{-5} to 10^{-6} atm of oxidizing agents in 1 atm of inert gas [290]. The use of H₂ as a reducing agent and Ti and Ca sponges were expected to reduce the partial pressure of oxygen but the possibility of oxide formation remains. In addition, it is thought that at 900°C, the thickening of this MgO·Al₂O₃ spinel was too rapid for the alloy to “break free” and continue spreading as was the case at 800°C. The transient variation in contact angle for the Al-Si-Mg alloys was likely the result of the time dependant balance between growth of the MgO·Al₂O₃ spinel and spreading of the Al-Si-Mg alloy.

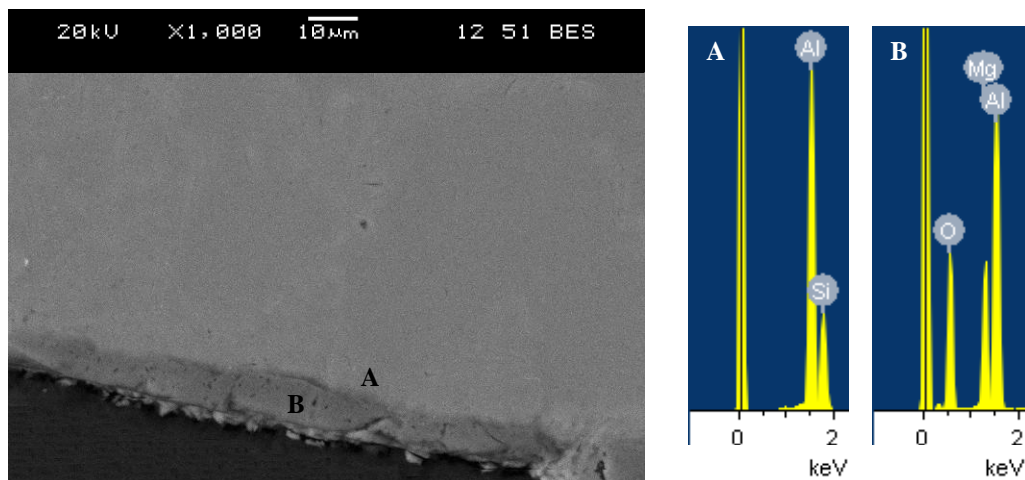


Figure 5-27: SEM Microstructure of Al-10 wt.% Si-1.25 wt.% Mg Sample Heated to 900°C Showing Interface Microstructure with Corresponding EDX Spot Analyses for Points A and B

5.4.3.4 Mechanism of Wettability with Si and Mg Addition

The change in wettability of SiC with Al in the presence of Si was minor because of the similar surface tensions of Al and Si. The main function of Si is to suppress Al_4C_3 formation, not to modify interfacial energies and wetting [284]. With the addition of Mg to Al-Si alloys, the contact angle rapidly decreased for the first 20 minutes then remained constant for the remaining 40 minutes. The rapid drop in contact angle could be the result of growth and “break-up” of the $\text{MgO}\cdot\text{Al}_2\text{O}_3$ spinel at the interface. At 900°C , the $\text{MgO}\cdot\text{Al}_2\text{O}_3$ spinel present may be too thick to be broken and was detrimental to the wetting kinetics. A summary of the observed mechanisms is outlined in Figure 5-28.

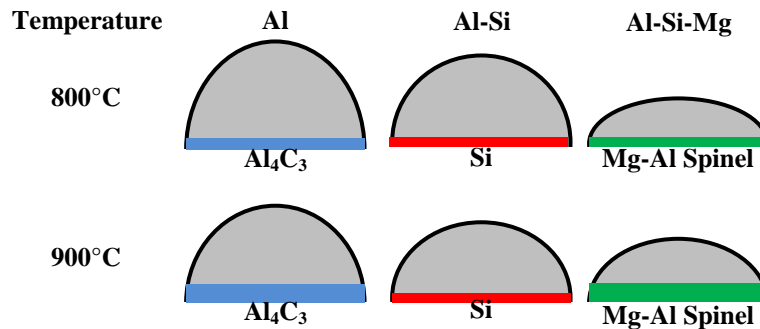


Figure 5-28: Schematic Diagram Showing Changes in Contact Angle With Temperature, Si and Mg Additions

The addition of Si had some influence on the wettability as shown in Figure 5-20 but the difference between using 2 wt.% Si and 10 wt.% was small. With the addition of Mg, only a small amount of Mg (1.25 wt.%) was required to observe positive results (Figure 5-21). Any additional Si being used to produce the Al-SiC grain refiners would ultimately end up in the Mg alloy, it would be ideal to obtain the beneficial wettability effects of Si addition without an excessive addition of Si. The next set of results then utilized Al-2 wt.% Si-1.25 wt.% Mg to obtain a balance of good wettability without excessive Si addition.

5.5 Wettability of Al-2 wt.% Si-1.25 wt.% Mg Alloy on SiC

Alloys corresponding to the composition of Al-2 wt.%-1.25 wt.% Mg were prepared and examined for their wettability behaviour (similar to the alloys in Section 5.4). The contact angles

were measured and the microstructures of the wettability samples were examined.

5.5.1 Contact Angle Measurements of Al-2 wt.% Si-1.25 wt.% Mg Alloy

The contact angle measurements for the Al-2 wt.% Si-1.25 wt.% Mg alloy are shown in Figure 5-29 (with the base Al alloy for comparison). The Al-2 wt.% Si-1.25 wt.% Mg alloy showed similar wettability behaviour to the other Al-Si-Mg alloys (Figure 5-21) with a decrease in contact angle after 20 minutes and a constant contact angle for up to 60 minutes. The Al-2 wt.% Si-1.25 wt.% Mg alloy did have a higher steady contact angle ($70-75^\circ$) at 800°C as compared to the Al-10 wt.% Si-1.25 wt.% Mg alloy in Figure 5-21a of $\sim 65^\circ$. The results in Figure 5-29a show that a Al-2 wt.% Si-1.25 wt.% Mg alloy can have similar wettability performance to a Al-10 wt.% Si-1.25 wt.% Mg alloy without adding an extra 8 wt.% of Si. The results for both the Al-10 wt.% Si-1.25 wt.% Mg and Al-2 wt.% Si-1.25 wt.% Mg alloys at 900°C underwent similar trends as shown in Figure 5-29b and Figure 5-21b respectively. The steady contact angle of the Al-2 wt.% Si-1.25 wt.% Mg alloy was $70-75^\circ$ while that of the Al-10 wt.% Si-1.25 wt.% Mg alloy was $65-70^\circ$. Microstructure analysis of the Al-2 wt.% Si-1.25 wt.% Mg alloy was conducted to determine the mechanisms of the observed wettability behaviour.

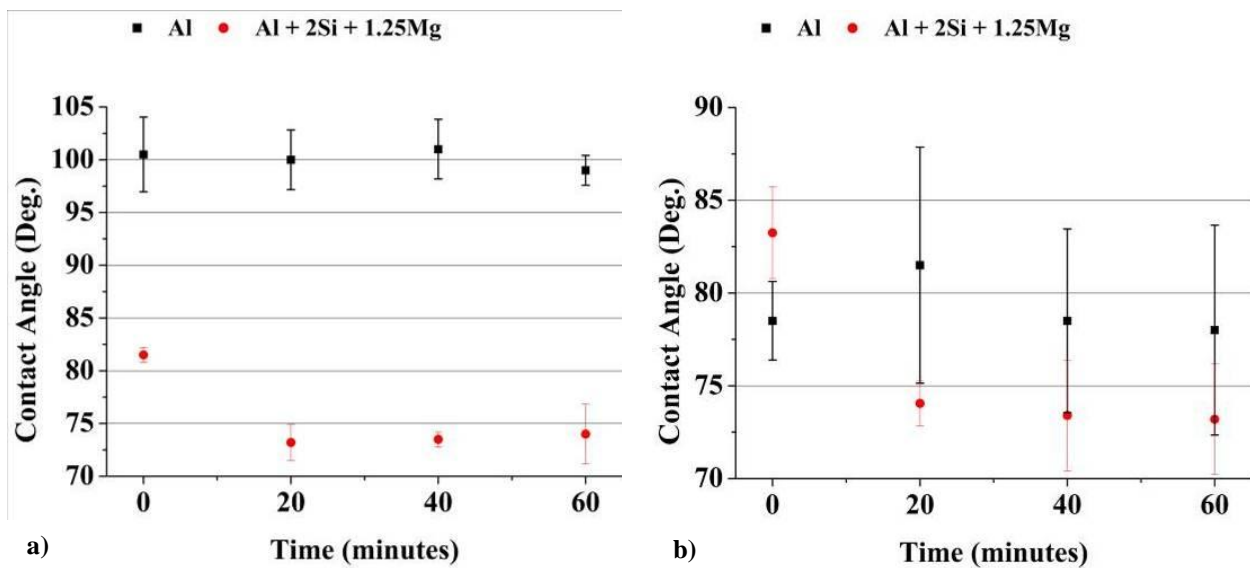


Figure 5-29: Variation in Contact Angle for Al and Al + 2 wt.% Si + 1.25 wt.% Mg Alloys with Time at a) 800°C and b) 900°C with Error Bars Representing One Standard Deviation

5.5.2 Microstructure of Al-2 wt.% Si-1.25 wt.% Mg Alloy

The SEM images of the Al-2 wt.% Si-1.25 wt.% Mg alloys at 800 and 900°C are shown in Figure 5-30 and Figure 5-31 respectively. The mechanism for the contact angle changes appear to be consistent with the Al-Si-Mg alloys in Section 5.4.3. At 800°C, a thin <10 μm MgO·Al₂O₃ spinel formed at the interface between the Al-2 wt.% Si-1.25 wt.% Mg alloy and SiC substrate as shown in Figure 5-30. The wetting interface looks very similar to the interface of the Al-2 wt.% Si-1.25 wt.% Mg alloy in Figure 5-26 with the presence of a Al-Mg-O rich phase at the edge of the sample.

Similarly, at 900°C, the Al-2 wt.% Si-1.25 wt.% Mg alloy had a thick (>10μm) Al-Mg-O rich interface that again was thought to be a MgO·Al₂O₃ spinel. The thick MgO·Al₂O₃ spinel would have been difficult to “break free” causing a similar contact angle to the Al-2 wt.% Si-1.25 wt.% Mg alloy at 800°C.

The Al-2 wt.% Si-1.25 wt.% Mg alloy enabled good wetting with SiC easing preparation for an Al-SiC based grain refiner for Mg-Al alloys. The presence of a MgO·Al₂O₃ spinel at the interface between the SiC and the Al-2 wt.% Si-1.25 wt.% Mg alloy could hinder the formation of the nucleating carbides required for Mg-Al grain refinement and is the focus of the subsequent section. The focus now moves into using an Al-2 wt.% Si-1.25 wt.% Mg alloy composition to act as a matrix to prepare the Al-SiC grain refiners and examine their microstructure and evaluate their refining potential in AZ91E Mg alloy.

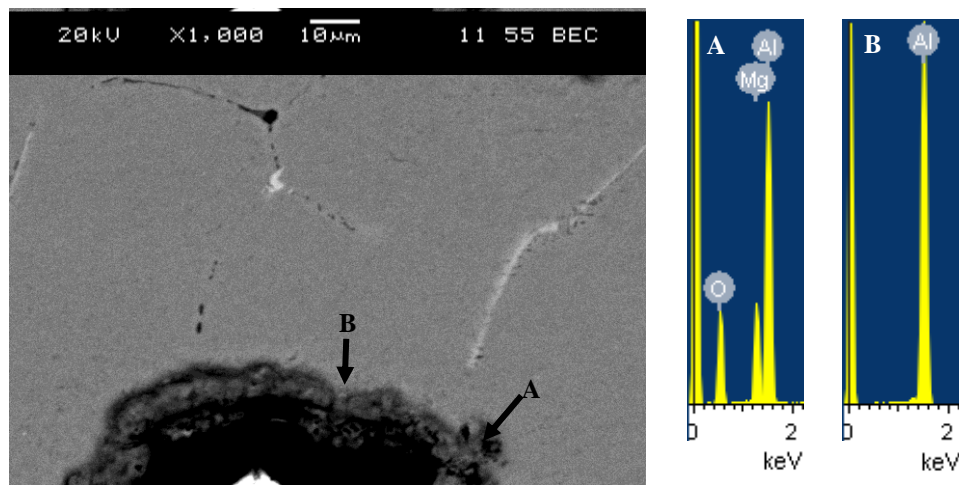


Figure 5-30: SEM Microstructure of Al-2 wt.% Si-1.25 wt.% Mg Sample Heated to 800°C Showing Interface Microstructure with Corresponding EDX Spot Analyses for Points A and B

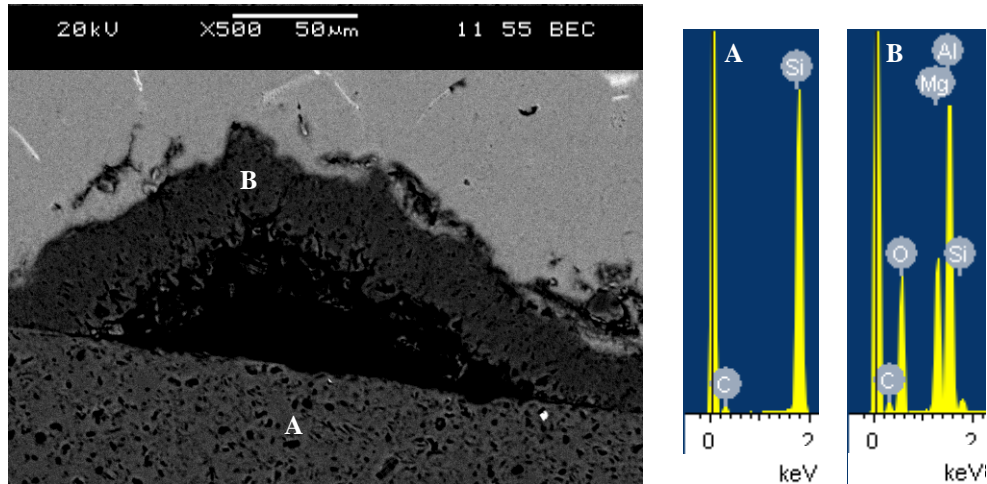


Figure 5-31: SEM Microstructure of Al-2 wt.% Si-1.25 wt.% Mg Sample Heated to 900°C Showing Interface Microstructure with Corresponding EDX Spot Analyses for Points A and B

5.6 Ex-situ Grain Refinement Using Al-SiC Refiners

With the results from Section 5.5, a composition that enabled good wettability for the formation of the Al-SiC refiners was determined. Further analysis was conducted to determine the reaction temperatures, concentrations of SiC and reaction times to produce homogenous Al-SiC refiners, with ex-situ nucleating particles that could be easily added to the AZ91E Mg alloy. This analysis was conducted by examining DSC results of heated Al-SiC alloys, XRD of prepared Al-SiC refiners and SEM analysis of the refiners.

5.6.1 Differential Scanning Calorimetry of Al-SiC Refiners

Sections 5.4 and 5.5 determined that the Al-2 wt.% Si-1.25 wt.% Mg alloy composition provided good wettability between Al and SiC for preparation of the Al-SiC refiners. Using DSC, samples of Al-5.9 and 11.6 wt.% SiC alloys were prepared to examine the influences of temperature, time and concentration on the reaction rates to form Al_4C_3 . The matrix was limited to pure Al instead of a Al-Si-Mg alloy to simplify interpretation of the results. According to Equation 23, the reaction between Al and SiC to form Al_4C_3 will result in Si formation. By placing Al-5.9 and 11.6 wt.% SiC alloys at 700, 800 and 900°C for up to 120 minutes, the extent of the reaction in Equation 23 could be determined by observing the changes in temperature and energy released upon solidification of the alloys. With increasing Si content, the alloy liquidus temperature would decrease and is expected to follow the phase diagram shown in Figure A-4

(Appendix A.1). A representative DSC curve is shown in Figure A-6 (Appendix A.4) with a summary of the results in Table 5-6.

Table 5-6: Summary of DSC Results for Al-5.9 and 11.6 wt.% SiC Alloys

Holding Temp. (°C)	Holding Time (min)	Al Liquidus Peak Area (J/g)	Alloy Liquidus (°C)	Si Peak Area (J/g)	Si Eutectic Formation Temp. (°C)
Al-5.9 wt.% SiC					
700	15	93.20	629.9	44.01	568.7
800	120	73.67	623.9	72.42	574.7
900	120	35.99	620.8	73.66	575.2
Al-11.6 wt.% SiC					
700	15	85.19	625.1	74.94	569.9
800	120	16.06	600.9	148.7	571.9
900	120	3.28	597.9	203.5	577

At 700°C, increasing the SiC concentration from 5.9 to 11.6 wt.% reduces the liquidus peak area from 93.20 to 85.19 J/g. The increased SiC also reduced the liquidus temperature from 629.9 to 625.1°C. This 5°C drop in liquidus temperature indicated that Si is forming during holding according to Equation 23 and going into solution with Al. Upon cooling, the Al alloy is now enriched with Si solute pushing its liquidus to lower temperatures. The Si peak areas also increased from 44.01 to 74.94 J/g, further indicating higher Si formation. The change in Si eutectic formation remains relatively constant as it was bound by the eutectic isotherm at 577°C (Figure A-4). In addition to the SiC concentration, temperature and time is expected to have a large contribution to the reaction rates in Equation 23. Comparing Al-11.9 wt.% SiC at 700 and 900°C it can be observed that increasing temperature and time results in significantly smaller liquidus formation peak areas (from 85.19 to 3.28 J/g), lower liquidus temperatures (625.1 to 597.9°C) and higher Si peak areas (74.94 to 203.5 J/g). Therefore, with either increasing concentration or temperature and time increased Si formation and hence increased Al₄C₃ (Equation 23) should result. An estimation to the extent of the conversion of SiC to Al₄C₃ could be made by examining the liquidus temperature as it changes with Si concentration and comparing it to the Al-Si phase diagram. A similar approach was conducted by Lloyd and Jin [318] in a 6061 Al alloy with SiC. Using 11.9 wt.% SiC should result in ~8 wt.% Si if the reaction in Equation 23 goes to completion. The associated Al formation temperature would be 605°C from Figure A-4. Using the results in Table 5-6, at 700°C, the Al formation temperature is

625.1°C corresponding to a Si concentration of ~5 wt.%. It was only when the samples were treated at 800 and 900°C did the Al formation temperatures drop to 600.9 and 597.9°C respectively corresponding to ~9 wt.% Si. Since it is impossible to form more Si than inputted from SiC, the discrepancy is attributed to purity of the Al and SiC used, homogeneity of the samples or the particle sizes of the samples. The resulting amount of estimated Al_4C_3 that formed is estimated at ~3 wt.%. The DSC results determined that an Al alloy with 11.9 wt.% SiC, heated to 800 or 900°C for 120 minutes would be most suitable for formation of Al_4C_3 . X-ray diffraction analysis was then conducted to identify the phases in a Al-2 wt.%-1.25 wt.% Mg-11.9 wt.% SiC alloy (denoted Al-SiC henceforth) produced by heating for 60 or 120 minutes at 800 and 900°C.

5.6.2 X-ray Diffraction of Al-SiC Grain Refiners

Samples for XRD analysis were prepared and examined to determine the phases present within the prepared alloys. The XRD plots of Al-SiC alloys produced at 700, 800 and 900°C are shown in Figure 5-32. The 700°C was only held for 15 minutes while the 800 and 900°C were held for one and two hours during preparation. All the refiners contained Al, SiC, Si, Mg_2Si and a SiAl_2O_5 phase. The SiAl_2O_5 phase is thought to be an oxide that forms due to holding the samples at elevated temperature for an extended time. An Al_2O_3 peak was also observed in the 800 and 900°C refiners indicating that holding the refiners at such elevated temperatures for extended periods of time is undesirable and leads to excessive oxidation. The presence of Al_4C_3 was observed in all the refiners but most prominent in the 800°C refiners. In addition, all the refiners contained an Al_4C_3 or Al_2MgC_2 peak at 34.2° that was stronger in the 800°C refiners than the 900°C refiners. Finally, the 800°C refiners also contained MgAl_2O_4 spinel peaks not observed in the 900°C refiners. It was thought that the 900°C refiners would be more susceptible to forming oxides because of the elevated temperature but the MgAl_2O_4 spinel peaks could be the result of Al_2MgC_2 in the refiner reacting with water or moisture during handling according to Equation 27.

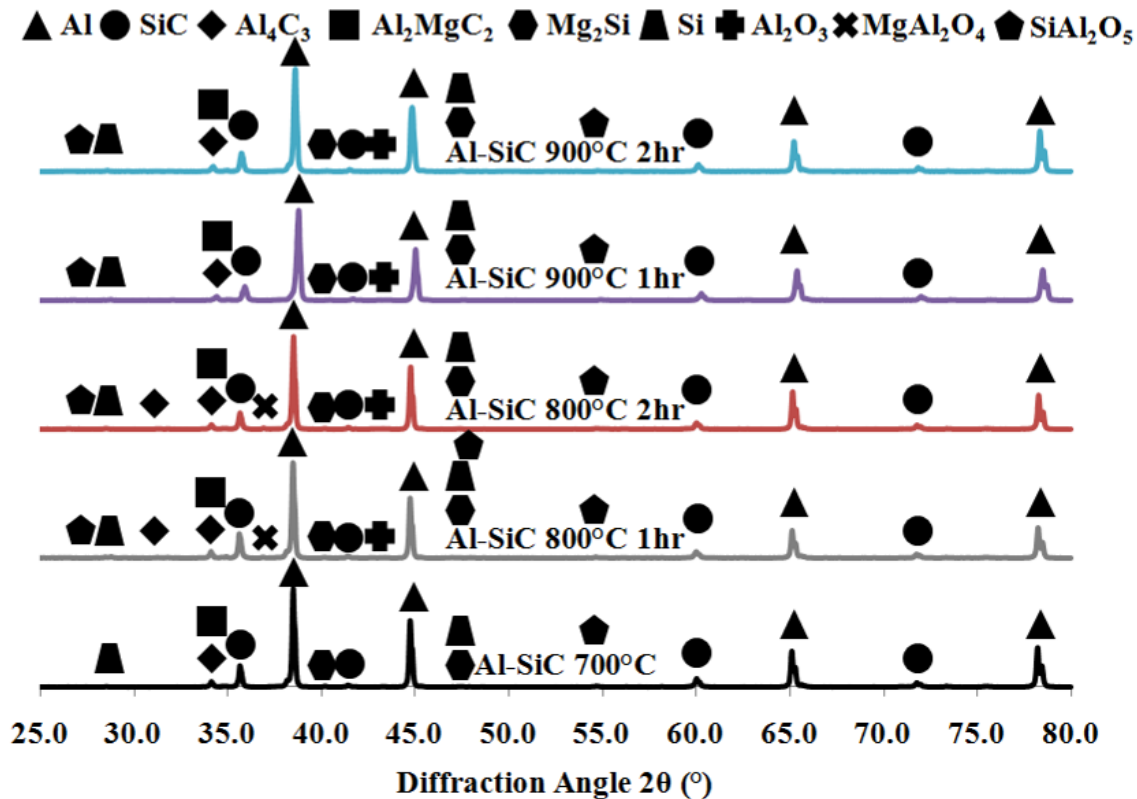


Figure 5-32: XRD Plot of Al-SiC Refiners

Further XRD analysis was conducted by dissolving the Al matrix in NaOH according to the procedure outlined in Section 3.4.1 to more easily detect other phases within the refiners. The resulting XRD plots of the refiners with the Al matrix dissolved are in Figure 5-33. By dissolving the matrix, peaks of MgO were observed in all the refiners indicating some oxidation of Mg is inevitable even when the temperature was only 700°C. The XRD plots in Figure 5-33 show the same phases as the plots in Figure 5-32. There were also additional Al₄C₃ peaks at 59.5° only observed in the 800°C refiners. In other locations of Al₄C₃ peaks, the intensity of the peaks was largest in the 800°C refiners indicating a higher weight fraction of these phases. In addition, the 800°C refiners contained additional MgAl₂O₄ peaks at 45, 56, 65 and 77.5° not observed in the other refiners. The MgAl₂O₄ is thought to be a by-product of the reaction of Al₂MgC₂ with water or moisture during handling according to Equation 27. The 800°C refiners tended to give a good combination of desired phases such as Al₄C₃ and Al₂MgC₂ without containing high intensity peaks of unwanted oxides such as Al₂O₃, MgO and SiAl₂O₅. The

microstructure of the refiners was then examined to observe the distribution of the observed phases.

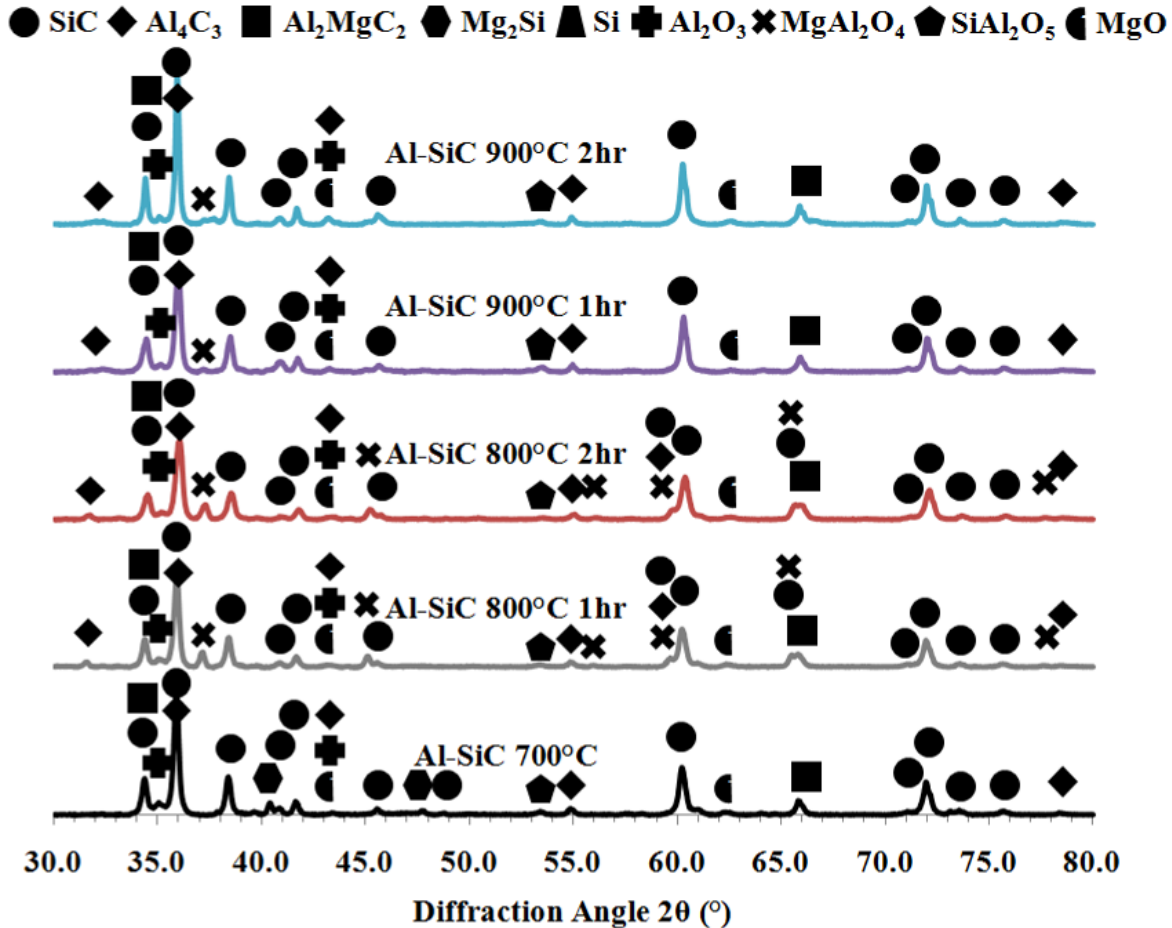


Figure 5-33: XRD Plot of Al-SiC Refiners After Al Matrix Dissolution

5.6.3 Microstructure of Al-SiC Refiners

The microstructures of the prepared Al-SiC refiners are shown in Figure 5-34 with the Al-SiC refiner produced at 700°C shown in Figure 5-34a. The microstructure contained well distributed needle shaped particles determined to be Si and Mg₂Si from the wettability and XRD results while there were >100 μm dark bands and patches of SiC both indicated by the arrows. There appeared to be no significant changes in the distribution of phases in the microstructures with different temperatures and holding times. However, with increasing temperature or time there was a thickening of a dark Al-Mg-C-O phase at the interface between the Al matrix and SiC bands. An example is indicated by the arrows in Figure 5-34b-e.

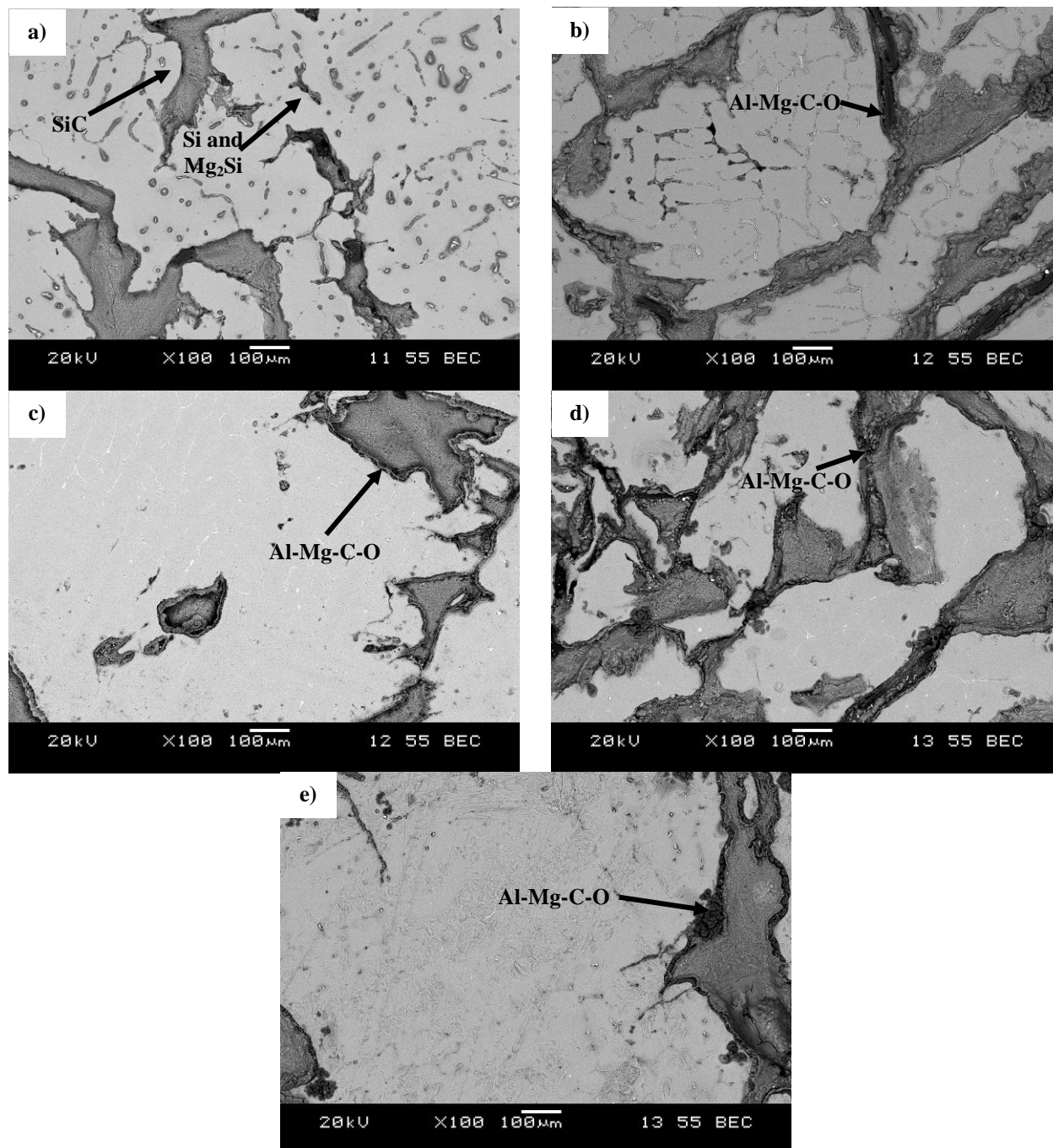


Figure 5-34: SEM Microstructure of Al-SiC Refiners at a) 700°C, b) 800°C for 1 Hour, c) 800°C for 2 Hour, d) 900°C for 1 Hour and e) 900°C for 2 Hour

A higher magnification SEM image of the Al-SiC refiner produced at 800°C for 2 hour is shown in Figure 5-35. An EDX spot analysis at the centre of the dark bands shows a high concentration of Si and smaller concentrations of Al, Mg, C and O. It is thought that the centres of the dark banded regions were mainly SiC particles. At the interface of the SiC bands and Al

matrix, the EDX spectrum shows a lower concentration of Si but higher concentrations of Al, Mg, O and C. It is this interface layer between the Al matrix and the SiC bands where the in-situ Al-Mg-C particles formed. The relative intensities of Mg, Al, C and O are expected to be skewed by the presence of the Al and Mg in the matrix and reaction of the observed phases with water during sample preparation.

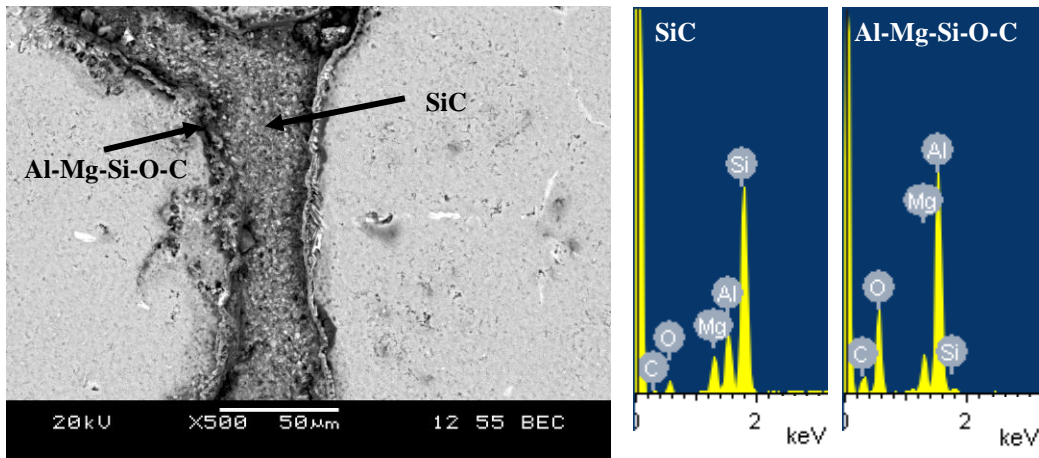


Figure 5-35: SEM Microstructure of Al-SiC Alloys Produced at 800°C for 2 Hour With EDX Spectrums from Points A and B

The wettability results determined that the Al-2 wt.% Si-1.25 wt.% Mg composition at 800°C provided the best contact between the Al alloy and SiC particles. The DSC results indicated that SiC concentrations of 11.9 wt.% at 800 and 900°C held for 2 hour enabled near complete reaction of Al and SiC. Namely, that sufficient heat and time was provided for reactions to occur. The XRD and SEM results showed that Al-SiC refiner produced at 800°C were most likely to contain desired Al_4C_3 and Al_2MgC_2 nucleating particles in a uniform microstructure. These results suggest that the Al-2 wt.%-1.25 wt.% Mg-11.9 wt.% SiC refiner (Al-SiC) produced at 800°C for 2 hour has excellent potential as an ex-situ Al-SiC grain refiner and was examined further by adding it to a AZ91E alloy.

5.6.4 Effects of Al-SiC Refiner Addition on Grain Size of AZ91E

The optical microstructures of AZ91E, AZ91E + C_2Cl_6 , AZ91E + filter + Ar bubbling and AZ91E + filter + Ar bubbling + 0.50 wt.% Al-SiC are shown in Figure 5-36. The grain structures

look similar in that they all are equiaxed in shape but differ according to their grain sizes summarized in Figure 5-37 with error bars representing one standard deviation.

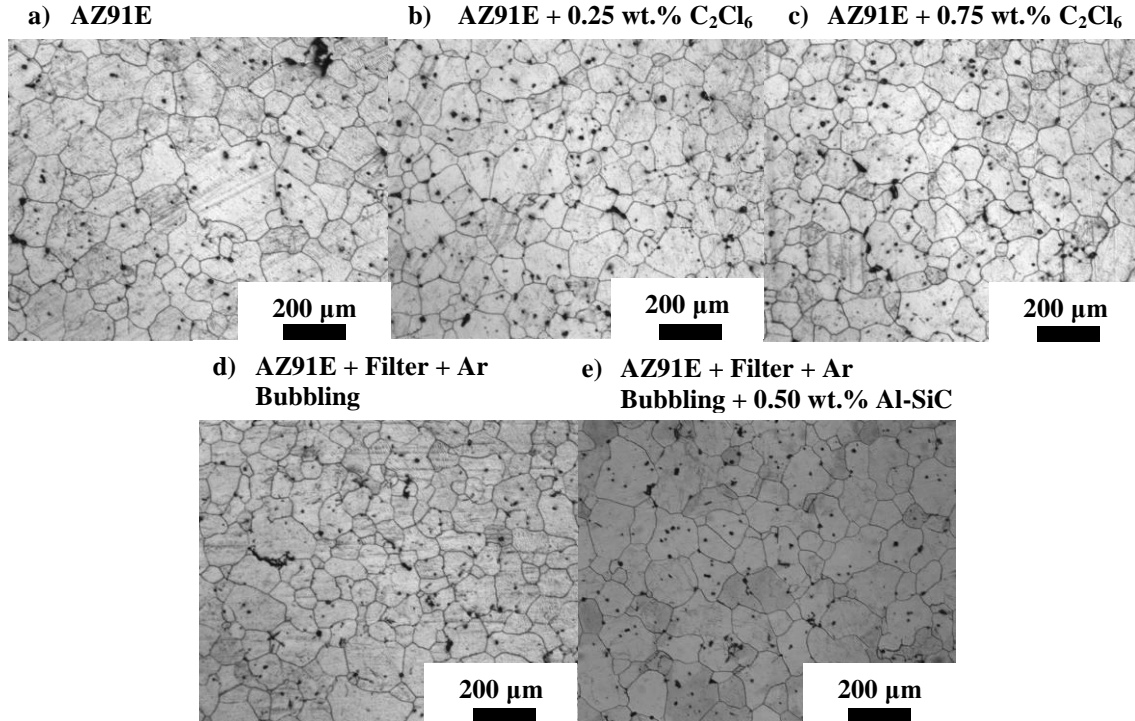


Figure 5-36: Grain Structures of AZ91E with C_2Cl_6 Addition, Filter + Ar Bubbling and Al-SiC Addition

The grain sizes of the base, 0.25 and 0.75 wt.% C_2Cl_6 treated and filter + Ar bubbling from Figure 5-12 are included in Figure 5-36 along with the grain size of AZ91E treated with 0.50 wt.% Al-SiC. The AZ91E, AZ91E + 0.25 wt.% C_2Cl_6 , AZ91E + 0.75 wt.% C_2Cl_6 , AZ91E + filter + Ar bubbling and AZ91E + filter + Ar bubbling + 0.50 wt.% Al-SiC castings had average grain sizes of 95, 75, 78, 73 and 73 μm respectively. Considering the error bars, all the conditions examined had ~20% finer grain size than the base AZ91E alloy. The mechanisms for grain refinement using C_2Cl_6 and Ar bubbling were discussed in Section 5.3. With C_2Cl_6 addition, transformation of stringy Mn-Al particles to blocky duplex nucleants with Al-Mg-C were observed within grain centres while Ar bubbling was thought to aid in distribution of appropriately sized Mn-Al particles. The microstructure of the Al-SiC refined alloys was then examined to determine their refining mechanism.

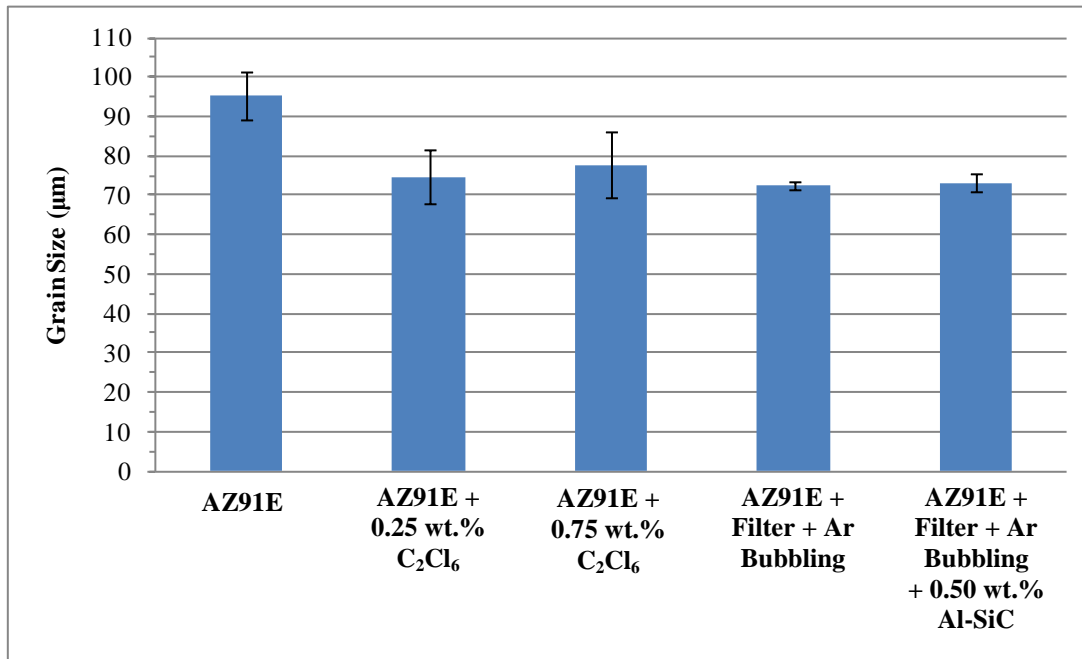


Figure 5-37: Effect of Al-SiC Addition on Grain Size of AZ91E with Error Bars Representing One Standard Deviation

5.6.5 Effects of Al-SiC Refiner Addition on Microstructure of AZ91E

Scanning electron microscopy was utilized to determine the mechanism for grain refinement using Al-SiC. The microstructure of a AZ91E + filter + Ar bubbling + 0.50 wt.% Al-SiC casting is shown in Figure 5-38. The microstructure contained primarily blocky Mn-Al particles that were sometimes in the centre of grains as indicated by the arrow in Figure 5-38a. A higher magnification BSE image of the blocky ~2-3 µm particles (d^* is ~2.6 µm) Mn-Al particle within the centre of the grain in Figure 5-38a is shown in Figure 5-38b and is nearly identical to the Mn-Al particle observed in Figure 5-14 with C₂Cl₆ addition. The combined BSE image in Figure 5-38b and element maps in Figure 5-38c show that the blocky Mn-Al or (Mn-Al-Fe) particles contained concentrations of Si not observed in the particle in Figure 5-14 but has a similar dark Al-Mg-C-O or Al-C-O based ring alongside the Mn-Al particle.

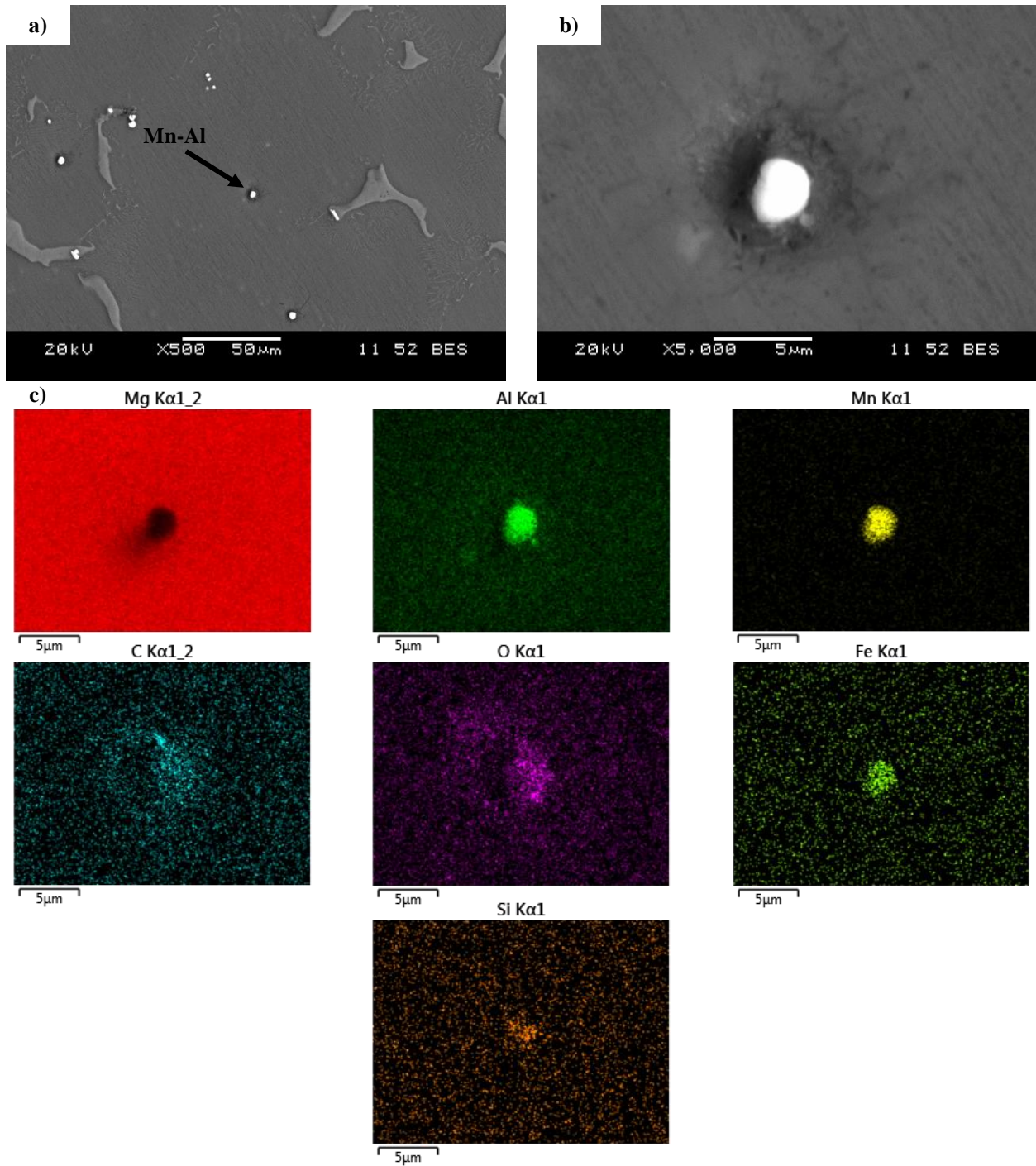


Figure 5-38: SEM Image of AZ91E + Filter + Ar Bubbling + 0.50 wt.% Al-SiC Showing a) General Microstructure, b) Mn-Al-Fe Based Intermetallic Alongside Al-Mg-C-O Phase and c) EDX Element Maps of Phases in b)

The microstructure was examined for any other phases that developed or were introduced with the addition of the Al-SiC refiner. The AZ91E + filter + Ar bubbling + 0.5 wt.% Al-SiC

casting contained agglomerated Al-Mg-C-O particles that can be observed in Figure 5-39 highlighted by the arrow. The agglomerated particles could be oxides or excess nucleants that were unable to position themselves to act as grain refiners and instead just entangled themselves with Mn-Al particles. These observations in Figure 5-39 further support the duplex nucleation mechanism of Mn-Al with Al-Mg-C-O nucleants. The excess agglomerated particles could then be detrimental to the mechanical properties of the sample as they may act as inclusions and reduce the overall homogeneity of the alloy.

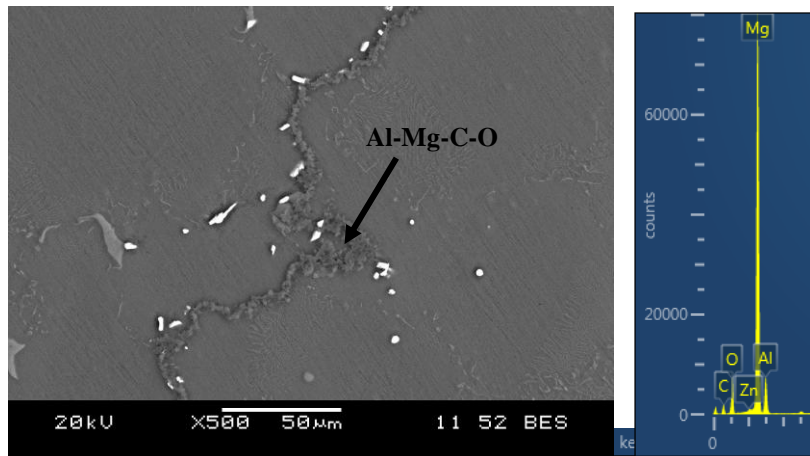


Figure 5-39: SEM Image of AZ91E + Filter + Ar Bubbling + 0.50 wt.% Al-SiC Showing Agglomerated Particles

Previous literature using C and SiC based additions show several mechanisms as outlined in Table 2-18 to Table 2-25. In the case of Al-SiC refiner, it is believed that a duplex mechanism is responsible for the observed grain refinement. The Mn-Al or Mn-Al-Fe are thought to be Al_8Mn_5 or $\text{Al}_8(\text{Mn,Fe})_5$. The exact compositions of the Al-Mg-C-O and Al-C-O particles observed in Figure 5-38 need to be determined. Looking at similar studies examining either addition of SiC alone, Al-SiC or Mg-SiC refiners to AZ91 Mg alloys (Table 2-22 to Table 2-24), the observed particles could be Al_4C_3 , Al_2CO or Al_2MgC_2 . The likelihood the particles being Al_2CO has been ruled out as it requires Al concentrations of 10 at.% or more [218]. Both Al_4C_3 and Al_2MgC_2 are reactive with water (Equation 17 and Equation 27 respectively) and could manifest as Al-Mg-C-O particles using EDX. Historically, Al_4C_3 has a larger presence within literature and is often suggested to be the source of refinement using C but there have been studies attributing C refinement in AZ91 using charcoal to Al_2MgC_2 [232]. In addition, observation of Al_2MgC_2

using TEM [132,139] is the only direct experimental confirmation of the often observed Al-C-O or Al-Mg-C-O nucleants, but formation of this compound was observed when SiC was added to a binary Mg-3 wt.% Al alloy. Thus, the nucleant observed during this study is likely Al_2MgC_2 with significant experimental and theoretical evidence. The apparent duplex phenomena with Mn-Al or Mn-Al-Fe particles likely only exists because the investigated alloy contains appreciable amounts of Mn and Fe that also could be suitable nucleants when no other more appropriate phases are present. The presence of Si in the nucleants (Figure 5-38) indicates that the nucleant resulted from the addition of the Al-SiC refiner as no other traces of Si were found in any other portion of the microstructure. The trace Si is then postulated to be a reaction product of the transformation of SiC to Al_2MgC_2 (Equation 26) with the by-products being Mg_2Si or SiAl_2O_5 as observed in the XRD plots of Figure 5-32 and Figure 5-33. The fractography of the AZ91E samples treated with Al-SiC were then examined and compared to the C_2Cl_6 treated and filter + Ar bubbling treated AZ91E.

5.6.6 Fractography of Al-SiC Refiner Treated AZ91E

Optical macrographs of the tensile fracture surfaces of the Al-SiC treated AZ91E castings are shown in Figure 5-40. Macrographs of the base AZ91E, 0.75 wt.% C_2Cl_6 treated AZ91E and AZ91E + filter + Ar bubbling treated castings are included for comparison. The inclusions observed on the AZ91E + filter + Ar bubbling + 0.50 wt.% Al-SiC (Figure 5-40d) casting look similar to the inclusions observed on the C_2Cl_6 and filter + Ar bubbling treated castings. However, the AZ91E + filter + Ar bubbling + 0.50 wt.% Al-SiC casting contained relatively large inclusions and appeared to be on the same level as the base AZ91E (Figure 5-40a) alloy in terms of cleanliness. The XRD analysis in Figure 5-32 and Figure 5-33 showed that the prepared Al-SiC refiners contained oxides of MgO, Al_2O_3 and SiAl_2O_5 . These oxides formed as a result of the high temperature preparation of the Al-SiC refiners and may be contaminating the AZ91E melts and introducing inclusions that may be detrimental to UTS and elongation despite the filter + Ar bubbling treatment. The inclusion on the fracture surface of the AZ91E + filter + Ar bubbling + 0.50 wt.% Al-SiC casting highlighted by the arrow in Figure 5-40d was examined further using SEM to determine if it had the same morphology as the inclusions in the C_2Cl_6 and filter + Ar bubbling castings.

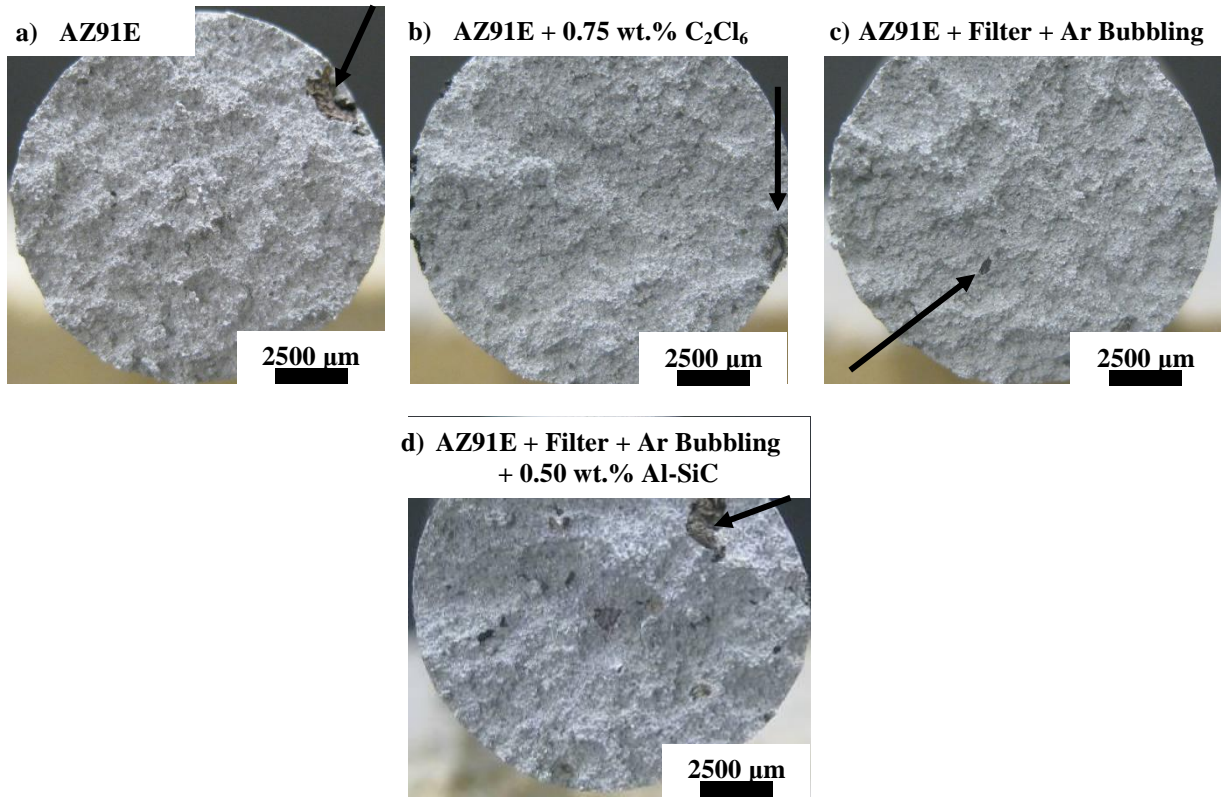


Figure 5-40: Optical Macrographs of Fracture Surfaces of a) AZ91E, b) AZ91E + 0.75 wt.% C₂Cl₆, c) AZ91E + Filter + Ar Bubbling and d) AZ91E + Filter + Ar Bubbling + 0.50 wt.% Al-SiC

Figure 5-41 is an SEM image with a corresponding EDX spectrum of the inclusion observed on the fracture surface of the AZ91E + filter + Ar bubbling + 0.50 wt.% Al-SiC casting. The EDX spectrum shows that the spot analysis conducted is Mg-O based and is similar to the inclusions in Figure 5-17.

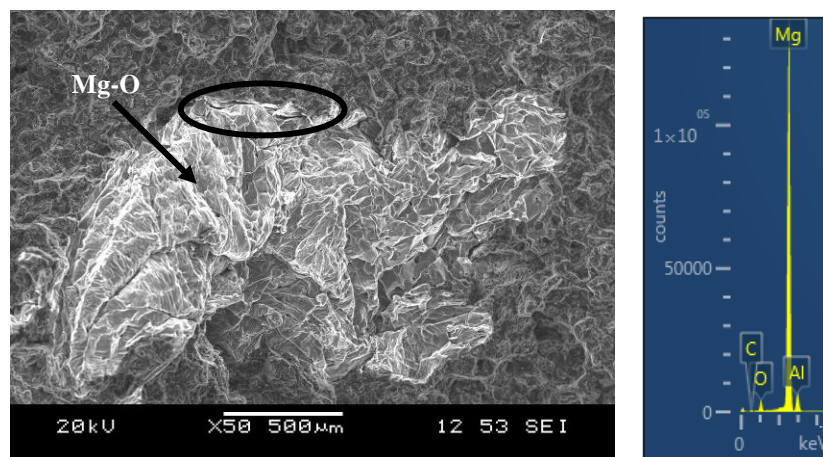


Figure 5-41: Fracture Surface of AZ91E + Filter + Ar Bubbling + 0.50 wt.% Al-SiC

The poor interface between the inclusion and the Mg matrix is highlighted by the circle in Figure 5-41 showing a large gap indicating poor bonding. The poor bonding between the inclusion and Mg matrix would compromise mechanical properties especially UTS and elongation. The effect of Al-SiC refiner addition on porosity was then examined.

5.6.7 Porosity of Al-SiC Treated AZ91E

Table 5-7 presents the average porosity results with error ranges representing one standard deviation. Porosity was measured using Archimedes principle. The porosity values for key conditions (Table 5-4) are listed, besides that for Al-SiC addition. The porosity of the Al-SiC treated castings is approximately the same as that for C₂Cl₆ and filter + Ar bubbling casting at 1%. The mechanical properties discussed in Section 5.6.8 are characteristic of the grain size and inclusion contents of the prepared alloys, and are not influenced by excessive porosity within the castings.

Table 5-7: Summary of Porosity Results for C₂Cl₆ and Al-SiC Refiner Addition on AZ91E

Casting Condition	Average Porosity (%)
AZ91E	0.7 +/- 0.2
AZ91E + 0.25 wt.% C₂Cl₆	0.8 +/- 0.4
AZ91E + 0.75 wt.% C₂Cl₆	0.9 +/- 0.1
AZ91E + Filter + Ar Bubbling	0.9 +/- 0.3
AZ91E + Filter + Ar Bubbling + 0.50 wt.% Al-SiC	0.8 +/- 0.6

5.6.8 Effects of Al-SiC Refiner Addition on Mechanical Properties of AZ91E

Figure 5-42 is a graph of average YS, UTS and elongation of AZ91E + filter + Ar bubbling + 0.50 wt.% Al-SiC with error bars representing one standard deviation. The mechanical properties of base AZ91E, 0.25 and 0.75 wt.% C₂Cl₆ treated and filter + Ar bubbling treated AZ91E castings from Figure 5-18 are also shown in Figure 5-42 for comparison. The AZ91E + filter + Ar bubbling + 0.50 wt.% Al-SiC castings had average YS, UTS and elongation of 106.5 MPa, 180.7 MPa and 3.8% respectively. The average YS of the Al-SiC treated casting is higher than that of the C₂Cl₆ and filter + Ar bubbling treated castings but its average UTS and elongation is only a slight improvement over that of the base AZ91E alloy. The aim of this research is to develop combined grain refinement and inclusion removal treatments that would provide a YS similar to that of the C₂Cl₆ treated castings while the UTS and elongations would

be comparable to those from the filter + Ar bubbling castings. It appears that the inclusions observed (Figure 5-39, Figure 5-40d and Figure 5-41) were detrimental to the UTS and elongation resulting in a casting with a high YS but UTS and elongation similar to that of the base alloy. In addition, stirring of the melt was required to introduce the Al-SiC refiner to the AZ91E alloy melt and this melt stirring caused turbulence in the melt that could have entrapped inclusions. Development of a technique to introduce the refiner, with minimum melt turbulence would be beneficial to maximizing mechanical properties.

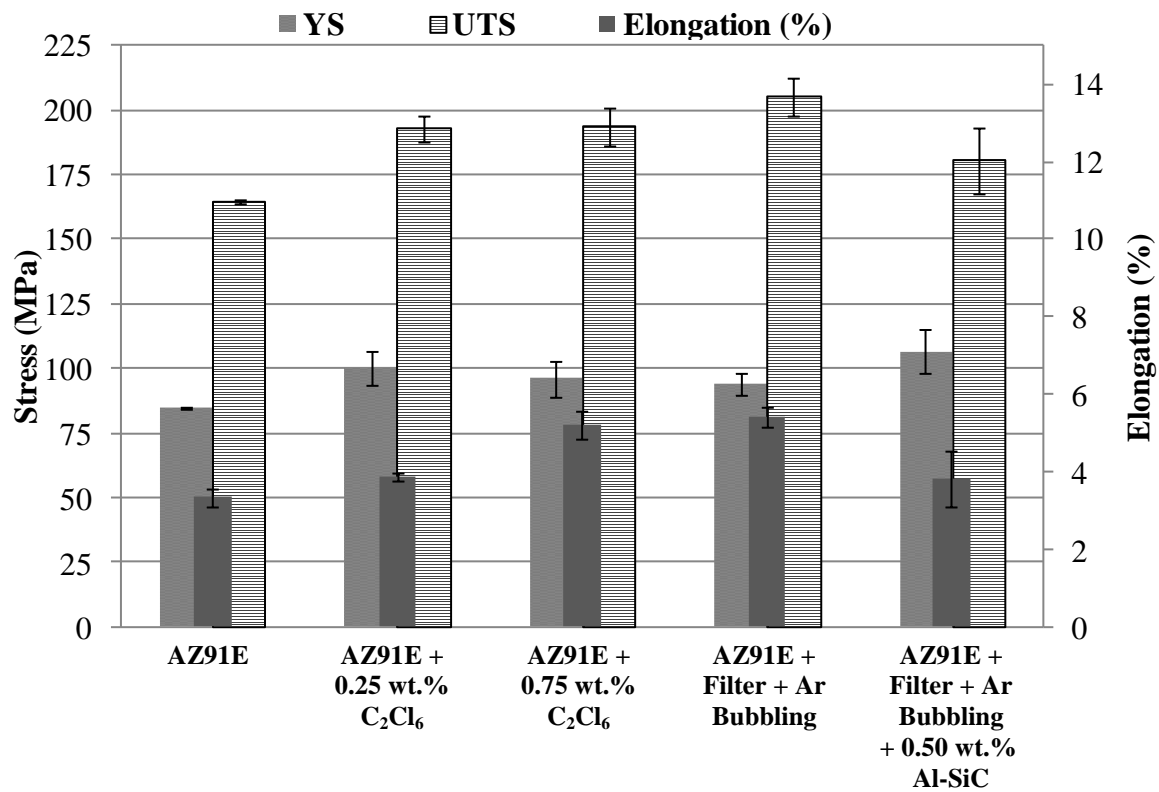


Figure 5-42: Effect of C₂Cl₆ Addition, Filtration + Ar Bubbling and Al-SiC Refiner Addition on Mechanical Properties of AZ91E with Error Bars Representing One Standard Deviation

The Al-SiC refiners were synthesized with significant considerations regarding wettability, reaction rates at elevated temperatures, microstructure homogeneity and characterisation in order to be viable. These considerations were required because the aim was to develop a refiner with desired nucleating particles produced ex-situ in a uniform manner. An alternative approach is to develop a refiner that would form the desired nucleating particles in-situ upon addition to a Mg alloy. The next section presents the results of the development of an in-situ SPS Al-C grain

refiner using powder metallurgy to take into account wettability, microstructure homogeneity and reactions at elevated temperatures. Results regarding the performance of the SPS Al-C refiner in AZ91E will also be presented and compared against C_2Cl_6 and Al-SiC additions.

5.7 In-situ Grain Refinement Using SPS Al-C Refiners

In-situ grain refiners were prepared by ball milling powders of Al and graphite, then consolidating the powders using SPS. The grain refiners were first characterized using XRD and SEM then their performance was examined by adding them to AZ91E Mg alloy.

5.7.1 X-ray Diffraction of SPS Al-C Refiners

Samples to represent the Al-C powders for 1-5 hour of the milling process were collected and analyzed using XRD. The Al-C refiner after SPS was also examined using XRD. The resulting plots are shown in Figure 5-43. For every hour of ball milling and after SPS, the samples contained only Al and C phases. No other phases were observed.

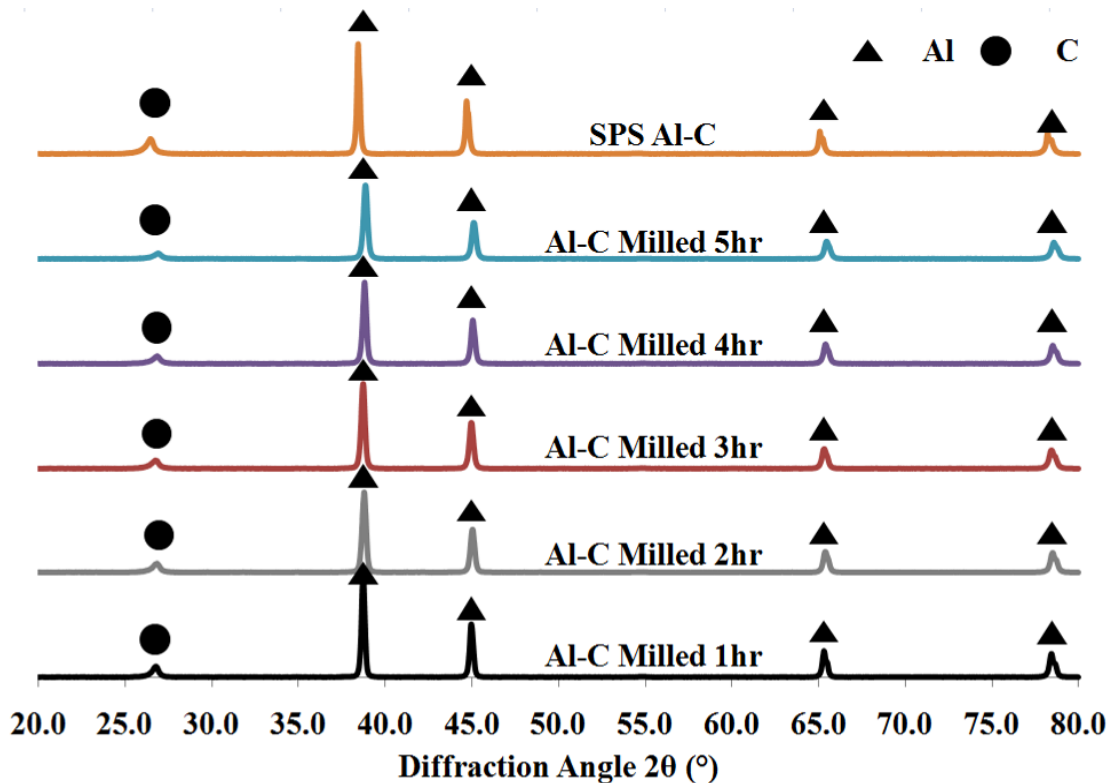


Figure 5-43: Influence of Milling Time and SPS on XRD of Al-C Refiner Powder

The changes in the C peak and Al (110) plane peaks with milling time and SPS are shown in Figure 5-44a and b respectively. With increasing milling time, there was a general broadening of peak widths and reduction in peak height for both C and Al. The shift to higher θ_{diff} values means smaller d_{inter} spacing's according to Equation 28 and is a result of the reduction in particles sizes and induced compressive strain on the milled powders [311]. After SPS treatment, the peaks shift to lower peak angles (higher d_{inter}) and the peaks become sharp because of the relief of strain and coarsening of particles because of the applied heat. Further microstructural examination of the Al-C SPS refiners was conducted to observe the distribution of Al and C phases.

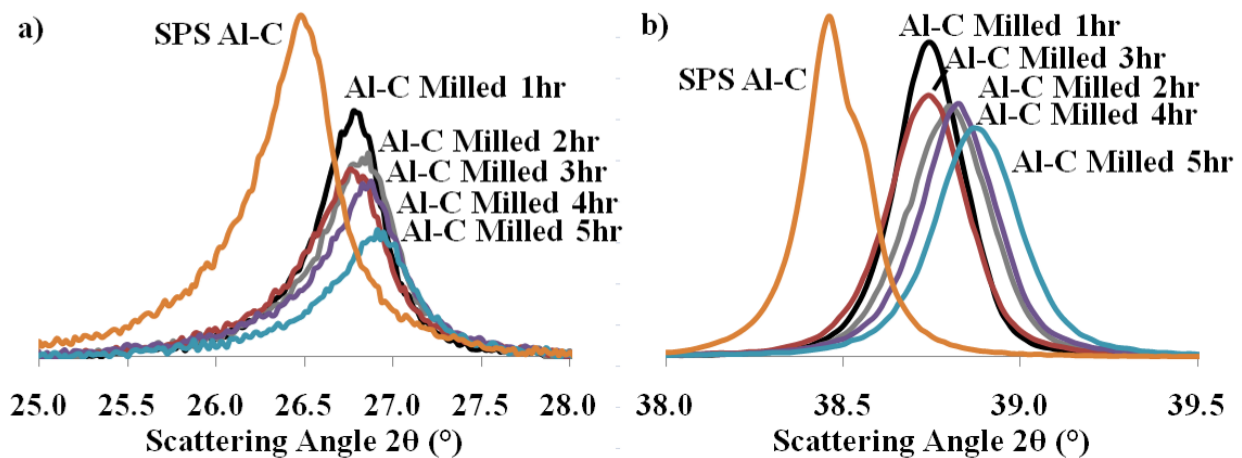


Figure 5-44: Influence of Milling Time and SPS on XRD of Al-C Refiner Powder of a) Graphite Basal Peak and b) Al (110) Peak

5.7.2 Microstructure of SPS Al-C Refiners

The microstructure of a Al-C SPS grain refiner is shown in Figure 5-45. The microstructure consisted of a light gray Al rich phase (denoted by A) and very fine ($\sim 1 \mu\text{m}$) thick C rich layers (denoted by B). The C layers also show the presence of O and this could be the remnants of oxide layers from prior sintering of the Al-C powders. However, one advantage of SPS is that it aids in the breakdown of oxide layers [300] and this is especially important for Al particles samples because they are usually covered with an aluminum oxide film [302]. In addition, no oxide phases were observed in the XRD patterns in Figure 5-43 indicating their contribution was minor if present at all. Another phase not observed in Figure 5-43 but was observed using SEM was the bright phase in Figure 5-45 denoted by C. This phase showed concentrations of Fe and Cr and is thought to be from contamination during ball milling as the vial and grinding balls

were made of 18 wt.% Cr steel. Its contribution was also not observed in the XRD patterns of Figure 5-43 indicating a minor contribution. The influence of the Al-C refiner on grain size, microstructure, fractography, porosity and mechanical properties were then examined.

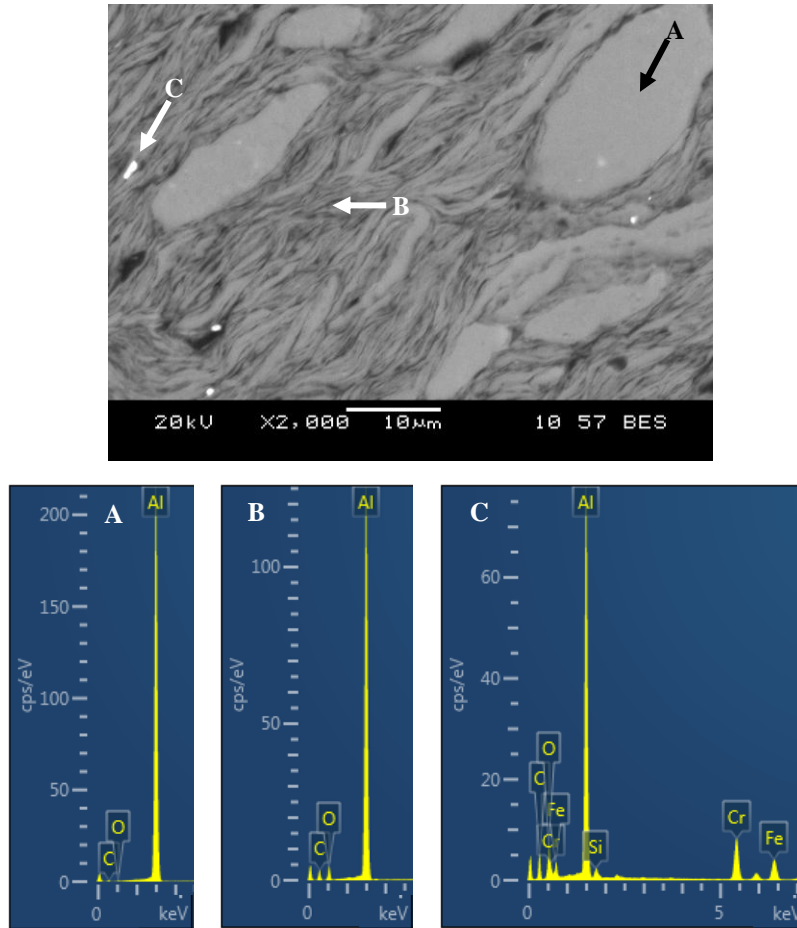


Figure 5-45: SEM Microstructure of Al-C Grain Refiner Showing Al Matrix and Fine C Rich Layers with Corresponding EDX Spot Analyses for Points A, B and C

5.7.3 Effects of SPS Al-C Refiner Addition on Grain Size of AZ91E

The influence of 0.25 and 0.50 wt.% Al-C addition on the grain size of AZ91E are shown in the optical micrographs in Figure 5-46. The influence of 0.25 and 0.75 wt.% C_2Cl_6 , filter + Ar bubbling and Al-SiC addition are included as well. Similarly, all the conditions observed, the resulting grain structure had equiaxed grains with their sizes presented in Figure 5-47 with error bars representing one standard deviation.

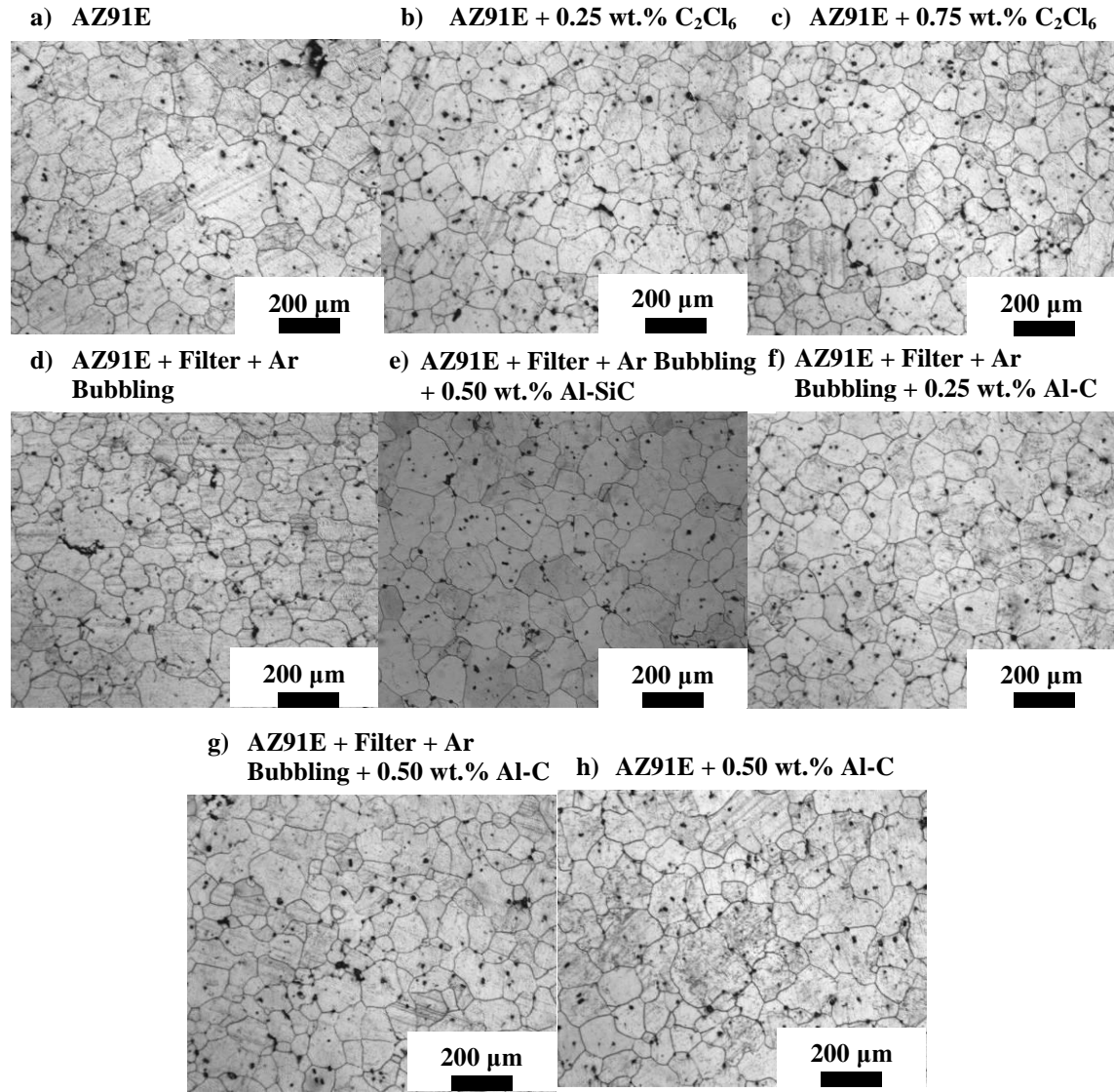


Figure 5-46: Grain Structures of AZ91E with C₂Cl₆ Addition, Filter + Ar Bubbling, Al-SiC Addition and Al-C Addition

The AZ91E alloy had an average grain size of 95 μm and the 0.25 and 0.75 wt.% C₂Cl₆ refined castings had grain sizes of 75 and 78 μm respectively. The AZ91E + filter + Ar bubbling and AZ91E + filter + Ar bubbling + 0.50 wt.% Al-SiC castings both had average grain sizes of 73 μm. The AZ91E + filter + Ar bubbling + Al-C castings had average grain sizes of 79 and 75 μm for 0.25 and 0.50 wt.% Al-C respectively. With 0.50 wt.% Al-C, the average grain size was 83 μm. Considering the error bars in Figure 5-47, the grain sizes of AZ91E + 0.25 wt.% C₂Cl₆, AZ91E + filter + Ar bubbling, AZ91E + filter + Ar bubbling + 0.50 wt.% Al-SiC and AZ91E + filter + Ar bubbling + 0.50 wt.% Al-C were very similar and

~20% smaller than the base alloy. Assuming 100 g of melt, the addition of 0.25 wt.% C_2Cl_6 results in ~0.025 g of carbon. Under the same condition, 0.50 wt.% of Al-SiC and Al-C results in ~0.055 g of SiC and ~0.125 g of carbon respectively, indicating that the carbon from C_2Cl_6 is a very potent form of carbon as compared to other carbon sources. A violent bubbling and stirring accompany the release of carbon from C_2Cl_6 upon addition to Mg with the released Cl cleaning the nucleating substrates for refinement. Further investigation was conducted to examine the changes in microstructure with the addition of Al-C.

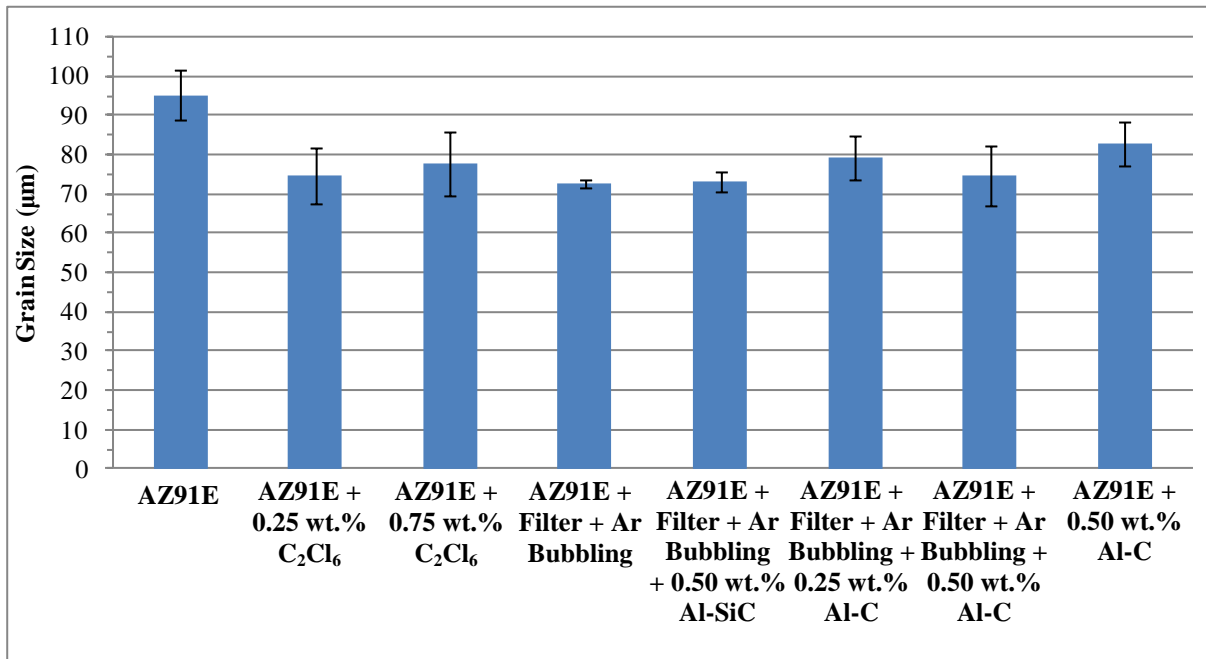


Figure 5-47: Effect of Al-C Addition on Grain Size of AZ91E with Error Bars Representing One Standard Deviation

5.7.4 Effects of SPS Al-C Refiner Addition on Microstructure of AZ91E

Scanning electron microscopy was utilized to determine the mechanism for grain refinement using Al-C. The microstructure of the AZ91E + 0.50 wt.% Al-C was similar to the microstructure of AZ91E + C_2Cl_6 (Figure 5-14a) and AZ91E + filter + Ar bubbling + 0.50 wt.% Al-SiC (Figure 5-38) with only blocky Mn-Al particles as shown in Figure 5-48a. Many of these blocky Mn-Al particles were observed within the centre of grains. A higher magnification image of one such Mn-Al particle within the centre of a grain (indicated by the arrow in Figure 5-48a) is shown in Figure 5-48b. The BSE image shows bright and dark areas

with element maps shown in Figure 5-48c. The grain refinement mechanism using Al-C is thought to be similar to C_2Cl_6 (Section 5.3) and Al-SiC additions (Section 5.6). The bright particles were Mn-Al or Mn-Al-Fe based and appear alongside dark Mg-Al-C-O or Al-C-O based $\sim 2\text{-}3\ \mu\text{m}$ (d^* is $\sim 2.6\ \mu\text{m}$) particles.

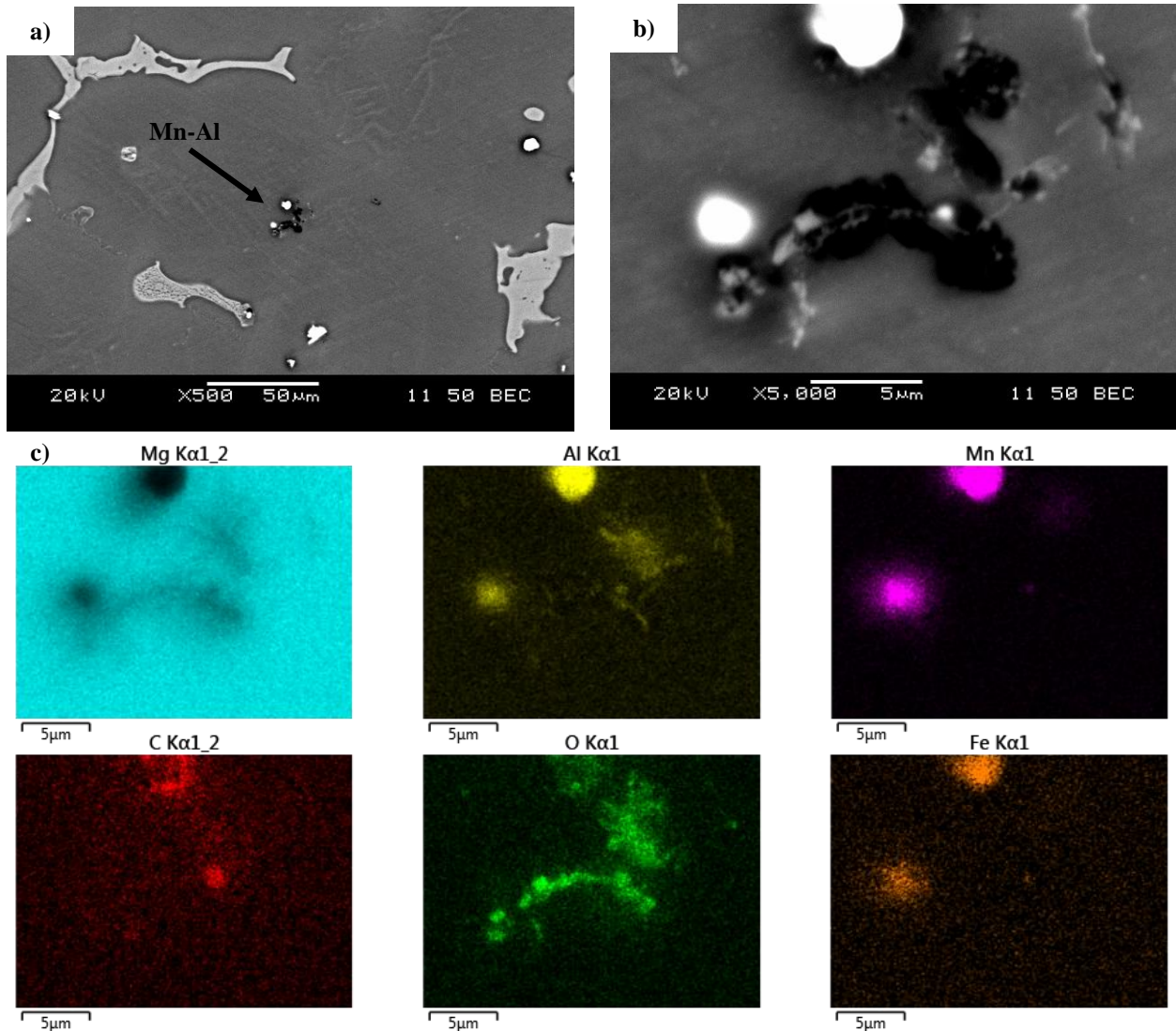


Figure 5-48: SEM Image of AZ91E + 0.50 wt.% Al-C Showing a) General Microstructure, b) Mn-Al-Fe Based Intermetallic Alongside Al-Mg-C-O Phase and c) EDX Element Maps of Phases in b)

Similar to Figure 5-48, Figure 5-49 shows the microstructure of a AZ91E + filter + Ar Bubbling + 0.50 wt.% Al-C castings with Mn-Al particles alongside Al-Mg-C-O based particles. With AZ91E + filter + Ar Bubbling + 0.50 wt.% Al-C, the Ar

bubbling enabled even distribution of Mn-Al particles allowing for more even grain refinement providing finer grain sizes (Figure 5-47) than AZ91E + 0.50 wt.% Al-C alone, as the Mn-Al particles were well distributed in the melt, the added Al-C could easily find a Mn-Al to enable nucleation.

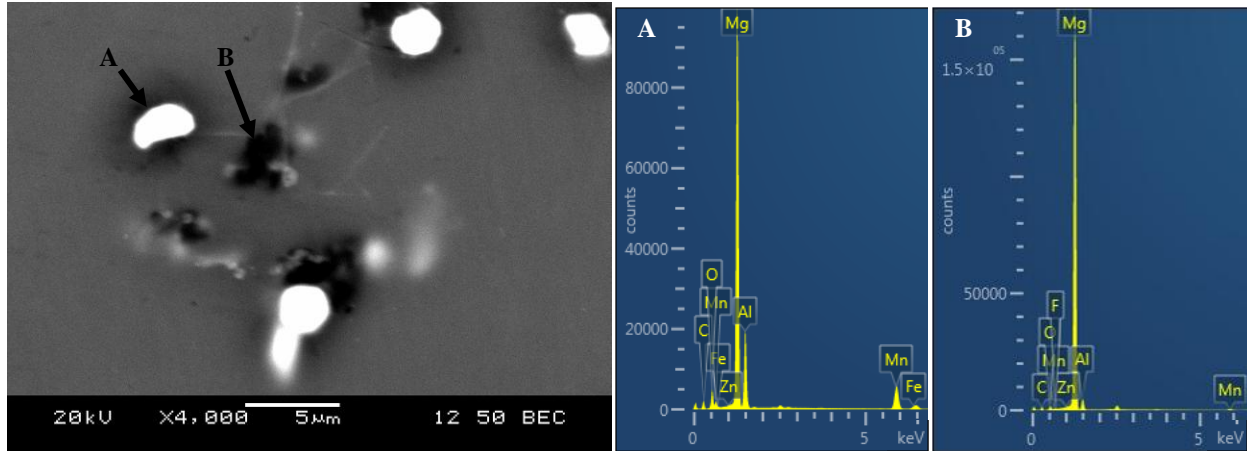


Figure 5-49: SEM Image of AZ91E + Filter + Ar Bubbling + 0.50 wt.% Al-C Showing EDX Spectrums of A and B.

Similar to Al-SiC refiner addition in Section 5.6, the addition of Al-C showed signs of duplex nucleation with Mn-Al or Mn-Al-Fe particles and Al-Mg-C-O or Al-C-O particles. Using the same reasoning that was applied to the Al-SiC refiner and the results of previous literature using C sources outlined in Table 2-18 to Table 2-21 and Table 2-25 the nucleant observed during this study is likely Al_2MgC_2 . The apparent duplex phenomena with Mn-Al or Mn-Al-Fe particles are because these phases also could be suitable nucleants when no other more appropriate phases were present. The addition of the Al-C refiner did not show any other phases within its microstructure unlike the Al-SiC refiner (Figure 5-39) that contained agglomerated particles.

5.7.5 Fractography of SPS Al-C Refiner Treated AZ91E

Optical macrographs of the fracture surfaces of the filter + Ar bubbling + Al-C and Al-C treated castings are shown in Figure 5-50. The fracture surfaces of the base AZ91E, C_2Cl_6 , filter + Ar bubbling and Al-SiC treated castings from Figure 5-40 are also included for comparison. Once again, the inclusions observed on the filter + Ar bubbling + Al-C and Al-C

treated castings looked similar to the inclusions in Figure 5-40, Figure 5-2 and Figure 5-6. The AZ91E + filter + Ar bubbling + 0.25 or 0.50 wt.% Al-C and AZ91E + 0.50 wt.% Al-C castings had inclusions on their fracture surfaces as shown in Figure 5-50e,f and g respectively. It is thought that the stirring action during addition of the Al-C refiners may have introduced additional oxides that could possibly reduce mechanical properties. Characterisation of the inclusions was conducted using SEM.

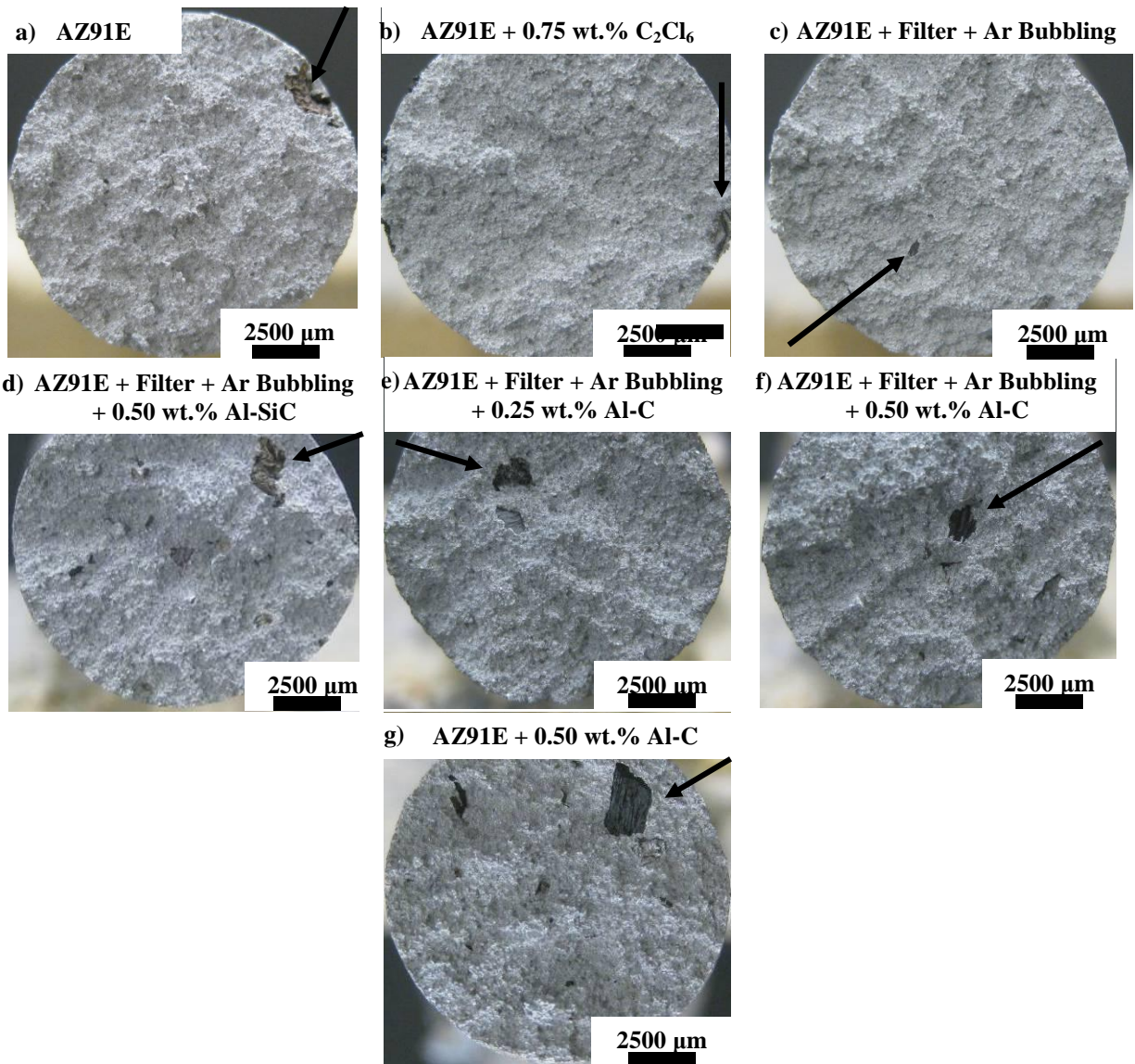


Figure 5-50: Optical Macrographs of Fracture Surfaces of a) AZ91E, b) AZ91E + 0.75 wt.% C₂Cl₆, c) AZ91E + Filter + Ar Bubbling, d) AZ91E + Filter + Ar Bubbling + 0.50 wt.% Al-SiC, e) AZ91E + Filter + Ar Bubbling + 0.25 wt.% Al-C, f) AZ91E + Filter + Ar Bubbling + 0.50 wt.% Al-C and g) AZ91E + 0.50 wt.% Al-C

Figure 5-51a and b show SEM images of the tensile fracture surfaces of AZ91E + filter + Ar bubbling + 0.50 wt.% Al-C and AZ91E + 0.50 wt.% Al-C respectively. For both fracture surfaces, traces of a Mg-O based oxide similar to the ones observed in Figure 5-17 were detected. Similarly, an EDX spectrum analysis was also taken near the oxide to ensure the detected O peak was not due to oxidation of the sample surface during preparation or handling. It is expected that the presence of some inclusions will reduce mechanical properties especially for the AZ91E + 0.50 wt.% Al-C casting as the inclusions are relatively large in size. The changes in casting porosity with Al-C refinement were also examined.

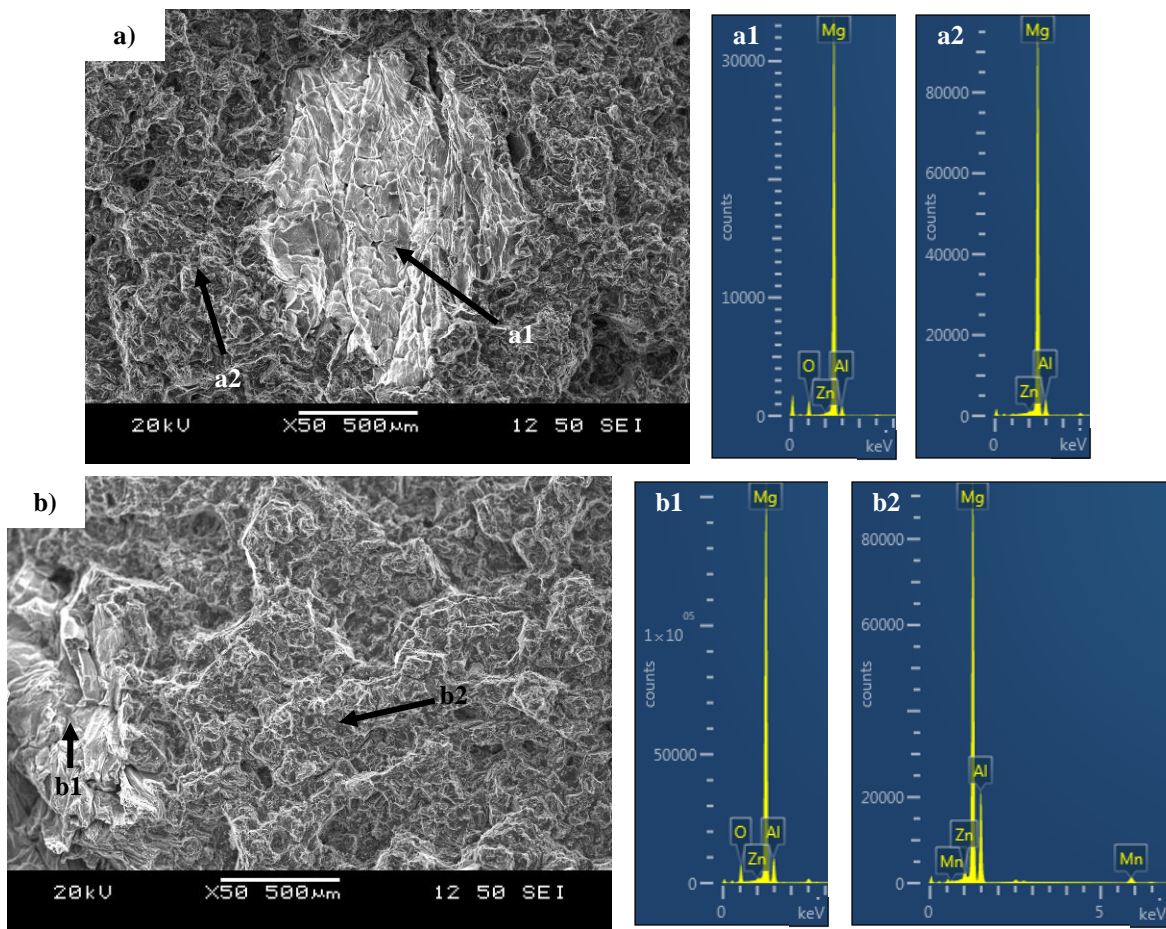


Figure 5-51: Fracture Surfaces of a) AZ91E + Filter + Ar Bubbling + 0.50 wt.% Al-C and b) AZ91E + 0.50 wt.% Al-C

5.7.6 Porosity of SPS Al-C Refiner Treated AZ91E

The average porosity results with error ranges representing one standard deviation are presented in Table 5-8. Porosity was measured using Archimedes principle. The porosity results for the C₂Cl₆, filter + Ar bubbling and Al-SiC addition are also presented for comparison. The use of the Al-C refiner maintained the low porosity values (~1%) observed in the other alloys maintaining that the mechanical properties obtained were influenced by inclusion content and grain size only and not to issues in feeding or shrinkage.

Table 5-8: Summary of Porosity Results for C₂Cl₆ and Al-C Refiner Addition on AZ91E

Casting Condition	Average Porosity (%)
AZ91E	0.7 +/- 0.2
AZ91E + 0.25 wt.% C₂Cl₆	0.8 +/- 0.4
AZ91E + 0.75 wt.% C₂Cl₆	0.9 +/- 0.1
AZ91E + Filter + Ar Bubbling	0.9 +/- 0.3
AZ91E + Filter + Ar Bubbling + 0.50 wt.% Al-SiC	0.8 +/- 0.6
AZ91E + Filter + Ar Bubbling + 0.25 wt.% Al-C	1.0 +/- 0.3
AZ91E + Filter + Ar Bubbling + 0.50 wt.% Al-C	1.1 +/- 0.1
AZ91E + 0.50 wt.% Al-C	1.3 +/- 0.8

5.7.7 Effects of SPS Al-C Refiner Addition on Mechanical Properties of AZ91E

The average mechanical properties, namely the YS, UTS and elongation of AZ91E, AZ91E + filter + Ar bubbling and AZ91E + filter + Ar bubbling + Al-C with error bars representing one standard deviation are presented in Figure 5-52. The mechanical properties of AZ91E + C₂Cl₆ and AZ91E + Al-SiC castings from Figure 5-42 are also included for comparison. Using C₂Cl₆, the highest YS was 100 MPa obtained with 0.25 wt.% while the highest UTS and elongation were 194 MPa and 5.2% respectively using 0.75 wt.%. By using AZ91E + filter + Ar bubbling + 0.50 wt.% Al-C, the average YS, UTS and elongation were 100.4 MPa, 204.5 MPa and 5.3% respectively. This casting scenario provided equivalent YS to the 0.25 wt.% C₂Cl₆ alloy and UTS and elongation to the 0.75 wt.% C₂Cl₆ alloy. The AZ91E + filter + Ar bubbling + 0.25 wt.% Al-C alloy had similar properties but with an average YS, UTS and elongation of 98 MPa, 201 MPa and 5.3% respectively.

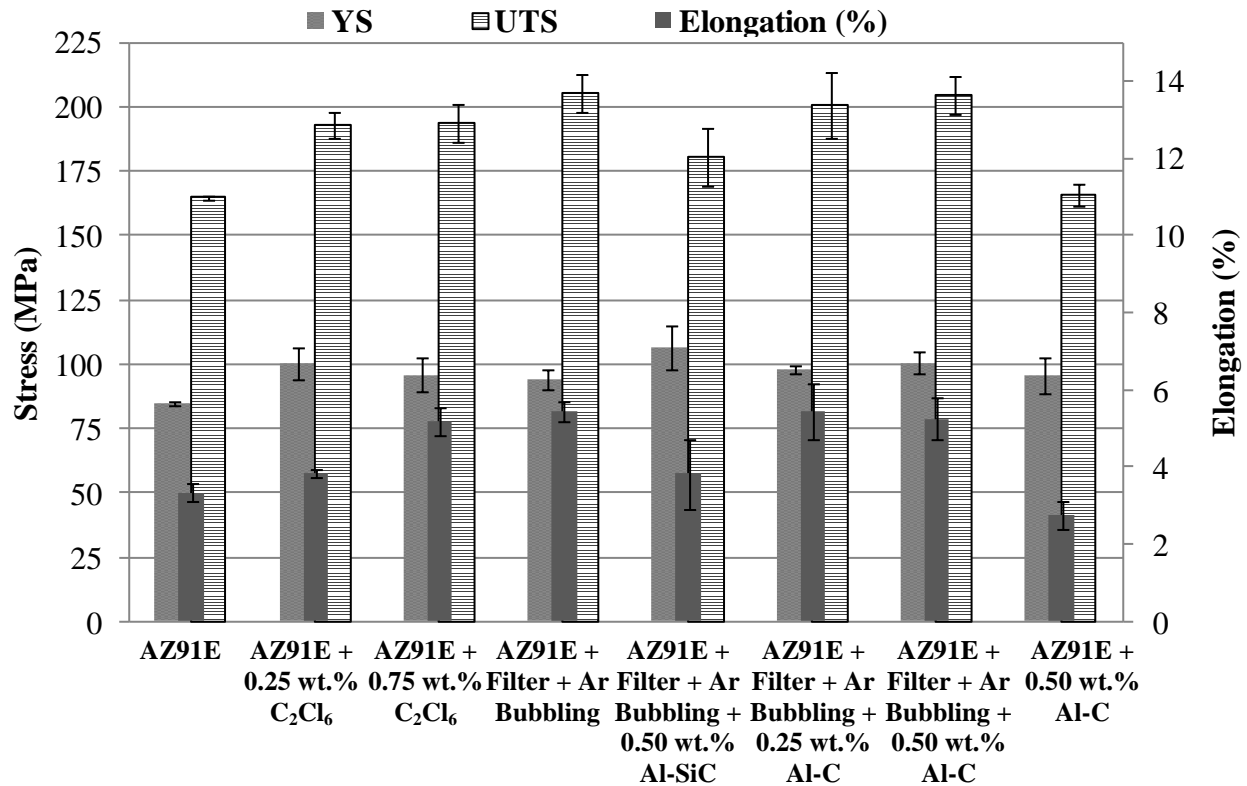


Figure 5-52: Effect of C₂Cl₆ Addition, Filter + Ar Bubbling, Al-SiC Refiner Addition and Al-C Refiner Addition on Mechanical Properties of AZ91E with Error Bars Representing One Standard Deviation

With the addition of 0.50 wt.% Al-C alone to AZ91E, the resulting YS was only slightly above that of the base alloy and the UTS was nearly the same as the base alloy. The average elongation with 0.50 wt.% Al-C was actually lower than the base alloy at 2.8% as compared to 3.3%. The amount of inclusions observed on the fracture surfaces correlate with the UTS and elongation results in Figure 5-52. With fewer inclusions observed on the fracture surface, the castings tended to have higher UTS and elongation's. The 0.75 wt.% C₂Cl₆ and filter + Ar bubbling treated castings had the fewest inclusions on their fracture surfaces and also had the highest UTS and elongation's of nearly 200 MPa and 5% respectively.

The addition of the Al-C refiner required stirring of the melt that agitated the melt surface and has the susceptibility to introduce oxides. In addition, during some experimental trials the Al-C refiner itself would begin to oxidize when it was added to the AZ91E alloy. The fine particle size of the Al made it more likely to oxidize when heated. Oxidation of the Al-C refiner would be mitigated by quickly plunging it under the melt surface but it might have introduced additional oxides into the melt. With filter + Ar bubbling combined with Al-C addition the

amount of entrapped oxides was reduced but can cause issues as observed by the low UTS and elongation of the AZ91E + 0.50 wt.% Al-C sample. Future research could examine developing a better mixing procedure to reduce the entrapment of oxides during grain refiner addition. However, A filter + Ar bubbling + 0.50 wt.% Al-C appears to have the most potential in improving the mechanical properties of AZ91E Mg alloy of the scenarios investigated.

Additional research was conducted to examine the solidification of Mg-6 and 9 wt.% Al alloys using in-situ neutron diffraction. Similar to the results in CHAPTER 4, each alloy was examined in a step-wise fashion while being irradiated by neutrons. The collected diffraction patterns were examined to produce fraction solid curves and also observe the growth of intermetallics.

5.8 Solidification Behaviour of Mg-6 wt.% Al and Mg-9 wt.% Al Alloys Using In-situ Neutron Diffraction

Similar to the in-situ neutron diffraction research in Sections 4.1 and 4.2 the solidification behaviours of Mg-6 wt.% Al and Mg-9 wt.% Al alloys were investigated. While the focus of the research in the Mg-Zn alloys was to examine grain refinement using in-situ neutron diffraction, the focus of the research using the Mg-Al alloys is to examine the influence of alloy composition and detection of intermetallic phases. The microstructure of the Mg-6 wt.% Al and Mg-9 wt.% Al alloys was first examined, followed by the neutron diffraction plots and fraction solid curves.

5.8.1 Microstructure of Mg-6 wt.% Al and Mg-9 wt.% Al Alloys

The Mg-Al phase diagram is shown in Figure A-3 with isopleths highlighting the compositions for Mg-6 wt.% Al and Mg-9 wt.% Al. Under equilibrium conditions, the liquidus temperatures for Mg-6 wt.% Al and Mg-9 wt.% Al are 615 and 595°C respectively. If you look at the Mg-Al phase diagram (Figure A-3), Mg-6 wt.% Al alloy will contain only Mg between the solidus and solvus temperatures. But as you cool below the solvus temperature, the Mg₁₇Al₁₂ phase will appear, although its volume fraction will be less than that for Mg-9 wt.% Al alloy. However, despite holding the samples at each temperature for 1 hour there is a possibility that non-equilibrium cooling and deviations from the phase diagram in Figure A-3 are present.

The general microstructure of the Mg-6 wt.% Al alloy after the in-situ neutron diffraction experiment is shown in Figure 5-53a.

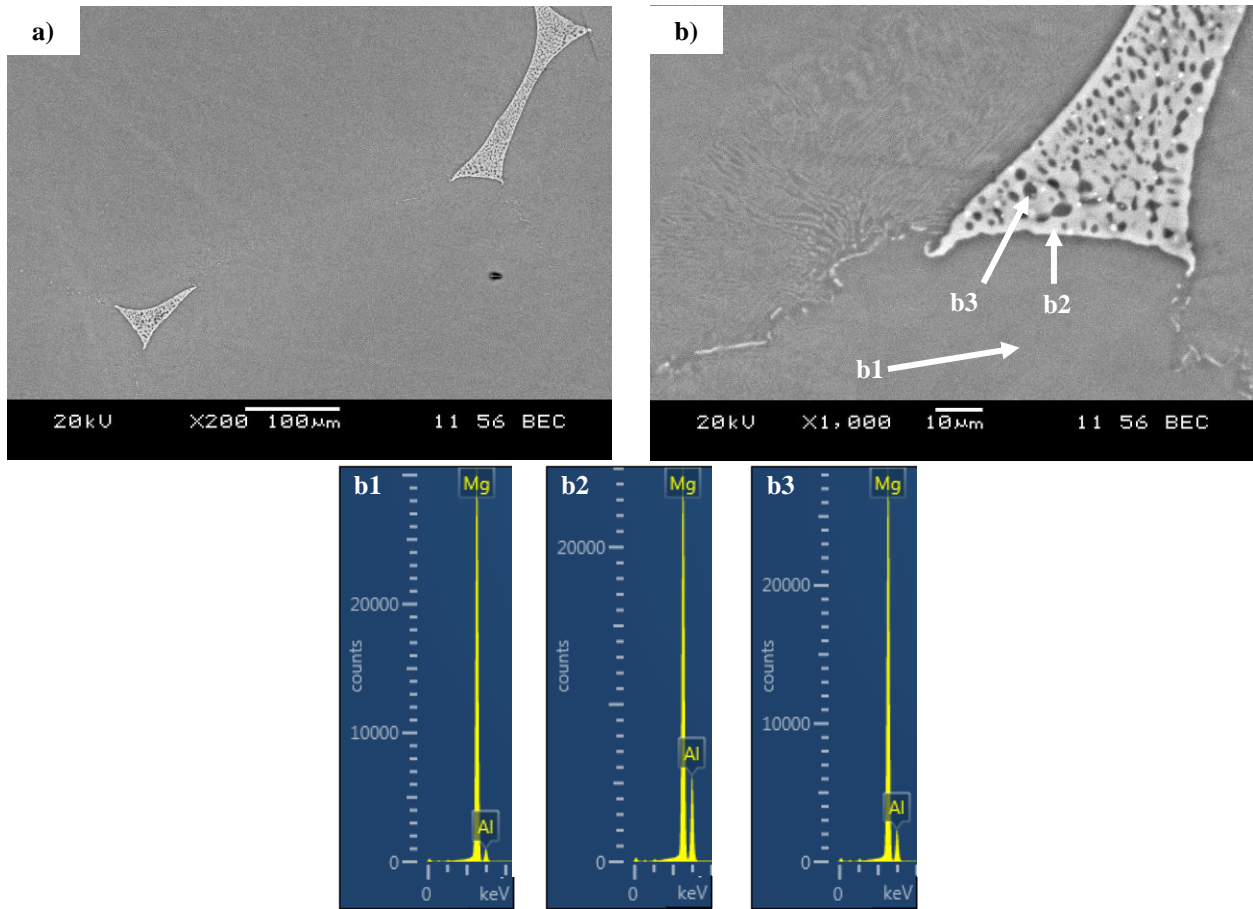


Figure 5-53: SEM Micrograph of Mg-6 wt.% Al Showing a) Primary Mg Matrix with Eutectic Mg₁₇Al₁₂ and b) Magnified Micrograph Showing Eutectic Mg₁₇Al₁₂ with Corresponding EDX Spot Analyses of Points b1, b2 and b3

The microstructure primarily consists of the Mg matrix but in some areas, individual intermetallic particles (<100 μm) can be observed. A higher magnification micrograph of the observed intermetallic phase is shown in Figure 5-53b. Spectrum b1 in Figure 5-53b reveals the Mg matrix has 5.9 wt.% Al in solid solution. The maximum allowable solid solution of Al in Mg is 11.1 wt.% at 437°C from Figure A-3. The composition (spectrum b2) of one of the intermetallic particles was typically Mg: 72.1 wt.% and Al: 27.9 wt.%. This composition corresponds to the liquid at the eutectic composition, indicating that the intermetallic particles observed result from the eutectic reaction forming eutectic Mg and eutectic Mg₁₇Al₁₂ (with a

typical composition of Mg: 60 wt.% and Al: 40 wt.%). The higher Mg concentration could be from increased contribution from the matrix just under the $Mg_{17}Al_{12}$ phase as the spectrum results from a volume of the alloy material rather than the just the surface. Spectrum b3 contained 86.0 wt.% Mg and 14.0 wt.% Al being most likely eutectic Mg. Adjacent to some large blocky eutectic phase was a small amount of sparsely distributed fine lamellar eutectic $Mg_{17}Al_{12}$, which likely contributed to some “extra-Al” readings for spectrum b3.

Similar to the Mg-6 wt.% Al microstructure, the Mg-9 wt.% Al alloy contained primary Mg as well as eutectic Mg and $Mg_{17}Al_{12}$. The general microstructure of the Mg-9 wt.% Al alloy is shown in Figure 5-54a.

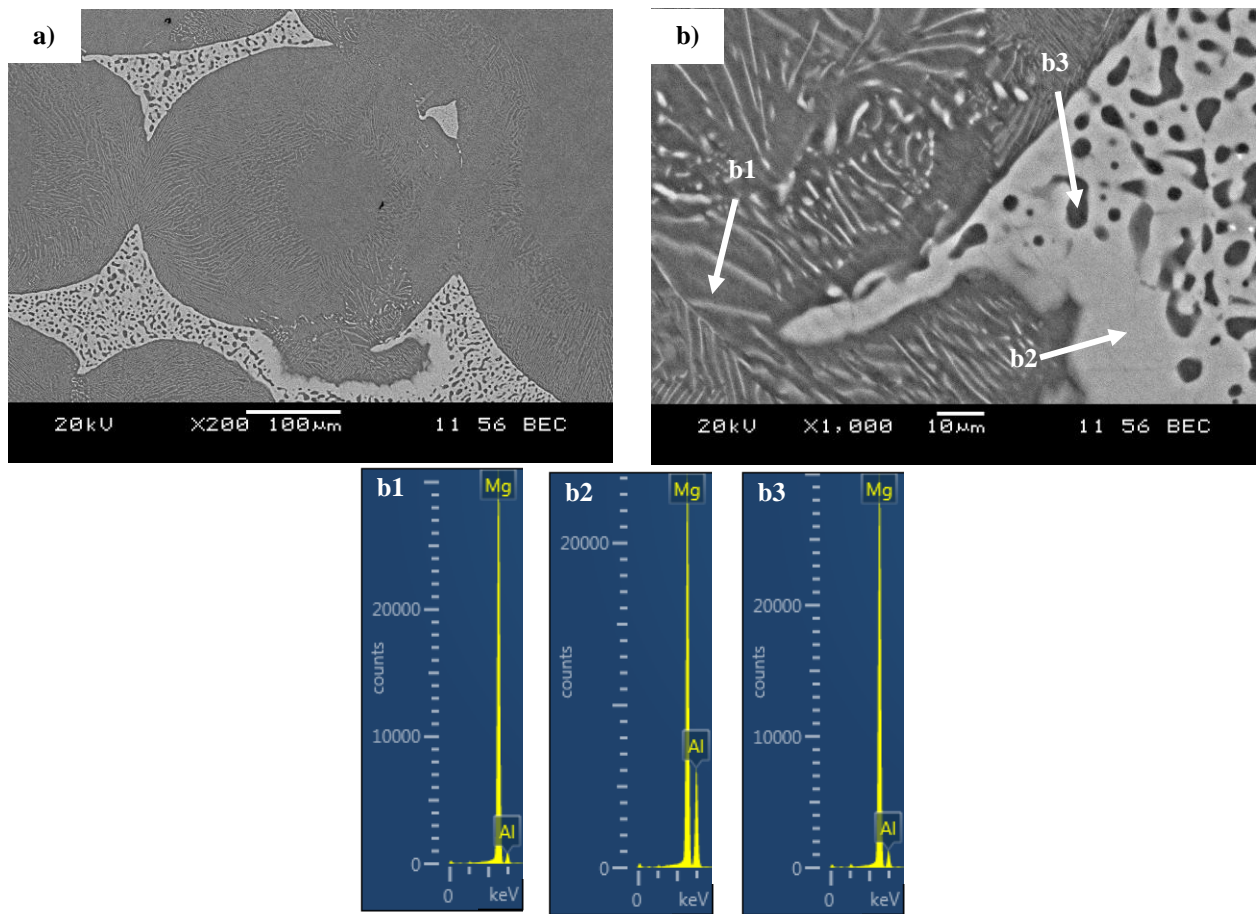


Figure 5-54: SEM Micrograph of Mg-9 wt.% Al Showing a) Primary Mg Matrix with Eutectic $Mg_{17}Al_{12}$ and b) Magnified Micrograph Showing Eutectic Mg and Alternating Al, Mg Rich Lamella with Corresponding EDX Spot Analyses of Points b1, b2 and b3

The Mg-9 wt.% Al alloy had much larger ($>100\ \mu\text{m}$) and more branching $\text{Mg}_{17}\text{Al}_{12}$ as compared to the Mg-6 wt.% Al alloy with more blocky islands of $\text{Mg}_{17}\text{Al}_{12}$. For both Mg-6 wt.% Al and Mg-9 wt.% Al, there is a possibility that the observed $\text{Mg}_{17}\text{Al}_{12}$ resulted from solid state reactions as shown by the solvus line separating the alpha and alpha + $\text{Mg}_{17}\text{Al}_{12}$ regions in Figure A-3. However, the relatively high cooling rate between temperature steps is expected to result in non-equilibrium cooling conditions and the observed intermetallic phases appear rather branched rather than well distributed precipitates as would be expected from a solid-state reaction had equilibrium cooling conditions persisted. Further evidence for the intermetallic phases forming from liquid at the eutectic composition will be presented in the neutron diffraction results. Micrographs from 40 frames at X200 from both Mg-6 wt.% Al and Mg-9 wt.% Al were examined to quantify the area percent of eutectic $\text{Mg}_{17}\text{Al}_{12}$. The Mg-6 wt.% Al and Mg-9 wt.% Al alloys had average area percentages of $0.3 \pm 0.15\%$ and $2.1 \pm 0.4\%$ of $\text{Mg}_{17}\text{Al}_{12}$ respectively. The error ranges represent t-student errors at a 95% confidence level. It is assumed that the area percentage of eutectic $\text{Mg}_{17}\text{Al}_{12}$ is equal to the volume percentage as the microstructures were uniform with solidification occurring evenly in all directions. With conversion to weight concentrations, the average amount of $\text{Mg}_{17}\text{Al}_{12}$ in Mg-6 wt.% Al and Mg-9 wt.% Al were 0.4 wt.% and 2.5 wt.% respectively. A higher magnification micrograph of Mg-9 wt.% Al is shown in Figure 5-54b. Eutectic Mg and $\text{Mg}_{17}\text{Al}_{12}$ as well as lamellar $\text{Mg}_{17}\text{Al}_{12}$ can be observed. The Mg-9 wt.% Al alloy had a much higher presence of both large eutectic as well as lamellar eutectic microstructures as compared to the Mg-6 wt.% Al alloy. Spectrum b1 is an EDX spot analysis of the Mg matrix near the eutectic at a location similar to spectrum b1 in Figure 5-53b and was mainly Mg with 5.2 wt.% Al in solid solution. This is comparable to the amount in Mg-6 wt.% Al with 5.9 wt.% Al. For the Mg-9 wt.% Al alloy, the excess Al is thought to have precipitated as $\text{Mg}_{17}\text{Al}_{12}$ resulting in large branches of the eutectic phase as shown in Figure 5-54a. Spectrum b2 is a spot analysis of the eutectic phase with Mg: 69.3 wt.% and Al: 30.7 wt.% which is very close to the concentration of $\text{Mg}_{17}\text{Al}_{12}$ (Mg: 67 wt.% and Al: 33 wt.%) and similar to the concentrations observed in Mg-6 wt.% Al (Figure 5-53b). Alongside the branched eutectic phase was a large network of very fine (1-2 μm) lamellar eutectic. Since the sample is held at each temperature for 1 hour there is ample opportunity for diffusion processes to promote a lamellar microstructure. This lamellar eutectic was only faintly observed in the Mg-6 wt.% Al alloy and if present was

observed at a much lower extent than the Mg-9 wt.% Al alloy. Spectrum b3 is an EDX spot analysis of the eutectic Mg with composition Mg: 92.3 wt.% and Al: 7.7 wt.%. There were no other phases or oxides observed within the alloys.

The neutron diffraction experiments involved bulk analysis with the diffraction intensity covering the entire sample. Thus, the presence of lamellar or blocky eutectic phases would be treated identically during the diffraction experiments. Only the nominal concentrations of Al in each alloy and the resulting fraction of eutectic versus matrix phases influenced the neutron results.

5.8.2 In-situ Neutron Diffraction Plots of Mg-6 wt.% Al and Mg-9 wt.% Al Alloys

Similar to the neutron diffraction plots for the Mg-Zn alloys in Sections 4.1 and 4.2, plots for the Mg-6 wt.% Al and Mg-9 wt.% Al alloys were prepared to examine neutron intensity against diffraction angle at different temperatures. As the Mg-Al alloys were examined using 6.5 mm in diameter samples without oscillation or agitation only the results from the $(10\bar{1}1)$ plane for Mg will be discussed as it had the highest intensity of all the diffracting planes and offers the best signal to noise ratio.

A graph representing the Mg $(10\bar{1}1)$ plane for the Mg-6 wt.% Al alloy is shown in Figure 5-55. Similar to the plots in Sections 4.1 and 4.2, when the sample is completely molten ($>620^{\circ}\text{C}$) no peaks are observed as neutrons undergo inelastic diffraction with the liquid and the neutron intensity remains relatively constant for the entire analyzed diffraction angle range. As solidification progressed, there was less liquid available to contribute to inelastic diffraction and neutrons began to scatter elastically with the solid phase. The solid phase manifested as peaks in the diffraction data. This transfer from inelastic to elastic diffraction continued as the sample cooled causing a reduction in the observed background and increase in the intensity of the peaks. A peak corresponding to the first instance of solid Mg formation was observed at 600°C . It was expected that the first peak would appear at 610°C as the equilibrium liquidus point from Figure A-3 is 615°C . Closer examination of the diffraction data at 610°C does show a small hump that could possibly be considered as the first instance of solid formation, but its low intensity makes it difficult to distinguish and quantify. Therefore, from the in-situ data, the first instance of solid detection for Mg-6 wt.% Al occurs at 600°C with a peak centred in the range of $56.75\text{-}56.85^{\circ}$. The angular position of the peaks increases as the temperature decreases

corresponding to thermal contraction of the solid metal (a reduction in the lattice spacing reflected by the shift in Bragg's peak position). The samples are allowed to cool freely so residual stresses are expected to be minimal. The contribution from the solid to the diffraction peak integrated area increases as the sample cools. The peaks appear larger and wider at each lower temperature step similar to the observations of Kasprzak *et al.* [306]. At temperatures of 520°C and lower, the background count around the peak (corresponding to the liquid) reaches a minimum and remains relatively constant with decreasing temperature. This minimum in background count indicates that the sample is fully solid as what would be expected under equilibrium conditions (~525°C from Figure A-3).

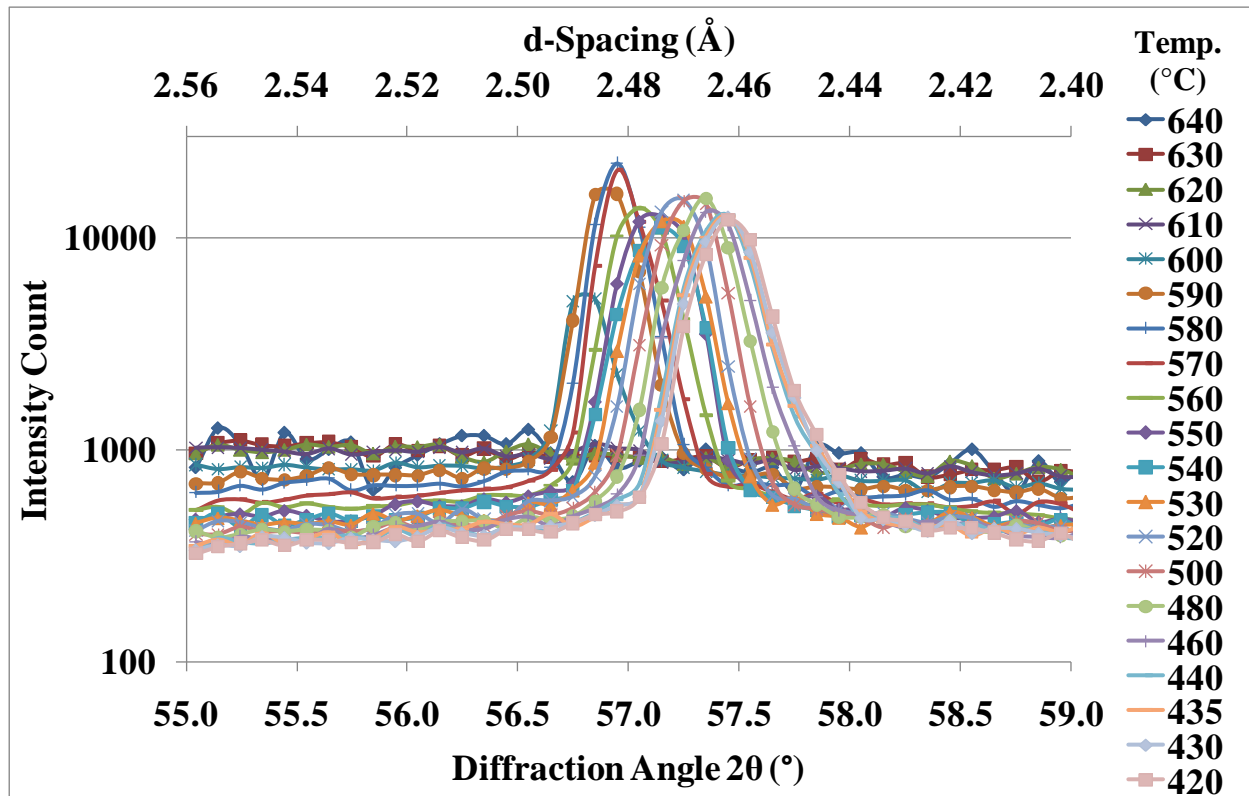


Figure 5-55: Neutron Diffraction Plot of Mg-6 wt.% Al, Mg (10 $\bar{1}1$) Plane

However, the presence of eutectic Mg and Mg₁₇Al₁₂ in Figure 5-53 indicated that solidification was under non-equilibrium conditions and that there were some enriched liquid regions that underwent the eutectic reaction. Since the calculated weight fraction of Mg₁₇Al₁₂ in Mg-6 wt.% Al was only 0.4 wt.% it was likely to be low in concentration to be detected in the diffraction pattern leading to the appearance of a more equilibrium type solidification. Since

eutectic $Mg_{17}Al_{12}$ was detected in the microstructure (Figure 5-53), the temperature of $420^{\circ}C$ was taken to correspond to a fully solid alloy with only solid contributing to the diffraction intensity. The peak corresponding to a fully solidified sample is centred at a diffraction angle of 57.45° . Figure 5-56 is the diffraction plot representing $Mg(10\bar{1}1)$ from the Mg-9 wt.% Al alloy.

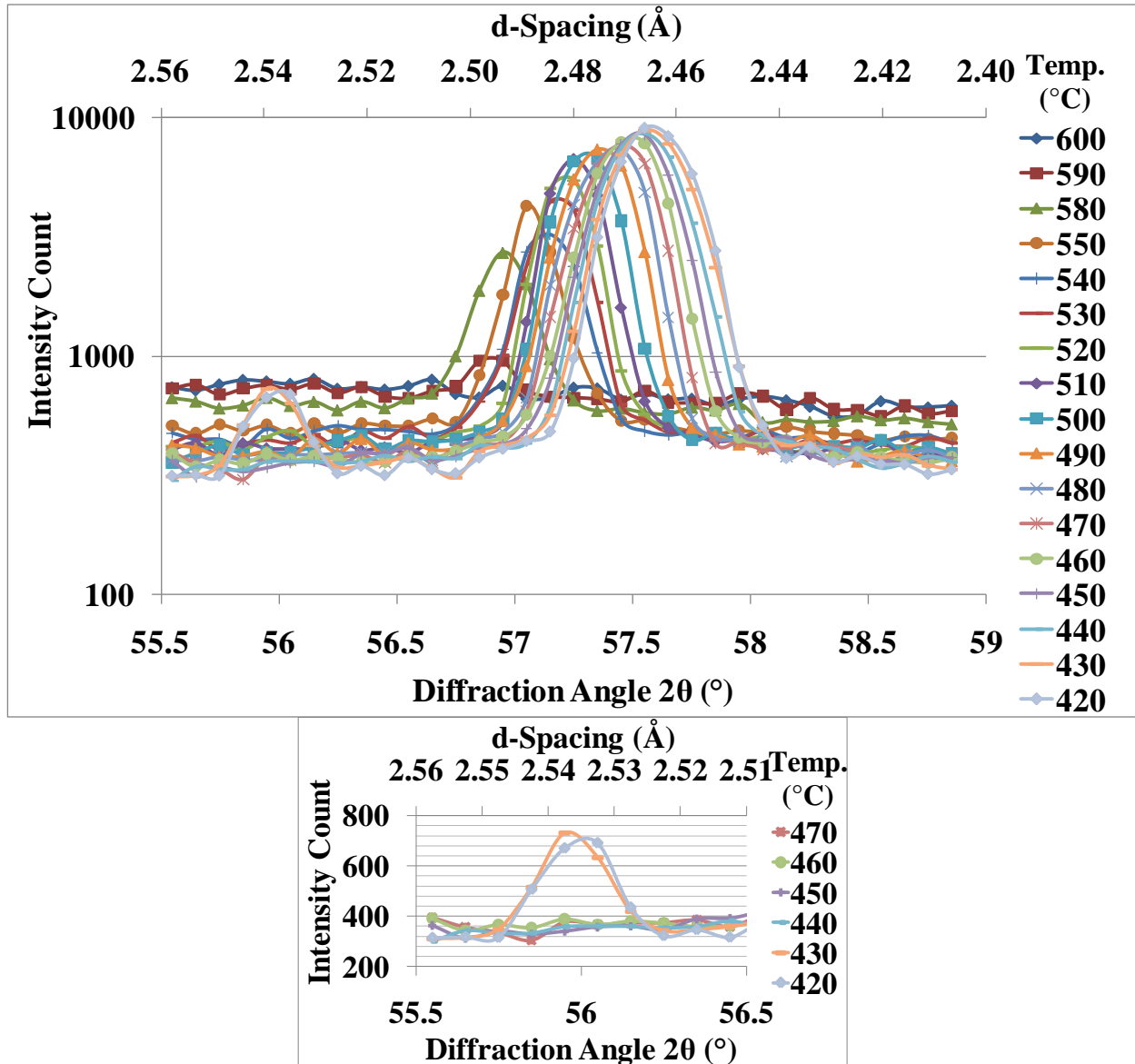


Figure 5-56: Neutron Diffraction Plot of Mg-9 wt.% Al, $Mg(10\bar{1}1)$ Plane and $Mg_{17}Al_{12}(330, 411)$ Planes (Selected Isotherms Omitted for Clarity)

The first clear peak occurs at $590^{\circ}C$ which matches the equilibrium liquidus point from Figure A-3 and published data of $\sim 595^{\circ}C$ [1]. The diffraction peak is centred at $56.85-56.95^{\circ}$.

This diffraction angle is slightly higher than that of the Mg-6 wt.% Al alloy and is attributed to additional Al in solution with Mg. The atomic radius of Al is 0.143 nm [13] and smaller than that for Mg (0.160 nm [1]). Increasing Al concentrations in Mg tends to decrease the dimensions of the Mg lattice. The diffraction peak at 420°C is centred at ~57.55°. A summary of the diffraction plot features for the Mg-6 wt.% Al and Mg-9 wt.% Al alloys are in Table 5-9. The neutron diffraction experiments also detected the (330) and (411) planes for Mg₁₇Al₁₂ as shown in Figure 5-56. If the Mg-9 wt.% Al alloy was undergoing equilibrium solidification, Mg₁₇Al₁₂ would form from a solid-state transformation at 375°C (Figure A-3), but the presence of a clear peak representing Mg₁₇Al₁₂ at 430°C indicates the phase formed from a eutectic reaction at a temperature between 440 and 430°C, correlating with published values of 437°C [1].

Table 5-9: Summary of Diffraction Plot Features of Mg-6 wt.% Al and Mg-9 wt.% Al Alloys

Alloy	Mg-6 wt.% Al	Mg-9 wt.% Al
Solidification start temperature (°C)	600	590
Centre of diffraction peak at solidification start (°)	56.75-56.85	56.85-56.95
Final temperature (°C)	420	420
Centre of diffraction peak at final temperature (°)	57.45	57.55

As discussed earlier, the microstructures of both Mg-6 wt.% Al (Figure 5-53) and Mg-9 wt.% Al (Figure 5-54) alloys contained blocky eutectic Mg₁₇Al₁₂ and the Mg₁₇Al₁₂ was present in a higher weight fraction in Mg-9 wt.% Al than Mg-6 wt.% Al. The formation of the eutectic phase is also observed in the diffraction plot of Mg-9 wt.% Al, Figure 5-56 from (330) and (411) plane reflections. The eutectic phase was not observed in the diffraction plot of Mg-6 wt.% Al (Figure 5-55) as its weight concentration of 0.4 wt.% was too low for detection. Therefore, under the present experimental conditions, using Mg-6 wt.% Al and Mg-9 wt.% Al, the crossover between detectable and non-detectable eutectic using in-situ neutron diffraction lies between 0.4 and 2.5 wt.% Al. The observation of Mg₁₇Al₁₂ peaks demonstrates that even low concentrations of intermetallic phases can be detected and characterized using in-situ neutron diffraction.

5.8.3 Fraction Solid Curves of Mg-6 wt.% Al and Mg-9 wt.% Al Alloys

Similar to the Mg-Zn alloys in CHAPTER 4, for the highest temperatures investigated (630°C for Mg-6 wt.% Al and 620°C for Mg-9 wt.% Al), the alloys were completely liquid and

their corresponding diffraction peak integrated intensities were zero until the nucleation temperatures of 600 and 590°C for Mg-6 wt.% Al and Mg-9 wt.% Al respectively. Subsequent decreasing temperatures represented continual increases in solid fraction until the alloys were fully solid. Since both the Mg-6 wt.% Al and Mg-9 wt.% Al alloys contained eutectic alpha and eutectic Mg₁₇Al₁₂, the lowest temperature (420°C) examined, the diffraction peak integrated intensities were at a maximum representing completely solid alloys. Every intermediate temperature between these two extremes represented an alloy undergoing solidification, with its diffraction peak integrated intensity representing the fraction solid. By determining the diffraction integrated intensity for each temperature, a plot of fraction solid versus temperature can be developed. The data was normalized to values between 0 (fully molten) to 1 (fully solid). The fraction solid curve versus temperature plots for the Mg (10 $\bar{1}$ 1) plane for both Mg-6 wt.% Al and Mg-9 wt.% Al alloys are shown in Figure 5-57.

The Mg-6 wt.% Al alloy showed ~0.3 fraction solid at 600°C and around one at 590°C and below, to 420°C. For the Mg-6 wt.% Al, the fraction solid curve is similar to the plot observed in Al alloys [306,307] that tend to show a very rapid solid growth over a very short temperature interval. For the Mg-9 wt.% Al alloy the resulting fraction solid curve showed a gradual growth in Mg as the alloy is cooled over the investigated temperature range. The results for this Mg-9 wt.% Al alloy are explained by the grain growth restriction effect of Al. Aluminum in Mg has a growth restriction factor of 11.9 with 3 wt.% Al [117]. With 9 wt.% Al addition (present study), the growth restriction effect of Al ($Q = 38.9$ K) is expected to be significant. It is thought that Al acts as a regulator to growing Mg grains causing a very gradual formation of solid within the temperature range investigated. The result is a more gradual transition of Mg from liquid to solid for the Mg-9 wt.% Al alloy. Fluctuations in the diffraction data between individual temperature steps for both alloys could be the result of planar and angular motion of grains within the melt which affects the observed diffraction intensities. This is a possible explanation for why the apparent fraction solid of Mg-6 wt.% Al may increase beyond one. The grains at one temperature step could have been oriented highly favourably for diffraction while at the next temperature step, the grains could have shifted and caused a decrease in diffraction intensity and related peak size.

Another factor could be the competition between neighbouring grains which are continually growing and consuming each other until they ultimately reach an equilibrium grain size. These

mechanisms were suggested to be a possible source of data fluctuations in the study by Iqbal *et al.* [303,304]. As the temperature decreases, the grains approach an equilibrated state and fluctuations in fraction solid decrease as observed in Figure 5-57 for Mg-6 wt.% Al at 460°C and lower.

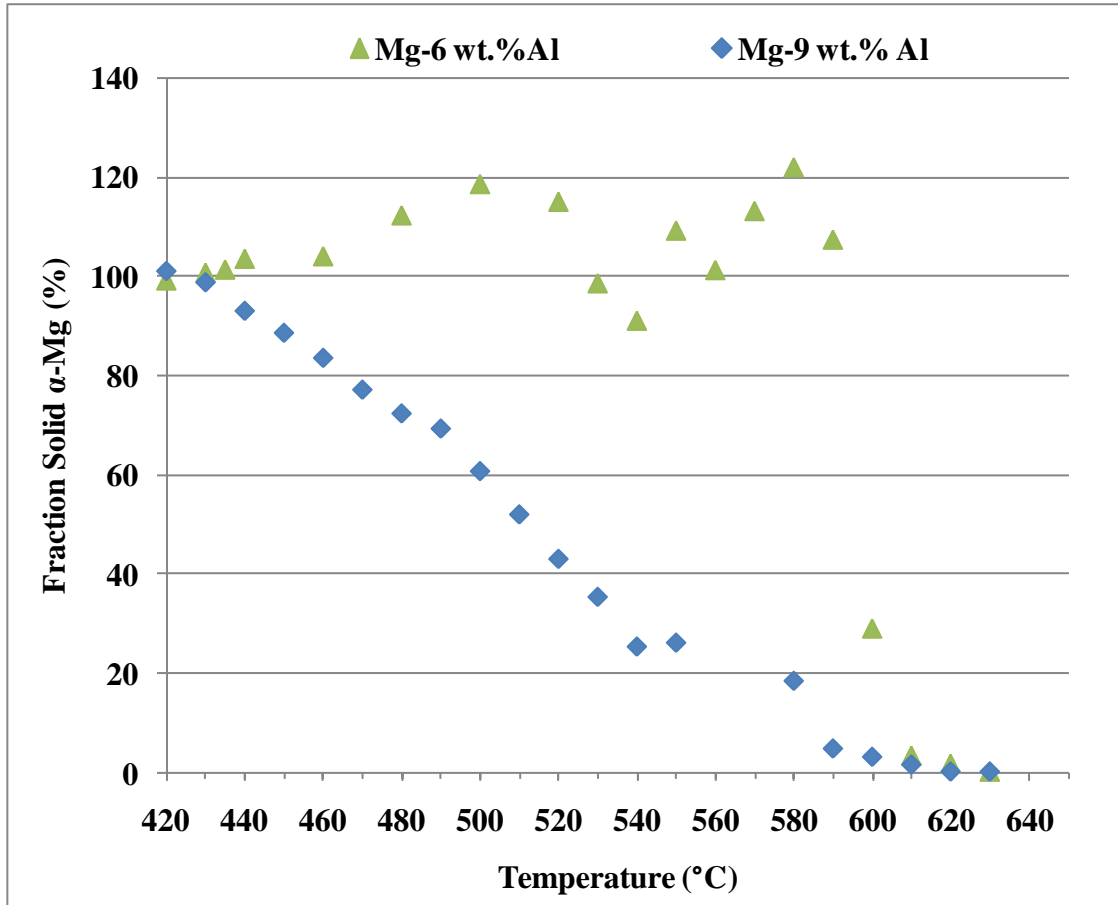


Figure 5-57: Fraction Solid Curves of Mg ($10\bar{1}1$) from In-situ Analysis of Mg-6 wt.% Al and Mg-9 wt.% Al Alloys' Solidification

The fluctuations for the Mg-6 wt.% Al alloy were larger than those of the Mg-9 wt.% Al alloy and were attributed to the more uniform microstructure of the Mg-9 wt.% Al alloy. The Mg-9 wt.% Al alloy had more branching $Mg_{17}Al_{12}$ distributed throughout the microstructure while the Mg-6 wt.% Al alloy had only pockets of $Mg_{17}Al_{12}$. The more uniform microstructure in the Mg-9 wt.% Al alloy would result in fewer fluctuations in the fraction solid data as the competition between neighbouring grains and liquid regions would be uniform throughout the

sample while in the Mg-6 wt.% Al alloy, the more uneven microstructure resulted in large difference in the distribution of solid and liquid material between temperature steps. Similar to the Mg-Zn and Mg-Zn-Zr alloys examined, it is thought that better statistical results could be obtained by oscillating the samples while they were being irradiated with neutrons. Also, larger samples sizes and lower temperature analysis to account for Debye-Waller effects are expected to improve counting statistics for future investigations. Further research can be conducted to examine the growth of the $Mg_{17}Al_{12}$ intermetallic phase in the same manner as was conducted for the Mg matrix. Therefore, fraction solid curves for individual intermetallic phases could be developed and examined with changing cooling rate and alloy concentration.

5.9 Chapter Summary

Combined filtration and Ar bubbling was effective in reducing the amount of oxide inclusions on the fracture surfaces of AZ91E Mg alloy. An environmentally friendly alternative to the combined inclusion removal and grain refinement performance of C_2Cl_6 addition was developed. The ex-situ Al-SiC grain refiner was produced by examining changes in wettability with composition, reactivity at different temperatures and phases within its microstructure but introduced unwanted oxides that reduced UTS and elongation. The in-situ Al-C grain refiner was produced by using SPS and contained only Al and C phases. Grain refinement by C_2Cl_6 , Al-SiC and Al-C addition was by a duplex mechanism involving Mn-Al and Al-Mg-C-O phases. In-situ neutron diffraction was able to detect the eutectic $Mg_{17}Al_{12}$ phase and characterize the fraction solid growth of Mg-6 and 9 wt.% Al alloys.

CHAPTER 6

CONCLUSIONS

This chapter contains the specific conclusions and the impact of this research.

6.1 Solidification of Mg-Zn and Mg-Zn-Zr Alloys Using In-situ Neutron Diffraction

1. The in-situ neutron diffraction plots of the Mg-3wt.% Zn alloy showed increasing neutron diffraction intensity with decreasing temperature corresponding to a continuous transition from liquid diffuse diffraction to elastic diffraction from a solid.
2. Larger sample volumes and sample oscillation aided in examining coarse grained Mg-Zn alloys.
3. The fraction solid growth of the $(10\bar{1}0)$, (0002) and $(10\bar{1}1)$ planes was more uniform in the Mg-5 wt.%-0.7 wt.% Zr alloy than the Mg-5 wt.% Zn alloy and resulted in equiaxed and irregular grain structures respectively. The results also closely followed FactSage™ simulations.

6.2 Inclusion Removal by Melt Filtration and Ar Bubbling

1. The use of a fine mesh filter within the well of the mould combined with Ar bubbling was effective in reducing the amount of oxide inclusions on the fracture surfaces while maintaining low porosity. The filter + Ar bubbling had better mechanical properties than those for the untreated alloy.

6.3 Modeling of Melt Filtration During Casting

1. The filter enabled a more regulated mould filling, reducing the possibility of oxide formation and entrapment. The liquid metal velocity in the runner system was ~0.5 m/s for filtered castings and 1 m/s for unfiltered castings.

6.4 Grain Refinement Using C₂Cl₆

1. The AZ91E castings had an average grain size, YS, UTS and elongation of 95 μm, 84.9 MPa, 164.7 MPa and 3.3%.
2. The 0.25 and 0.75 wt.% C₂Cl₆ refined castings provided a significant decrease in average grain size (21 and 18%), and increases in average YS (18 and 11%), UTS (17 and 17%) and elongation (18 and 58%) respectively as compared to the AZ91E castings.
3. Grain refinement and inclusion removal was done in one step with C₂Cl₆ addition. Grain refinement was achieved by a mechanism involving duplex formation of blocky Mn-Al particles and an Al-Mg-C-O phase.

6.5 Preparation of Al-SiC Refiners

1. The Al-2 wt.% Si-1.25 wt.% Mg-11.9 wt.% SiC alloy prepared at 800°C for 2 hours offered a good combination of high wettability, near complete reaction of Al and SiC, contained desired nucleating particles and had a uniform microstructure.

6.6 Grain Refinement Using Al-SiC

1. The AZ91E + filter + Ar bubbling + 0.50 wt.% Al-SiC castings provided a significant decrease in average grain size (23%), and increase in average YS (25%), UTS (10%) and elongation (15%) respectively as compared to the AZ91E castings.
2. Ex-situ grain refinement using Al-SiC resulted in blocky Mn-Al particles and duplex nucleants of Mn-Al and Al-Mg-C-O (likely Al₂MgC₂) phases.
3. Addition of Al-SiC offered higher YS than C₂Cl₆ treated AZ91E but had lower UTS and elongation because of agglomerated particles and melt stirring potentially entrapping inclusions.

6.7 Grain Refinement Using SPS Al-C

1. AZ91E + filter + Ar bubbling + 0.50 wt.% Al-C castings provided a significant decrease in average grain size (21%), and increase in average YS (18%), UTS (24%) and elongation (60%) respectively as compared to the AZ91E castings.
2. In-situ grain refinement using SPS Al-C was similar to Al-SiC resulting in blocky Mn-Al particles and duplex nucleants of Mn-Al and Al-Mg-C-O (likely Al₂MgC₂) phases.

3. This casting scenario provided equivalent YS to the 0.25 wt.% C_2Cl_6 alloy and UTS and elongation to the 0.75 wt.% C_2Cl_6 alloy.

6.8 Solidification of Mg-Al Alloys Using In-situ Neutron Diffraction

1. The Mg-9 wt.% Al alloy contained branched and lamellar $Mg_{17}Al_{12}$ while the Mg-6 wt.% Al alloy contained mainly blocky $Mg_{17}Al_{12}$.
2. In-situ neutron diffraction enabled detection of the formation of $Mg_{17}Al_{12}$ in Mg-9 wt.% Al.
3. The Mg-6 wt.% Al alloy solidified with a high solid fraction appearing quickly after nucleation while the Mg-9 wt.% Al alloy showed a more gradual transition from completely liquid to completely solid.

6.9 Academic, Industrial and Societal Impact of the Dissertation

The major contributions to literature were:

1. Novel grain refiners were produced using wettability analysis and SPS.
2. An effective inclusion removal (filter + Ar bubbling) and grain refinement was accomplished using environmentally friendly carbon alternatives (Al-C and Al-SiC) to C_2Cl_6 .
3. Pioneering solidification research using in-situ neutron diffraction of Mg alloys has been successfully completed enabling a greater scientific understanding of nucleation, grain refinement and phase formation in Mg alloys.

With effective inclusion removal techniques, development of new carbon grain refiners with performance equivalent to C_2Cl_6 addition and increased knowledge of Mg solidification using in-situ neutron diffraction, Mg alloys with high mechanical properties could be realized. Enhanced mechanical properties of Mg alloys would allow their use in more structurally demanding automotive and aerospace applications, furthering goals of component weight reduction for increased vehicle performance with reduced emissions.

CHAPTER 7

FUTURE WORK

The current study examined different carbon grain refiners and their performance in improving mechanical properties of AZ91E Mg alloy. Research utilizing in-situ neutron diffraction to examine the solidification of Mg-Zn and Mg-Al alloys was also conducted. Further investigations are required to examine the influence of different addition levels, refiner composition and other addition parameters (holding time, addition temperature and addition technique) on the grain refinement and mechanical properties of other Mg systems. The influence of cooling rate, other grain refiners and commercial alloy systems should also be examined using in-situ neutron diffraction.

7.1 Grain Refiner Preparation and Addition Parameters

Addition of the Al-SiC and Al-C grain refiners was carried out using a stirrer that may have introduced oxides within the melt. Future research could examine the potential for combining melt bubbling with grain refinement in one step, possibly by using a mixed Ar + CO₂ bubbling gas. The preparation parameters used to prepare the Al-SiC and Al-C grain refiners could be widened to include different addition levels, addition temperatures, holding times, sintering times and refiner composition to a variety of Mg alloy systems and binary alloys of Mg-Al. The Al-SiC refiner could also be prepared under an inert gas or under vacuum to prevent the formation of oxides that could be introduced into the melt during refining.

7.2 In-situ Neutron Diffraction

Further Mg alloy systems including commercial alloys (e.g. AZ91, ZK61 and AE42) could be examined using in-situ neutron diffraction. Casting parameters such as cooling rate, influence of carbon grain refiners and composition could also be examined for better understating of Mg alloy solidification.

APPENDICES

A.1 Phase Diagrams

A representation of the Al-C-Mg phase equilibria is shown in Figure A-1. The equilibrium Mg-Zn, Mg-Al and Al-Si phase diagrams are shown in Figure A-2 to Figure A-4 respectively.

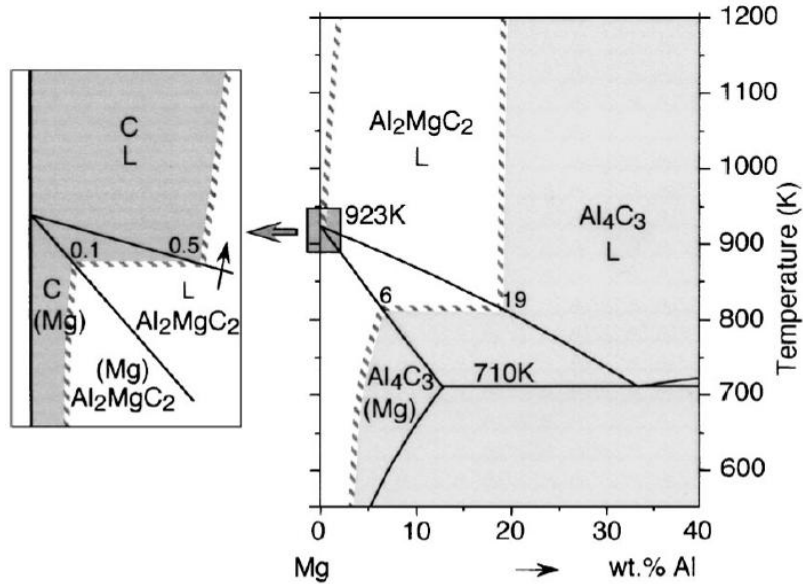


Figure A-1: Tentative Representation of the Al-C-Mg Phase Equilibria below 1000 K [280]

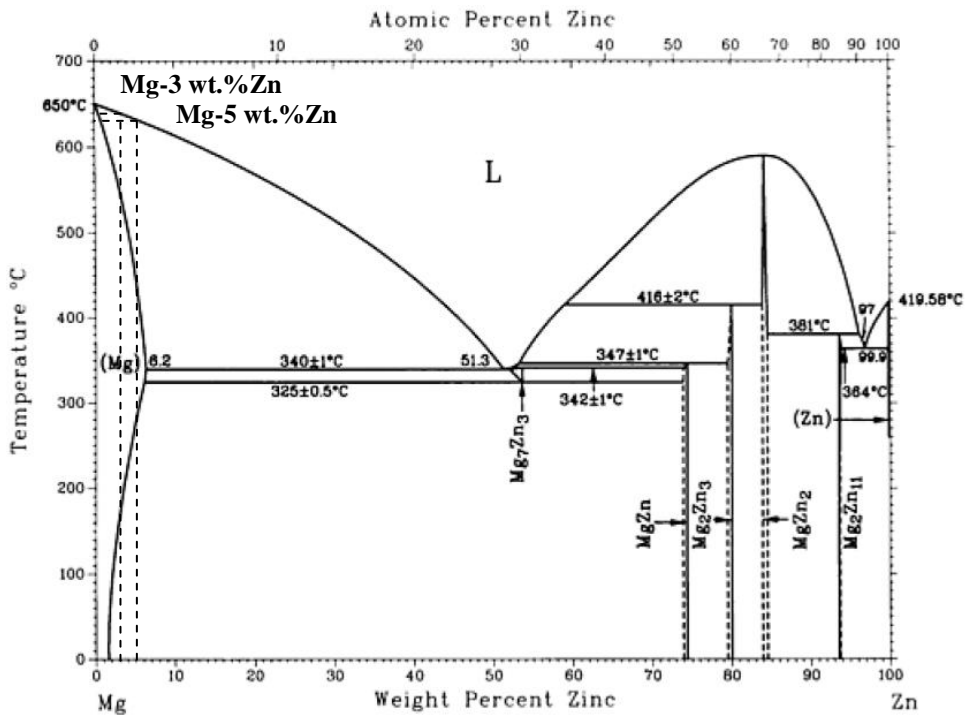


Figure A-2: Mg-Zn Phase Diagram [1]

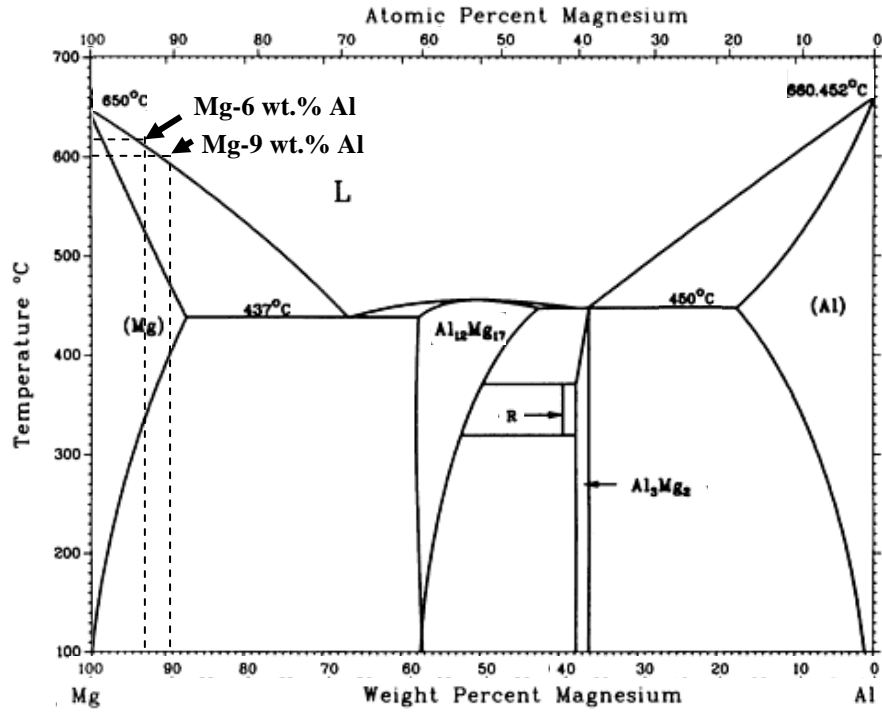


Figure A-3: Mg-Al Phase Diagram [1]

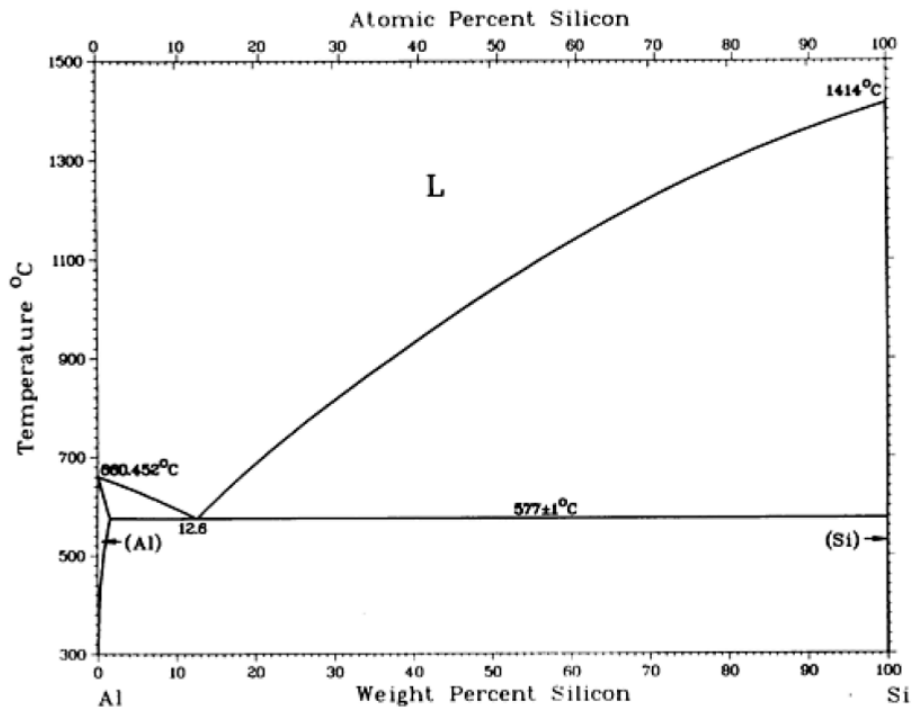


Figure A-4: Al-Si Phase Diagram [13]

A.2 Additional Grain Refinement Techniques

These grain refinement techniques were included in Table 2-13 and are discussed in further detail in the following sections.

A.2.1 Aluminum-Boron (Al-B) Grain Refiner

Suresh *et al.* [141,255] and Nishino *et al.* [256] examined grain refinement using a Al-4 wt.% B grain refiner and observed AlB_2 nucleants because of its low planar disregistry of ~6% (Table 2-9). A summary of the results are in Table A-1.

Table A-1: Grain Size and Mechanical Properties with the Addition of Al-4 wt.% B to AZ91 and Pure Mg

Alloy	Grain Size (μm)/% Reduction	YS (MPa)	UTS (MPa)	Elongation (%)	Ref.
Pure Mg	1300 to 210/84	~45 to ~66	~96 to ~139	-	[141]
AZ91	100 to 30/70	95 to 113	180 to 229	3.3 to 4.9	[255]
AZ91	300 to 80/73	-	-	-	[256]

The refining effect of B was compared against C_6Cl_6 . The C_6Cl_6 began to show signs of fading after 40 minutes while the B added alloys showed a fine grain size up to 100 minutes [256]. Ma *et al.* [143] combined B and C to produce Al-1 wt.% B-0.6 wt.% C refining AZ63 alloy from 710 to 70 μm (90% reduction) using 2 wt.% addition [143]. The refiner contained Al and 2-8 μm Al_3BC particles as its planar disregistry with Mg is 8.8% (Table 2-9) along their basal planes [143]. However, these additions were not compared to C additions. Similar to what is used for Al alloys, Ti based additions have shown promise in Mg alloys.

A.2.2 Titanium Based Additions

Typically Ti based additions are made using Al as a carrier with many Al-Ti based additions containing TiB_2 or TiC particles which are thought to behave as grain refiners for Mg-Al alloys [269]. Titanium based additions will be discussed according to other elements their produced with Al-Ti refiners first, then Al-Ti-B and finally Al-Ti-C refiners.

A.2.2.1 Aluminum-Titanium (Al-Ti) Grain Refiners

For Al-Ti based additions, the major contributions are from TiAl₃ and Ti solute. The planar disregistry of TiAl₃ is relatively high (Table 2-9) leading to some refinement but a contribution to the grain refining potential of Al-Ti based grain refiners stems from the high growth restriction factor (Q, Section 2.6) value of Ti. It has been calculated that m(k-1) for Ti is $\sim 5.95 \times 10^4$ K/wt.% and Ti is believed to behave in a manner to the peritectic reaction of Zr [118]. As indicated in Table 2-8 (Section 2.6), the m(k-1) value for Ti is much larger than other solutes that are added to Mg melts. The growth restriction effect of Ti is unfortunately limited by its low solubility (0.006 wt.%) in Mg melts. The m(k-1) value for Zr is lower than that of Ti, but the higher solubility of Zr (0.45 wt.% as compared to 0.006 wt.% for Ti) in Mg makes it a better choice to grain refine Mg alloys free of Al from a constitutional viewpoint [117]. A summary of the grain refinement experiments using Ti-Al based additions is provided in Table A-2.

Table A-2: Grain Refining Results of Ti-Al based Additions

Refiner Details (wt.%)	Alloy	Grain Size (μm)/% Reduction	Mechanism	Ref.
Al-5Ti	Mg	~ 575 to $\sim 475/17$	TiAl ₃ nucleants	[142]
TiAl₃	Mg	5000-6000 to 2000/60-67	TiAl ₃ nucleants	[2]
Al-10Ti	AZ31	1100 to 110/90	-	[118,257]

A.2.2.2 Aluminum-Titanium-Boron (Al-Ti-B) Grain Refiners

Aluminum-Titanium-Boron based refiners are of interest because planar disregistry calculations (Table 2-9) and edge-to-edge model results showed that TiB₂ is a potential nucleant for Mg [144] (Table 2-10). Both Al-5 wt.% Ti-1 wt.% B (containing TiB₂ and TiAl₃) and Al-1 wt.% Ti-3 wt.% B (containing TiB₂ and AlB₂) refined AZ91E. The grain refinement was attributed to TiB₂ and AlB₂ providing nucleating sites and only TiB₂ providing growth restriction [258]. The Al-5 wt.% Ti-1 wt.% B refiner was also observed to delay dendrite coherency and increase coherency fraction of solid from 10 to 20% [259]. However, only the Al-1 wt.% Ti-3 wt.% B refiner was able to reduce hot tearing because it was free of coarse, brittle TiAl₃ [260].

Wang *et al.* [261] produced a Al-TiB₂ alloy free of TiAl₃ by using a Ti:B = 1:2.5 and Cao *et al.* [262] eliminated TiAl₃ in a Al-TiB₂ alloy with Ti:B = 2 by holding the Al-TiB₂ alloy in the molten state for preparation of Mg based composites reinforced by TiB₂. The results of

many authors indicate that TiB_2 could act as a nucleant while excess additions help refine the grain size by providing growth restriction. Adjusting Ti and B levels enables control of TiB_2 , AlB_2 and $TiAl_3$ phases. A summary of the grain refinement experiments using Ti-Al based additions is provided in Table A-3.

Table A-3: Grain Refining Results of Al-Ti-B based Additions

Refiner Details (wt.%)	Alloy	Grain Size (μm)/% Reduction	Mechanism	Ref.
Al-5Ti-0.2B	Mg	~575 to ~400/30	TiB_2 nucleants	[142]
Al-5Ti-1B	Mg	~575 to ~325/43	AlB_2 nucleants	
Al-3Ti-3B	AZ31	300 to 50/83	TiB_2 and AlB_2 nucleants and TiB_2 growth restriction	[263]
Al-4Ti-5B	AZ31	1100 to 80/93	TiB_2 nucleants	[91]
Al-5Ti-1B	AM60B	348 to 76/78	TiB_2 nucleants	[264]
Al-5Ti-1B	AZ91D	422 to 79/81	TiB_2 nucleants	[265]
Al-5Ti-1B	AZ91E	1122 to 256/77	TiB_2 nucleants and TiB_2 growth restriction	[258,266]
Al-1Ti-3B	AZ91E	1122 to 361/68	TiB_2 and AlB_2 nucleants and TiB_2 growth restriction	
Al-5TiB₂	AZ91E	782 to 318/59	TiB_2 nucleants	[250]
Mg-50TiB₂	AZ91D	240 to 50/79	TiB_2 nucleants	[145]

A.2.2.3 Aluminum-Titanium-Carbon (Al-Ti-C) Grain Refiners

Aluminum-Titanium-Carbon refiners typically contain very fine TiC particles that are not stable and will form Al_4C_3 . This transformation of TiC to Al_4C_3 can be accelerated using Si and B additions producing a refiner with Al_4C_3 for Mg alloys [267].

Xu *et al.* [146] used a Al-Ti-C-Y grain refiner to reduce the grain size of AZ31 Mg alloy. Addition of Al-Ti-C-Y refined the grain size by TiC nucleating particles and Al_3Y particles were found at the grain boundaries indicating their potential in restricting grain growth [319]. The additions that had lower planar disregistry (Table 2-9), tended to provide better refinement but were not an absolute measure of refiner performance because of a variation in particle morphologies [142].

Titanium based additions are very effective in a wide range of Mg-Al alloys as observed by their promising grain refinement results but are likely not as cost effective as C based additions. A summary of the grain refinement experiments using Ti-Al based additions is provided in

Table A-4. Newly developed refiners using ZnO, Al₂Y and AlN have also shown grain refinement in Mg alloys.

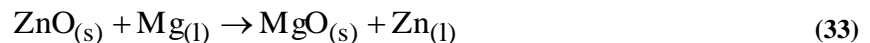
Table A-4: Grain Refining Results of Al-Ti-C based Additions

Refiner Details (wt.%)	Alloy	Grain Size (µm)/% Reduction	Mechanism	Ref.
Al-3Ti-0.15C	Mg	~575 to ~350/39	TiC nucleants	[142]
Al-4Ti-1.15C	AZ31	600 to 390/35	TiC nucleants	
Al-4Ti-1.15C-6Si	AZ31	600 to 550/8	Al ₄ C ₃ nucleants poisoned by TiAl _x Si _y	[267]
Al-4Ti-1.15C-0.6B	AZ31	600 to 320/47	AlB ₂ nucleants	
Al-4Ti-1.15C-6Si-0.6B	AZ31	600 to 150/75	Al ₄ C ₃ , TiC and residual TiB ₂ acting as nucleants	
Al-0.6Ti-1C	AZ31	~850 to ~340/60	Al ₄ C ₃ and TiC	
Al-1Ti-1C	AZ31	~850 to ~200/76	Al ₄ C ₃ and TiC	[268]
Al-1.6Ti-0.4C	AZ31	~850 to ~500/41	TiC	
Al-Ti-C-Y	AZ31	580 to 170/71	TiC nucleants and Al ₃ Y growth restriction	[146]

A.2.3 Grain Refinement by ZnO, Al₂Y and AlN Additions

The edge-to-edge model (Table 2-10) demonstrated that ZnO, Al₂Y and AlN were all potential refiners for Mg alloys and their refining performance were examined experimentally as shown in Table A-5.

The addition of ZnO resulted in the presence of MgO that may have arisen from oxidation of the melt or reduction of ZnO according to Equation 33 [154] that may limit its performance:



The liberated Zn is thought to increase solute within the melt providing some growth restriction [154,270]. However, ZnO addition was unable to reduce hot tearing susceptibility in permanent mould castings [271].

The grain size of the Al₂Y refined sample in Table A-5 increased to 40 µm with holding the sample at 550°C for 48 hours demonstrating the high thermal stability of Al₂Y and its ability to form a Mg-Al-Y precipitate, pinning grain boundaries [155].

Table A-5: Grain Refining Results of ZnO, Al₂Y and AlN Additions

Alloy (wt.%)	Addition Level (wt.%)	Grain Size (μm)/% Reduction	Ref.
ZnO Addition			
Mg	3	1100 to 410/63	[154]
Mg-3Zn	1	420 to 310/26	
Mg-9Al	3	288 to 93/68	[270]
AZ91E	0.75	217 to 108/50	
Al₂Y Addition			
Mg-10Y	1 (Al) ¹	180 to 36/80	[155]
AlN Addition			
Mg-3Al	0.5	450 to 120/73	[156]
AZ31	0.2	not specified	[148]

¹The addition of 1 wt.% Al to Mg-10 wt.% Y alloy at 730°C resulted in the formation of in-situ Al₂Y

The presence of AlN particles in Mg melts provides nucleation sites [107] because of AlN's low planar registry with Mg (Table 2-9). The refining performance of AlN was compared to TiC, Al₄C₃ and SiC on a Mg-1 wt.% Al alloy [107]. The base alloy had a grain size of 550 μm. Grain size measurements of the refined alloys at the centre of the samples with 1 vol.% addition of each refiner were measured. The grain sizes obtained with TiC, AlN, Al₄C₃ and SiC were ~460, ~420, ~320 and ~300 μm respectively [107]. The results are consistent with other experimental and theoretical results that AlN while effective, is not as potent as other particles such as SiC and Al₄C₃. The results also confirm the edge-to-edge matching results of Qiu *et al.* [144] where SiC should be a more potent nucleant than TiC. The addition of Mg₃N₂ has been used as an alternative means to produce in-situ AlN but this may have also introduced MgO impurities [149].

A.2.4 Grain Refinement by ZrB₂ Additions

The grain refinement of both ex-situ and in-situ ZrB₂ additions to Mg were examined using commercially purchased ZrB₂ (~4 μm) and synthesized ZrB₂ (via reacting Al-Ti-B and Al-Zr master alloys at 800°C for 30 minutes) respectively [16]. The grain size of the unrefined alloy was ~450 μm and reduced to 100 and 60 μm with 0.1 and 0.5 wt.% purchased ZrB₂ respectively while the synthesized ZrB₂ reduced the grain size to ~100 μm with addition levels equivalent to 0.25 wt.% Zr [16]. The grain refinement effect was present but the Mg alloy examined only had

an equivalent of 2 wt.% Al (from master alloy addition) so the effect on high Al content alloys is unclear. The focus of most grain refiner development utilized heterogeneous nucleation (Section 2.7.2) but some researchers examined using grain growth restriction (Section 2.6) for grain refinement.

A.2.5 Grain Refinement by Sr Additions

Strontium's refining effect is by solute restriction and has been observed for low and high content Mg-Al alloys. Solution heat treatment at 400, 500 and 600°C for 4 hours on a Al-10 wt.% Sr master alloy prior to addition to AZ31 improved grain refinement because the Al₄Sr particles in the master alloy became finer and dissolved more easily when added to Mg [187]. Grain refinement in AZ91D was observed by growth restriction and a duplex mechanism with grain centres containing Mg-Sr-Al-Fe-Mn intermetallics when Sr was added. It was thought that Sr reacted to form Mg-Sr intermetallics and with Al-Fe-Mn particles, nucleated Mg [186]. Combined Sr and C additions have shown even better refinement results than Sr alone. Some of the major refining results are shown in Table A-6.

With C addition alone, Al-C-O particles were observed and a higher number of these particles were observed with combined C and Sr additions. When the Sr content was 0.5 wt.%, Al-C-O and Al-C-O-Sr particles were observed. The nucleation mechanism was thought to be Al₄C₃ with O from sample contamination [106] and the Sr may have contributed to grain growth restriction by forming a diffusion layer ahead of the solid/liquid interface allowing nucleating crystals a chance to grow [106] also described by Lee *et al.* [92,107]. Combined Ce and Sr additions provided enhanced grain refinement than Sr or Ce alone in AZ91 via additive grain growth restriction [184].

Table A-6: Grain Refining Results of Sr Addition

Alloy (wt.%)	Addition Level (wt.%)	Grain Size (μm)/% Reduction	Ref.
Sr Addition			
Mg-3Al	0.01 to 0.1	grain size increase	
Mg-3Al	1	~325 to ~200/38	[92,107]
Mg-9Al	1	~200 to ~175/13	
AM60B	0.1	~500 to 450-500/10 to 0	[191]
AZ91E	0.1	650-600 to 400-300/38 to 50	
AZ91D	0.6	235 to 53/77	[186]
Sr and C Addition			
AZ91C+0.25C₂Cl₆	0.013	250 to 120/52	[183]
Mg-3Al+0.2C	0.2	180 to ~130/28	[106]
Mg-3Al+0.2C	0.5	180 to ~110/39	
AZ31+0.2C	0.2	180 to 140/71 ¹	[109]

¹The mechanical properties of the alloys also improved with the base AZ31 alloy having UTS of 168 MPa and elongation of 9.6% and the AZ31+0.2 wt.% C + 0.2 wt.% Sr having a UTS of 200 MPa and elongation of 14-15%.

A.2.6 Grain Refinement by Ca Additions

The effect of Ca addition to Mg-Al melts is of particular interest to researchers because Ca provides a high constitutional undercooling (Table 2-8) at the advancing solid-liquid interface during solidification [18,92,107,192]. Traditionally, Ca addition has been used to promote the formation of Al₂Ca, an intermetallic particle that effectively pins grain boundaries and improves the creep resistance of Mg-Al alloys [188]. A summary of the refining results using Ca addition are in shown in Table A-7.

Some results show conflicting observations with Ca addition increasing grain size. The reasons may be due to impurity levels, alloy composition and addition levels examined. Du *et al.* [193] observed Al-C-O-Ca particles within the casting when combined C and Ca were added that requires further research to determine their influence.

There was no obvious poisoning effect of 0.1 wt.% Fe addition sequence on the combined refining effect of 0.2 wt.% Ca and 0.2 wt.% C in Mg-3 wt.% Al [194]. It was thought that Fe would poison refinement if added after C inoculation as observed in previous studies [242] but Ca prevents the poisoning effects of Fe by an unclear mechanism that may involve segregation to the interface of phases preventing reactions [194]. The nucleating particles for cases where Ca, Fe and C were all present were duplex phases with Al-C-O-Fe cores and Al-C-O coatings

suspected to be Al_4C_3 on Al-Fe or Al-Fe-C phases [194]. In previous research, the duplex phase formed only if Fe was added before C inoculation [241].

Improvements in tensile properties were observed with Ca addition to Mg and AZ31 [2] and Ca or Ca and Si were effective but not as effective as 0.5 wt.% Al_4C_3 (described in Section 2.11.4.3) [2].

In addition to Mn and Fe additions that appear to have grain refining and coarsening characteristics (Sections 2.11.2-2.11.3 and 2.11.4.3) depending on the conditions, Be is another well known grain coarsening agent.

Table A-7: Grain Refining Results of Ca Addition

Alloy (wt.%)	Addition Level (wt.%)	Grain Size (μm)/% Reduction	Ref.
Ca Addition			
Mg	0.4	~1000 to ~270/73	[92,107]
Mg	0.26 (CaC_2) ¹	2300 to ~125/95	[192]
Mg	0.3	5000-6000 to ~1000/80 to 83	[2]
Mg-3Al	0.5	520 to 160/69	[193]
AZ31	0.3	~400 to ~150/63	[2]
AZ91	0.4	65 to 20/69	[188]
AZ91D	1	21 to 14.5/30 ²	[189]
AZ91D	1	218 to 846	[190]
Ca and C Addition			
AZ31+0.2C	0.2	180 to 130/73 ³	[109]
Mg-3Al+0.2C	0.2	175 to 110/37	[193]
Ca and Si Addition			
AZ31	0.3 ⁴	~400 to ~100/75	[2]
Mg	0.5 ⁵	6000-5000 to 800-600/87 to 88	[3]
Ca and Ce Addition			
AZ91+0.8Ce	0.2	36 to 23/36	[184]

¹Electromagnetic suspension casting with C not influencing results because used pure Mg

²Refined castings had lower mechanical properties because of the presence of brittle Al_2Ca particles at the grain boundaries

³Mechanical properties of the alloys also improved with the base AZ31 alloy having UTS of 168 MPa and elongation of 9.6% and the AZ31+0.2 wt.% C + 0.2 wt.% Ca having a UTS of 200 MPa and elongation of 14-15%

⁴0.3 wt.% Ca and Si

⁵Used Al-Si-Ca master alloy with Si:Ca being 1.5:1

A.2.7 Grain Coarsening Additions

Beryllium, when alloyed with Mg has an exceptional ability to reduce oxidation [320] but has a significant coarsening effect on Mg-Al alloys [196,206] and this effect extends to Mg-6 wt.% Zn, Mg-2 wt.% Ca, Mg-3 wt.% mischmetal (containing Ce, La and Pr), Mg-3 wt.% Nd alloys and Mg-0.5 wt.% Zr when Be was added at 730°C using a Al-5 wt.% Be master alloy [321]. The grain coarsening results with Be are presented in Table A-8 with Mg-3 wt.% Al for comparison. Further increases in grain size to 2500 µm were observed with 100 ppm of Be to Mg-0.5 wt.% Zr that remained unchanged despite additional 0.5 wt.% Zr [321].

Table A-8: Grain Size Versus Be Content for Various Mg Alloys [321]

Alloy (wt.%)	Be Concentration (ppm)	Grain Size (µm)	Percentage Increase Relative to Base (%)
Mg-3Al	0/10/50	290/720/~1700	-/148/486
Mg-6Zn	0/10/50	195/310/1470	-/61/654
Mg-2Ca	0/10/50	~200/~450/~1400	-/125/600
Mg-3(Ce, La and Pr)	0/10/50	320/~750/1550	-/134/384
Mg-3Nd	0/10/50	~300/~700/~1250	-/133/316
Mg-0.5Zr	0/10/50	120/~200/~600	-/67/400

Melt superheating and C inoculation are ineffective in Mg-Al alloys if 0.01 wt.% Be, Ti or Zr are present. Longer reaction times can usually overcome the coarsening effects of Zr or Ti but not for the case of Be [221]. The coarsening was attributed to C forming more stable carbides with Zr, Ti or Be than Al. Increasing reaction times reduced Zr, Ti, Be concentrations sufficiently to allow for Al₄C₃ to form, more in the cases for Zr and Ti and less in the case of Be [221]. However, Be coarsens other Mg alloy systems free of Al so the explanation that Be forms a more stable carbide with C than Al is doubtful. It appears that Be coats any type of nucleant and renders it useless but more detailed microstructural work is required for confirmation [321].

Additions of Mn to C refined Mg alloys with Al concentrations of 2 wt.% or less usually tended to cause grain coarsening if the Mn concentration was beyond 0.2 wt.% for the Mg-2 wt.% Al case [221]. The mechanism was attributed to poisoning from possible Mn-Al intermetallics that could form depending on the Mn/Al ratio. Rare-earth additions from

0.5-0.8 wt.% also poisoned C refined AZ92A alloys and could not be refined with subsequent superheating but could be refined if only superheating was conducted with no previous C refinement [221]. Rare-earth carbides were expected to be more stable than Al_4C_3 [221].

A.3 X-ray Diffraction Plot of SiC Substrate Used for Wettability Experiments

The XRD plot of one of the SiC substrates is shown in Figure A-5. Using X'Pert HighScore Plus [322] diffraction analysis software, the SiC substrate most closely resembled the α polytype.

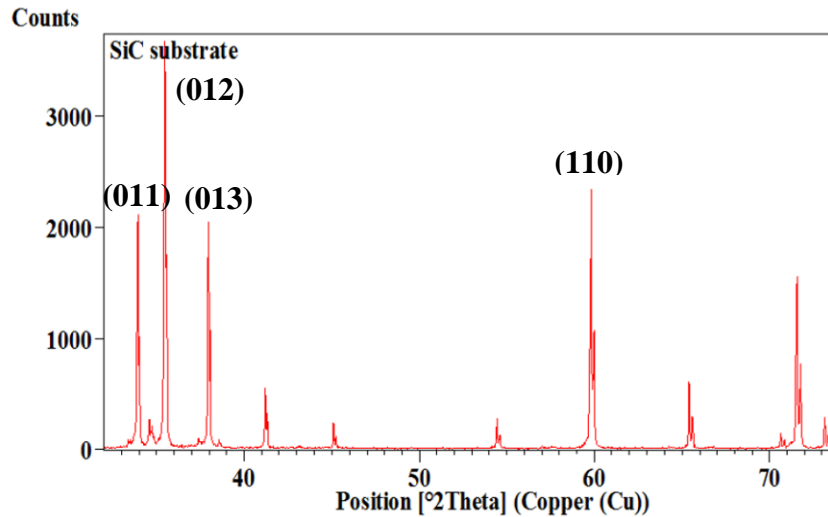


Figure A-5: XRD Spectrum of As-received SiC Substrate Showing α Polytype

A.4 Differential Scanning Calorimetry Plot

A DSC plot of the Al-5.9 wt.% SiC alloy heated to 700°C for 15 minutes then cooled is shown in Figure A-6. The data from Table 5-6 was generated by noting the temperatures and latent heat generated (peak areas) of the primary Al and eutectic Si phases during cooling. The final peak temperatures were utilized to ensure all the solidifying material was being considered. Similar plots were generated for the other Al-SiC alloys held at 700, 800 and 900°C for 15, 60 or 120 minutes.

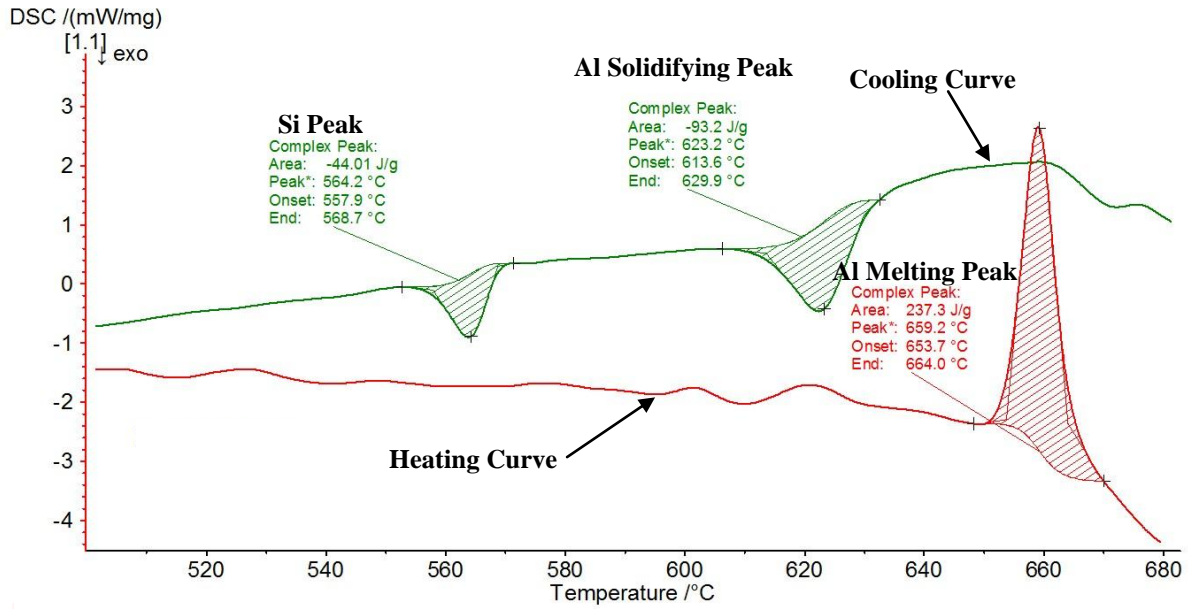


Figure A-6: Differential Scanning Calorimetry Plot of Al-5.9 wt.% SiC Alloy Heated to 700°C for 15 Minutes

REFERENCES

1. Avedesian, M. and Baker, H. Magnesium and Magnesium Alloys. Materials Park, USA, ASM International, 1999.
2. Feng, X., Wenwen, D. and Yangshan, S., "Microstructure Refinement of Magnesium Based Alloy." International Conference on Magnesium - Science, Technology and Applications. (2005): 143-146.
3. Duan, Z.C., Sun, Y.S., Wei, Y., Du, W.W., Xue, F. and Zhu, T.B., "Microstructure and Tensile Properties of Magnesium Alloy Modified by Si/Ca Based Refiner." Transactions of the Nonferrous Metals Society of China (English Edition). Vol. 15 (2005): 878-883.
4. StJohn, D.H., Easton, M.A., Qian, M. and Taylor, J.A., "Grain Refinement of Magnesium Alloys: A Review of Recent Research, Theoretical Developments, and their Application." Metallurgical and Materials Transactions A. Vol. 44 (2012): 2935-2949.
5. Ding, H. and Liu, X., "The Grain Refinement Efficiency of Ni-C on Mg-Al Alloys." Materials Letters. Vol. 63 (2009): 635-637.
6. Vogel, S.C. and Carpenter, J.S., "Brief Introduction to Neutron Scattering and Global Neutron User Facilities." JOM. Vol. 64 (2012): 104-111.
7. Powell, B.R., Luo, A.A. and Krajewski, P.E. Magnesium Alloys for Lightweight Powertrains and Automotive Bodies in Advanced Materials in Automotive Engineering. Rowe, J., Editor, Cambridge, UK, Woodhead Publishing Limited, 150-209, 2012.
8. Edgar, R.L. Global Overview on Demand and Applications for Magnesium Alloys in Magnesium Alloys and their Applications. Kainer, K.U., Editor, Weinheim, Germany, Wiley-VCH Verlag GmbH & Co. KGaA, 1-8, 2006.
9. Liu, Y., Liu, X. and Xiufang, B., "Grain Refinement of Mg-Al Alloys with Al₄C₃-SiC/Al Master Alloy." Materials Letters. Vol. 58 (2004): 1282-1287.
10. Qiu, D., Zhang, M.X., Taylor, J.A., Fu, H.M. and Kelly, P.M., "A Novel Approach to the Mechanism for the Grain Refining Effect of Melt Superheating of Mg-Al Alloys." Acta Materialia. Vol. 55 (2007): 1863-1871.
11. Magers, D. and Willekens, J., "Global Outlook on the Use of Magnesium Die-castings in Automotive Applications." International Magnesium Conference. (1998): 105-112.
12. Westengen, H. and Aune, T.K. Magnesium Casting Alloys - Casting Alloys in Magnesium Technology: Metallurgy, Design Data, Automotive Applications Friedrich, H. and Mordike, B., Editors, Berlin, Heidelberg, Germany, Springer-Verlag, 2006.
13. Davis, J.R. Aluminum and Aluminum Alloys. Materials Park, USA, ASM International, 1993.
14. Cole, G. Magnesium Vision 2020: A North American Automotive Strategic Vision for Magnesium. Quinn, J., Hetrick, E. and Bairley, S., Editors, Southfield, USA, USAMP, 2006.
15. Ramachandran, T.R., Sharma, P.K. and Balasubramanian, K., "Grain Refinement of Light Alloys." 68th World Foundry Congress. (2008): 189-193.
16. Klösch, G., McKay, B.J. and Schumacher, P., "Preliminary Investigation on the Grain Refinement Behavior of ZrB₂ Particles in Mg-Al Alloys." TMS Annual Meeting and Exhibition Magnesium Technology Symposium. (2006): 69-75.
17. Lu, L., Dahle, A.K. and StJohn, D.H., "Grain Refinement Efficiency and Mechanism of Aluminium Carbide in Mg-Al Alloys." Scripta Materialia. Vol. 53 (2005): 517-522.

18. StJohn, D.H., Qian, M., Easton, M.A., Cao, P. and Hildebrand, Z., "Grain Refinement of Magnesium Alloys." Metallurgical and Materials Transactions A. Vol. 36 (2005): 1669-1679.
19. Lun Sin, S., Elsayed, A. and Ravindran, C., "Inclusions in Magnesium and its Alloys: A Review." International Materials Reviews. Vol. 58 (2013): 419-436.
20. Hu, H. and Luo, A., "Inclusions in Molten Magnesium and Potential Assessment Techniques." JOM. Vol. 48 (1996): 47-51.
21. Ditze, A. and Scharf, C. Recycling of Magnesium. Clausthal-Zellerfeld, Germany, Papierflieger Verlag, 2008.
22. Oymo, D., Karlsen, D.O., Pinfeld, P.M.D., Mellerud, T. and Lie, O., "Particle Removal in Pure Magnesium." Conference of Light Metals. (1994): 1017-1024.
23. Simensen, C.J. and Oberlander, B., "A Survey of Inclusions in Magnesium." Praktische Metallographie. Vol. 17 (1980): 125-135.
24. Tartaglia, J.M. and Grebetz, J.C., "Observation of Intermetallic Particle and Inclusions Distributions in Magnesium Alloys." TMS Annual Meeting and Exhibition Magnesium Technology Symposium. (2000): 113-121.
25. Bakke, P. and Karlsen, D.O., "Inclusion Assessment in Magnesium and Magnesium Base Alloys." SAE International Congress and Exposition. (1997): 61-73.
26. Emley, E.F. Principles of Magnesium Technology. London, UK, Pergamon Press Ltd., 1966.
27. Kubaschewski, O. and Alcock, C.B. Metallurgical Thermochemistry. Oxford, UK, Pergamon Press, 1979.
28. Kubaschewski, O., Alcock, C.B. and Spencer, P.J. Materials Thermochemistry. Oxford, UK, Pergamon Press, 1979.
29. Pekguleryuz, M. Melting, Alloying, Refining - Zirconium-free Alloys in Magnesium Technology: Metallurgy, Design Data, Automotive Applications. Friedrich, H. and Mordike, B., Editors, Berlin, Germany, Springer-Verlag, 109-127, 2006.
30. Busk, R.S. and Jackson, R.B., "Use of SF₆ in the Magnesium Industry." 37th Annual World Conference on Magnesium. (1980): 1-4.
31. Gao, H.T., Wu, G.H., Fan, Y., Ding, W.J. and Zhu, Y.P., "Effects of Purification Fluxes Containing Boride on AZ91 Alloy." Materials Science Forum. Vol. 488-489 (2005): 25-30.
32. Housh, S.E. and Petrovich, V., "Magnesium Refining: A Fluxless Alternative." SAE International Congress and Exposition. (1992): 1-7.
33. Schubert, W. and Gjestland, H., "Use of SO₂ as Protection Gas in Magnesium Diecasting." 7th International Conference on Magnesium Alloys and their Applications. (2006): 761-766.
34. Cashion, S.P., Ricketts, N.J. and Hayes, P.C., "The Mechanism of Protection of Molten Magnesium by Cover Gas Mixtures Containing Sulphur Hexafluoride." Journal of Light Metals. Vol. 2 (2002): 43-47.
35. Cashion, S.P., Ricketts, N.J. and Hayes, P.C., "Characterisation of Protective Surface Films Formed on Molten Magnesium Protected by Air/SF₆ Atmospheres." Journal of Light Metals. Vol. 2 (2002): 37-42.
36. Chen, H., Liu, J. and Huang, W., "Oxidation Behavior of Molten Magnesium in Air/HFC-134a Atmospheres." Journal of Materials Science. Vol. 41 (2006): 8017-8024.

37. Dorsam, H., "Magnesium Melting/casting and Remelting in Foundries." TMS Annual Meeting and Exhibition Magnesium Technology Symposium. (2000): 99-105.
38. Ha, W. and Kim, Y.J., "Effects of Cover Gases on Melt Protection of Mg Alloys." Journal of Alloys and Compounds. Vol. 422 (2006): 208-213.
39. Lyon, P., Rogers, P.D., King, J.F., Cashion, S.P. and Ricketts, N.J., "Magnesium Melt Protection at Magnesium Elektron Using HFC-134a." TMS Annual Meeting and Exhibition Magnesium Technology Symposium. (2003): 11-14.
40. Milbrath, D.S., "Development of 3MTM NovecTM 612 Magnesium Protection Fluid as a Substitute for SF₆ Over Molten Magnesium." 2nd International Conference on SF₆ and the Environment. (2002).
41. Ricketts, N.J. and Cashion, S.P., "Hydrofluorocarbons as a Replacement for Sulphur Hexafluoride in Magnesium Processing." TMS Annual Meeting and Exhibition Magnesium Technology Symposium. (2001): 31-36.
42. Xiong, S.M. and Liu, X.L., "Microstructure, Composition, and Depth Analysis of Surface Films Formed on Molten AZ91D Alloy Under Protection of SF₆ Mixtures." Metallurgical and Materials Transactions A. Vol. 38 (2007): 428-434.
43. Zeng, Y.W., Peng, L.M., Mao, X.M., Zeng, X.Q. and Ding, W.J., "A New Low GWP Protective Atmosphere Containing HFC-152a for Molten Magnesium Against Ignition." Materials Science Forum. Vol. 488-489 (2005): 73-76.
44. Mirak, A.R., Divandari, M., Boutorabi, S.M.A. and Taylor, J.A., "Effect of Oxide Film Defects Generated During Mould Filling on Mechanical Strength and Reliability of Magnesium Alloy Castings (AZ91)." International Journal of Cast Metals Research. Vol. 25 (2012): 188-194.
45. Griffiths, W.D. and Lai, N.W., "Double Oxide Film Defects in Cast Magnesium Alloy." Metallurgical and Materials Transactions A. Vol. 38 (2007): 190-196.
46. Campbell, J. Castings. Boston, USA, Elsevier Butterworth Heinemann, 2003.
47. Bakke, P., Svalestuen, J. and Albright, D., "Metal quality - The Effects on Die Casters and End Users." SAE World Congress & Exhibition. (2002): 299-305.
48. Tathgar, H.S., Bakke, P. and Engh, T.A., "Impurities in Magnesium and Magnesium Based Alloys and Their Removal." 5th International Conference on Magnesium Alloys and Their Applications. (2000): 767-779.
49. Lagowski, B., "Reacted Sand Inclusions and their Effect on the Tensile Properties of Magnesium Alloys." AFS Transactions. Vol. 87 (1979): 387-390.
50. Wu, G., Xie, M., Zhai, C., Zeng, X., Zhu, Y. and Ding, W., "Purification Technology of AZ91 Magnesium Alloy Wastes." Transactions of the Nonferrous Metals Society of China (English Edition). Vol. 13 (2003): 1260-1264.
51. Gale, W.F. and Totemeier, T.C. Smithells Metals Reference Book. Oxford, UK, Elsevier Butterworth-Heinemann, 2004.
52. Haynes, W.M. CRC Handbook of Chemistry and Physics, Boca Raton, USA, CRC Press; Taylor & Francis, 2010.
53. Liang, M.J., Wu, G.H., Ding, W.J. and Wang, W., "Effect of Inclusion on Service Properties of GW103K Magnesium Alloy." Transactions of the Nonferrous Metals Society of China (English Edition). Vol. 21 (2011): 717-724.
54. Wang, W., Huang, Y., Wu, G., Wang, Q., Sun, M. and Ding, W., "Influence of Flux Containing YCl₃ Additions on Purifying Effectiveness and Properties of Mg-10Gd-3Y-0.5Zr Alloy." Journal of Alloys and Compounds. Vol. 480 (2009): 386-391.

55. Wang, W., Wu, G., Sun, M., Huang, Y., Wang, Q. and Ding, W., "Effects of Flux Containing YCl_3 on the Yttrium Loss, Mechanical and Corrosion Properties of Mg-10Gd-3Y-0.5Zr Alloy." Materials Science and Engineering A. Vol. 527 (2010): 1510-1515.
56. Wang, W., Wu, G., Wang, Q., Huang, Y. and Ding, W., "Gd Contents, Mechanical and Corrosion Properties of Mg-10Gd-3Y-0.5Zr Alloy Purified by Fluxes Containing GdCl_3 Additions." Materials Science and Engineering A. Vol. 507 (2009): 207-214.
57. Wang, W., Wu, G.H., Wang, Q.D., Huang, Y.G., Sun, M. and Ding, W.J., "Investigation of Flux Containing GdCl_3 on Recycling Mg-Gd-Y-Zr Scraps." Transactions of the Nonferrous Metals Society of China (English Edition). Vol. 18 (2008): s292-s298.
58. Gao, H.T., Wu, G.H., Ding, W.J. and Zhu, Y.P., "Purifying Effect of New Flux on Magnesium Alloy." Transactions of the Nonferrous Metals Society of China (English Edition). Vol. 14 (2004): 530-536.
59. Forakis, P., Richard, E. and Argo, D., "Fluxless Refining of Clean Diecast Scrap for Noranda's AJ52 High Temperature Mg-Al-Sr Alloys." TMS Annual Meeting and Exhibition Magnesium Technology Symposium. (2002): 49-54.
60. Westengen, H. Recycling in Magnesium Technology: Metallurgy, Design Data, Automotive Applications Friedrich, H. and Mordike, B., Editors, Berlin, Germany, Springer-Verlag, 633-664, 2006.
61. Baker, C.F., "Molten Magnesium Operations - Establishing and Maintaining Quality." SAE International Congress and Exposition. (1990): 1-5.
62. Couling, S., Bennett, F. and Leontis, T., "Fluxless Melting of Magnesium." Light Metals. Vol. 1 (1977): 545-560.
63. Couling, S.L. and Leontis, T.E., "Improved Protection of Molten Magnesium with Air/ CO_2 / SF_6 Gas Mixtures." Light Metals. Vol. 4 (1980): 997-1009.
64. Couling, S.L., "Use of Air/ CO_2 / SF_6 Gas Mixtures for Improved Protection of Molten Magnesium." 36th Annual World Conference on Magnesium. (1979): 54-57.
65. Fruehling, J.W. and Hanawalt, J.D., "Protective Atmospheres for Melting Magnesium Alloys." Transactions of the American Foundrymen's Society. Vol. 77 (1969): 159-164.
66. Walzak, M.J., Davidson, R.D., McIntyre, N.S., Argo, D. and Davis, B.R., "Interfacial Reactions Between SF_6 and Molten Magnesium." TMS Annual Meeting and Exhibition Magnesium Technology Symposium. (2001): 37-41.
67. Maiss, M. and Benninkmeijer, C.A.M., "Atmospheric SF_6 Trends, Sources and Prospects." Environmental Science and Technology. Vol. 32 (1998): 3077-3086.
68. Chen, H., Liu, J. and Huang, W., "Characterization of the Protective Surface Films Formed on Molten Magnesium in Air/HFC-134a Atmospheres." Materials Characterization. Vol. 58 (2007): 51-58.
69. You, G., Long, S. and Li, R., "Effective Protection of Magnesium Melt Surface from Oxidation Using HFC125-containing Shielding Gas." Materials Science Forum. Vol. 546-549 (2007): 119-122.
70. Revankar, V., Baker, P., Schultz, A. and Brandt, H., "A Replacement for SF_6 : The MagShield System." 57th Annual World Magnesium Conference. (2000): 51-55.
71. Bach, F.W., Karger, A., Pelz, C. and Schaper, M., "Use of CO_2 -snow for Protecting Molten Magnesium from Oxidation." TMS Annual Meeting and Exhibition Magnesium Technology Symposium. (2005): 3-6.
72. Karger, A., Bach, F.W. and Pelz, C., "Protective System for Magnesium Melt." Materials Science Forum. Vol. 488-489 (2005): 85-8.

73. Martins, L. and Kannan, S., "Six Steps to Reducing Inclusion Defects." Modern Casting. Vol. 93 (2003): 39-42.
74. Smith, R.M., "The Control of Non-metallic Inclusions by Woven Refractory Cloth Filtration for Investment Casting Foundries." 42nd Annual Technical Meeting of the Investment Casting Institute. (1994): 13:1-13:26.
75. Nazari, E., Razavi, S.H. and Boutorabi, S.M.A., "Effect of Filtration on the Morphology and Mechanical Properties of Mg Molten Alloy Entering the Mould Cavity." Journal of Materials Processing Technology. Vol. 210 (2010): 461-465.
76. Bakke, P., Engh, T.A., Bathen, E., Oymo, D. and Nordmark, A., "Magnesium Filtration with Ceramic Foam Filters and Subsequent Quantitative Microscopy of the Filters." Materials and Manufacturing Processes. Vol. 9 (1994): 111-138.
77. Makarov, S., Ludwig, R. and Apelian, D., "Electromagnetic Separation Techniques in Metal Casting. I. Conventional Methods." IEEE Transactions on Magnetics. Vol. 36 (2000): 2015-2021.
78. Wu, G., Sun, M., Dai, J.C. and Ding, W., "Effects of Filter Materials on Microstructure and Mechanical Properties of AZ91." China Foundry. Vol. 7 (2010): 400-407.
79. Le, Q., Zhang, Z., Cui, J. and Chang, S., "Study on the Filtering Purification of AZ91 Magnesium Alloy." Materials Science Forum. Vol. 610-613 (2009): 754-757.
80. Tardif, S., Tremblay, R., Dube, D. and Zhang, Z., "New Filtering Method for Casting Inclusion-free Tensile and Creep Test Specimens of Magnesium Alloys." 40th Annual Conference of Metallurgists of CIM - Light Metals Symposium. (2001): 225-235.
81. Wang, J., Zhou, J.X., Tong, W.H. and Yang, Y.S., "Effect of Purification Treatment on Properties of Mg-Gd-Y-Zr Alloy." Transactions of the Nonferrous Metals Society of China (English Edition). Vol. 20 (2010): 1235-1239.
82. Wang, J., Dong, X.G. and Yang, Y.S., "Influence of Melt Purification on Mechanical Properties of AZ31 Magnesium Alloy." International Journal of Cast Metals Research. Vol. 25 (2012): 165-169.
83. Emadi, D., Thomson, J.P., Sadayappan, K. and Sahoo, M., "Effects of Grain Refinement and Melt Filtration on the Mechanical Properties of Sand and Permanent Mold Cast Magnesium AZ91D Alloy." TMS Annual Meeting and Exhibition Magnesium Technology Symposium. (2005): 335-339.
84. Yim, C.D., Wu, G. and You, B.S., "Effect of Gas Bubbling on Tensile Elongation of Gravity Mold Castings of Magnesium Alloy." Materials Transactions. Vol. 48 (2007): 2778-2781.
85. Wu, G.H., Dai, J.C., Sun, M. and Ding, W.J., "Non-flux Purification Behavior of AZ91 Magnesium Alloy." Transactions of the Nonferrous Metals Society of China (English Edition). Vol. 20 (2010): 2037-2045.
86. Karlsen, D.O., Oymo, D., Westengen, H., Pinfeld, P.M.D. and Stromhaug, S.I., "Development of Grain Refiner for Al-containing Mg-alloys." 32nd Annual Conference of Metallurgists of CIM - Symposium on Light Metals Processings and Applications. (1993): 397-408.
87. Kim, Y.M., Yim, C.D., Kim, Y.H. and You, B.S., "The Role of Carbon for Grain Refinement in Mg-Al Base Alloys." TMS Annual Meeting and Exhibition Magnesium Technology Symposium. (2007): 121-126.

88. Zhang, A.M., Hao, H. and Zhang, X.G., "Grain Refinement Mechanism of Al-5C Master Alloy in AZ31 Magnesium Alloy." Transactions of the Nonferrous Metals Society of China (English Edition). Vol. 23 (2013): 3167-3172.
89. Davis, J.A., Eastwood, L.W. and DeHaven, J., "Grain Refinement of Magnesium Casting Alloys." Transactions of the American Foundrymen's Society. Vol. 53 (1945): 352-362.
90. StJohn, D.H., Cao, P., Qian, M. and Easton, M.A., "A Brief History of the Development of Grain Refinement Technology for Cast Magnesium Alloys." TMS Annual Meeting and Exhibition Magnesium Technology Symposium. (2013): 3-8.
91. Wang, Y., Zeng, X. and Ding, W., "Effect of Al-4Ti-5B Master Alloy on the Grain Refinement of AZ31 Magnesium Alloy." Scripta Materialia. Vol. 54 (2006): 269-273.
92. Lee, Y.C., Dahle, A.K. and StJohn, D.H., "The Role of Solute in Grain Refinement of Magnesium." Metallurgical and Materials Transactions A. Vol. 31 (2000): 2895-2906.
93. Kim, Y.M., Wang, L. and You, B.S., "Grain Refinement of Mg-Al Cast Alloy by the Addition of Manganese Carbonate." Journal of Alloys and Compounds. Vol. 490 (2010): 695-699.
94. Pan, Y., Liu, X. and Yang, H., "Role of C and Fe in Grain Refinement of an AZ63B Magnesium Alloy by Al-C Master Alloy." Journal of Materials Science and Technology. Vol. 21 (2005): 822-826.
95. Yano, E., Tamura, Y., Motegi, T. and Sato, E., "Effect of Carbon Powder on Grain Refinement of an AZ91E Magnesium Alloy." Materials Transactions. Vol. 44 (2003): 107-110.
96. Haerle, A.G., Murray, R.W., Mercer II, W.E., Mikucki, B.A. and Miller, M.H., "The Effect of Non-metallic Inclusions on the Properties of Die Cast Magnesium." SAE International Congress and Exposition. (1997): 75-84.
97. Bakke, P., Pettersen, K., Guldborg, S. and Sannes, S., "The Impact of Metal Cleanliness on Mechanical Properties of Die Cast Magnesium Alloy AM50." 7th International Conference on Magnesium Alloys and their Applications. (2006): 739-745.
98. Chen, Y.J., Hsu, W.N. and Shin, J.R., "The Effect of Ultrasonic Treatment on Microstructural and Mechanical Properties of Cast Magnesium Alloys." Materials Transactions. Vol. 50 (2009): 401-408.
99. Gao, H.T., Wu, G.H., Ding, W.J. and Zhu, Y.P., "Purifying Effect of New Flux on Magnesium Alloy." Transactions of the Nonferrous Metals Society of China (English Edition). Vol. 14 (2004): 530-536.
100. Haerle, A.G., Mikucki, B.A. and Mercer II, W.E., "New Technique for Quantifying Non-metallic Inclusion Content in Magnesium." Light Metal Age. Vol. 54 (1996): 22-29.
101. Jang, D.I. and Kim, S.K., "Development of Non-SF₆ Strip Casting Process for Mg Alloys." Materials Science Forum. Vol. 620-622 (2009): 149-152.
102. Elsayed, A., Lun Sin, S., Vandersluis, E., Hill, J., Ahmad, S. and Ravindran, C., "Recycling and Degassing of AZ91E Magnesium Alloy Castings and its Effects on Mechanical Properties and Microstructure." AFS Transactions. Vol. 122 (2012): 423-429.
103. Wang, G.G., Froese, B. and Bakke, P., "Process and Property Relationships in AM60B Die Castings." TMS Annual Meeting and Exhibition Magnesium Technology Symposium. (2003): 65-69.
104. Horstemeyer, M.F., Yang, N., Gall, K., McDowell, D.L., Fan, J. and Gullett, P.M., "High Cycle Fatigue of a Die Cast AZ91E-T4 Magnesium Alloy." Acta Materialia. Vol. 52 (2004): 1327-1336.

105. Wang, J., Yang, Y.S. and Tong, W.H., "Effect of Purification Treatment on Corrosion Resistance of Mg-Gd-Y-Zr Alloy." Transactions of the Nonferrous Metals Society of China (English Edition). Vol. 21 (2011): 949-954.
106. Du, J., Yang, J., Kuwabara, M., Li, W. and Peng, J., "Effect of Strontium on the Grain Refining Efficiency of Mg-3Al Alloy Refined by Carbon Inoculation." Journal of Alloys and Compounds. Vol. 470 (2009): 228-232.
107. Lee, Y.C., Dahle, A.K. and StJohn, D.H., "Grain Refinement of Magnesium." TMS Annual Meeting and Exhibition Magnesium Technology Symposium. (2000): 211-218.
108. Jin, Q., Eom, J.P., Lim, S.G., Park, W.W. and You, B.S., "Effects of C₂Cl₆ Addition on Grain Refinement and Mechanical Properties of AZ31 Magnesium Alloy." Metals and Materials International. Vol. 9 (2003): 453-458.
109. Du, J., Yang, J., Kuwabara, M., Li, W. and Peng, J., "Effects of Carbon and/or Alkaline Earth Elements on Grain Refinement and Tensile Strength of AZ31 Alloy." Materials Transactions. Vol. 49 (2008): 2303-2309.
110. Huang, Y., Hort, N., Anopuo, O., Kainer, K.U., Vidrich, G., Schiffl, A. and Liu, Y., "Microstructural Investigations of Mg-Al Alloys Containing Small Amount of SiC Nucleants." TMS Annual Meeting and Exhibition Magnesium Technology Symposium. (2007): 421-426.
111. StJohn, D.H., Cao, P., Qian, M. and Easton, M.A., "A New Analytical Approach to Reveal the Mechanisms of Grain Refinement." Advanced Engineering Materials. Vol. 9 (2007): 739-746.
112. Callister, W.D. Material Science and Engineering: An Introduction. Hoboken, USA, John Wiley and Sons, Inc., 2003.
113. Dieter, G.E. Mechanical Metallurgy. London, UK, McGraw Hill, 1988.
114. Song, C., Han, Q. and Zhai, Q., "Review of Grain Refinement Methods for As-cast Microstructure of Magnesium Alloy." China Foundry. Vol. 6 (2009): 93-103.
115. Kim, Y.M., Yim, C.D. and You, B.S., "Grain Refining Mechanism in Mg-Al Base Alloys with Carbon Addition." Scripta Materialia. Vol. 57 (2007): 691-694.
116. Vinotha, D., Raghukandan, K., Pillai, U.T.S. and Pai, B.C., "Grain Refining Mechanisms in Magnesium Alloys - An Overview." Transactions of the Indian Institute of Metals. Vol. 62 (2009): 521-532.
117. Lu, L., Dahle, A.K., Taylor, J.A. and StJohn, D.H., "Theoretical and Practical Considerations of Grain Refinement of Mg-Al Alloys." Materials Science Forum. Vol. 488-489 (2005): 299-302.
118. Wang, Y., Zeng, X., Ding, W., Luo, A.A. and Sachdev, A.K., "Grain Refinement of AZ31 Magnesium Alloy by Titanium and Low-frequency Electromagnetic Casting." Metallurgical and Materials Transactions A. Vol. 38 (2007): 1358-1366.
119. Kumar, R. and Mahanty, R.K., "Grain Size Control of Magnesium." British Foundryman. Vol. 66 (1973): 39-42.
120. Zhang, J., Wang, S., Qi, X. and Xu, B., "Effects of La on the Microstructures and Mechanical Properties of AZ91 Magnesium Alloy and its Mechanism." 2011 International Conference on Mechatronics and Materials Processing. (2011): 1650-1653.
121. Dahle, A.K., Lee, Y.C., Nave, M.D., Schaffer, P.L. and StJohn, D.H., "Development of the As-cast Microstructure in Magnesium-aluminium Alloys." Journal of Light Metals. Vol. 1 (2001): 61-72.

122. Porter, D.A. Phase Transformations in Metals and Alloys. London, UK, Chapman and Hall, Inc., 1992.
123. Greer, A.L., Bunn, A.M., Tronche, A., Evans, P.V. and Bristow, D.J., "Modelling of Inoculation of Metallic Melts: Application to Grain Refinement of Aluminium by Al-Ti-B." Acta Materialia. Vol. 48 (2000): 2823-2835.
124. Murty, B.S., Kori, S.A. and Chakraborty, M., "Grain Refinement of Aluminum and its Alloys by Heterogeneous Nucleation and Alloying." International Materials Reviews. Vol. 47 (2002): 3-29.
125. Mitra, R. and Mahajan, Y.R., "Interfaces in Discontinuously Reinforced Metal Matrix Composites: An Overview." Bulletin of Materials Science. Vol. 18 (1995): 405-434.
126. Stefanescu, D.M., Barice, W.J., Brown, R.B., Chong, D. and Craig, D.B. Vol. 15: Casting. Materials Park, USA, ASM International, 1988.
127. Gao, L., Liang, S.M., Chen, R.S. and Han, E.H., "Correlation of Recalescence with Grain Refinement of Magnesium Alloys." Transactions of the Nonferrous Metals Society of China (English Edition). Vol. 18 (2008): 288-291.
128. Bramfitt, B.L., "The Effect of Carbide and Nitride Additions on the Heterogeneous Nucleation Behavior of Liquid Iron." Metallurgical Transactions. Vol. 1 (1970): 1987-1995.
129. Hildebrand, Z., Qian, M., StJohn, D. and Frost, M., "Influence of Zinc on the Soluble Zirconium Content in Magnesium and the Subsequent Grain Refinement by Zirconium." TMS Annual Meeting and Exhibition Magnesium Technology Symposium. (2004): 241-245.
130. Villars, P. and Calvert, L.D. Pearson's Handbook of Crystallographic Data for Intermetallic Phases. Materials Park, USA, ASM International, 1991.
131. StJohn, D.H., Easton, M.A. and Qian, M., "An Inverse Growth Restriction Model for Predicting Solidified Grain Size." 12th International Conference on Modeling of Casting, Welding, and Advanced Solidification Processes. (2009): 477-484.
132. Huang, Y., Zheng, X., Liu, B., Anopuo, O., Hort, N., Kainer, K.U. and Kim, G.S., "Grain Refinement of Mg-Al Alloys by Carbon Inoculation." TMS Annual Meeting and Exhibition Magnesium Technology Symposium. (2010): 419-424.
133. Cai, Y., Taplin, D., Tan, M.J. and Zhou, W., "Nucleation Phenomenon in SiC Particulate Reinforced Magnesium Composite." Scripta Materialia. Vol. 41 (1999): 967-971.
134. Cai, Y., Tan, M.J., Shen, G.J. and Su, H.Q., "Microstructure and Heterogeneous Nucleation Phenomena in Cast SiC Particles Reinforced Magnesium Composite." Materials Science and Engineering A. Vol. 282 (2000): 232-239.
135. Han, H., Miao, H., Liu, S. and Chen, Y., "Grain Refinement of AZ91D Magnesium Alloy by In-situ Al₄C₃ Particles." 1st International Congress on Advanced Materials. (2011): 429-432.
136. Gao, S.Y., Cui, J.Z., Li, Q.C. and Zhang, Z.Q., "The Research on the Effect of MgCO₃ on the Grain Refinement in AZ31 Magnesium Alloy." Materialwissenschaft und Werkstofftechnik. Vol. 41 (2010): 652-656.
137. Han, H., Lü, C., Miao, H., Liu, S., Wang, S. and Yang, X., "Fabrication of a New Mg-50% Al₄C₃-6% Ce Master Alloy and its Refinement Mechanism on AZ91D Alloy." Xiyou Jinshu Cailiao Yu Gongcheng/Rare Metal Materials and Engineering. Vol. 42 (2013): 28-31.

138. Liu, S., Chen, Y. and Han, H., "Grain Refinement of AZ91D Magnesium Alloy by a New Mg-50%Al₄C₃ Master Alloy." Journal of Alloys and Compounds. Vol. (2009).
139. Huang, Y., Kainer, K.U. and Hort, N., "Mechanism of Grain Refinement of Mg-Al Alloys by SiC Inoculation." Scripta Materialia. Vol. 64 (2011): 793-796.
140. Easton, M.A., Schiffli, A., Yao, J.Y. and Kaufmann, H., "Grain Refinement of Mg-Al(-Mn) Alloys by SiC Additions." Scripta Materialia. Vol. 55 (2006): 379-382.
141. Suresh, M., Srinivasan, A., Pillai, U.T.S. and Pai, B.C., "Grain Refinement Mechanism in Al-4B Master Alloy Added Pure Mg." Materials Science Forum. Vol. 710 (2012): 161-166.
142. Watanabe, Y., Gao, Y.B., Guo, J.Q., Sato, H., Miura, S. and Miura, H., "Heterogeneous Nucleation of Pure Magnesium on Al₃Ti, TiC, TiB₂, and AlB₂ Particles." Japanese Journal of Applied Physics. Vol. 52 (2013): 01AN04 1-7.
143. Ma, G., Han, G. and Liu, X., "Grain Refining Efficiency of a New Al-1B-0.6C Master Alloy on AZ63 Magnesium Alloy." Journal of Alloys and Compounds. Vol. 491 (2010): 165-169.
144. Qiu, D., Zhang, M.X., Fu, H.M., Kelly, P.M. and Taylor, J.A., "Crystallography of Recently Developed Grain Refiners for Mg-Al Alloys." Philosophical Magazine Letters. Vol. 87 (2007): 505-514.
145. Liu, S., Zhang, Y., Han, H. and Li, B., "Effect of Mg-TiB₂ Master Alloy on the Grain Refinement of AZ91D Magnesium Alloy." Journal of Alloys and Compounds. Vol. 487 (2009): 202-205.
146. Xu, C., Lu, B., Lü, Z. and Liang, W., "Grain Refinement of AZ31 Magnesium Alloy by Al-Ti-C-Y Master Alloy." Journal of Rare Earths. Vol. 26 (2008): 604-608.
147. PCPDFWIN V. 2.3. Newton Square, USA, International Centre for Diffraction Data, 2002.
148. Gu, S.W., Hao, H., Fang, C.F., Ji, S.H. and Zhang, X.G., "Effects of AlN Particles and Electromagnetic Stirring on As-cast Structure of AZ31 Alloys." 7th International Forum on Advanced Material Science and Technology. (2011): 771-774.
149. Zhao, H.L., Zhou, Z.X., Liu, X.D. and Guan, S.K., "Influence of Mg₃N₂ Powder on Microstructures and Mechanical Properties of AZ31 Mg Alloy." Journal of Central South University of Technology (English Edition). Vol. 15 (2008): 459-462.
150. Zhang, M.X. and Kelly, P.M., "Edge-to-edge Matching and its Applications: Part I. Application to the simple HCP/BCC system." Acta Materialia. Vol. 53 (2005): 1073-1084.
151. Zhang, M.X. and Kelly, P.M., "Edge-to-edge Matching and its Applications: Part II. Application to Mg-Al, Mg-Y and Mg-Mn alloys." Acta Materialia. Vol. 53 (2005): 1085-1096.
152. Zhang, M.X., Kelly, P.M., Qian, M. and Taylor, J.A., "Crystallography of Grain Refinement in Mg-Al Based Alloys." Acta Materialia. Vol. 53 (2005): 3261-3270.
153. Zhang, M.X., Kelly, P.M., Qian, M. and Taylor, J.A., "Application of Edge-to-edge Matching Model to Grain Refinement in Mg-Al Based Alloys." Journal of Materials Science and Technology. Vol. 21 (2005): 77-80.
154. Fu, H.M., Qiu, D., Zhang, M.X., Wang, H., Kelly, P.M. and Taylor, J.A., "The Development of a New Grain Refiner for Magnesium Alloys Using the Edge-to-edge Model." Journal of Alloys and Compounds. Vol. 456 (2008): 390-394.

155. Qiu, D., Zhang, M.X., Taylor, J.A. and Kelly, P.M., "A New Approach to Designing a Grain Refiner for Mg Casting Alloys and its Use in Mg-Y-based Alloys." Acta Materialia. Vol. 57 (2009): 3052-3059.
156. Fu, H.M., Zhang, M.X., Qiu, D., Kelly, P.M. and Taylor, J.A., "Grain Refinement by AlN Particles in Mg-Al Based Alloys." Journal of Alloys and Compounds. Vol. 478 (2009): 809-812.
157. Qian, M., Cao, P., Easton, M.A., McDonald, S.D. and StJohn, D.H., "An Analytical Model for Constitutional Supercooling-driven Grain Formation and Grain Size Prediction." Acta Materialia. Vol. 58 (2010): 3262-3270.
158. StJohn, D.H., Easton, M.A., Qian, M., Cao, P. and Birmingham, M.J., "Introduction to the Interdependence Theory of Grain Formation and its Application to Aluminium, Magnesium and Titanium Alloys." 5th International Conference on Light Metals Technology. (2011): 206-209.
159. Easton, M.A. and StJohn, D.H., "An Analysis of the Relationship Between Grain Size, Solute Content, and the Potency and Number Density of Nucleant Particles." Metallurgical and Materials Transactions A. Vol. 36 (2005): 1911-1920.
160. StJohn, D.H., Easton, M.A., Cao, P. and Qian, M., "New Approach to Analysis of Grain Refinement." International Journal of Cast Metals Research. Vol. 20 (2007): 131-135.
161. Easton, M.A. and StJohn, D.H., "A Model of Grain Refinement Incorporating Alloy Constitution and Potency of Heterogeneous Nucleant Particles." Acta Materialia. Vol. 49 (2001): 1867-1878.
162. StJohn, D.H., Qian, M., Easton, M.A. and Cao, P., "The Interdependence Theory: The Relationship Between Grain Formation and Nucleant Selection." Acta Materialia. Vol. 59 (2011): 4907-4921.
163. Saunders, W.P. and Strieter, F.P., "Alloying Zirconium to Magnesium." Transactions of the American Foundrymen's Society. Vol. 60 (1952): 581-594.
164. Sauerwald, F. Patent Number: 2228781, USA, (1941).
165. Qian, M. and Das, A., "Grain Refinement of Magnesium Alloys by Zirconium: Formation of Equiaxed Grains." Scripta Materialia. Vol. 54 (2006): 881-886.
166. Qian, M., StJohn, D.H. and Frost, M.T., "Effect of Soluble and Insoluble Zirconium on the Grain Refinement of Magnesium Alloys." 2nd Osaka International Conference on Platform Science and Technology for Advanced Magnesium Alloys. (2003): 593-598.
167. Qian, M., StJohn, D.H. and Frost, M.T., "Zirconium Alloying and Grain Refinement of Magnesium Alloys." TMS Annual Meeting and Exhibition Magnesium Technology Symposium. (2003): 209-214.
168. Qian, M., Graham, D., Zheng, L., StJohn, D.H. and Frost, M.T., "Alloying of Pure Magnesium With Mg - 33.3 wt-%Zr Master Alloy." Materials Science and Technology. Vol. 19 (2003): 156-162.
169. Qian, M., StJohn, D.H., Frost, M.T. and Barnett, M.R., "Grain Refinement of Pure Magnesium Using Rolled Zirmax® Master Alloy (Mg-33.3Zr)." TMS Annual Meeting and Exhibition Magnesium Technology Symposium. (2003): 215-220.
170. Qian, M., StJohn, D.H. and Frost, M.T., "Characteristic Zirconium-rich Coring Structures in Mg-Zr Alloys." Scripta Materialia. Vol. 46 (2002): 649-654.
171. Qian, M., StJohn, D.H. and Frost, M.T., "Heterogeneous Nuclei Size in Magnesium-zirconium Alloys." Scripta Materialia. Vol. 50 (2004): 1115-1119.

172. Qian, M., Hildebrand, Z.C.G. and StJohn, D.H., "The Loss of Dissolved Zirconium in Zirconium-refined Magnesium Alloys After Remelting." Metallurgical and Materials Transactions A. Vol. 40 (2009): 2470-2479.
173. Qian, M., StJohn, D.H. and Frost, M.T. A New Zirconium-Rich Master Alloy for the Grain Refinement of Magnesium Alloys in Magnesium Alloys and their Applications. Kainer, K.U., Editor, Weinheim, Germany, Wiley-VCH Verlag GmbH & Co. KGaA, 706-712, 2005.
174. Cao, P., Qian, M., StJohn, D.H. and Frost, M.T., "Uptake of Iron and its Effect on Grain Refinement of Pure Magnesium by Zirconium." Materials Science and Technology. Vol. 20 (2004): 585-592.
175. Sun, M., Easton, M.A., StJohn, D.H., Wu, G., Abbott, T.B. and Ding, W., "Grain Refinement of Magnesium Alloys by Mg-Zr Master Alloys: The Role of Alloy Chemistry and Zr Particle Number Density." Advanced Engineering Materials. Vol. 15 (2013): 373-378.
176. Qian, M., Zheng, L., Graham, D., Frost, M.T. and StJohn, D.H., "Settling of Undissolved Zirconium Particles in Pure Magnesium Melts." Journal of Light Metals. Vol. 1 (2001): 157-165.
177. Saha, P. and Viswanathan, S., "An Analysis of the Grain Refinement of Magnesium by Zirconium." TMS Annual Meeting and Exhibition Magnesium Technology Symposium. (2011): 175-180.
178. Bamberger, M., "Structural Refinement of Cast Magnesium Alloys." Materials Science and Technology. Vol. 17 (2001): 15-24.
179. Kabirian, F. and Mahmudi, R., "Effects of Zirconium Additions on the Microstructure of As-cast and Aged AZ91 Magnesium Alloy." Advanced Engineering Materials. Vol. 11 (2009): 189-193.
180. Zhang, S., "Phase constitution and morphologies of Mg-Zn-Zr alloy (MB15)." Acta Metallurgica Sinica. Vol. 25 (1989): A346-A351.
181. Flemings, M.C. Solidification Processing. New York, USA, McGraw-Hill, 1974.
182. Günther, R., Hartig, C. and Bormann, R., "Grain Refinement of AZ31 by (SiC)_p: Theoretical Calculation and Experiment." Acta Materialia. Vol. 54 (2006): 5591-5597.
183. Aliravci, C.A., Gruzleski, J.E. and Dimayuga, F.C., "Effect of Strontium on the Shrinkage Microporosity in Magnesium Sand Castings." AFS Transactions. Vol. 100 (1992): 353-362.
184. Liu, S.F., Li, B., Wang, X.H., Su, W. and Han, H., "Refinement Effect of Cerium, Calcium and Strontium in AZ91 Magnesium Alloy." Journal of Materials Processing Technology. Vol. 209 (2009): 3999-4004.
185. Wallace, J.F., Schwam, D. and Zhu, Y., "The Influence of Potential Grain Refiners on Magnesium Foundry Alloys." AFS Transactions. Vol. 111 (2003): 1061-1075.
186. Pan, Y., Liu, X. and Yang, H., "Sr Microalloying for Refining Grain Size of AZ91D Magnesium Alloy." Journal Wuhan University of Technology, Materials Science Edition. Vol. 22 (2007): 74-76.
187. Yang, M., Pan, F., Cheng, R. and Tang, A., "Effects of Solutionized Al-10Sr Master Alloys on Grain Refinement of AZ31 Magnesium Alloy." Journal of Alloys and Compounds. Vol. 461 (2008): 298-303.

188. Hirai, K.J., Somekawa, H.T., Takigawa, Y.N. and Higashi, K.J., "Effects of Ca and Sr addition on Mechanical Properties of a Cast AZ91 Magnesium Alloy at Room and Elevated Temperature." Materials Science and Engineering A. Vol. 403 (2005): 276-280.
189. Li, P., Tang, B. and Kandalova, E.G., "Microstructure and Properties of AZ91D Alloy with Ca Additions." Materials Letters. Vol. 59 (2005): 671-675.
190. Elsayed, A., Lee, K. and Ravindran, C., "Effect of Ca and Mn Additions on the Castability and Mechanical Properties of AZ91D Mg Alloy Permanent Mold Castings." AFS Transactions. Vol. 117 (2009): 659-672.
191. Loughnane, T., Zhang, D., Singh, D. and Neitzert, T., "The Effects of Grain Refinement on the Castability of Magnesium Permanent Mould Castings." TMS Annual Meeting and Exhibition Magnesium Technology Symposium. (2005): 309-314.
192. Ma, Y.T., Zhang, X.G. and Hao, H., "Effect of CaC₂ Particulates Concentration on Microstructure and Tensile Properties of Elemental Magnesium." Transactions of the Nonferrous Metals Society of China (English Edition). Vol. 18 (2008): s283-s287.
193. Du, J., Yang, J., Kuwabara, M., Li, W. and Peng, J., "Improvement of Grain Refining Efficiency for Mg-Al Alloy Modified by the Combination of Carbon and Calcium." Journal of Alloys and Compounds. Vol. 470 (2009): 134-140.
194. Du, J., Wang, H.L., Zhou, M.C. and Li, W.F., "Poisoning-free Effect of Calcium on Grain Refinement of Mg-3%Al Alloy Containing Trace Fe by Carbon Inoculation." Transactions of the Nonferrous Metals Society of China (English Edition). Vol. 23 (2013): 307-314.
195. I.G.Farbenindustrie. Patent Number: 359425, UK, (1931).
196. Nelson, C.E., "Grain Size Behavior in Magnesium Casting Alloys." Transactions of the American Foundrymen's Society. Vol. 56 (1948): 1-23.
197. Tiner, N., "Superheating of Magnesium Alloys." Metals Technology. Vol. 12 (1945): 1-19.
198. Cao, P., Qian, M. and StJohn, D.H., "Mechanism for Grain Refinement of Magnesium Alloys by Superheating." Scripta Materialia. Vol. 56 (2007): 633-636.
199. Tamura, Y., Yagi, J., Haitani, T., Motegi, T., Kono, N., Tamehiro, H. and Saito, H., "Observation of Manganese-bearing Particles in Molten AZ91 Magnesium Alloy by Rapid Solidification." Materials Transactions. Vol. 44 (2003): 552-557.
200. Motegi, T., "Grain-refining Mechanisms of Superheat-treatment of and Carbon Addition to Mg-Al-Zn alloys." Materials Science and Engineering A. Vol. 413-414 (2005): 408-411.
201. Motegi, T., Yano, E., Tamura, Y. and Sato, E., "Clarification of Grain Refining Mechanisms of Superheat-treated Mg-Al-Zn Alloy Castings." Materials Science Forum. Vol. 350 (2000): 191-198.
202. Schwam, D. and Zhu, X., "The Effect of Cooling Rate on Grain Size of Magnesium Alloys Cast in a Permanent Mold." AFS Transactions. Vol. 116 (2008): 841-848.
203. Achenbach, K., Nipper, H.A. and Piwowarsky, E., "Melting of Magnesium Casting Alloys/Beitraege zur Frage der Schmelzfuehrung von Magnesium-Gusslegierungen." Giesserei. Vol. 26 (1939): 621-628.
204. Tamura, Y., Haitani, T., Yano, E., Motegi, T., Kono, N. and Sato, E., "Grain Refinement of High-purity Mg-Al Alloy Ingots and Influences of Minor Amounts of Iron and Manganese on Cast Grain Size." Materials Transactions. Vol. 43 (2002): 2784-2788.

205. Mahoney, C.H., Tarr, A.L. and LeGrand, P.E., "A Study of Factors Influencing Grain Size in Magnesium Alloys and a Carbon Inoculation Method for Grain Refinement." Metals Technology. Vol. 12 (1945): 1-20.
206. Tamura, Y., Motegi, T., Kono, N. and Sato, E., "Effect of Minor Elements on Grain Size of Mg-9%Al Alloy." Materials Science Forum. Vol. 350 (2000): 199-204.
207. Holm, V.C.F. and Krynitsky, A.I., "Observation on the Control of Grain Size in Magnesium Casting Alloys." Journal of Research of the National Bureau of Standards. Vol. 39 (1947): 265-270.
208. Mahoney, C.H., Lee, H.C., Tarr, A.L. and Le Grand, P.E. 2436520, United States of America, (1948).
209. Cao, P., Qian, M. and StJohn, D.H., "Native Grain Refinement of Magnesium Alloys." Scripta Materialia. Vol. 53 (2005): 841-844.
210. Cao, P., Qian, M. and StJohn, D.H., "Effect of Manganese on Grain Refinement of Mg-Al Based Alloys." Scripta Materialia. Vol. 54 (2006): 1853-1858.
211. I.G.Farbenindustrie. Patent Number: 444757, Belgium, (1942).
212. Cao, P., Qian, M. and StJohn, D.H., "Grain Refinement of Magnesium-aluminium Alloys by Iron Inoculation." Materials Forum. Vol. 29 (2005): 301-305.
213. Cao, P., Qian, M. and StJohn, D.H., "Effect of Iron on Grain Refinement of High-purity Mg-Al Alloys." Scripta Materialia. Vol. 51 (2004): 125-129.
214. Karlsen, D.O., Oymo, D., Westengen, H., Pinfeld, P.M.D. and Strømhaug, S.I., "Development of Grain Refiner for Al-Containing Mg Alloys." 32nd Annual Conference of Metallurgists of CIM. (1993): 397-408.
215. Wang, Z., Kang, Y., Dong, W., Zhao, H., Liu, J. and Xu, Y., "Study of Grain Refinement and SiC Nanoparticle Reinforced Magnesium Alloys." International Conference on Magnesium - Science, Technology and Applications. (2005): 889-892.
216. Wang, Z.H., Zhang, X.L., Li, S.B., Liu, K. and Du, W.B., "Grain Refinement and Mechanism of Carbon inoculation in Mg-Al Magnesium Alloys." 12th IUMRS International Conference on Advanced Materials. (2014): 98-102.
217. Thomson, J.P., Liu, P., Sadayappan, M. and Sahoo, M., "Effect of C₂Cl₆ on Mechanical Properties and Microstructure of Gravity Permanent Mold Cast AZ91E." AFS Transactions. Vol. 112 (2004): 995-1006.
218. Jin, Q., Eom, J.P., Lim, S.G., Park, W.W. and You, B.S., "Reply to Comments on 'Grain Refining Mechanism of a Carbon Addition Method in a Mg-Al Magnesium Alloy'." Scripta Materialia. Vol. 52 (2005): 421-423.
219. Wang, Z.H., Kang, Y.L., Zhao, H.J. and Xue, Y., "Grain Refinement of Mg-Al Magnesium Alloys by Carbon Inoculation." Transactions of the Nonferrous Metals Society of China (English Edition). Vol. 16 (2006): 1851-1854.
220. Jin, Q., Eom, J.P., Lim, S.G., Park, W.W. and Yoo, B.S., "A Study on the Grain Refining Effects of Carbon Inoculation by C₂Cl₆ Addition on AZ31 Magnesium Alloy." 2nd Osaka International Conference on Platform Science and Technology for Advanced Magnesium Alloys. (2003): 587-592.
221. Kurfman, V.B., "Nucleation Catalysis by Carbon Additions to Magnesium Alloys." Transactions of the American Institute of Mining, Metallurgical and Petroleum Engineers. Vol. 221 (1961): 540-546.

222. Jin, Q., Eom, J.P., Lim, S.G., Park, W.W. and You, B.S., "Grain Refining Mechanism of a Carbon Addition Method in a Mg-Al Magnesium Alloy." Scripta Materialia. Vol. 49 (2003): 1129-1132.
223. Yichuan, P., Xiangfa, L. and Hua, Y., "Grain Refinement of an AZ63B Magnesium Alloy by an Al-1C Master Alloy." Zeitschrift fuer Metallkunde/Materials Research and Advanced Techniques. Vol. 96 (2005): 1398-1403.
224. Zhang, E., Wang, G.J., Xu, J.W. and Hu, Z.C., "Grain Refinement of AZ91D by Spinning Spray of Carbon Dioxide Gas and its Effect on Mechanical Property." Materials Science and Technology. Vol. 26 (2010): 956-961.
225. Chen, T., Jiang, X., Huang, H., Ma, Y., Li, Y. and Hao, Y., "Semisolid Microstructure of AZ91D Magnesium Alloy Refined by MgCO₃." International Journal of Metalcasting. Vol. 6 (2012): 43-54.
226. Ma, Y.Q., Chen, R.S. and Han, E.H., "Keys to Improving the Strength and Ductility of the AZ64 Magnesium Alloy." Materials Letters. Vol. 61 (2007): 2527-2530.
227. Li, K., Wang, F., Wang, Q. and Zhou, N.G., "Grain Refining Mechanism of Carbon Inoculation on Mg-Al Alloy." Journal of Shanghai Jiaotong University (Science). Vol. 17 (2012): 301-305.
228. Bae, J.H., Kim, Y.M., Yim, C.D., Kim, H.S. and You, B.S., "Effect of Inoculation Method of Refiner on the Grain Refinement of AZ91 Alloy." TMS Annual Meeting and Exhibition Magnesium Technology Symposium. (2013): 275-279.
229. Fisher, P.A. and Petch, J.H.T. Patent Number: 784445, UK, (1956).
230. Qian, M. and Cao, P., "Discussions on Grain Refinement of Magnesium Alloys by Carbon Inoculation." Scripta Materialia. Vol. 52 (2005): 415-419.
231. Lu, L., Dahle, A.K. and StJohn, D.H., "Heterogeneous Nucleation of Mg-Al Alloys." Scripta Materialia. Vol. 54 (2006): 2197-2201.
232. Suresh, M., Srinivasan, A., Pillai, U.T.S. and Pai, B.C., "The Effect of Charcoal Addition on the Grain Refinement and Ageing Response of Magnesium Alloy AZ91." Materials Science and Engineering A. Vol. 528 (2011): 8573-8578.
233. Suresh, M., Srinivasan, A., Ravi, K.R., Pillai, U.T.S. and Pai, B.C., "Microstructural Refinement and Tensile Properties Enhancement of Mg-3Al Alloy Using Charcoal Additions." Materials Science and Engineering A. Vol. 528 (2011): 2502-2508.
234. Wang, M., Du, J. and Li, W., "Poisoning Effect of Combined Addition of Fe and Mn on Carbon Inoculation of Mg-3%Al Alloy." International Conference on Biotechnology, Chemical and Materials Engineering, CBCME 2011. (2012): 226-230.
235. Nimityongskul, S., Jones, M., Choi, H., Lakes, R., Kou, S. and Li, X., "Grain Refining Mechanisms in Mg-Al Alloys with Al₄C₃ Microparticles." Materials Science and Engineering A. Vol. 527 (2010): 2104-2111.
236. Han, G., Liu, X. and Ding, H., "Grain Refinement of Mg-Al Based Alloys by a New Al-C Master Alloy." Journal of Alloys and Compounds. Vol. 467 (2009): 202-207.
237. Han, G. and Liu, X., "Duplex Nucleation in Mg-Al-Zn-Mn Alloys with Carbon Inoculation." Journal of Alloys and Compounds. Vol. 487 (2009): 194-197.
238. Du, J., Yang, J., Kuwabara, M., Li, W. and Peng, J., "Effects of Manganese and/or Carbon on the Grain Refinement of Mg-3Al Alloy." Materials Transactions. Vol. 49 (2008): 139-143.

239. Liu, S., Zhang, Y. and Han, H., "Role of Manganese on the Grain Refining Efficiency of AZ91D Magnesium Alloy Refined by Al_4C_3 ." Journal of Alloys and Compounds. Vol. 491 (2010): 325-329.
240. Du, J., Yang, J., Kuwabara, M., Li, W. and Peng, J., "Effect of Iron and/or Carbon on the Grain Refinement of Mg-3Al Alloy." Materials Transactions. Vol. 48 (2007): 2903-2908.
241. Du, J., Wang, M., Fan, T. and Li, W., "Influence of Fe on the Formation of Nucleation in Carbon-inoculated Mg-3% Al Alloy." International Conference on Advanced Engineering Materials and Technology, AEMT 2011. (2011): 1588-1593.
242. Du, J., Wang, M. and Li, W., "Effects of Fe Addition and Addition Sequence on Carbon Inoculation of Mg-3% Al Alloy." Journal of Alloys and Compounds. Vol. 502 (2010): 74-79.
243. Liu, B., Fan, Y., Peng, Q., Mi, G. and Wang, L., "Grain Refinement and Mechanism of $CaAl_{0.5}W_{0.5}$ Compound in Mg-Al Alloys." Rare Metals. Vol. 29 (2010): 630-634.
244. Chen, T.J., Ma, Y., Lv, W.B., Li, Y.D. and Hao, Y., "Grain Refinement of AM60B Magnesium Alloy by SiC Particles." Journal of Materials Science. Vol. 45 (2010): 6732-6738.
245. Luo, A., "Development of Matrix Grain Structure During the Solidification of a Mg(AZ91)/SiC_p Composite." Scripta Metallurgica et Materiala. Vol. 31 (1994): 1253-1258.
246. Erman, A., Groza, J., Li, X., Choi, H. and Cao, G., "Nanoparticle Effects in Cast Mg-1wt% SiC Nano-composites." Materials Science and Engineering A. Vol. 558 (2012): 39-43.
247. Nie, K.B., Wang, X.J., Hu, X.S., Xu, L., Wu, K. and Zheng, M.Y., "Microstructure and Mechanical Properties of SiC Nanoparticles Reinforced Magnesium Matrix Composites Fabricated by Ultrasonic Vibration." Materials Science and Engineering A. Vol. 528 (2011): 5278-5282.
248. Schiffl, A. and Easton, M.A., "Influence of SiC Particles on the Grain Refinement of an Mg-Al Alloy." Materials Science Forum. Vol. 618-619 (2009): 445-448.
249. Ravi, K.R., Gangadharan, S., Joseph, N.A., Sindhubairavi, S. and Anburaj, J., "Influence of Al_4C_3 Particles on Grain Refinement of Mg-3Al Alloys." Transactions of the Indian Institute of Metals. Vol. 65 (2012): 607-612.
250. Lee, K., Ravindran, C. and Murty, B.S., "Grain Refinement of AZ91E with TiB_2 and Al_4C_3 Additions." AFS Transactions. Vol. 118 (2010): 319-329.
251. Azad, A., Bichler, L. and Elsayed, A., "Effect of a Novel Al-SiC Grain Refiner on the Microstructure and Properties of AZ91E Magnesium Alloy." International Journal of Metalcasting. Vol. 7 (2013): 49-58.
252. Günther, R., Hartig, C., Anopuo, O., Hort, N. and Bormann, R., "The Role of Solutes for Grain Refinement by (SiC)_p: Experiment and Theoretical Calculation." TMS Annual Meeting and Exhibition Magnesium Technology Symposium. (2008): 95-99.
253. Luo, X.Q., Guo, H.M. and Yang, X.J., "Heterogeneous Nucleation for AZ91 with In situ Synthesis Al_4C_3 ." International Conference on Manufacturing Science and Engineering, ICMSE 2009. (2010): 1069-1072.
254. Elecktron, M. 608942, United Kingdom, (1944).
255. Suresh, M., Srinivasan, A., Ravi, K.R., Pillai, U.T.S. and Pai, B.C., "Influence of Boron Addition on the Grain Refinement and Mechanical Properties of AZ91 Mg Alloy." Materials Science and Engineering A. Vol. 525 (2009): 207-210.

256. Nishino, N., Kawahara, H., Shimizu, Y. and Iwahori, H. Grain Refinement of Magnesium Casting Alloys by Boron Addition in Magnesium Alloys and their Applications. Kainer, K.U., Editor, Weinheim, Germany, Wiley-VCH Verlag GmbH & Co. KGaA, 59-64, 2000.
257. Zeng, X., Wang, Y., Ding, W. and Luo, A. Patent Number: 8016967, USA, (2011).
258. Elsayed, A., Murty, B.S. and Ravindran, C., "Effects of Aluminium-Titanium-Boron Based Grain Refiners on AZ91E Magnesium Alloy Grain Size and Microstructure." International Journal of Metal Casting. Vol. 5 (2011): 29-41.
259. Vlasceanu, M., Lun Sin, S., Elsayed, A. and Ravindran, C., "Effect of Al-5Ti-1B on Grain Refinement, Dendrite Coherency and Porosity of AZ91E Magnesium Alloy." International Journal of Cast Metals Research. Vol. 28 (2014): 39-46.
260. Elsayed, A., Ravindran, C. and Murty, B.S., "Effect of Al-Ti-B Based Master Alloys on Grain Refinement and Hot Tearing Susceptibility of AZ91E Magnesium Alloy." Materials Science Forum. Vol. 690 (2011): 351-354.
261. Wang, Y., Wang, H.Y., Ma, B.X., Xiu, K. and Jiang, Q.C., "Effect of Ti/B on Fabricating TiB₂p/AZ91 Composites by Employing a TiB₂p/Al Master Alloy." Journal of Alloys and Compounds. Vol. 422 (2006): 178-183.
262. Cao, W., Zhang, C., Fan, T. and Zhang, D., "In-situ Synthesis of TiB₂/Mg Composite by Flux-assisted Synthesis Reaction of the Al-Ti-B System in Molten Magnesium." Key Engineering Materials. Vol. 351 (2007): 166-170.
263. Zhang, A., Hao, H., Li, M., Song, Y. and Zhang, X., "Effects of Al-3Ti-3B Alloy on Grain Refinement of AZ31 Magnesium Alloy." Tezhong Zhuzao Ji Youse Hejin/Special Casting and Nonferrous Alloys. Vol. 31 (2011): 491-495.
264. Chen, T., Wang, R., Ma, Y. and Hao, Y., "Grain Refining Technique of AM60B Alloy by Al-Ti-B Master Alloy." China Foundry. Vol. 8 (2011): 380-385.
265. Chen, T.J., Wang, R.Q., Ma, Y. and Hao, Y., "Grain Refinement of AZ91D Magnesium Alloy by Al-Ti-B Master Alloy and its Effect on Mechanical Properties." Materials and Design. Vol. 34 (2012): 637-648.
266. Elsayed, A., Ravindran, C. and Murty, B.S., "Grain Refinement and Fading of Aluminum-Titanium-Boron Based Refiner on AZ91E Magnesium Alloy." AFS Transactions. Vol. 118 (2010): 311-317.
267. Ding, H., Li, H. and Liu, X., "Different Elements-induced Destabilisation of TiC and its Application on the Grain Refinement of Mg-Al Alloys." Journal of Alloys and Compounds. Vol. 485 (2009): 285-289.
268. Han, G., Liu, X.F. and Ding, H.M., "Grain Refinement of AZ31 Magnesium Alloy by New Al-Ti-C Master Alloys." Transactions of the Nonferrous Metals Society of China (English Edition). Vol. 19 (2009): 1057-1064.
269. Boily, S. and Blouin, M. Patent Number: 433942, USA, (2004).
270. Saha, S. and Ravindran, C., "Grain Refinement of AZ91E and Mg-9 wt.% Al Binary Alloys Using Zinc Oxide." AFS Transactions. Vol. 118 (2014).
271. Lee, K., "A Study on Grain Refinement of AZ91E Magnesium Alloy with Al-5TiB₂, Al-Al₄C₃ and ZnO Additions." MASc. Thesis, Ryerson University (2010): 1-90.
272. Qin, G.W., Ren, Y., Huang, W., Li, S. and Pei, W., "Grain Refining Mechanism of Al-containing Mg Alloys with the Addition of Mn-Al Alloys." Journal of Alloys and Compounds. Vol. 507 (2010): 410-413.

273. Hultgren, R. and Mitchell, D.W., "Grain Refinement of Magnesium Alloys Without Superheating." Metals Technology. Vol. 161 (1945): 323-327.
274. Du, J., Wang, M., Zhou, M. and Li, W., "Evolutions of Grain Size and Nucleating Particles in Carbon-inoculated Mg-3% Al Alloy." Journal of Alloys and Compounds. Vol. 592 (2014): 313-318.
275. Li, K., Sun, Z.G., Wang, F., Zhou, N.G. and Hu, X.W., "First-principles Calculations on Mg/Al₄C₃ Interfaces." Applied Surface Science. Vol. 270 (2013): 584-589.
276. Subramanian, J., Guan, K.C., Kuma, J. and Gupta, M., "Feasibility Study on Utilizing Carbon Dioxide During the Processing of Mg-Al Alloys." Journal of Materials Processing Technology. Vol. 211 (2011): 1416-1422.
277. Han, G., Ma, G. and Liu, X., "Effect of Manganese on the Microstructure of Mg-3Al Alloy." Journal of Alloys and Compounds. Vol. 486 (2009): 136-141.
278. Laser, T., Nürnberg, M.R., Janz, A., Hartig, C., Letzig, D., Schmid-Fetzer, R. and Bormann, R., "The Influence of Manganese on the Microstructure and Mechanical Properties of AZ31 Gravity Die Cast Alloys." Acta Materialia. Vol. 54 (2006): 3033-3041.
279. Luo, A., "Heterogeneous Nucleation and Grain Refinement in Cast Mg(AZ91)/SiCp Metal Matrix Composites." Canadian Metallurgical Quarterly. Vol. 35 (1996): 375-383.
280. Viala, J.C., Claveyrolas, G., Bosselet, F. and Bouix, J., "Chemical Behaviour of Carbon Fibres in Magnesium Base Mg-Al Alloys." Journal of Materials Science. Vol. 35 (2000): 1813-1825.
281. Ferro, A.C. and Derby, B., "Wetting Behaviour in the Al-Si/SiC System: Interface Reactions and Solubility Effects." Acta Metallurgica Et Materialia. Vol. 43 (1995): 3061-3073.
282. Laurent, V., Chatain, D. and Eustathopoulos, N., "Wettability of SiC by Aluminium and Al-Si Alloys." Journal of Materials Science. Vol. 22 (1987): 244-250.
283. Laurent, V., Chatain, D. and Eustathopoulos, N., "Wettability of SiO₂ and Oxidized SiC by Aluminium." Materials Science and Engineering A. Vol. 135 (1991): 89-94.
284. Laurent, V., Rado, C. and Eustathopoulos, N., "Wetting Kinetics and Bonding of Al and Al Alloys on α -SiC." Materials Science and Engineering A. Vol. 205 (1996): 1-8.
285. Mortensen, A., "Interfacial Phenomena in the Solidification Processing of Metal Matrix Composites." Materials Science and Engineering A. Vol. 135 (1991): 1-11.
286. Oh, S.Y., Cornie, J.A. and Russell, K.C., "Wetting of Ceramic Particulates with Liquid Aluminum Alloys: Part I. Experimental Techniques." Metallurgical Transactions A. Vol. 20 (1989): 527-532.
287. Oh, S.Y., Cornie, J.A. and Russell, K.C., "Wetting of Ceramic Particulates with Liquid Aluminum Alloys: Part II. Study of Wettability." Metallurgical Transactions A. Vol. 20 (1989): 533-541.
288. Viala, J.C., Fortier, P. and Bouix, J., "Stable and Metastable Phase Equilibria in the Chemical Interaction Between Aluminium and Silicon Carbide." Journal of Materials Science. Vol. 25 (1990): 1842-1850.
289. Alonso, A., Pamies, A., Narciso, J., Garcia-Cordovilla, C. and Louis, E., "Evaluation of the Wettability of Liquid Aluminum with Ceramic Particulates (SiC, TiC, Al₂O₃) by Means of Pressure Infiltration." Metallurgical Transactions A. Vol. 24 (1993): 1423-1432.

290. Eustathopoulos, N., Drevet, B. and Nicholas, M.G. Wettability at High Temperatures. Amsterdam, The Netherlands, Pergamon, 1999.
291. Naidich, Y.V., Chubashov, Y.N., Ishchuk, N.F. and Krasovskii, V.P., "Wetting of Some Nonmetallic Materials by Aluminum." Soviet Powder Metallurgy and Metal Ceramics. Vol. 22 (1983): 481-483.
292. Peteves, S.D., Tambuyser, P., Helbach, P., Audier, M., Laurent, V. and Chatain, D., "Microstructure and Microchemistry of the Al/SiC Interface." Journal of Materials Science. Vol. 25 (1990): 3765-3772.
293. Keene, B.J., "Review of Data for the Surface Tension of Pure Metals." International Materials Reviews. Vol. 38 (1993): 157-192.
294. Dou, L., Yuan, Z., Li, J. and Wang, X., "Surface Tension of Molten Al-Si Alloy at Temperatures Ranging from 923 to 1123 K." Chinese Science Bulletin. Vol. 53 (2008): 2593-2598.
295. Rivollet, I., Chatain, D. and Eustathopoulos, N., "Simultaneous Measurement of Contact Angles and Work of Adhesion in Metal-ceramic Systems by the Immersion-emersion Technique." Journal of Materials Science. Vol. 25 (1990): 3179-3185.
296. Wang, D.J. and Wu, S.T., "The Influence of Oxidation on the Wettability of Aluminum on Sapphire." Acta Metallurgica Et Materialia. Vol. 42 (1994): 4029-4034.
297. Pai, B.C., Ramani, G., Pillai, R.M. and Satyanarayana, K.G., "Role of Magnesium in Cast Aluminium Alloy Matrix Composites." Journal of Materials Science. Vol. 30 (1995): 1903-1911.
298. Goicoechea, J., Garcia-Cordovilla, C., Louis, E. and Pamies, A., "Surface Tension of Binary and Ternary Aluminium Alloys of the Systems Al-Si-Mg and Al-Zn-Mg." Journal of Materials Science. Vol. 27 (1992): 5247-5252.
299. Anson, J.P., Drew, R.A.L. and Gruzleski, J.E., "Surface Tension of Molten Aluminum and Al-Si-Mg Alloy Under Vacuum and Hydrogen Atmospheres." Metallurgical and Materials Transactions B. Vol. 30 (1999): 1027-1032.
300. Chawake, N., Pinto, L.D., Srivastav, A.K., Akkiraju, K., Murty, B.S. and Kottada, R.S., "On Joule Heating During Spark Plasma Sintering of Metal Powders." Scripta Materialia. Vol. 93 (2014): 52-55.
301. Saheb, N., Iqbal, Z., Khalil, A., Hakeem, A.S., Al Aqeeli, N., Laoui, T., Al-Qutub, A. and Kirchner, R., "Spark Plasma Sintering of Metals and Metal Matrix Nanocomposites: A Review." Journal of Nanomaterials. Vol. 2012 (2012): Article ID 983470.
302. Omori, M., "Sintering, Consolidation, Reaction and Crystal Growth by the Spark Plasma System (SPS)." Materials Science and Engineering A. Vol. 287 (2000): 183-188.
303. Iqbal, N., van Dijk, N.H., Verhoeven, V.W.J., Hansen, T., Katgerman, L. and Kearley, G.J., "Periodic Structural Fluctuations During the Solidification of Aluminum Alloys Studied by Neutron Diffraction." Materials Science and Engineering A. Vol. 367 (2004): 82-88.
304. Iqbal, N., van Dijk, N.H., Verhoeven, V.W.J., Montfrooij, W., Hansen, T., Katgerman, L. and Kearley, G.J., "Experimental Study of Ordering Kinetics in Aluminum Alloys During Solidification." Acta Materialia. Vol. 51 (2003): 4497-4504.
305. Kasprzak, W., Sediako, D., Sahoo, M., Walker, M. and Swainson, I., "Characterization of Hypereutectic Al-19%Si Alloy Solidification Process Using In-situ Neutron Diffraction and Thermal Analysis Techniques." TMS Annual Meeting and Exhibition. (2010): 93-104.

306. Kasprzak, W., Sediako, D., Walker, M., Sahoo, M. and Swainson, I., "Solidification Analysis of an Al-19 Pct Si Alloy Using In-situ Neutron Diffraction." Metallurgical and Materials Transactions A. Vol. 42 (2011): 1854-1862.
307. Sediako, D., Kasprzak, W., Swainson, I. and Garlea, O., "Solidification Analysis of Al-Si Alloys Modified with Addition of Cu Using In-situ Neutron Diffraction." TMS Annual Meeting and Exhibition. (2011): 279-289.
308. D'Elia, F., Ravindran, C., Sediako, D. and Donaberger, R., "Solidification Analysis of Al-5 wt-%Cu Alloy Using *In Situ* Neutron Diffraction." Canadian Metallurgical Quarterly. Vol. 54 (2014): 9-15.
309. D'Elia, F., Ravindran, C., Sediako, D., Kainer, K.U. and Hort, N., "Hot Tearing Mechanisms of B206 Aluminum-Copper Alloy." Materials and Design. Vol. 64 (2014): 44-55.
310. Oosthuizen, P. and Naylor, D. Introduction to Convective Heat Transfer Analysis. New York, USA, McGraw-Hill, 1999.
311. Cullity, B.D. Elements of X-ray Diffraction. Reading, USA, Addison-Wesley, 1956.
312. Kuo, J.H., Weng, R.J. and Hwang, W.S., "Effects of Solid Fraction on the Heat Transfer Coefficient at the Casting/Mold Interface for Permanent Mold Casting of AZ91D Magnesium Alloy." Materials Transactions. Vol. 47 (2006): 2547-2554.
313. Weng, R.J., Kuo, J.H., Wu, C.H. and Hwang, W.S., "Effects of Solid Fraction and Operating Pressure on the Heat Transfer Coefficient at the Casting/Mold Interface for AZ91D Magnesium Alloy." AFS Transactions. Vol. 113 (2005): 901-910.
314. SolidCast Training Course Workbook. Slinger, USA, Finite Solutions Inc., 2010.
315. Berg, J.C. Wettability. New York, Marcel Dekker Inc, 1993.
316. Iseki, T., Kameda, T. and Maruyama, T., "Interfacial Reactions Between SiC and Aluminium During Joining." Journal of Materials Science. Vol. 19 (1984): 1692-1698.
317. Warren, R. and Andersson, C.H., "Silicon Carbide Fibres and their Potential for Use in Composite Materials. Part II." Composites. Vol. 15 (1984): 101-111.
318. Lloyd, D.J. and Jin, I., "Method of Assessing the Reactivity Between SiC and Molten Al." Metallurgical Transactions A. Vol. 19 (1988): 3107-3109.
319. Li, J., Geng, H., Yang, Z., Wang, Y., Cui, F. and Sun, C., "Effects of Y on Microstructure and Mechanical Properties of AZ91 Magnesium Alloy." Foundry. Vol. 54 (2005): 53-56.
320. Gauthier, G. Patent Number: 2224151, USA, (1940).
321. Cao, P., Qian, M. and StJohn, D.H., "Grain Coarsening of Magnesium Alloys by Beryllium." Scripta Materialia. Vol. 51 (2004): 647-651.
322. X'Pert HighScore Plus. Almelo, The Netherlands, PANalytical, 2009.